

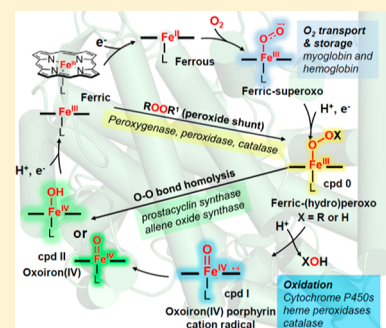
## Oxygen Activation and Radical Transformations in Heme Proteins and Metalloporphyrins

Xiongyi Huang<sup>†,‡,✉</sup> and John T. Groves<sup>\*,†,✉</sup>

<sup>†</sup>Department of Chemistry, Princeton University, Princeton, New Jersey 08544, United States

<sup>‡</sup>Department of Chemistry, California Institute of Technology, Pasadena, California 91125, United States

**ABSTRACT:** As a result of the adaptation of life to an aerobic environment, nature has evolved a panoply of metalloproteins for oxidative metabolism and protection against reactive oxygen species. Despite the diverse structures and functions of these proteins, they share common mechanistic grounds. An open-shell transition metal like iron or copper is employed to interact with O<sub>2</sub> and its derived intermediates such as hydrogen peroxide to afford a variety of metal–oxygen intermediates. These reactive intermediates, including metal-superoxo, -(hydro)peroxo, and high-valent metal–oxo species, are the basis for the various biological functions of O<sub>2</sub>-utilizing metalloproteins. Collectively, these processes are called oxygen activation. Much of our understanding of the reactivity of these reactive intermediates has come from the study of heme-containing proteins and related metalloporphyrin compounds. These studies not only have deepened our understanding of various functions of heme proteins, such as O<sub>2</sub> storage and transport, degradation of reactive oxygen species, redox signaling, and biological oxygenation, etc., but also have driven the development of bioinorganic chemistry and biomimetic catalysis. In this review, we survey the range of O<sub>2</sub> activation processes mediated by heme proteins and model compounds with a focus on recent progress in the characterization and reactivity of important iron–oxygen intermediates. Representative reactions initiated by these reactive intermediates as well as some context from prior decades will also be presented. We will discuss the fundamental mechanistic features of these transformations and delineate the underlying structural and electronic factors that contribute to the spectrum of reactivities that has been observed in nature as well as those that have been invented using these paradigms. Given the recent developments in biocatalysis for non-natural chemistries and the renaissance of radical chemistry in organic synthesis, we envision that new enzymatic and synthetic transformations will emerge based on the radical processes mediated by metalloproteins and their synthetic analogs.



### CONTENTS

1. Introduction	2492		
2. Key Intermediates Involved in O <sub>2</sub> Activation by Heme Proteins and Model Compounds	2493		
2.1. Oxy–Ferrous (Superoxo-ferric) Intermediates	2493		
2.1.1. Structural Features	2493		
2.1.2. Nature of Fe–O <sub>2</sub> Bonding	2493		
2.1.3. Metal-Dioxygen Intermediates of Metalloporphyrins	2494		
2.2. Ferric-(hydro)peroxo Intermediates	2496		
2.2.1. Ferric-(hydro)peroxo Intermediates of Heme Proteins	2496		
2.2.2. Ferric-(hydro)peroxo Intermediates of Metalloporphyrins	2496		
2.3. Heterolytic O–O Bond Cleavage of Ferric–Hydroperoxo Intermediates	2498		
2.3.1. O–O Bond Cleavage of cpd 0 to Generate Cpd I in Heme Proteins	2498		
2.3.2. O–O Bond Cleavage in Metal-Peroxo Porphyrin Complexes	2499		
2.4. Compound I: Oxoiron(IV) Porphyrin Cation Radicals	2502		
2.4.1. Compounds I of Heme Proteins	2502		
2.4.2. Compounds I of Iron Porphyrins	2502		
2.4.3. Manganese Porphyrin Analogues of Compound I	2505		
2.5. Compound II and Its Protonation State–ferryl or Hydroxoiron(IV)	2506		
2.6. Preventing Protein Oxidative Damage by Cpd I	2508		
3. C–H Functionalization Reactions Mediated by Oxoiron(IV) Porphyrin Cation Radicals (Compound I)	2508		
3.1. Factors that Affect Oxoiron(IV) Porphyrin Cation Radical Reactivity for HAT	2509		
3.1.1. Thermodynamic Properties of Cpd I	2509		
3.1.2. Effect of Axial Ligands and Porphyrin Peripheral Substituents on Cpd I Reactivity	2510		
3.1.3. Correlation of Thermodynamic Driving Force with Rate Constants of HAT	2510		
3.1.4. Two-State and Multistate Reactivity	2511		

**Special Issue:** Oxygen Reduction and Activation in Catalysis

**Received:** June 21, 2017

**Published:** December 29, 2017

3.1.5. Quantum Tunneling in Hydrogen Atom Transfer	2513
3.2. Intermediacy of Substrate Radicals–Oxygen Rebound	2514
3.3. Redirecting Substrate Radicals to Reaction Pathways Other than Oxygen Rebound	2517
3.3.1. Decarboxylation Mediated by P450 OleT <sub>JE</sub>	2517
3.3.2. P450-Catalyzed Desaturation Reactions	2518
3.3.3. Oxidative Rearrangement Catalyzed by PntM (CYP161C2)	2519
3.3.4. Mn-Catalyzed C–H Halogenations	2520
3.4. Oxygen-Atom Transfer Reactions Catalyzed by Compound I	2521
3.5. O–O Bond Formation Mediated by Oxometalloporphyrins	2523
3.5.1. Oxygen Evolution from Oxometal Complexes	2523
3.5.2. Chlorite Dismutase	2525
3.6. Single Electron Transfer (SET) Reactions of Cpd I	2527
4. Reactions Mediated by Heme–Oxygen Intermediates Other than Cpd I	2528
4.1. Homolytic O–O Bond Cleavage of Peroxides by Heme Proteins	2528
4.2. Reactions Initiated by Ferric-Superoxo Intermediates	2531
4.3. O <sub>2</sub> Reduction Catalyzed by Heme/Cu Terminal Oxidases and Related Model Compounds	2532
5. Conclusions and Outlook	2536
Author Information	2537
Corresponding Author	2537
ORCID	2537
Notes	2537
Biographies	2537
Acknowledgments	2537
Abbreviations	2537
References	2537

## 1. INTRODUCTION

The highly exergonic four-electron reduction of oxygen to water has an enthalpy change of  $-80$  kcal/mol. The biochemical processes that mediate this reduction provide the energy that sustains all aerobic organisms on earth.<sup>1</sup> Paradoxically,

however, the utilization of O<sub>2</sub>-derived energy in aerobic biology represents a significant challenge due to the thermodynamic stability of O<sub>2</sub> in its triplet ground state.<sup>1–5</sup> The first one-electron reduction of O<sub>2</sub> to superoxide ion is endergonic by 7.8 kcal/mol, which makes the stepwise, one-electron processes unfavorable (Figure 1). Direct 2e<sup>−</sup> reactions between ground-state O<sub>2</sub> (*S* = 1) and many closed-shell organic substrates are spin forbidden unless a stepwise route via diradical intermediates is available. To overcome these difficulties of exploiting O<sub>2</sub>, nature has evolved families of enzymes to transport O<sub>2</sub> and to catalyze, manipulate, and control its reduction. A majority of these enzymes contain transition metals such as iron, copper, and sometimes manganese with unpaired *d*-electrons.<sup>6</sup> These open-shell systems with variable oxidation and electronic states can facilitate the activation of triplet ground-state oxygen and participate at different stages of O<sub>2</sub> reduction (Figure 1). The study of these processes, known collectively as oxygen activation, is a central theme in biology and has driven the development of metallobiochemistry and bioinorganic chemistry since their inception.

Heme-containing proteins have assumed a key position in our understanding of O<sub>2</sub>-activation mediated by metalloproteins. The general catalytic cycle for oxygen reduction is shown in Figure 2, which starts with the binding of O<sub>2</sub> to a ferrous heme to afford a ferric-superoxo adduct, followed by reduction to ferric-hydroperoxo, and high-valent, iron-oxo (ferryl) intermediates via O–O bond scission. The rich chemistry that occurs between the heme iron and dioxygen provides the basis for the diverse roles of heme proteins in O<sub>2</sub> metabolism, including O<sub>2</sub> transport (myoglobin and hemoglobin), reduction of O<sub>2</sub> to water (cytochrome *c* oxidases), degradation of reactive oxygen species (catalases and peroxidases), and catalysis of a variety of oxygenation reactions of organic substrates such as steroid hydroxylation, a monooxygenation typical of cytochrome P450s, and dioxygenation reactions (heme dioxygenases).<sup>7</sup> The use of metal-cofactors to effect serial reductive activation of O<sub>2</sub> is not limited to heme proteins but represents a general strategy employed by nature to harness the oxidation power of dioxygen. The reaction sequence and reactive intermediates similar to that shown in Figure 2a are widely present in a variety of O<sub>2</sub>-activating metalloenzymes such as nonheme iron oxygenases and copper-containing oxygenases and oxidases (Figure 2b).<sup>6,8–11</sup> Accordingly, in spite of their diverse structures and

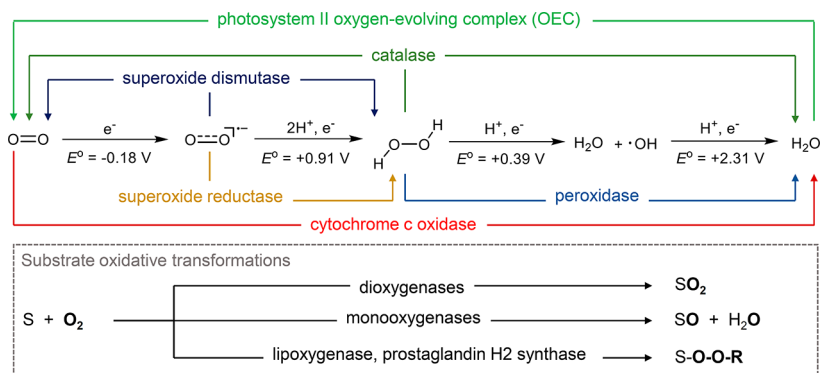


**Figure 1.** Reduction sequence of O<sub>2</sub> and representative metalloenzymes related to O<sub>2</sub> activation. Reduction potentials shown are versus normal hydrogen electrode (NHE).<sup>5</sup>

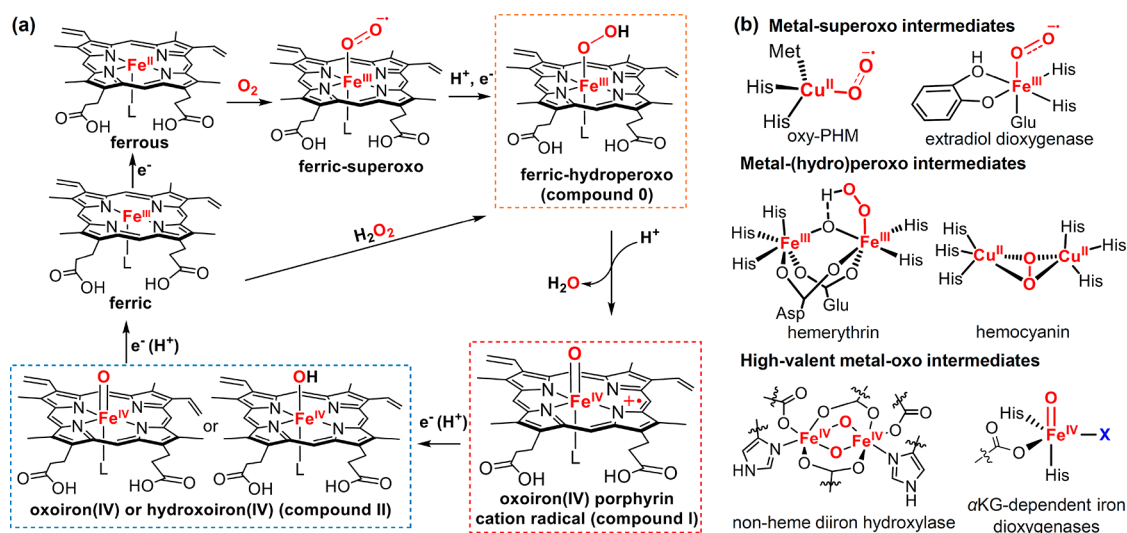


**Figure 2.** (a) Interaction of dioxygen with heme and heme–oxygen intermediates in heme proteins. (b) Representative metal–oxygen intermediates in metalloproteins (PHM: peptidylglycine  $\alpha$ -hydroxylating monooxygenase).

functions, these metalloproteins share many common mechanistic grounds in terms of O<sub>2</sub> activation and catalysis.<sup>1,6,12</sup>

In this interpretive review, we will survey the range of O<sub>2</sub> activation processes mediated by heme proteins and related model compounds with a focus on recent progress in the characterization and reactivity of important iron–oxygen intermediates through mid-2017. Key aspects of background material in the field will also be presented to provide context and perspective. The underlying structural and electronic factors contributing to O<sub>2</sub> activation chemistry will be delineated. The topics of O<sub>2</sub>-activation and oxidative transformations mediated by heme proteins and metalloporphyrins have been extensively reviewed previously.<sup>3,4,7,13–32</sup> While most of these reviews focus on either heme proteins or synthetic models, this review will provide a comprehensive perspective of the spectrum of oxidative transformations mediated by the iron–oxygen species in both heme proteins and analogous synthetic model compounds. We will discuss the fundamental mechanistic features of these transformations and how a variety of oxidative pathways are developed from a common mechanistic foundation. For model compounds, we will mainly focus on metalloporphyrins. Other porphyrinoid ligands, such as corrolazines, porphyrazines, and phthalocyanines will not be discussed in detail. Readers can refer to several recent reviews on these families of model compounds.<sup>29,33–35</sup>

## 2. KEY INTERMEDIATES INVOLVED IN O<sub>2</sub> ACTIVATION BY HEME PROTEINS AND MODEL COMPOUNDS

### 2.1. Oxy–Ferrous (Superoxoferric) Intermediates

**2.1.1. Structural Features.** The first step of O<sub>2</sub> activation by heme proteins is the binding of dioxygen to the heme iron, forming an oxy–ferrous intermediate (or ferric-superoxo intermediate, see discussions in section 2.1.2). Heme proteins exhibit varied O<sub>2</sub> binding features. For instance, O<sub>2</sub> transport proteins like hemoglobin and myoglobin have very high O<sub>2</sub> association rate constants (10<sup>7</sup> M<sup>-1</sup> s<sup>-1</sup>) and moderate to high dissociation rate constants (0.1–20 s<sup>-1</sup>).<sup>36,37</sup> Heme-containing NO or CO sensor proteins are tuned to coordinate these tighter-binding molecules and show little binding of O<sub>2</sub> even in

O<sub>2</sub>-saturated solutions.<sup>38,39</sup> In P450s, O<sub>2</sub> binds to ferrous heme with rate constants around 10<sup>6</sup> M<sup>-1</sup> s<sup>-1</sup>,<sup>40</sup> and the resulting ferric-superoxo intermediate is prone to undergo autoxidation to the ferric state if it is not further reduced to form the ferric hydroperoxo compound 0.<sup>41</sup> It is important to note that heme in the ferric state has a very weak oxygen-affinity and will not bind oxygen at ambient temperatures. It is the ease of electron transfer from iron to O<sub>2</sub> that is important for the formation of the ferric-superoxo intermediate and thus O<sub>2</sub> binding. For instance, highly electron-withdrawing Fe(II) porphyrin such as Fe(TPPBr<sub>8</sub>) is very inert toward dioxygen (TPPBr<sub>8</sub> =  $\beta$ -pyrrole brominated 5,10,15,20-tetrakis(pentafluorophenyl)-porphyrin).<sup>42</sup>

The structural and electronic properties of the ferric-superoxo intermediate are crucial for understanding the O<sub>2</sub> activation in heme proteins. In the 1930s, Pauling and Coryell found that oxygenated hemoglobin (oxy-Hb) was diamagnetic and proposed that dioxygen was bound to heme in a bent, end-on mode.<sup>43,44</sup> This geometric feature was confirmed by an oxy–ferrous model compound synthesized by Collman and by crystal structures of oxy-Mb and oxy-Hb solved by Phillips and Shaanan, respectively.<sup>45–47</sup> Following these pioneering efforts, crystal structures of ferric-superoxo intermediates have been solved for a number of heme proteins (Figure 3).<sup>48–52</sup> All reported structures reveal an end-on coordination of dioxygen to the iron with a Fe–O bond distance around 1.8 Å, an O–O bond distance ranging from 1.22 to 1.30 Å, and an Fe–O–O angle ranging from 110° to 160°.

**2.1.2. Nature of Fe–O<sub>2</sub> Bonding.** The electronic structure of Fe–O<sub>2</sub> heme complexes is remarkable because it forms a species with a singlet electronic ground state arising from the combination of high-spin ( $S = 2$ ) ferrous heme and triplet O<sub>2</sub>. The nature of Fe–O<sub>2</sub> bonding has been a subject of active debate for decades.<sup>53</sup> There are three models to explain Fe–O<sub>2</sub> bonding (Figure 4).<sup>54</sup> In Pauling's model, an  $S = 0$  state was assigned to both a dioxygen and a ferrous center.<sup>43,44</sup> In contrast, Weiss proposed that the Fe–O<sub>2</sub> species would be best described as a ferric-superoxide complex in which a low-spin ( $S = 1/2$ ) ferric center is antiferromagnetically coupled to a doublet superoxide anion O<sub>2</sub><sup>-</sup>.<sup>55</sup> In a third model initially suggested by McClure and refined by Goddard, an

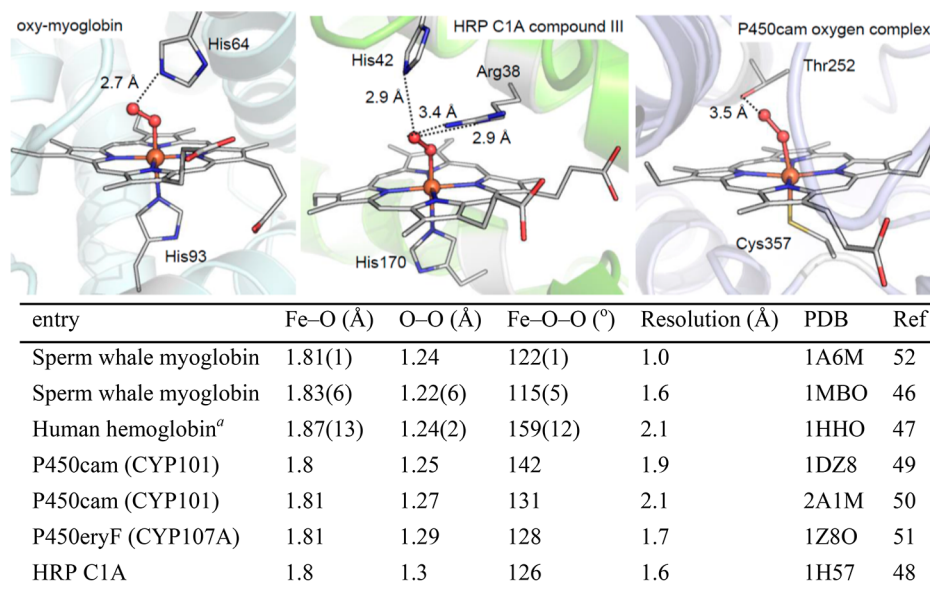


**Figure 3.** Structural parameters of ferric-superoxo intermediates of representative heme proteins (oxy-myoglobin, PDB: 1A6M; HRP compound III, PDB: 1H57; P450cam oxygen complex, PDB: 1DZ8). <sup>a</sup>Data presented are for the  $\beta$  subunit of oxyhemoglobin in structure 1HHO.

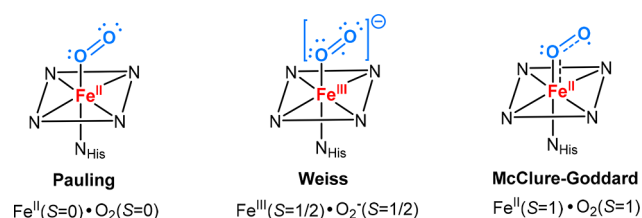


**Figure 4.** Three models for Fe–O<sub>2</sub> bonding in the ferric-superoxo intermediate. Adapted from ref 64. Copyright 2013 American Chemical Society.

intermediate-spin ( $S = 1$ ) ferrous center antiferromagnetically coupled to <sup>3</sup>O<sub>2</sub> in a 3-center-4-electron bond affords the singlet Fe–O<sub>2</sub> species (“Ozone model”).<sup>56,57</sup>

Mössbauer studies have lent support to the Weiss model. The Mössbauer parameters of oxyhemoglobin (isomer shift  $\delta = 0.2$ – $0.3$  mm/s, quadrupole splitting  $\Delta E_{\text{Q}} = 2.00$ – $2.20$  mm/s), first measured by Lang and Marshall, are consistent with a low-spin ferric center.<sup>58</sup> Sharrock and co-workers have reported similar parameters for oxygenated reduced P450cam ( $\delta = 0.31$  mm/s and  $\Delta E_{\text{Q}} = 2.15$  mm/s at 4.2K).<sup>59</sup> The Weiss model is further supported by resonance Raman spectroscopic studies, in which a ferric center was indicated by the oxidation state marker band of oxyHb ( $\nu = 1377$  cm<sup>-1</sup>).<sup>60–62</sup>

Through density functional theory (DFT) and valence bond (VB) approaches, Shaik has shown that Fe–O<sub>2</sub> contains a dative  $\sigma(\text{Fe}–\text{O})$  interaction between vacant  $3d_z^2$  and  $\pi^*(\text{O}_2^-)$  and a rather weak  $\pi$  interaction between  $d_{yz}(\text{Fe})$  and  $\pi_1^*(\text{O}_2)$ .<sup>53</sup> The H-bonding from a distal histidine residue (His64) in oxy-Mb and the electrostatic polarization from protein backbone stabilizes the negative charges on O<sub>2</sub>. Although Fe–O<sub>2</sub> primarily follows the bonding scheme of the Weiss model, the VB analysis showed a mixing of the other two models, whose contributions depend on protein hosts and active site environments, making Fe–O<sub>2</sub> difficult to describe according to canonical oxidation state formalisms. Recent Fe K-edge X-ray absorption spectroscopy (XAS) studies by Sarangi et al. have shown that oxy-Hb is best described as a ferric

superoxide species (Weiss model) in solution. However, in crystalline oxy-Hb, the Fe K pre-edge feature indicates Fe<sup>2+</sup>  $S = 0$  character, consistent with the Pauling model. This surprising change of electronic configuration with environment supports the multiconfigurational description.<sup>63</sup> The impact of local environment on the Fe–O<sub>2</sub> bonding was also revealed by an iron L-edge XAS study of a ferric-superoxo “picket fence” porphyrin with 1-methylimidazole (1-MeIm) axial ligand, Fe(TpivPP)(1-MeIm)O<sub>2</sub> (TpivPP = *meso*-tetra( $\alpha,\alpha,\alpha,\alpha$ -*O*-pivalamidophenyl)porphyrin, Figure 5b).<sup>64</sup> The results showed a strong  $\pi$ -interaction between  $d_{yz}(\text{Fe})$  and  $\pi_1^*(\text{O}_2)$  as opposed to the weak  $\pi$ -interaction calculated for oxy-Mb. This difference is likely caused by the much weaker hydrogen bonding to peroxo distal oxygen (N $\cdots$ O distance  $\sim 3.9$  Å compared to 2.67 Å in oxy-myoglobin) and the lack of active site polarization in this model compound.

**2.1.3. Metal-Dioxygen Intermediates of Metalloporphyrins.** Studies of biomimetic synthetic iron porphyrins have greatly aided in the understanding of O<sub>2</sub> binding and activation in heme proteins. An early study by Traylor et al. showed that the O<sub>2</sub> affinity of imidazole-ligated iron(II) porphyrin (1, Figure 5a) was over 3800 times stronger than that of a pyridine-ligated one (2, Figure 5a), whereas both complexes showed similar CO binding affinities.<sup>65</sup> This difference was thought to originate from the large  $\pi$  basicity of imidazole, which could better stabilize the weak O<sub>2</sub> ligand. Much progress has been made with sterically protected porphyrin scaffolds like “picket-fence” porphyrins, which prevent the irreversible bimolecular condensation of Fe(II) porphyrins to form  $\mu$ -oxo-bridged diiron(III) complexes upon reacting with O<sub>2</sub>. This strategy was first implemented by Collman and led to the characterization of the first Fe–O<sub>2</sub> porphyrin compound in the 1970s.<sup>45,66</sup> This model binds O<sub>2</sub> reversibly with affinity similar to those of Hb and Mb. More importantly, the Fe–O<sub>2</sub> intermediate prepared by Collman is diamagnetic and showed a bent end-on binding geometry of dioxygen just as postulated by Pauling. With a similar approach, many synthetic Fe–O<sub>2</sub> complexes have been synthesized and characterized with varied O<sub>2</sub> binding affinities tuned by ligand environments.<sup>22,24</sup> Very recently, the Scheidt

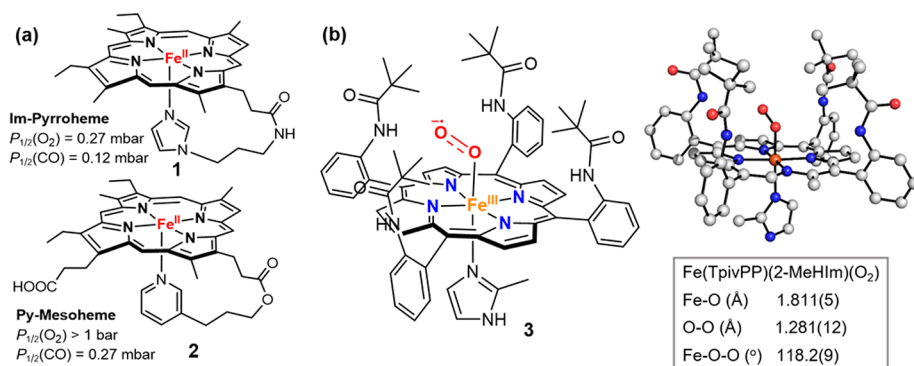


**Figure 5.** (a) Structure of Im-pyrrohome and Py-mesocheme and their binding affinities to  $\text{O}_2$  and CO. (b) Structural parameters of  $\text{Fe}(\text{TpivPP})(2\text{-MeHIm})(\text{O}_2)$  are from ref 67.

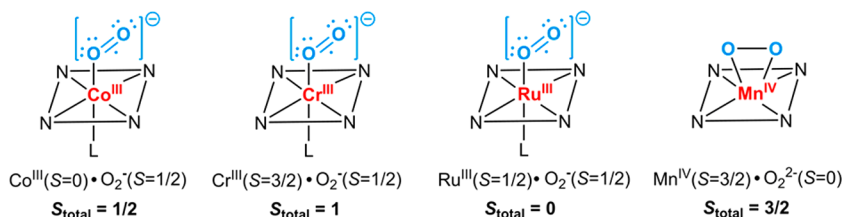


**Figure 6.** Bonding and electronic properties of various metal-dioxygen porphyrin complexes.

and Schulz groups have used multitemperature X-ray crystallography and Mössbauer spectroscopy to study three ferric-superoxo complexes based on “picket fence” porphyrin TpivPP with 1-methyl-, 1-ethyl-, or 2-methylimidazoles as axial ligand, respectively.<sup>67</sup> Their results showed a low energy for the rotation of the Fe– $\text{O}_2$  unit. An 80K structure of  $\text{Fe}(\text{TpivPP})(\text{O}_2)$  (**3**, Figure 5b) with 2-methylimidazole (2-MeHIm) axial ligand allowed them to accurately determine the position of both oxygen atoms, whose structural details were veiled in previous studies because of the high thermal motion and  $\text{O}_2$  disorder. They obtained a Fe–O distance of 1.811(5) Å, O–O bond lengths of 1.281(12) Å, Fe–O–O angle of 118.2°, and an off-axis tilt of Fe–O bond of 6.2°.

Heme-containing metal–organic frameworks (MOFs) have recently been used as a platform to study the Fe– $\text{O}_2$  adduct because of the spatial separation of heme centers in the MOF scaffold and the gas-absorption properties of MOFs. This approach allows for solvent–free generation of ferric-superoxo intermediates. A rare 5-coordinate heme– $\text{O}_2$  complex could be obtained by reacting a Zr-based porphyrinic MOF PCN-224Fe<sup>II</sup> (PCN stands for porous coordination network) with  $\text{O}_2$  at –78 °C.<sup>68</sup> The species revealed a characteristic  $\eta^1$  end-on binding mode of  $\text{O}_2$  with a Fe–O distance of 1.79(1) Å, O–O distance of 1.15(4), and an Fe–O–O angle of 118(4)°. PCN-224Fe<sup>II</sup> showed a low  $\text{O}_2$ -binding enthalpy of –8 kcal/mol, about half of those of other heme model compounds with imidazole axial ligands. This weak  $\text{O}_2$  affinity suggests the importance of electron-donation from axial ligands ( $\sigma$ -donation in the case of imidazole) for the formation of Fe– $\text{O}_2$  complexes.

Transition-metals other than iron have also been explored for  $\text{O}_2$  binding in both synthetic metalloporphyrins and heme proteins. A great number of studies have focused on cobalt dioxygen complexes, which have a doublet ground state ( $S = 1/2$ ) and thus can be probed by EPR spectroscopy.<sup>69–73</sup> Co– $\text{O}_2$  is best described as a Co(III) superoxo species with the unpaired electron largely on the  $\text{O}_2$  moiety. Co– $\text{O}_2$  also adopts

a  $\eta^1$  end-on binding mode as revealed by the structures of both Co-Mb and model compounds (Figure 6).<sup>71,74</sup> Co<sup>II</sup>– $\text{O}_2$  binds dioxygen reversibly but with much lower affinity compared to their iron analogs ( $P_{1/2}$  around 60 Torr vs 0.49–1.1 Torr for iron).<sup>72</sup> As in iron porphyrins, axial ligands are important for Co– $\text{O}_2$  binding. A Co– $\text{O}_2$  intermediate without an axial ligand was recently synthesized in a MOF scaffold PCN-224, which showed a much lower  $\text{O}_2$ -binding enthalpy (–3.6 kcal/mol) compared to that of model compound with an imidazole ligand (–13.3 kcal/mol).<sup>75</sup> In contrast, cobalt(II) octaethylporphyrin supported on a highly oriented pyrolytic graphite showed a favorable  $\text{O}_2$  binding ( $\Delta H^\circ = -16.7 \pm 3.6 \text{ kcal/mol}$ ), owing to the partial electron donation from the graphite substrate.<sup>76</sup>

In addition to iron and cobalt, manganese, chromium, and ruthenium dioxygen adducts have also been investigated in porphyrinoid scaffolds.<sup>24</sup> We will only briefly summarize their structural and electronic features (Figure 6). Dioxygen adducts of manganese(II) porphyrins have unique features compared to other metal-dioxygen species. Mn(II) binds oxygen with the loss of the axial ligand that usually stabilizes the metal– $\text{O}_2$  moiety.<sup>77,78</sup> Mn– $\text{O}_2$  exhibits an intermediate spin ( $S = 3/2$ ) and a large zero-field splitting (–2.4  $\text{cm}^{-1}$ ).<sup>79–81</sup> The 900 to 990  $\text{cm}^{-1}$  IR stretching frequencies  $\nu(\text{O}_2)$  of Mn– $\text{O}_2$  are much lower than those of end-on Fe– $\text{O}_2$  and Co– $\text{O}_2$  complexes (1100–1200  $\text{cm}^{-1}$ ).<sup>82</sup> These properties indicate that  $\text{O}_2$  binds to Mn(II) in a symmetric  $\eta^2$  side-on mode, a Mn<sup>IV</sup>– $\text{O}_2^{2-}$  formalism. Oxy-Ru(II) porphyrins are diamagnetic and have O–O stretching frequency of 1103  $\text{cm}^{-1}$ , suggesting a low-spin Ru(III) superoxide formulation as described in the Weiss model of Fe– $\text{O}_2$ .<sup>83–85</sup> For Cr<sup>II</sup>– $\text{O}_2$  porphyrins, a 1142  $\text{cm}^{-1}$  O–O stretching frequency and a  $S = 1$  ground state also indicates a Weiss model, in which a high-spin  $S = 3/2$  Cr(III) and an  $S = 1/2$  superoxide anion are antiferromagnetically coupled.<sup>79,86</sup>

## 2.2. Ferric-(hydro)peroxo Intermediates

### 2.2.1. Ferric-(hydro)peroxo Intermediates of Heme Proteins

The binding of dioxygen to ferrous heme facilitates its reductive activation. In many hemoproteins such as nitric oxide synthase and cytochrome P450s, an electron and a proton are transferred to the oxy-ferrous complex to afford a ferric-hydroperoxo intermediate  $[\text{Fe}(\text{III})-\text{O}-\text{OH}]$ , also known as compound 0 (cpd 0). Distinct from most heme proteins, cytochrome c oxidase (CcO) utilizes a copper cofactor complexed with active site residues, including an unusual His-Tyr cross-link, to facilitate the  $\text{O}_2$  activation. This arrangement leads to the formation of an analogous ferric-peroxo-cupric intermediate.  $\text{O}_2$  activation by CcO is discussed in detail in section 4.3 of this review.

Cpd 0 species have proven to be short-lived, posing significant challenges for their characterization. Cryogenic radiolytic reduction, as first demonstrated by Davydov and Symons,<sup>87–89</sup> has proven to be very useful for the study of cpd 0.<sup>90</sup> This method utilizes the hydrated electrons generated through radiolysis to reduce the ferrous-dioxygen intermediate in frozen solvent matrices. The combination of radiolytic cryoreduction with spectroscopic methods, especially EPR and ENDOR spectroscopies employed by Hoffman et al., have afforded critical insight into the electronic and structural properties of cpd 0.<sup>91</sup> By controlling the cryogenic conditions, ferric-peroxo anion species  $[\text{Fe}(\text{III})-\text{O}-\text{O}^-]$  could be obtained and its protonation at the distal oxygen to form the conjugate acid  $[\text{Fe}(\text{III})-\text{O}-\text{O}-\text{H}]$ , cpd 0 upon thermal annealing could be monitored by EPR spectroscopy. It is now known that cpd 0 has a low-spin ferric,  $S = 1/2$  ground state. The  $g_1$  value of cpd 0 was found to be indicative of the protonation state of the distal oxygen, with a  $g_1 > 2.30$  commonly observed for the ferric-hydroperoxo state.<sup>92</sup> The thermal annealing experiments also showed that the ease of proton delivery varied widely across heme proteins. For instance, Mb ferric-peroxo is stable near 100 K, whereas the ferric-peroxo anion of P450cam is readily protonated above 55 K.<sup>93–95</sup> This ease of protonation may be related to the presence of the proton relay channel in P450cam. Very recently, Kincaid et al. have characterized ferric-(hydro)peroxo intermediates of lactoperoxidase (LPO) via cryoradiolysis/resonance Raman (rR) spectroscopy.<sup>96</sup> Under alkaline conditions (pH 8.2), the ferric-peroxo intermediate is the major form for LPO and no protonation occurred via thermal annealing. Under acidic conditions (pH 5.6), however, a mixture of LPO-peroxo and LPO-hydroperoxo intermediates were formed. Intriguingly, upon thermal annealing to 170 K, LPO-peroxo did not convert to the hydroperoxo species, and its rR intensity decreased substantially, whereas LPO-hydroperoxo was more stable with peak intensities almost unchanged. Radiolytic cryoreduction has also enabled the structural characterization of the fleeting ferric-(hydro)peroxo species with X-ray crystallography. In 2007, Schlichting et al. reported a crystal structure of compound 0 by controlled radiolytic reduction of ferrous-dioxygen intermediate of chloroperoxidase (CPO).<sup>97</sup> Cpd 0 of CPO showed an O–O distance of 1.5 Å, a long Fe–O distance of 1.9 Å, and an Fe–O–O angle of  $131^\circ$  (Figure 7a). Soon afterward, Unno and co-workers reported the characterization of a ferric peroxoanion compound of myoglobin, which showed a Fe–O distance of 1.85 Å, Fe–O–O angle of  $120^\circ$ , and a short O–O distance of 1.33 Å (Figure 7b), which distinguishes it from an O-protonated hydroperoxo state.<sup>98</sup> Peroxymyoglobin was also characterized

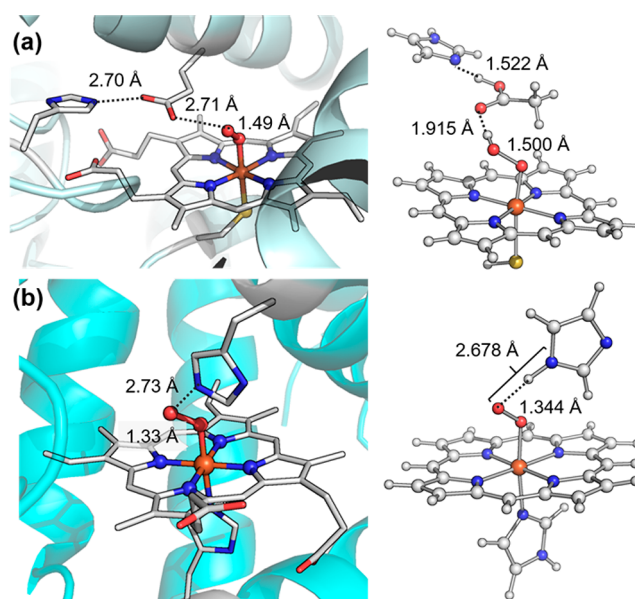


**Figure 7.** (a) Crystal structure of CPO-0 (PDB: 2J5M) (left) and the QM/MM optimized structure of doublet CPO-0 (generated with molecular coordinates provided in ref 97). (b) Crystal structure of the ferric-peroxo intermediate of Mb (PDB: 2Z6T) and the corresponding QM/MM optimized structure (doublet ground state) (generated with molecular coordinates provided in ref 98).

by Andersson et al. in 2008 and similar structural features were reported.<sup>99</sup>

### 2.2.2. Ferric-(hydro)peroxo Intermediates of Metalloporphyrins

In parallel with the progress with heme proteins, synthesis and characterization of cpd 0 analogs in

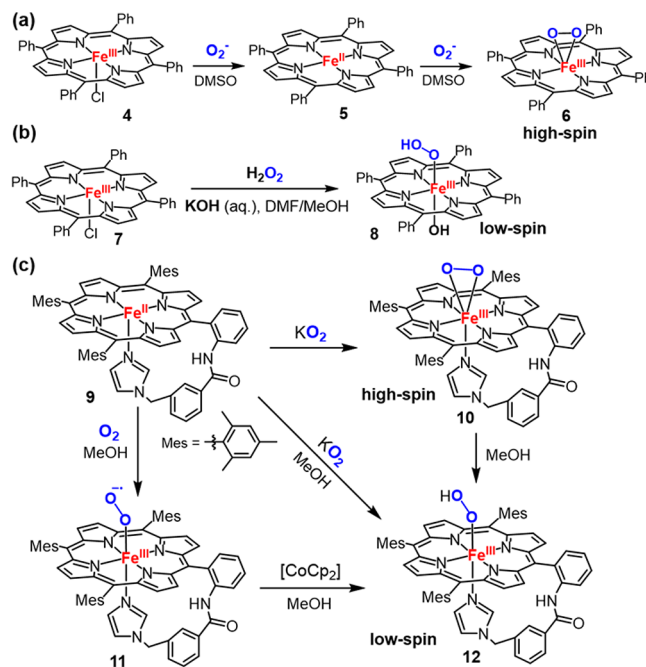


**Figure 8.** (a) Formation of a high-spin side-on  $\eta^2$ -peroxo ferric intermediate (6). (b) Formation of low-spin end-on  $\eta^1$ -hydroperoxo ferric intermediate (8). (c) Conversion of a high-spin side-on  $\eta^2$ -peroxo ferric intermediate (10) into low-spin end-on  $\eta^1$ -hydroperoxo ferric intermediate (12). Adapted with permission from ref 106. Copyright 2009 Wiley-VCH.

model compounds have also been actively explored. Valentine and co-workers reported the first preparation of a ferric porphyrin peroxide complex  $\text{Fe}(\text{TPP})\text{O}_2^-$  (**6**, Figure 8) by treating  $\text{Fe}^{\text{III}}(\text{TPP})\text{Cl}$  (**4**) with 2 equiv of  $\text{KO}_2$  or  $\text{Fe}^{\text{II}}(\text{TPP})$  (**5**) with 1 equiv of  $\text{KO}_2$  in aprotic solvents.<sup>100,101</sup> This species exhibited a characteristic EPR spectrum of a rhombic high-spin  $\text{Fe}(\text{III})$  ( $S = 5/2$ ) complex with a broad and intense resonance at  $g \sim 4.2$ , which is in contrast to the low-spin  $S = 1/2$  state observed for typical cpd 0 species ( $g$  values  $\sim 2$ ). Similar complexes can also be formed by  $1e^-$  electrochemical reduction of ferrous dioxygen intermediates.<sup>102</sup> The infrared O–O stretching vibration of **6** at  $806\text{ cm}^{-1}$  and the lack of an axial basic ligand suggested that this complex is a side-on  $\eta^2$ -peroxy ferric species.<sup>101</sup> Several  $\eta^1$  end-on ferric–hydroperoxo models were synthesized by Tajima et al. via addition of  $\text{H}_2\text{O}_2$  to ferric porphyrins at low temperatures and subsequently characterized by UV–vis and EPR spectroscopies at 77 K.<sup>103–105</sup> The EPR spectra of these complexes showed a low-spin ferric intermediate with  $g$  values  $\sim 2$ , similar to those observed for cpd 0 in heme proteins. In Tajima's conditions to prepare  $\eta^1$  end-on ferric-peroxy complexes (**11**), methanol was used as a cosolvent, and hydroxide or imidazole was added as the axial ligand (Figure 8b), in contrast to the conditions of preparing the side-on  $\eta^2$ -peroxy ferric species **10**, in which an aprotic-solvent was used and no axial ligand was present. Recently, the impact of axial ligands and solvent on ferric-peroxy bonding mode has been extensively studied by Naruta et al. They successfully synthesized both ferric–peroxy and ferric–hydroperoxy complexes of  $\text{Fe}^{\text{II}}(\text{TMPIm})$ , an iron porphyrin complex bearing a covalently linked imidazole axial ligand (**9**, Figure 8).<sup>106,107</sup> The ferric-peroxy complex **10** was characterized to be a rare seven-coordinate, side-on ferric-peroxy species with axial association of the covalently linked imidazole. An EPR signal for **10** at  $g \sim 4.2$  and an rR O–O stretching vibration at  $807\text{ cm}^{-1}$ , which is characteristic for a high-spin  $\eta^2$ -peroxy–ferric heme species, supports this formulation. Addition of methanol to **10** led to the formation of a low spin end-on hydroperoxyferric complex, **12**, as judged by changes in the EPR spectra from  $g \sim 4.2$  to a new set of signals at  $g = 2.31, 2.19$ , and 1.95. The identity of **12** was further confirmed by a  $4\text{ cm}^{-1}$  upshift of  $\nu(\text{O}–\text{O})$  in MeOD solvent. The Mössbauer spectrum of **12** showed an isomer shift of  $0.25\text{ mm/s}$  and a

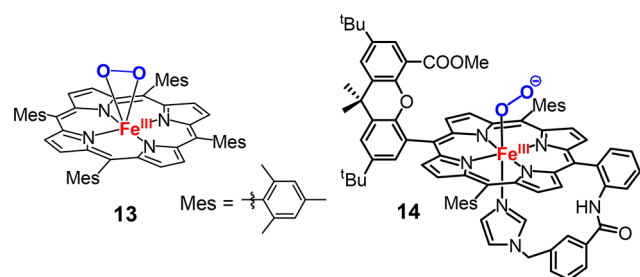


**Figure 9.** Chemical structure of  $[(\text{TMP})\text{Fe}^{\text{III}}(\text{O}_2^{2-})]$  (**13**) and an end-on ferric-peroxy anion species containing a bulky TMPIm ligand (**14**).

quadrupole splitting of  $2.16\text{ mm/s}$ , which is in agreement with those of the previously characterized low-spin hydroperoxy–heme species.<sup>108</sup>

Addition of methanol to a 6-coordinated ferric-peroxy complex  $[(\text{TMP})\text{Fe}^{\text{III}}(\text{O}_2^{2-})]$  (**13**, Figure 9), however, led to a direct decomposition of **13**. This striking difference highlights the importance of the imidazole axial ligand in stabilizing the

ferric–hydroperoxy species. Soon afterward, the synthesis of an end-on ferric-peroxy anion intermediate was successfully achieved by the same group with a TMPIm ligand containing a bulky xanthene substituent hanging over the porphyrin (**14**, Figure 9).<sup>109</sup> The EPR spectrum of **14** is characteristic of a low-spin ferric complex with  $g$  values of 2.27, 2.16, and 1.96, consistent with those of end-on ferric-peroxy intermediates in heme proteins prepared via radiolytic reduction. Addition of methanol to this species made a new low-spin ferric complex with  $g$  values of 2.32, 2.19, and 1.95 and  $\nu(\text{O}–\text{O})$  of  $807\text{ cm}^{-1}$ . The small increase in the spread of  $g$  values and a  $g_1 > 2.3$  are indicative of an end-on ferric–hydroperoxy complex.

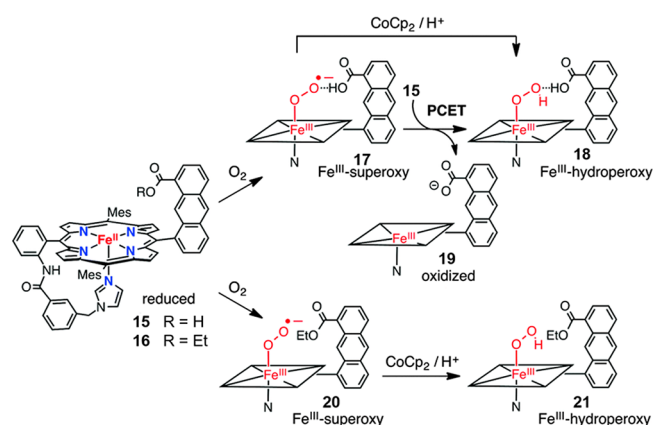


**Figure 10.** Impact of the second coordination sphere on the formation of a ferric-(hydro)peroxy intermediate. Adapted with permission from ref 110. Copyright 2016 Royal Society of Chemistry.

The effect of the second coordination sphere on the formation of ferric hydroperoxy intermediates was recently explored by the same group with an iron(II) porphyrin containing both a covalently appended proton donor and an axial imidazole ligand (**15**, Figure 10).<sup>110</sup> This complex can bind oxygen to afford the ferric-superoxo intermediate **17**. Intriguingly, **17** can be reduced by **15** to afford a  $\text{Fe}^{\text{III}}$ -hydroperoxy intermediate **18** presumably via a PCET pathway. This process would be inhibited by converting the carboxylic acid moiety on xanthene to an ester. The corresponding iron(II) porphyrin **16** can still form a ferric–hydroperoxy intermediate **21** upon reacting with cobaltocene ( $\text{CoCp}_2$ ) via a PCET pathway. Compared to **21**, **18** showed a higher  $\nu(\text{Fe}–\text{O})$  ( $579\text{ cm}^{-1}$  vs  $576\text{ cm}^{-1}$ ) and a lower  $\nu(\text{O}–\text{O})$  ( $807\text{ cm}^{-1}$  vs  $811\text{ cm}^{-1}$ ) compared to **21**, indicating that the intramolecular H-bond interaction enhances the Fe–O but weakens the O–O bonding.

Ferric hydroperoxy intermediates have also been investigated using electrochemical methods.<sup>102,110–114</sup> The use of electrodes modified with iron porphyrins was used to probe for reactive iron porphyrin intermediates under electrocatalytic conditions.<sup>111,114</sup> The electrochemical methods also represent a potentially “cleaner” way to generate iron porphyrin intermediates by circumventing the need of reducing agents. A recent example is the preparation of  $[\text{Fe}^{\text{III}}(\text{TPFPP})(\text{O}_2)]^-$  and  $[(\text{MeIm})\text{Fe}^{\text{III}}(\text{TPFPP})(\text{OOH})]$  intermediates via electrochemical reduction of the corresponding ferric-superoxo intermediate  $[\text{Fe}^{\text{III}}(\text{TPFPP})(\text{O}_2^\bullet)]$  (TPFPP = 5,10,15,20-tetrakis(pentafluorophenyl)porphyrin).<sup>112</sup>

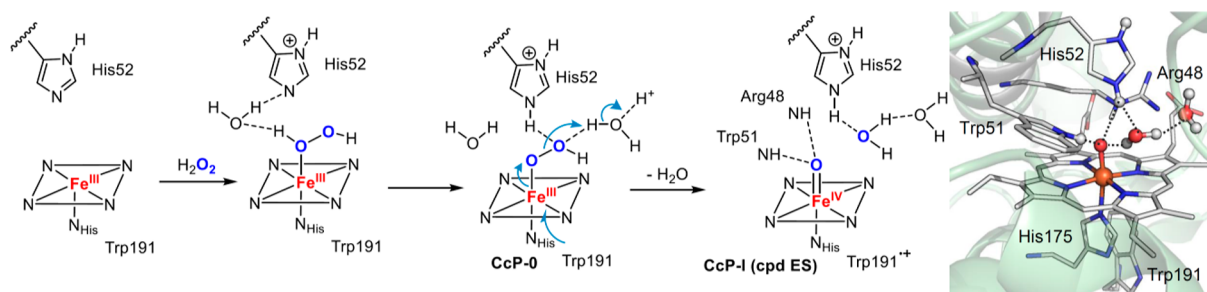


Figure 11. Cpd I generation in cytochrome c peroxidase (CcP), PDB: 4CVJ.

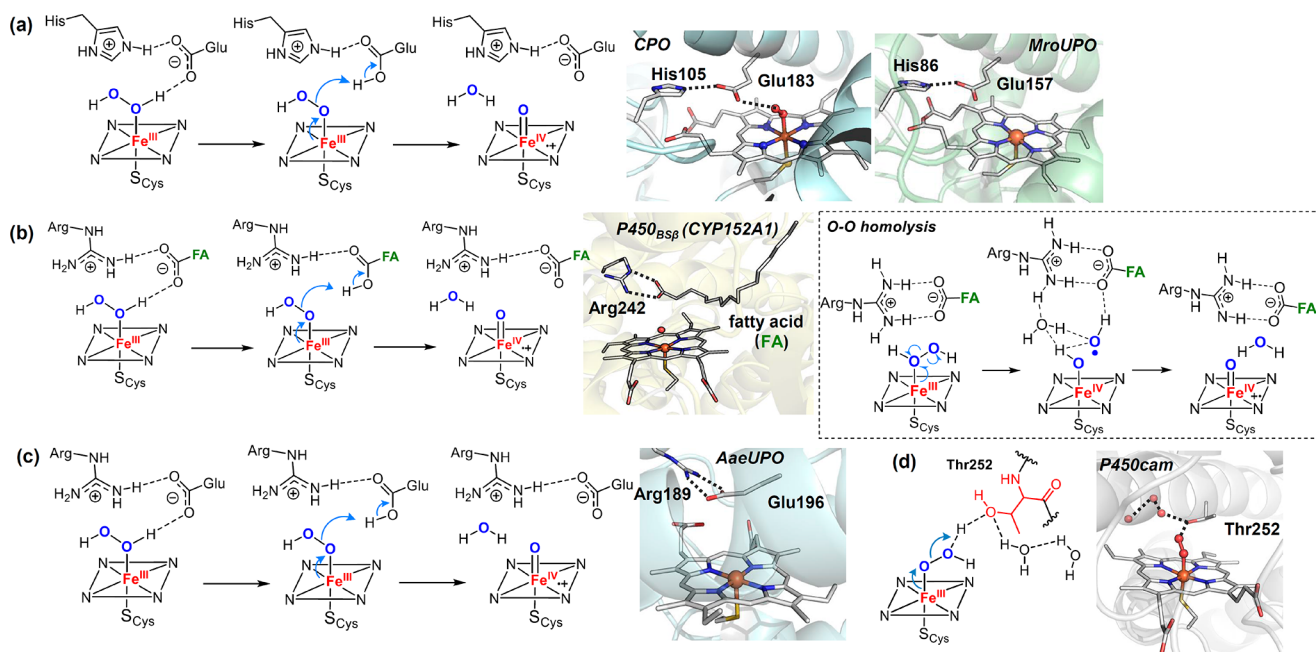


Figure 12. Proposed mechanism for generation of cpd I from cpd 0. The following structures are used: (a) Cpd 0 of CPO (CPO-0) from *Leptoxiphium fumago* (PDB: 2J5M) and the active site structure of *MroUPO* (PDB: 5FUJ); (b)  $P450_{Bsp}$  from *Bacillus subtilis* complexed with a fatty acid substrate (PDB: 1I2O); (c) crystal structure of peroxygenase from *Agrocybe aegerita* (PDB: 2YP1); and (d) oxygen complex of  $P450_{cam}$  from *Pseudomonas putida* (PDB: 1DZ8).

### 2.3. Heterolytic O–O Bond Cleavage of Ferric–Hydroperoxy Intermediates

**2.3.1. O–O Bond Cleavage of cpd 0 to Generate Cpd I in Heme Proteins.** The main role of the ferric–hydroperoxy species (cpd 0) in  $O_2$  activation is to generate the key oxoiron(IV) porphyrin cation radical intermediate, which is the canonical compound I (cpd I). Historically, the terms compound I and compound II (the one-electron-reduction product of cpd I) stem from very early spectroscopic studies of the reaction of horseradish peroxidase (HRP) with hydrogen peroxide. In 1937, using an ocular spectroscope, Keilin and Mann observed a red intermediate with a Soret band near 420 nm upon addition of  $H_2O_2$  to HRP.<sup>115</sup> Four years later, Theorell identified a more short-lived green intermediate formed initially in the reaction between HRP and  $H_2O_2$  (thus termed “cpd I”),<sup>116</sup> which then converted into the red species (termed “cpd II”) observed by Keilin and Mann. Similar intermediates were also observed by Stern and Chance for catalase.<sup>117–119</sup> Jones and Dunford suggested the presence of an HRP- $H_2O_2$  precursor complex in preequilibrium with HRP and  $H_2O_2$  (termed “cpd 0”) formed prior to the cpd I generation based on exacting kinetic measurements of this reaction.<sup>120–123</sup>

It is now known that cpd 0 is an Fe(III)–OOH intermediate and is generated via  $H_2O_2$  binding to the resting ferric heme. The subsequent cpd I formation involves the protonation of Fe(III)–OOH (cpd 0) at the distal oxygen and the subsequent heterolytic scission of the O–O bond to release water. Cpd 0 generation and the ensuing O–O bond cleavage in peroxidases are facilitated by residues at distal pocket acting as acid–base catalysts, as proposed first by Poulos and Kraut.<sup>124</sup> This proposal originated from their studies of cytochrome *c* peroxidase (CcP), in which a highly conserved histidine/arginine (His52/Arg48) diad in the distal pocket was found to be crucial for cpd I generation.<sup>124,125</sup> It has been suggested that upon binding of  $H_2O_2$  to the ferric heme, His52 acts as a general base catalyst to deprotonate the proximal oxygen to form cpd 0 and then act as a general acid catalyst to protonate the distal oxygen of cpd 0, whereas Arg48 stabilized the leaving oxygen through hydrogen bonding. Recently, this mechanistic picture was further elaborated by Raven and Moody using neutron cryo-crystallography to visualize the crucial protons (deuterons) at the active site.<sup>126</sup> Surprisingly, their results showed that His52 remained protonated after the formation of CcP cpd I, suggesting that a second proton was delivered to cpd 0, presumably by proton relay through the H-bonded water



network, for the O–O bond heterolysis of [Fe(III)–O–OH] (Figure 11).<sup>127</sup> In addition to the regulation of proton delivery to the peroxo distal oxygen to create a better leaving group (the “pull” effect), the O–O bond cleavage is further facilitated by the  $\sigma$ -donation (electron push) from an axial histidine ligand by providing electron density to the antibonding O–O orbital.<sup>128</sup> The low-spin electronic configuration of Fe–OOH is thought to facilitate O–O bond cleavage via interaction of the filled  $d_{xz}$  orbital on iron with the low-lying  $\sigma^*(\text{O}–\text{O})$  orbital.<sup>129</sup> This “push-pull” effect is a general mechanistic feature for the O–O bond to generate cpd I in heme proteins.<sup>128,130</sup>

The presence of residues acting as acid–base catalysts is common in heme proteins that utilize  $\text{H}_2\text{O}_2$  to generate compound I. For instance, the histidine/asparagine residue pair found in catalases functions similarly to the His/Arg pair in peroxidases to promote compound I generation,<sup>131</sup> while chloroperoxidase (CPO) and unspecific peroxigenases (UPO, also sometimes termed APO) employ a Glu/His or Glu/Arg acid–base pair. In CPO, as well as the UPO from *M. rotula*, glutamate hydrogen bonds to a histidine that stabilizes the negative charge built on the glutamate during O–O bond cleavage (Figure 12a),<sup>132,133</sup> whereas in UPO from *A. aegerita*, glutamate hydrogen bonds to an arginine to achieve this stabilization effect (Figure 12c).<sup>133,134</sup> CYP152, a family of hydrogen peroxide-utilizing P450 peroxigenases, lack the key histidine or glutamate residue to promote O–O cleavage. Instead, these proteins utilize the carboxyl group from a fatty acid substrate as an acid–base catalyst to rearrange the protons of  $\text{H}_2\text{O}_2$  and aid the compound I generation (Figure 12b).<sup>135,136</sup> An alternative pathway for cpd I generation involves a O–O homolytic cleavage of the ferric- $\text{H}_2\text{O}_2$  adduct followed by a hydrogen-atom abstraction (HAT) from the Fe(IV)–OH intermediate by the incipient hydroxyl radical.<sup>137–139</sup> Recent computational studies of P450<sub>SP $\alpha$</sub>  (CYP152B1) by Shaik et al. indicated that the carboxyl group of the fatty acid substrate keeps the HO· radical toward the H–O bond of the Fe(IV)–OH intermediate and facilitates the HAT and cpd I generation (dashed bracket in Figure 12b). Inspired by the role of substrate carboxyl group in CYP152, Watanabe et al. have used short-alkyl-chain fatty acids as cocatalysts and decoy molecules to expand the substrate scope of CYP152 to include a variety of substrates that lack the carboxyl acid groups.<sup>140,141</sup> In this case, short-alkyl-chain fatty acids served as the proton donor required for O–O bond activation.

Unlike peroxidases, most P450s generate their compound 0 through reduction of iron-bound dioxygen, initially generating a ferric-peroxo anion species. Therefore, two protons are needed to produce cpd I, one for protonating the distal oxygen to generate cpd 0 and the other for facilitating O–O bond cleavage to generate water.<sup>25</sup> As revealed by the crystal structure of P450cam, these protons are delivered through a hydrogen bonding network of a water channel involving the key residue Thr252 that hydrogen bonds to the distal oxygen and forms an extended hydrogen bonding network with water molecules in the active site (Figure 12d).<sup>49,50</sup> This threonine is highly conserved in most P450 enzymes.<sup>142</sup> Mutation of this site to alanine does not affect the formation of cpd 0 but diminishes the hydroxylation reactivity, affording  $\text{H}_2\text{O}_2$  and the ferric heme, a so-called uncoupling process.<sup>21,94</sup>

The conversion of  $\text{O}_2$ -dependent P450s into peroxigenases that can utilize hydrogen peroxide as a cosubstrate and terminal oxidant has generated considerable current interest. The low

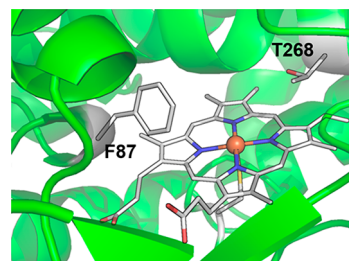


**Figure 13.** Key mutation sites (F87 and T268) for the induction of peroxigenase activity in P450<sub>BM3</sub> (PDB: 1BVY).

cost and high step-economy of using  $\text{H}_2\text{O}_2$  as well as the increased process efficiency derived from not having to recycle reducing cofactors (e.g., NAD(P)H) make such peroxigenase-P450s highly attractive as biocatalysts.<sup>140</sup> Protein engineering techniques such as directed evolution have been extensively used to obtain variants that can efficiently utilize  $\text{H}_2\text{O}_2$  for monooxygenation reactions.<sup>143,144</sup> The mutation of a conserved phenylalanine (F87 in P450<sub>BM3</sub>, Figure 13) within a substrate recognition site to a smaller residue (alanine, glycine, or valine) has been shown to be crucial for the introduction of peroxigenase activity into  $\text{O}_2$ -dependent P450s.<sup>144,145</sup> Recently, Watanabe et al. found that the mutation of the highly conserved threonine (T268 in P450<sub>BM3</sub>, Figure 13) into glutamic acid substantially enhanced the peroxigenase activity of a number of P450s, including P450<sub>BM3</sub>, P450<sub>cam</sub>, and CYP119.<sup>146</sup> The glutamic acid mutation is thought to mimic the role of the substrate carboxyl group in CYP152 for O–O bond activation.

In addition to O–O bond heterolytic cleavage of iron-peroxo intermediates to generate cpd I, some heme proteins can interact with alkyl hydroperoxides to form alkoxy radicals and ferryl intermediates (cpd II). A representative example is allene oxide synthase, which converts fatty acid hydroperoxides into allene oxides. This reaction is discussed in detail in section 4.1.

**2.3.2. O–O Bond Cleavage in Metal-Peroxo Porphyrin Complexes.** Metal-mediated O–O bond cleavage was extensively explored in model metalloporphyrin compounds.<sup>15</sup> In particular, acylperoxy-iron(III) porphyrins have afforded many insights to the mechanistic details of this step.<sup>147–151</sup> It has been shown that the addition of *m*-chloroperbenzoic acid (*m*CPBA) to the solution of HO–Fe<sup>III</sup>(TMP) (**22**, Figure 14a) led to the formation of acylperoxy-iron(III) complex **23**. This species undergoes facile acid-catalyzed O–O bond heterolysis to afford cpd I **24** with a first-order rate constant ( $k_{\text{hetero}}$ ) of  $6.1 \times 10^{-3} \text{ s}^{-1}$  ( $-48 \text{ }^\circ\text{C}$ ) and an  $E_a = 4 \pm 0.4 \text{ kcal/mol}$ ,  $\Delta H^\ddagger = 3.6 \pm 0.4 \text{ kcal/mol}$ , and  $\Delta S^\ddagger > -25 \text{ cal mol}^{-1} \text{ K}^{-1}$ .<sup>149,151</sup> In nonpolar solvents and the absence of acids, however, O–O bond homolysis occurred to afford an unusual iron(III) porphyrin *N*-oxide species, **26**, and a diacylperoxide as products, whereas a ferryl species, **25**, was formed for alkyl acylperoxy-iron(III) complexes due to more rapid decarboxylation of the alkyl acyl radicals. The impact of the porphyrin *meso*-substituents and axial ligands on O–O bond cleavage have been investigated by Watanabe et al.<sup>152</sup> They found that both electron-donating *meso*-substituents and imidazole axial ligands enhanced the O–O heterolytic cleavage (Figure 14b). For instance, the  $k_{\text{hetero}}$  of the most electron-donating [(*m*CPB)–Fe<sup>III</sup>(TTMPP)] was found to be  $\sim 55$ -fold faster than that of (*m*CPB)Fe<sup>III</sup>(TDMPP) (*m*CPB = *m*-chloroperbenzoate). The presence of 1-methylimidazole (1-MeIm) axial ligand increased

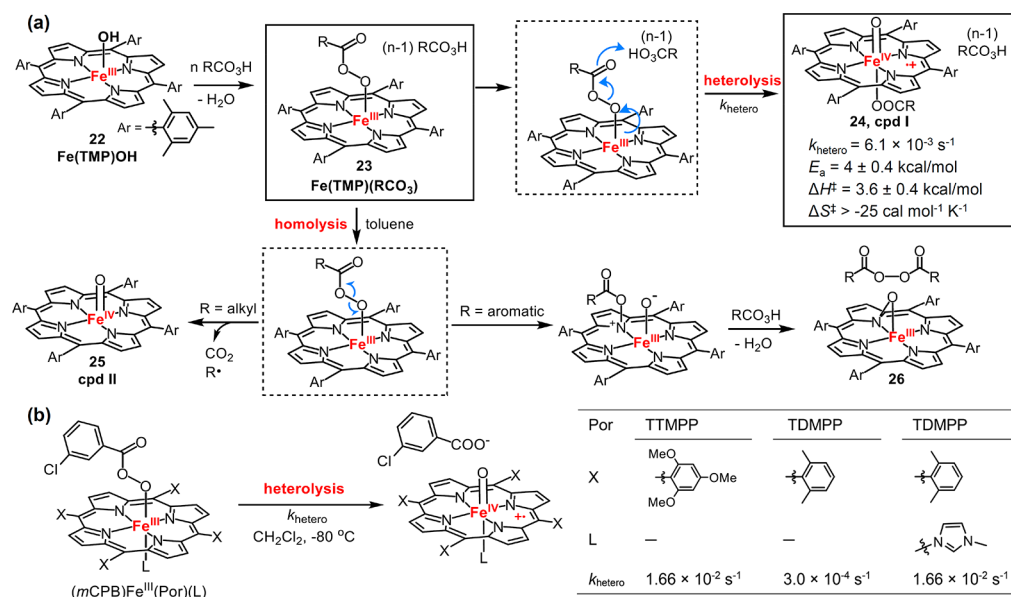


**Figure 14.** (a) O–O bond heterolysis and homolysis of acylperoxy-iron(III) porphyrins. (b) Effect of axial ligands and *meso*-substituents on O–O bond heterolytic cleavage of acylperoxy-iron(III) porphyrins.

$k_{\text{hetero}}$  by over 50-fold for  $[(m\text{CPB})\text{Fe}^{\text{III}}(\text{TDMPP})]$ . The effects of axial ligands were also investigated for O–O bond homolysis in toluene, in which imidazole ligation showed a much less rate enhancement (2.5-fold for 1-MeIm).

More recently, acylperoxy-iron(III) porphyrin intermediates have been further studied with different porphyrin ligand scaffolds and axial ligands under both stoichiometric and

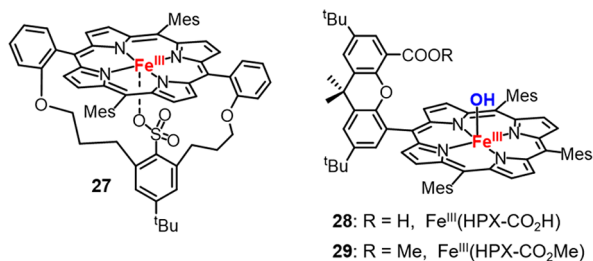


**Figure 15.** Chemical structures of compound 27,  $\text{Fe}^{\text{III}}(\text{HPX}-\text{CO}_2\text{H})$  (28), and  $\text{Fe}^{\text{III}}(\text{HPX}-\text{CO}_2\text{Me})$  (29).

catalytic conditions.<sup>14,153–157</sup> It was found that the rates of oxygen atom transfer reactions mediated by acylperoxy-iron(III) porphyrins were orders of magnitude slower than those of corresponding cpd I species,<sup>153,156–158</sup> demonstrating that cpd I is the active intermediate for the oxygenation reactivity. Woggon and van Eldik et al. synthesized an iron(III) porphyrin with covalently appended sulfonate axial ligand (27, Figure 15).<sup>153</sup> Upon reacting with *m*CPBA, this complex

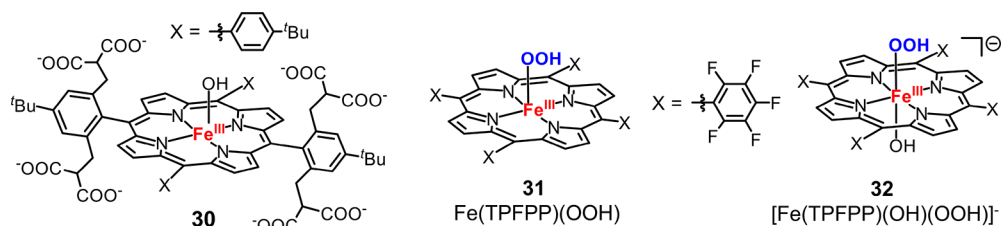


**Figure 16.** Chemical structures of compound 30,  $\text{Fe}(\text{TPFPP})(\text{OOH})$  (31), and  $[\text{Fe}(\text{TPFPP})(\text{OH})(\text{OOH})]^-$  (32).

generated cpd I with  $k_{\text{hetero}}$  of  $2.4 \pm 0.1 \text{ s}^{-1}$  (238 K). The faster  $k_{\text{hetero}}$  determined in this case was attributed to the high polarity of acetonitrile solvent. Nocera et al. studied the impact of the secondary coordinating environment on O–O bond cleavage with so-called “hangman” iron porphyrins containing either a carboxylic acid ( $\text{HPX}-\text{CO}_2\text{H}$ ) or a methyl ester ( $\text{HPX}-\text{CO}_2\text{Me}$ ) functional group, respectively (Figure 15).<sup>155</sup> Both complexes afforded cpd I upon *m*CPBA oxidation in  $\text{CH}_2\text{Cl}_2$  with similar rates, whereas in toluene, the O–O homolysis was inhibited for  $\text{Fe}^{\text{III}}(\text{HPX}-\text{CO}_2\text{H})$ , and only  $\text{Fe}^{\text{III}}(\text{HPX}-\text{CO}_2\text{Me})$  afforded the O–O homolysis product porphyrin *N*-oxide. This result suggests that the presence of the acidic group facilitates the  $2e^-$  pathway for O–O bond cleavage in the same manner as peroxidases. The nature of the leaving group O–X within the peroxy unit  $[\text{Fe}-\text{O}-\text{OX}]$  also affected the preference between  $2e^-$  and  $1e^-$  pathways. Alkyl hydroperoxides such as  $^t\text{BuOOH}$  and cumene hydroperoxide, which have weaker alkoxy leaving groups, were shown to follow a homolytic O–O bond scission pathway upon reacting with  $\text{Fe}(\text{III})$  porphyrins.<sup>159,160</sup>

The O–O bond cleavage of ferric–hydroperoxy intermediates are mainly studied indirectly in oxidation reactions.<sup>148,150,161–163</sup> It has been shown that iron(III) porphyrins could react with  $\text{H}_2\text{O}_2$  in protic solvents to afford porphyrin cation radical intermediate.<sup>164,165</sup> Recently, van Eldik studied the reaction between  $\text{H}_2\text{O}_2$  and an iron(III) octa-anionic porphyrin complex (30, Figure 16).<sup>166</sup> They found that cpd I was formed at  $\text{pH} < 9$ , whereas one-electron oxidized oxoiron(IV) intermediate was observed at  $\text{pH} > 9$ . At  $\text{pH} =$

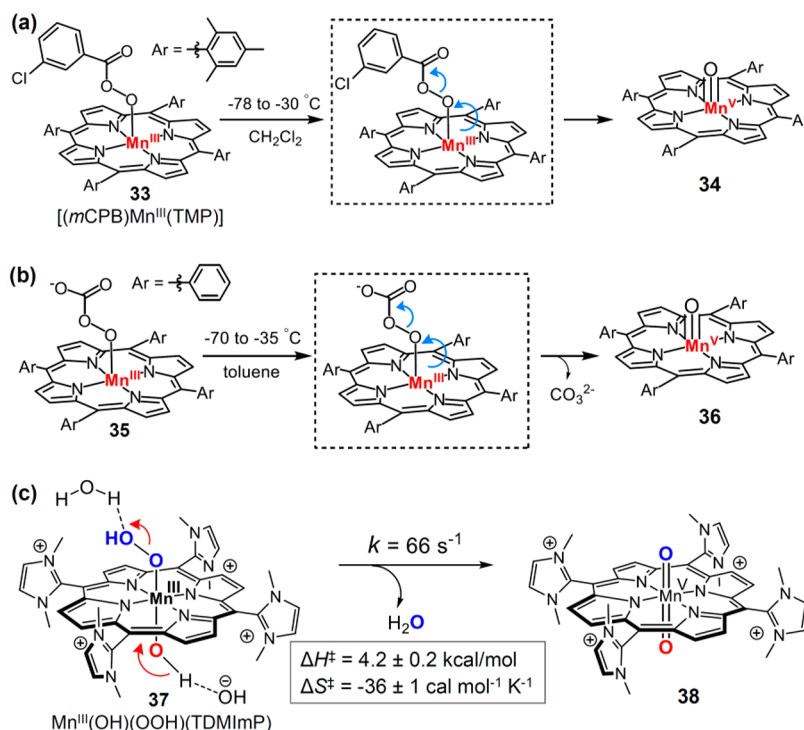


**Figure 17.** (a) Conversion of  $[(mCPB)Mn^{III}(TMP)]$  into oxoMn(V) intermediate **34**. (b) Conversion of manganese(III)-peroxycarbonate **35** into oxoMn(V) intermediate **36**. (c) “Push-pull” mechanism for the O–O bond heterolysis of  $[Mn^{III}(OH)(OOH)(TDMImP)]$ .

**Table 1. Structural and Spectroscopic Parameters of Representative Compound I Intermediates of Heme Proteins**

entry	$S_{total}$	$J$ ( $cm^{-1}$ )	$D$ ( $cm^{-1}$ )	$ J /D$	$\delta$ (mm/s)	$\Delta E_Q$ (mm/s)	$d(Fe^{IV}=O)$ (Å)	ref
HRP-I	3/2	$ J  \leq 2$	26	$\sim 0.1$	0.08	1.25	1.64 <sup>a</sup>	173
Catalase-I	3/2	$\sim 10$	$\sim 25$	0.4	–	–	–	176
LiP-I <sup>b</sup>	3/2	$\sim 10$	$\sim 33$	0.29	–	–	–	174
APX-I <sup>c</sup>	3/2	–	–	0.28	–	–	–	175
CPO-I	1/2	–37	36	1.02	0.15	1.02	1.661 <sup>d</sup>	179
CYP119A1-I	1/2	–52 <sup>d</sup>	40 <sup>ed</sup>	1.30	0.11	0.90	1.670 <sup>d</sup>	182
SeCYP119–1	1/2	–	–	1.43	0.07	1.49	–	201
CYP158A2*-I <sup>e</sup>	1/2	–	–	–	0.13	0.90	1.669 <sup>d</sup>	260
P450cam-I	1/2	–	–	1.38	0.11	0.90	–	180

<sup>a</sup>From ref 187. <sup>b</sup>LiP = lignin peroxidase. <sup>c</sup>APX = ascorbate peroxidase. <sup>d</sup>From ref 181. <sup>e</sup>CYP158A2 \* refers to CYP158A2 Y352F mutant.

8, the rate constants for the coordination and dissociation of  $H_2O_2$  was determined to be  $k_1 = 2259 \pm 149 M^{-1} s^{-1}$ ,  $k_{-1} = 1.1 \pm 0.1 s^{-1}$ , and O–O heterolytic cleavage rate constant was measured to be  $\sim 0.18 s^{-1}$ . In another study, the same group also synthesized two different ferric–hydroperoxy intermediates: five-coordinate high-spin  $[Fe^{III}(TPFPP)(OOH)]$  and six-coordinate low-spin  $[Fe^{III}(TPFPP)(OH)(OOH)]^-$  (**31** and **32**, Figure 16).<sup>167</sup> These two species displayed very different modes of O–O bond cleavage in which the former underwent O–O homolysis to afford an oxoiron(IV) porphyrin complex and the latter formed cpd I via O–O heterolysis.

Manganese-peroxy porphyrin complexes have afforded a particularly informative example of metal-mediated O–O bond scission. Groves and co-workers have prepared an acylperoxomanganese(III) porphyrin  $[(mCPB)Mn^{III}(TMP)]$  (**33**, Figure 17a) by both direct acylation of manganese-dioxygen intermediate and direct addition of peroxyacid salts to manganese(III) porphyrins.<sup>168</sup> Warming a  $CH_2Cl_2$  solution of **33** from  $-78$  °C to  $-30$  °C led to the formation of an oxoMn(V) intermediate **34**. Weiss et al. prepared a manganese(III)-peroxycarbonate intermediate **35** by treating manganese-

dioxygen complex with  $CO_2$  at  $-70$  °C, which readily converted to oxoMn(V) species **36** by elevating the temperature to  $-35$  °C (Figure 17b).<sup>169</sup> Bruice et al. studied the effect of axial ligands on oxygen transfer from various percarboxylic acids and alkyl hydroperoxides to manganese(III) porphyrins. They found that the nitrogen base ligation lead to more than a 100-fold increase in O–O bond cleavage rate and subsequent oxygen transfer.<sup>170</sup> Recently, Groves et al. have determined the activation parameters of O–O bond heterolysis for a water-soluble manganese porphyrin cpd 0,  $[Mn^{III}(OH)(OOH)(TDMImP)]$  (**37**, Figure 17c).<sup>171</sup> That work determined that the optimal pH was in the range of 8.5–11.5 for the reaction between  $H_2O_2$  and  $Mn^{III}(TDMImP)$ . The  $H_2O_2$  oxidation was significantly slowed outside this range. Significantly, O–O bond cleavage was pH-independent over that range, proceeding with a first-order rate constant of  $66 \pm 12 s^{-1}$ . The activation parameters,  $\Delta H^\ddagger = 4.2 \pm 0.2 kcal/mol$  and  $\Delta S^\ddagger = -36 \pm 1 cal mol^{-1} K^{-1}$ , revealed a remarkably low enthalpic barrier for this reaction. The pH independence suggests a concerted “push-pull” mechanism for O–O cleavage, in which the axial OH ligand is partially deprotonated to become more electron-

donating (“push”) and the terminal oxygen of hydroperoxo is partially protonated to release a water molecule to the medium (“pull” effect) to afford the product *trans*-dioxomanganese(V) species (Figure 17c).

## 2.4. Compound I: Oxoiron(IV) Porphyrin Cation Radicals

**2.4.1. Compounds I of Heme Proteins.** Compound I (cpd I) is the primary intermediate that gives rise to the diverse oxidative reactivities of most heme proteins. The electronic structure of cpd I is best described as an  $S = 1$  ferryl coupled to an  $S = 1/2$  porphyrin  $\pi$  cation radical, which can afford either doublet or quartet states.<sup>172,173</sup> The net spin of cpd I is thus determined by the exchange coupling parameter ( $J$ ) between the ferryl and the porphyrin cation radical (Table 1). Weak ferromagnetic coupling ( $J = 0\text{--}10\text{ cm}^{-1}$ ) and a net spin  $S = 3/2$  have been observed for cpd I of several peroxidases and catalase,<sup>173–178</sup> whereas for heme-thiolate proteins like CPO and P450s strong antiferromagnetic coupling ( $|J| > 40\text{ cm}^{-1}$ ) was seen and a total spin of  $S = 1/2$  was observed using EPR and Mössbauer spectroscopy.<sup>18,179–182</sup> The two-oxidizing-equivalent intermediate in cytochrome *c* peroxidase (CcP) obtained after  $\text{H}_2\text{O}_2$  oxidation, known as compound ES, has unusual features compared to those of cpd I of most heme proteins. The UV spectrum of CcP-ES lacks the characteristic 690 nm absorbance of the porphyrin cation radical, and its EPR spectrum exhibited a unique free radical signal ( $g_{\perp} = 2.006$ ,  $g_{\parallel} = 2.034$ ).<sup>183</sup> It is recognized now that CcP compound ES is a ferryl porphyrin intermediate like compound II with an uncoupled protein radical at a tryptophan residue near the axial histidine (Figure 11).<sup>184</sup>

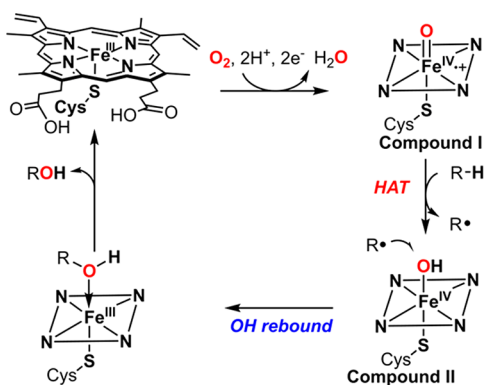


**Figure 18.** Oxygen rebound mechanism for C–H hydroxylation catalyzed by cytochrome P450s.

While cpd I of horseradish peroxidase and chloroperoxidase have been well characterized for decades,<sup>179,185–187</sup> the direct observation and characterization of a cytochrome P450 cpd I (P450-I) was much more challenging. Best known for their roles in drug metabolism and oxidative tailoring in biosynthetic pathways, P450s catalyze remarkably selective aliphatic C–H functionalization reactions.<sup>16</sup> The oxygen rebound mechanism (Figure 18), first proposed by Groves in the 1970s,<sup>188–190</sup> invoked the oxoiron(IV) porphyrin cation radical, compound I, as the “active oxygen species.” Compound I was proposed to activate aliphatic C–H substrates via hydrogen atom transfer (HAT) to the ferryl oxygen. Subsequently, the incipient substrate radical recombines with the Fe(IV)–OH of compound II (oxygen rebound) to afford hydroxylation products. Because of the exceptional reactivity of P450

enzymes, efforts to understand P450-I have attracted sustained attention for four decades. Further, these pursuits have provided valuable insights for the development of new catalysts for selective aliphatic C–H functionalization.

The main obstacles for studying P450-I included its very short lifetime and low yield.<sup>18,191–193</sup> Chloroperoxidase cpd I (CPO-I) has long been used as an analog of P450-I because it also contains an axial cysteine thiolate. However, CPO-I can only hydroxylate weak benzylic C–H bonds.<sup>194</sup> This lack of reactivity for C–H activation led to proposals of other possible intermediates such as an oxoFe(V) electromer or Fe(III)–OOH for P450 reactivity.<sup>195–197</sup> The long-sought P450-I was finally elucidated in 2010.<sup>182</sup> Rittle and Green greatly improved the yield of cpd I of a thermophilic cytochrome P450, CYP119. Spectroscopic studies of CYP119-I revealed a broad UV absorbance around 690 nm typical of a porphyrin cation radical (Figure 19a) and a Mössbauer isomer shift of 0.11 mm/s and quadrupole splitting of 0.90 mm/s signaling iron(IV). An antiferromagnetic coupling between  $S = 1$  ferryl and porphyrin cation radical with a  $|J/D|$  of 1.3 was determined by EPR spectroscopy. These data clearly showed that CYP119-I is an antiferromagnetically coupled ( $S = 1/2$ ) oxoiron(IV) porphyrin cation radical. Unpaired electron density of the axial thiolate was also suggested. More importantly, CYP119-I was found to be highly reactive for C–H hydroxylation with apparent second-order rate constants ranging from  $10^4$  to  $10^7\text{ M}^{-1}\text{ s}^{-1}$  (Figure 19b). Following the characterization of CYP119-I, compounds I of CYP158A2 Y352F variant and P450cam have also been characterized.<sup>180,181</sup> All these P450 compounds I have similar spectroscopic features and exhibit high reactivity toward alkyl C–H bonds.

Unspecific peroxygenases (UPO, initially termed APO for aromatic peroxygenase) comprise a large and newly discovered family of P450-like, heme thiolate hydroxylases of fungal origin.<sup>198</sup> These enzymes are showing considerable promise as biocatalysts with high reactivity toward even aliphatic hydrocarbons.<sup>199</sup> Compound I of an unspecific peroxygenase from the common edible mushroom *Agrocybe aegerita* (*AaeUPO*) was recently characterized by Wang and Groves et al.<sup>200</sup> UPOs are very significant and unusual because they can oxidize strong C–H bonds with  $\text{H}_2\text{O}_2$  as oxidant and do not require any cofactors. *AaeUPO*-I displays similar UV–vis features as CYP119-I and fast rate constants for the hydroxylation of strong C–H bonds (up to 100 kcal/mol) in the range of  $10\text{--}10^5\text{ M}^{-1}\text{ s}^{-1}$  (Figure 19c and 19d).<sup>200</sup>

Very recently, Green et al. reported the characterization of a selenocysteine-ligated cpd I of CYP119 (SeCYP119-I).<sup>201</sup> Given the structural similarity and the difference in electronic properties between selenocysteine and cysteine, SeCYP119-I provides a good opportunity to study the effect of electron-donation of axial ligands on cpd I reactivity. Compared to CPO-I and CYP119-I, SeCYP119-I exhibits a larger  $|J/D|$  value ( $|J/D| = 1.43$ ) and a smaller isomer shift  $\delta = 0.07\text{ mm/s}$ , suggesting a stronger electron-donation from selenolate [R–Se<sup>–</sup>] axial ligand. Reactivity studies showed that CYP119-I and SeCYP119-I were formed at similar rates ( $5 \times 10^6\text{ M}^{-1}\text{ s}^{-1}$  and  $7 \times 10^6\text{ M}^{-1}\text{ s}^{-1}$  for CYP119 and SeCY119, respectively) upon treating corresponding ferric enzymes with *m*CPBA. But SeCYP119-I was more reactive toward C–H bonds than CYP119-I, leading to a significantly less accumulation of SeCYP119-I during reactions with substrates.

**2.4.2. Compounds I of Iron Porphyrins.** The first synthesis and characterization of an oxoiron(IV) porphyrin

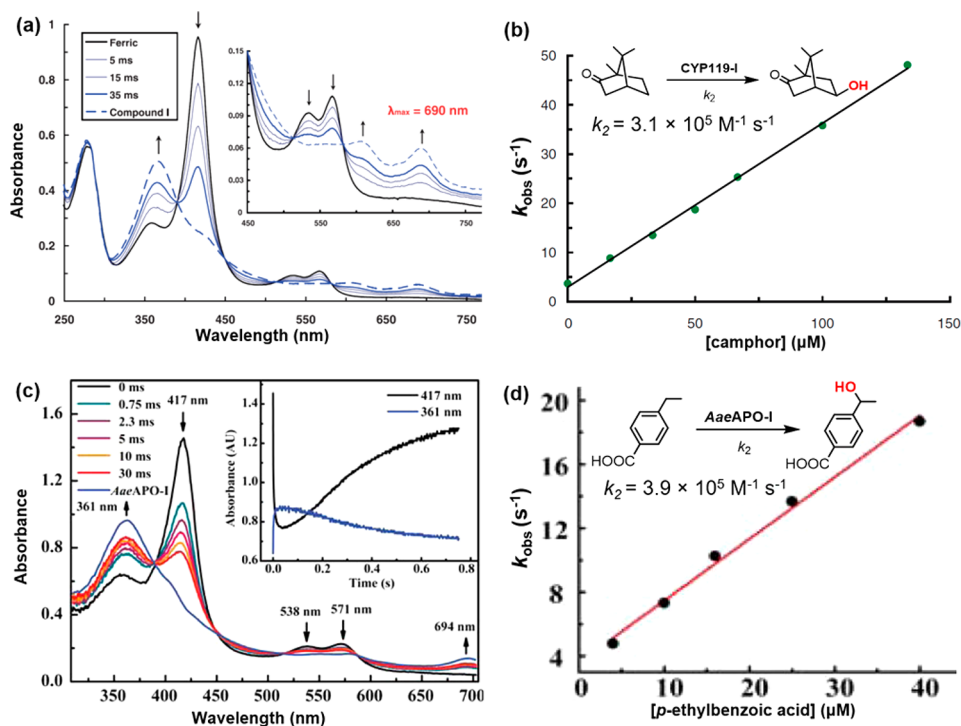


**Figure 19.** (a) UV-vis transients observed upon 1:1 mixing of 20  $\mu\text{M}$  ferric CYP119 with 40  $\mu\text{M}$  *m*CPBA. Maximum yield of CYP119-I was  $\sim 70\%$  at 35 ms. (b) Observed first-order decay rates vs camphor concentration. (c) UV-vis transients observed upon 1:1 mixing of 13  $\mu\text{M}$  ferric *Aae*UPO with 25  $\mu\text{M}$  *m*CPBA. Maximum yield of *Aae*UPO-I was  $\sim 70\%$  at 30 ms. (d) Observed first-order decay rates vs *p*-ethylbenzoic acid concentration. (a) and (b) were adapted with permission from ref 182. Copyright 2010 American Association for the Advancement of Science. (c) and (d) were adapted from ref 200. Copyright 2012 American Chemical Society.

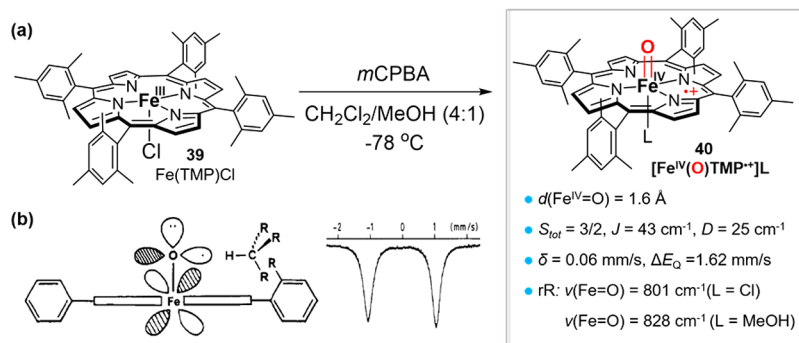


**Figure 20.** (a) The synthesis of the first model cpd I ( $(\text{TMP}^{\bullet+})\text{Fe}^{\text{IV}}=\text{O}$ ) and its structural and electronic parameters. (b) Depiction of the C–H activation mode of  $(\text{TMP}^{\bullet+})\text{Fe}^{\text{IV}}=\text{O}$  and its Mössbauer spectrum, which indicates high-valent iron. Adapted from ref 205. Copyright 1983 American Chemical Society.

cation radical model compound was achieved by our group in 1981.<sup>202</sup> Treatment of a sterically hindered iron porphyrin,  $\text{Fe}^{\text{III}}(\text{TMP})\text{Cl}$  (39, Figure 20a) with *m*CPBA in  $\text{CH}_2\text{Cl}_2/\text{MeOH}$  (4:1) at  $-78^\circ\text{C}$  produced a green compound formulated as  $[\text{Fe}^{\text{IV}}(\text{O})\text{TMP}^{\bullet+}]\text{L}$  (40, Figure 20a). This species had a Soret band at 406 nm and a broad absorption at 645 nm, typical of a porphyrin cation radical. EXAFS data showed a short Fe–O bond length of 1.6  $\text{\AA}$ . A ferryl iron–oxygen stretch,  $\nu(\text{Fe}=\text{O})$  of  $801 \text{ cm}^{-1}$  ( $\text{L} = \text{Cl}$ ) and  $828 \text{ cm}^{-1}$  ( $\text{L} = \text{MeOH}$ ), was obtained by resonance Raman spectroscopy.<sup>203</sup> Magnetic susceptibility and EPR studies showed a total spin of 3/2 with strong ferromagnetic coupling between the ferryl and porphyrin cation radical ( $J > 40 \text{ cm}^{-1}$ ). These features stand in sharp contrast to the antiferromagnetic coupling observed in P450 cpd I.<sup>204</sup> This green species  $[\text{O}=\text{Fe}^{\text{IV}}\text{TMP}^{\bullet+}]$  was found to be reactive in oxygen atom transfer reactions.<sup>205</sup> The direct

oxidation of norbornene by  $[\text{O}=\text{Fe}^{\text{IV}}\text{TMP}^{\bullet+}]$  in the presence of  $\text{H}_2^{18}\text{O}$  led to the formation of an epoxide product with 99%  $^{18}\text{O}$  incorporation, indicating facile ferryl–oxygen exchange with water.

A number of compound I analogues were synthesized with varied substitutions at *meso*- and pyrrole- $\beta$  positions of the porphyrin ligand. These studies have been summarized in a number of reviews.<sup>15,26,27,31,32,206–208</sup> In general, both *meso*- and pyrrole- $\beta$  substituents affect cpd I electronic structures via altering the energy of porphyrin SOMO/HOMO orbitals  $a_{1u}$  and  $a_{2u}$  (Figure 21a). In unsubstituted porphyrins,  $a_{2u}$  is the higher-energy orbital and is singly occupied in cpd I. Since  $a_{2u}$  has a large spin density at *meso*-positions (as well as the pyrrole nitrogens), the increase of electron-deficiency of *meso*-substituents will substantially stabilize  $a_{2u}$ .<sup>27</sup> For instance, the most electron-withdrawing pentafluorophenyl derivative,

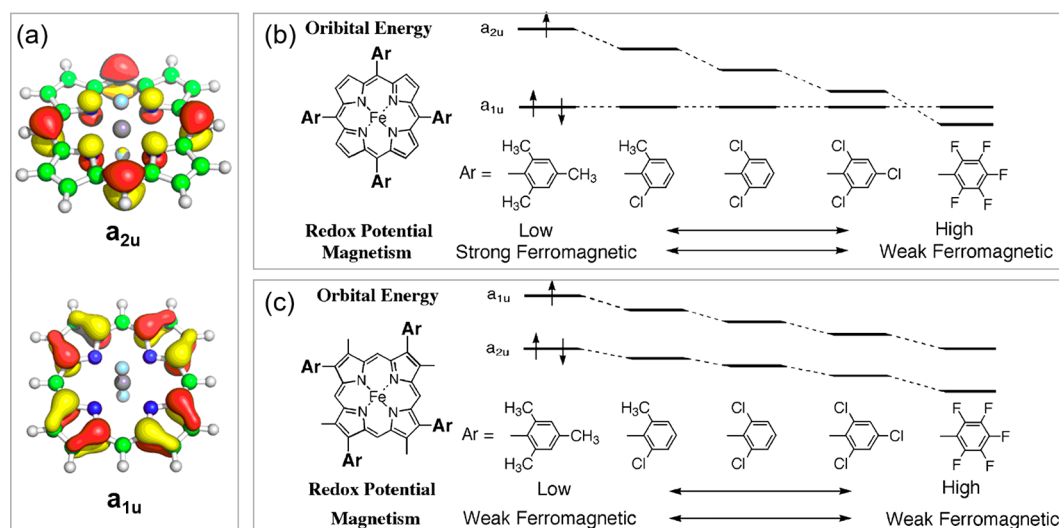


**Figure 21.** (a) Orbital diagrams of porphyrin  $a_{1u}$  and  $a_{2u}$  orbitals. (b) Effect of *meso*-substituents on the electronic structure of cpd I. (c) Effect of pyrrole- $\beta$  substituents on the electronic structure of cpd I. (b and c) were adapted from ref 27. Copyright 2002 Elsevier B. V.

$Fe^{IV}(O)(TPFP^{*+})$ , has an  $a_{1u}$  porphyrin radical configuration (Figure 21b). Fujii et al. showed that compounds I with pyrrole  $\beta$ -substituents are generally  $a_{1u}$  porphyrin radicals, and the electronic properties of pyrrole  $\beta$ -substituents were shown to have similar influences on  $a_{1u}$  and  $a_{2u}$  (Figure 21c). The nature of the porphyrin radical ( $a_{1u}$  or  $a_{2u}$ ) has a large impact on its exchange interaction with iron center, in which large ferromagnetic coupling ( $J > 30 \text{ cm}^{-1}$ ) was observed for  $a_{2u}$  radicals due to large pyrrole nitrogen orbital coefficients and, by

group (Figure 22).<sup>212</sup> This species was generated by reacting a cationic iron(III) porphyrin complex  $Fe^{III}(4\text{-TMPyP})$  with *m*CPBA under rapid-mixing conditions. The resulting  $[Fe^{IV}(O)(4\text{-TMPyP}^{*+})]$  could oxidize a range of C–H bonds with second-order rate constants, ranging from  $(2.85 \pm 0.3) \times 10^6 \text{ M}^{-1} \text{ s}^{-1}$  for xanthene to  $(7.5 \pm 0.1) \times 10^3 \text{ M}^{-1} \text{ s}^{-1}$  for ethylbenzoic acid. The rate constant of ethylbenzoic acid oxidation is comparable to those of CYP119 and CPO cpd I for ethylbenzene oxidation.<sup>213</sup> It was suggested that stabilization of the porphyrin  $a_{2u}$  HOMO and the increased electron deficit at the metal core due to the cationic porphyrin contribute to the

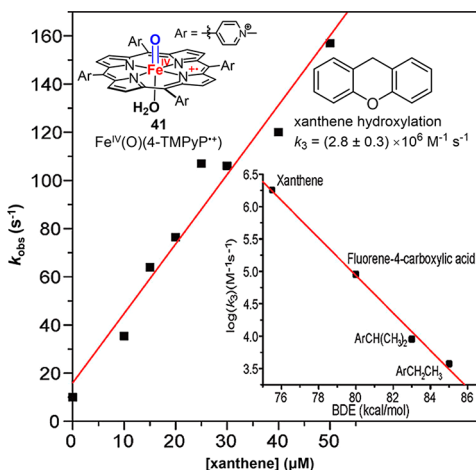


**Figure 22.** Observed rate constant  $k_{\text{obs}}$  at 673 nm vs xanthene concentration for its oxidation by 41 at pH 4.7, 14.5 °C, yielding second-order rate constant  $k_3 = (2.8 \pm 0.3) \times 10^6 \text{ M}^{-1} \text{ s}^{-1}$ . Inset: correlation of  $k_3$  with C–H bond dissociation energy. Adapted from ref 212. Copyright 2009 American Chemical Society.

contrast, weak antiferromagnetic coupling ( $J < 10 \text{ cm}^{-1}$ ) for  $a_{1u}$  radicals.<sup>209,210</sup>

Although these cpd I analogs display a range of oxygen transfer reactions, their second-order rate constants for C–H activation ( $k$ ) are generally less than  $10 \text{ M}^{-1} \text{ s}^{-1}$ .<sup>211</sup> These values for the model compounds are 3 to 6 orders of magnitude slower than those recently measured for P450-I or UPO-I. A highly reactive synthetic compound I was reported by our

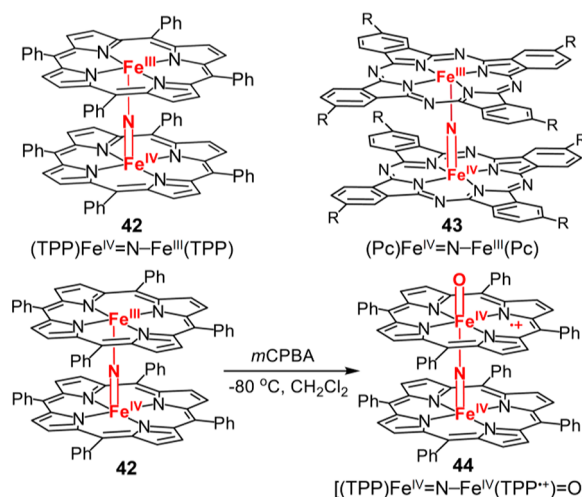


**Figure 23.** Structures of  $\mu$ -nitrido diiron porphyrins and phthalocyanines (Pc) and formation of cpd I 44 from 42 and *m*CPBA.

very high activity of  $[Fe^{IV}(O)(4\text{-TMPyP}^{*+})]$ . The significance of these findings is that no unusual properties of the protein architecture need to be invoked to explain high rates of C–H bond cleavage by heme proteins.

Very recently, Sorokin and co-workers have reported the synthesis of a series of dimeric oxoiron(IV) cation radical species  $[(L)Fe^{IV}=N-Fe^{IV}(L^{*+})=O]$  by treating  $\mu$ -nitrido diiron porphyrins or phthalocyanines (Pc) with peroxides or *m*CPBA (42 and 43, Figure 23).<sup>214,215</sup> A high-valent  $\mu$ -nitrido

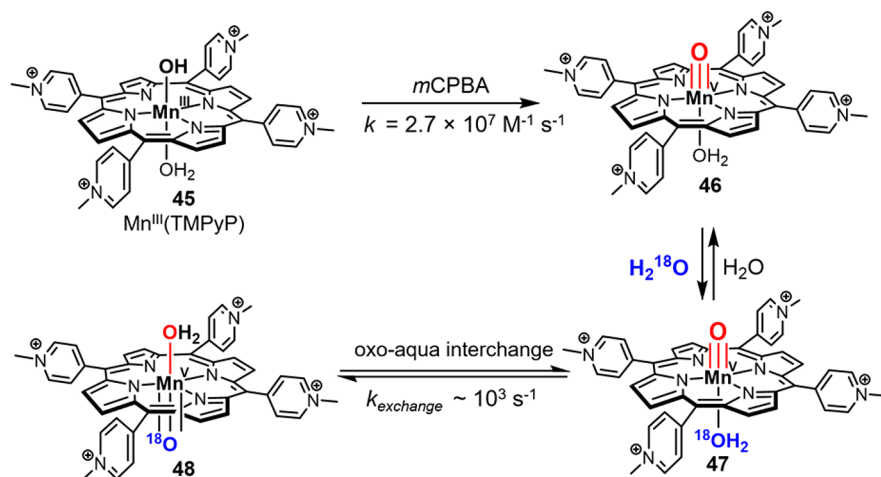


**Figure 24.** Generation of a cpd I manganese porphyrin analogue and the oxo-aqua interconversion of oxoMn(V) intermediate.

diiron-oxo porphyrin cation radical intermediate [(TPP)-Fe<sup>IV</sup>=N-Fe<sup>IV</sup>(TPP<sup>•+</sup>)=O] was successfully isolated and characterized (44, Figure 23).<sup>216</sup> This species has a green color similar to other porphyrin cation radicals and has a half-life of ~20 min at -80 °C. The single narrow EPR signal at  $g = 2.001$  suggested an  $S = 1/2$  state with the unpaired electron localized on the porphyrin macrocycle. In line with the EPR results, magnetic susceptibility measurements revealed a strong antiferromagnetic coupling between two iron centers with  $-J_{\text{Fe-Fe}} > 600 \text{ cm}^{-1}$ , which leads to a  $S_{\text{FeFe}} = 0$ . The Mössbauer spectrum showed a very small isomer shift (0.00(1) mm/s) and a moderate quadrupole splitting (0.75(2) mm/s), also consistent with iron(IV). These high-valent  $\mu$ -nitrido diiron-oxo complexes have exceptional activity for C-H activation.<sup>217</sup> Under catalytic conditions, they were shown to activate C-H bonds of methane (BDE = 104 kcal/mol) to afford formic acid with total turnover numbers (TTN) up to ~220.<sup>218</sup> Recent computational studies showed that the activation barriers of [(L)Fe<sup>IV</sup>=N-Fe<sup>IV</sup>(L<sup>•+</sup>)=O] type intermediates for methane oxidation are over 10 kcal/mol lower than that of a model P450 cpd I.<sup>219</sup> The calculation also suggests that the donor properties of the bridged nitrido group dramatically increased the basicity of the oxo group, which is crucial for the high reactivity of this class of compounds.

#### 2.4.3. Manganese Porphyrin Analogues of Compound I

Synthetic manganese porphyrin analogues of compound I have long been known to have high reactivity toward C-H bonds.<sup>220</sup> While relatively stable oxoMn(IV) porphyrin species have been isolated and well-characterized,<sup>221,222</sup> the direct characterization of oxoMn(V) porphyrin complexes has been very challenging due to their high reactivity. The presence of reactive oxoMn(V) porphyrin complexes has been usually implicated from reactivity patterns and <sup>18</sup>O-exchange into products from water.<sup>223–225</sup> The first Mn porphyrin compound I (MnPor-I) to be kinetically evaluated was generated by treating Mn<sup>III</sup>TMPyP with a peroxyacid such as *m*CPBA using rapid-mixing stopped-flow techniques (45 to 46, Figure 24).<sup>226</sup> MnPor-I 46 rapidly converted to previously characterized oxoMn(IV) via 1e<sup>-</sup> reduction with a first-order rate constant of 5.7 s<sup>-1</sup>. Unlike compound I of iron porphyrins, MnPor-I was diamagnetic, displaying a well-resolved and unshifted proton NMR spectrum and lacked the characteristic broad absorbance between 650–700 nm of porphyrin cation radical, suggesting MnPor-I was an oxoMn(V) species.<sup>227</sup> 46 catalyzed very fast

olefin epoxidation with a second-order rate constant of  $6.5 \times 10^5 \text{ M}^{-1} \text{ s}^{-1}$ . A 35% <sup>18</sup>O incorporation into the epoxidation products was also observed when carrying out the reaction in the presence of H<sub>2</sub><sup>18</sup>O, which is in accordance with an aqua-

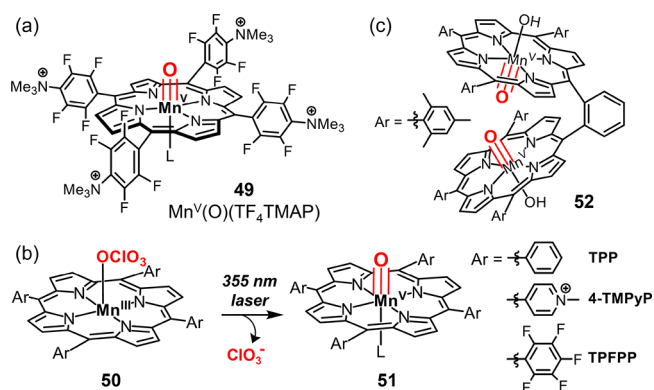


**Figure 25.** (a) Chemical structure of Mn<sup>V</sup>(O)(TF<sub>4</sub>TMAP). (b) Generation of oxoMn<sup>V</sup> intermediates via laser flash photolysis (LFP). (c) A dinuclear oxoMn<sup>V</sup> intermediate 52.

oxo interconversion via prototropy as suggested by Meunier (47 to 48, Figure 24).<sup>223,225</sup> By contrast, manganese-substituted heme proteins, such as Mn-HRP, form only manganese(IV) species and a protein radical.<sup>228</sup> Apparently, the reduction potential of oxoMn(V)protoporphyrin IX is too high to be tolerated by the more redox sensitive protein.

A related oxoMn(V) porphyrin was synthesized by treating cationic [Mn<sup>III</sup>(TF<sub>4</sub>TMAP)](CF<sub>3</sub>SO<sub>3</sub>)<sub>3</sub> (49, Figure 25) with two equivalents of alkaline hydrogen peroxide.<sup>229</sup> This species transformed olefins to epoxides with good yields (~50%). In line with the <sup>18</sup>O exchange experiment of 46, the epoxidation mediated by 49 with H<sub>2</sub><sup>18</sup>O<sub>2</sub> in H<sub>2</sub><sup>18</sup>O water led to a 45% <sup>18</sup>O incorporation. Newcomb et al. prepared a series of oxoMn<sup>V</sup> porphyrins (Figure 25b) in organic solvents via laser flash photolysis (LFP) of corresponding Mn<sup>III</sup> perchlorate porphyrin complexes.<sup>230</sup> The second-order rate constants for olefin epoxidation by these complexes were in the range from 10<sup>4</sup> to 10<sup>6</sup> M<sup>-1</sup> s<sup>-1</sup>, consistent with that of water-soluble oxoMn<sup>V</sup>(TMPyP). For oxoMn<sup>V</sup>(TPFPP), the second-order rate constant for ethylbenzene oxidation was determined to be  $1.2 \times 10^5 \text{ M}^{-1} \text{ s}^{-1}$ , more than 10<sup>5</sup> times faster than the

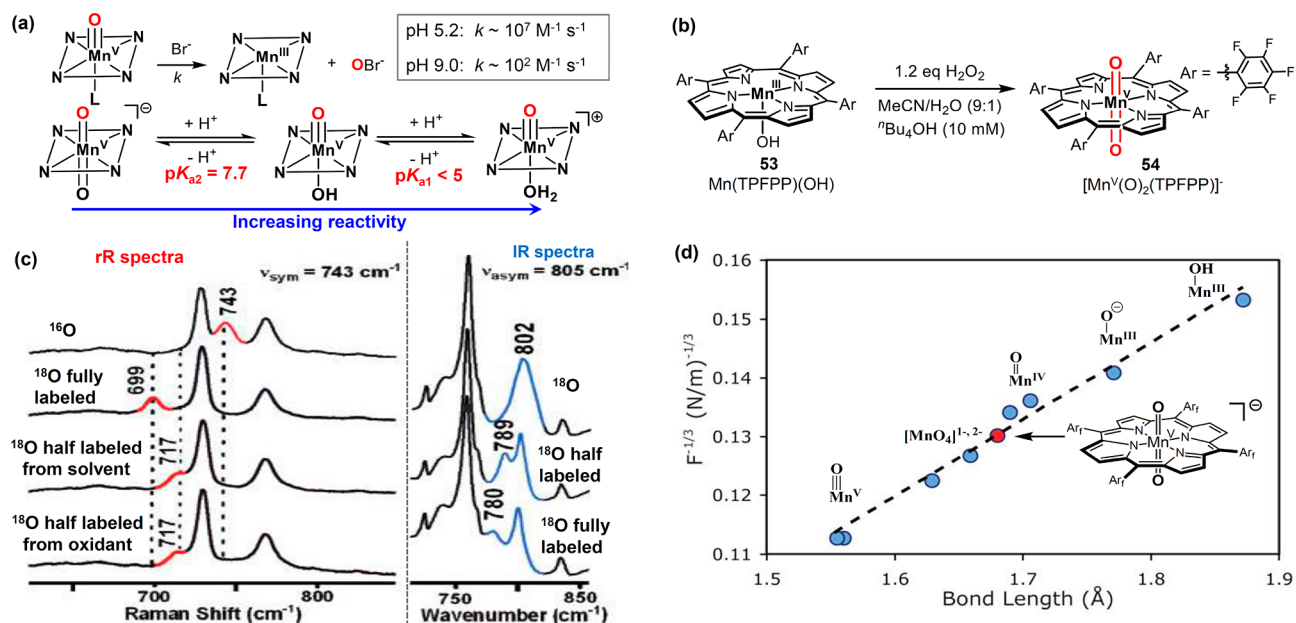


**Figure 26.** (a) pH-dependent reactivity of Mn(III) porphyrins for halide oxidation and the acid-base equilibria between the *trans*-dioxoMn(V), oxo-hydroxo Mn(V), and oxo-aqua Mn(V) species. (b) Synthesis of a *trans*-dioxoMn(V) porphyrin 54. (c) Characterization of 54 via rR and IR spectroscopies. (d) Mn–O bond length vs  $1/F^{1/3}(\text{Mn–O})$ . (c) and (d) were adapted from ref 233. Copyright 2007 American Chemical Society.

corresponding iron complex.<sup>211</sup> A dinuclear oxoMn<sup>V</sup> porphyrin complex has been described by Naruta et al. This species was prepared from the oxidation of a manganese(III) porphyrin dimer with *m*CPBA in the presence of excess tetrabutylammonium hydroxide (<sup>n</sup>Bu<sub>4</sub>OH) (Figure 25c).<sup>231</sup> Interestingly, decomposition of this oxoMn<sup>V</sup> dimer produced oxygen. A number of oxoMn<sup>V</sup> complexes have been prepared with other porphyrinoid ligands such as corroles and corrolazines, as recently reviewed by Goldberg et al.<sup>29</sup>

In addition to these oxoMn<sup>V</sup> complexes, an unusual *trans*-dioxoMn(V) porphyrin structure was deduced from the pH-dependent halide oxidation mediated by oxoMn<sup>V</sup> porphyrins. Apparent second-order rate constants spanned a range of 5 orders of magnitude from  $\sim 10^7 \text{ M}^{-1} \text{ s}^{-1}$  at pH 5.2 to  $\sim 10^2 \text{ M}^{-1} \text{ s}^{-1}$  at pH 9.<sup>232</sup> This profound pH dependence was analyzed to result from two acid–base equilibria between the *trans*-dioxoMn(V), oxo–hydroxo Mn(V), and oxo-aqua Mn(V) species, which displayed increasing oxygen-atom-transfer activities along the sequence. Proton ionizations with  $\text{p}K_{\text{a}1} < 5$  and  $\text{p}K_{\text{a}2} = 7.7$  were estimated for oxo-aqua species from the Nernst eq (Figure 26a). The synthesis and characterization of such *trans*-dioxoMn(V) porphyrin complexes were reported by Groves and Spiro. These complexes were synthesized by treating Mn(III) porphyrins with H<sub>2</sub>O<sub>2</sub> in the presence of excess <sup>n</sup>Bu<sub>4</sub>OH (Figure 26b).<sup>233,234</sup> These compounds exhibited Raman  $\nu_{\text{sym}}(\text{O}=\text{Mn}^{\text{V}}=\text{O})$  values of 741–744 cm<sup>-1</sup>, which were decreased by 21–26 cm<sup>-1</sup> and 39–44 cm<sup>-1</sup>, respectively, upon single and double <sup>18</sup>O substitution on O=Mn<sup>V</sup>=O moiety. Significantly,  $\nu_{\text{asym}}(\text{O}=\text{Mn}^{\text{V}}=\text{O})$  values detected by IR were predictably different, confirming the linear, triatomic structure of the dioxoMn(V) unit (Figure 26c). A similar Mn<sup>V</sup>(O) intermediate was synthesized by Nam et al. and was assigned as a six coordinate *trans*-oxohydroxo Mn(V) complex.<sup>235</sup> However, a Mn–O distance of 1.68 Å determined by EXAFS indicates a double rather than a triple bond between Mn and oxygen. It is very likely that this species is also a *trans*-dioxoMn(V) complex.

On the basis of the  $\nu_{\text{sym}}$  and  $\nu_{\text{asym}}$  data obtained for compound 54, the Mn–O bond force constant ( $F$ ) and stretch–stretch constant ( $k$ ) were determined to be 454 and 67.2 N/m, respectively. Using the recently reported EXAFS bond length of 54 and available data of various terminal monooxo-manganese complexes,<sup>235</sup> a linear correlation was found between  $F^{-1/3}$  and Mn–O bond lengths (Figure 26d), in line with predictions of Badger’s rule.<sup>236,237</sup> A similar correlation between  $F^{-1/3}$  and Fe–O bond lengths has previously been reported by Green et al. for oxoiron(IV) porphyrins.<sup>236</sup> Although *trans*-dioxo metal porphyrins have been characterized for second- and third-row transition metals such as Ru<sup>VI</sup> and Os<sup>VI</sup>,<sup>238–242</sup> manganese remains the only known first-row transition metal that can form a *trans*-dioxo species. The isolated *trans*-dioxoMn(V) porphyrins were less reactive toward typical substrates but could be activated via decreasing the pH. This pH-dependent reactivity supports the previously proposed acid–base equilibria between the *trans*-dioxoMn(V), oxo–hydroxo Mn(V), and oxo-aqua Mn(V) species and their increasing reactivity for oxidation reactions.<sup>227,243</sup> DFT calculations indicated that this trend correlated with corresponding energy gaps between unreactive singlet ground state and higher-energy triplet and quintet states.<sup>244</sup>

## 2.5. Compound II and Its Protonation State—ferryl or Hydroxoiron(IV)

The one-electron-reduction of oxoiron(IV) porphyrin cation radicals, cpd I, affords a ferryl porphyrin (cpd II), which also has an iron(IV) center ( $S = 1$ ), similar to that of cpd I but lacking the porphyrin cation radical. The protonation state of cpd II has generated considerable research interest because of its importance in determining cpd I reactivity (see section 3.1).<sup>245</sup> HRP-II, Mb-II, and CcP compound ES were among the earliest cpd II or cpd II-like species to be spectroscopically characterized.<sup>115,122,173,246–248</sup> The first synthetic ferryl porphyrin model compound was described by Balch et al.<sup>249</sup> X-ray absorption measurements of these intermediates showed a Fe–



Table 2. Structural and Spectroscopic Parameters of Representative Compound II of Heme Proteins<sup>a</sup>

entry	$d(\text{Fe}^{\text{IV}}\text{-O})^b$ (Å)	$\delta$ (mm/s)	$\Delta E_Q$ (mm/s)	$\text{p}K_a(\text{Fe}^{\text{IV}}\text{-OH})$	ref
HRP-II	$1.70 \pm 0.02$ (6.0)	0.03 (6.9)	1.61 (6.9)	$\leq 3.5$	245
Mb-II	1.66 (3.9)	0.07 (3.9)	1.58 (3.9)	$\leq 2.7$	256
CcP-ES	1.67 (6.0)	0.05 (7.0)	1.55 (7.0)	$\leq 4$	245
Catalase-II	1.78 (5.3)	0.02 (5)	2.28 (5)	13.1	262
CPO-II	1.82 (6.5)	0.10 (6.5) <sup>c</sup>	2.06 (6.5) <sup>c</sup>	$\geq 8.2$	250 259,
CYP119-II	—	0.12 (8.0)	1.94 (8.0)	12.2	260
CYP158-II	1.84 (9.0)	0.10 (9.0)	2.05 (9.0)	12.0	260

<sup>a</sup>pHs are shown in parentheses. <sup>b</sup>Fe–O bond distances obtained from EXAFS studies. <sup>c</sup>Parameters for the major component. A minor component is present with  $\delta = 0.11$  mm/s and  $\Delta E_Q = 1.59$  mm/s.

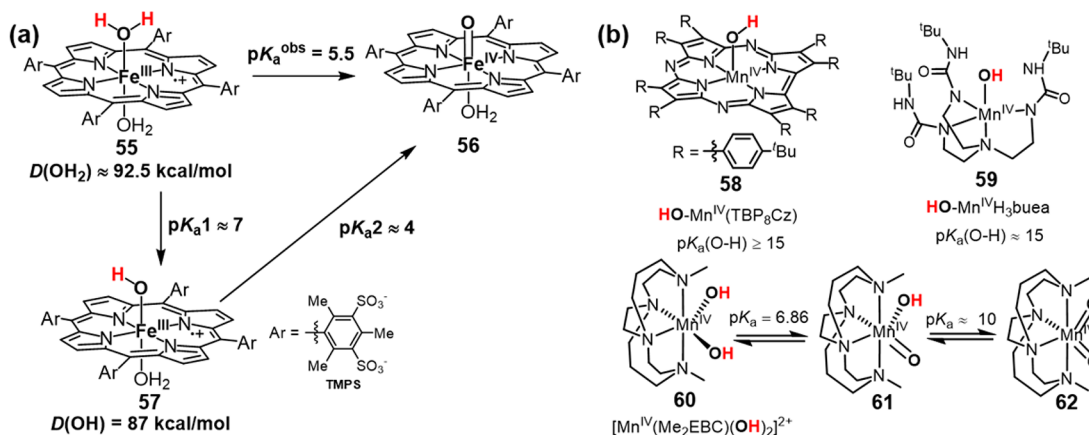


Figure 27. (a) Basicities of model hydroxo- and oxoiron(IV) porphyrin complexes. The second protonation provides an additional 5 kcal/mol driving force for HAT. (b) Acidities of several Mn<sup>IV</sup>-OH complexes.

O bond lengths in the range of 1.64–1.70 Å, indicating a Fe=O unit.<sup>248,250–252</sup> The Fe=O structure is also consistent with the resonance Raman studies in which Fe(IV)–O stretching vibrations were detected in the range from 740 to 870 cm<sup>-1</sup>.<sup>236</sup> These results, however, contradicted data obtained with X-ray crystallography, in which much larger (>1.80 Å) Fe–O bond distances were determined.<sup>48,253,254</sup> This discrepancy arose mainly from the radiolytic reduction caused by the hydrated electrons generated by the X-ray irradiation during data collection. For instance, Poulos and co-workers found that the Fe–O distance of CcP-ES changed linearly with the radiation dosage. The Fe–O distance measured at high-X-ray doses was 0.17 Å longer than that measured at low doses (1.9 Å vs 1.73 Å).<sup>255</sup> Structures obtained by nonionizing neutron cryocrystallography also support a Fe(IV)=O structure for CcP-ES with a Fe–O distance around 1.6 Å.<sup>126</sup> Since HRP-II, Mb-II, and CcP-ES exist in Fe(IV)=O state with pH as low as 4.5, their conjugate acid (Fe(IV)-OH) would have to be highly acidic (Table 2).<sup>245</sup> Recently, a more accurate measurement of the Mb-II  $\text{p}K_a$  was performed by Green et al. An upper limit of 2.7 for  $\text{p}K_a(\text{Mb-II})$  was determined by probing Mb-II over a wide pH range (3.9–9.5) with a combination of EXAFS, Mössbauer, and resonance Raman spectroscopies.<sup>256</sup> No evidence of a protonated Mb-II was obtained.

The cpd II of chloroperoxidase (CPO) stands in sharp contrast to HRP-II, Mb-II, and CcP-ES. The EXAFS measurements by Green, Dawson, and Gray revealed a Fe–O length of 1.82 Å at pH 5.5 and pH 6.7.<sup>250</sup> The visible spectrum of CPO-II remained unchanged from pH 3–7, suggesting a  $\text{p}K_a(\text{CPO-II}) \geq 8.2$  (assuming CPO-II is 95% protonated at pH = 6.9). The unusual basicity of CPO-II is explained by the strong electron donation by the axial thiolate, which leads to a more

basic ferryl oxygen. This “push” effect of a cysteine axial ligand suggests that cpd II of other heme-thiolate proteins might also be basic.<sup>257–259</sup> In 2013, Green and co-workers studied the protonation event of a P450 cpd II (CYP158-II) using rapid-mixing pH-jump experiments coupled with a variety of spectroscopic techniques. Both deprotonated and protonated forms of CYP158-II were well-characterized, and a remarkably basic  $\text{p}K_a$  of 12 was determined.<sup>260</sup> The ferryl protonation led to an elongation of Fe–O bond from 1.68 to 1.84 Å and a shortening of Fe–S bond from 2.36 to 2.27 Å along with an increase in quadrupole splitting and isomer shift, consistent with the generation of a Fe(IV)-OH species. The  $\text{p}K_a(\text{cpd II})$  of another P450, CYP119, was also determined in the same study. Unlike CYP158, wild-type CYP119 did not accumulate cpd II. Mutational studies have shown that Y352 is important for generation of CYP158-II, as it can serve as an electron source to reduce cpd I to cpd II. In CYP119, a leucine residue (L316) is in the position corresponding to Y352 in CYP158. The redox inactive leucine might prevent efficient cpd I reduction to generate cpd II. Indeed, an L316Y mutation was found to substantially increase the yield of CYP119-II. Despite having a different active site environment, CYP119 displayed a very similar  $\text{p}K_a(\text{cpd II})$  to that of CYP158. Very recently, the protonation of cpd II of a heme-thiolate peroxxygenase, *Aae*APO, has been investigated by Groves and co-workers.<sup>261</sup> A  $\text{p}K_a$  of 10.0 was obtained from pH-jump double-mixing stopped-flow experiments.

Very recently, Green et al. reported a  $\text{p}K_a$  of 13.1 for cpd II of *Helicobacter pylori* catalase (HPC).<sup>262</sup> The high  $\text{p}K_a$  value of HPC-II suggests that the tyrosinate axial ligand of catalase is electron-donating enough to maintain a highly basic ferryl, even though it forms a hydrogen bond with a conserved arginine

residue. Another case of a basic cpd II without a thiolate axial ligand was recently reported by Raven and Moody. They showed that cpd II of ascorbate peroxidase (APX-II) exists as  $\text{Fe}^{\text{IV}}\text{-OH}$ .<sup>263</sup> A neutron diffraction analysis of APX-II prepared via soaking APX crystals in *m*-CPBA solution revealed a long Fe–O bond distance of 1.84 Å, apparently confirming an earlier X-ray determination for that protein by the same authors.<sup>264</sup> The cause of protonation in APX-II and the protonation state of compound II of other peroxidases remains to be determined.

The basicity of metal–oxo moieties in model compounds has been much less studied. Recently, Boaz and Groves investigated the protonation of cpd II of several water-soluble sulfonated iron porphyrins.<sup>265</sup> A two-proton equilibrium with an apparent  $\text{pK}_{\text{a}}^{\text{obs}} = 5.5$  was determined for the protonation of  $[\text{O}=\text{Fe}^{\text{IV}}(\text{TMPS})(\text{OH}_2)]$  (56, Figure 27a). The resulting bis-aqua complex is an iron(III) porphyrin cation radical species 55 that is at the same net oxidation state. The absence of the accumulation of monoprotonated species 57 indicated that the first ferryl protonation with  $\text{pK}_{\text{a}1} (\sim 4)$  must produce a much more basic intermediate,  $\text{pK}_{\text{a}2} \sim 7$ . The increase in basicity is apparently due to a change in iron oxidation state from a protonated ferryl to a hydroxoferric porphyrin cation radical through an electromeric equilibrium after the first protonation. The effect of this two-proton electromeric equilibrium was shown to have a significant effect on the C–H scission reactivity of the corresponding compound I analog,  $[\text{O}=\text{Fe}^{\text{IV}}(\text{TMPS}^{\bullet+})(\text{OH}_2)]$ . In terms of the Bordwell equation, such a two-proton equilibrium leads to an increase in the overall driving force of 5–6 kcal/mol because two O–H bonds are being formed at the transition state (defined as  $D(\text{OH}_2)$  in Figure 27a), with one proton coming from the substrate and the other from the medium.

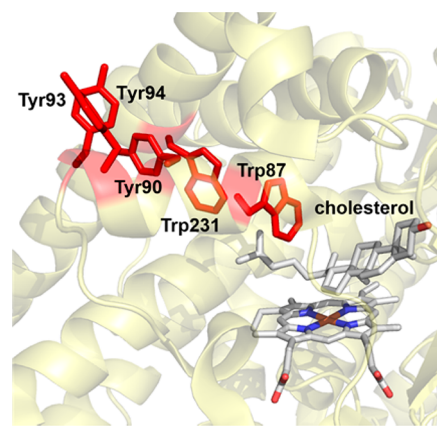
Several oxoMn(IV) porphyrins have been synthesized and characterized in the presence of strong base.<sup>221,222</sup> Fujii et al. successfully prepared and characterized a series of  $\text{Mn}^{\text{IV}}=\text{O}$  and  $\text{Mn}^{\text{IV}}\text{-OH}$  complexes with salen ligands via direct deprotonation of corresponding  $\text{Mn}^{\text{III}}\text{-OH}_2$  salen cation radical complexes.<sup>266,267</sup> But the  $\text{pK}_{\text{a}}$ 's of these Mn–OH species have yet to be reported. Since manganese is less electronegative than iron, Mn(IV)–OH should be less acidic than Fe(IV)–OH. There are several acidity data reported for  $\text{Mn}^{\text{IV}}\text{-OH}$  complexes with corrolazine or nonheme ligands (Figure 27b).<sup>268</sup> For instance, a lower limit around 15 was estimated for a  $\text{Mn}^{\text{IV}}\text{-OH}$  corrolazine complex 58 (Figure 27b).<sup>269</sup> A similar  $\text{Mn}^{\text{IV}}\text{-OH}$   $\text{pK}_{\text{a}}$  ( $\sim 15$ ) was also estimated for a nonheme  $\text{Mn}^{\text{IV}}\text{-OH}$  species 59.<sup>270</sup> Busch et al. synthesized a dihydroxomanganese(IV) complex 60 based on a cross-bridged cyclam ligand.  $\text{pK}_{\text{a}}$  of 6.86 and 10 were determined for the first and the second deprotonation, respectively.<sup>271</sup>

## 2.6. Preventing Protein Oxidative Damage by Cpd I

Compounds I of P450s and UPOs have remarkable activity and can activate very inert C–H bonds in substrates. It is not a coincidence that they also exhibit the highest compound II basicities among heme proteins. As discussed in detail in section 3.1.1, the thermodynamic driving force for C–H activation by cpd I depends on the reduction potential of cpd I and the basicity of cpd II. According to the Bordwell equation,<sup>272–274</sup> an increase of one  $\text{pK}$  unit in cpd II basicity would enhance the O–H bond strength of cpd II by 1.37 kcal/mol. Therefore, the high cpd II basicity of P450s and UPOs would allow them to break strong C–H bonds with relatively low reduction potentials, which, at least in part, prevents the

oxidative damage of protein superstructure by cpd I. The presence of chains of near-by tyrosine and tryptophan residues could provide further protection of enzymes during these oxidative transformations.<sup>275,276</sup> These redox-active residues

**Scheme 1. Chain of Redox Active Trp/Tyr Residues in CYP11A1 (PDB: 3N9Y)**



have been proposed to transport oxidizing equivalents of cpd I to protein surfaces. This protection machinery could be important for P450 catalysis, in which compounds I that are not consumed due to inefficient substrate oxidation could be effectively quenched. For instance, a five-residue Tyr/Trp chain has been identified in CYP11A1, which includes residues Trp87, Trp231, Tyr90, Tyr93, and Tyr94 (Scheme 1). Trp87 is critical for triggering the protection machinery. Once Trp87 gets oxidized by cpd I to form a cation radical, the oxidizing equivalent on Trp87 will rapidly transit through Trp231 and Tyr90 to surface-exposed Tyr93 and Tyr94. Kinetic simulations of CYP11A1 have indicated a  $\sim 3 \mu\text{s}$  survival time for cpd I before its oxidizing equivalents are transferred to the protein surface.<sup>275</sup> In this regard, C–H activation by cpd I could be viewed as an inner sphere process that competes with a slower, long-range outer-sphere electron transfer.

## 3. C–H FUNCTIONALIZATION REACTIONS MEDIATED BY OXOIRON(IV) PORPHYRIN CATION RADICALS (COMPOUND I)

The majority of reactions mediated by cpd I are initiated via hydrogen atom transfer (HAT). These reactions not only include aliphatic hydroxylation as introduced above but also encompass a broad range of oxidative transformations such as desaturation, decarboxylation, C–C bond scission, and a variety of rearrangement reactions. Like C–H hydroxylation, these alternative reaction pathways involve an initial hydrogen atom transfer (HAT) via cpd I and the generation of an intermediate substrate radical. A common mechanistic feature shared by these reactions is the redirection of substrate to other reaction pathways leading to nonoxygenated products.<sup>277–279</sup> This strategy represents a general approach to develop novel catalytic systems for developing novel C–H functionalization reactions. In this section, we will first discuss fundamental aspects of HAT and oxygen rebound steps in cpd I-mediated reactions, as well as various factors that affect these two steps. Further, we will introduce several representative examples of nonconventional C–H activation transformations catalyzed by P450s and metalloporphyrins. In particular, we will delineate

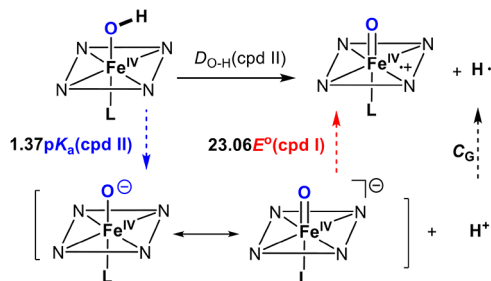
how substrate radical intermediates are controlled to achieve

different types of reactions.

### Scheme 2. Determination of $D(\text{O}-\text{H})$ from the One-Electron Reduction Potential of Compound I and the $pK_a$ of Compound II<sup>a</sup>

$$D_{\text{O-H}}(\text{cpd II}) = 23.06E^\circ(\text{cpd I}) + 1.37pK_a(\text{cpd II}) + C_G \text{ (kcal/mol)} \quad (1)$$

$$D_{\text{O-H}}(\text{cpd II}) = 23.06E^\circ(\text{cpd I}) + 1.37pH + C_G \text{ (kcal/mol)} \quad (2)$$



<sup>a</sup> $C_G$  is a constant depending on the solvent and electrode (57.6 kcal/mol for aqueous solution and the normal hydrogen electrode). When  $E^\circ(\text{cpd I})$  at a given pH is determined, eq 2 can be used to calculate  $D(\text{O}-\text{H})$ .  $D(\text{O}-\text{H})$  obtained via eq 1 and eq 2 is the bond dissociation free energy (BDFE). If the entropic difference between protonated and unprotonated cpd II is negligible, the same equations can be used to calculate the bond dissociation enthalpies (BDE) of O-H bonds using constant  $C_H$  (55.8 kcal/mol for aqueous solution and normal hydrogen electrode).<sup>274</sup>

## 3.1. Factors that Affect Oxoiron(IV) Porphyrin Cation Radical Reactivity for HAT

### 3.1.1. Thermodynamic Properties of Cpd I.

For a given C-H bond, the driving force of HAT reactions will be determined by the free energy of the O-H bond formed in cpd II [ $D_{\text{O-H}}(\text{cpd II})$ ]. Using thermochemical cycles to estimate bond dissociation free energies from measurable  $pK_a$  values and oxidation potentials has a long history,<sup>280</sup> which was systematically developed by Bordwell<sup>280</sup> and extended to metal-oxo species by Mayer.<sup>272-274</sup> In accordance with the Bordwell equation (eqs 1 and 2, Scheme 2).<sup>272-274</sup> The bond dissociation free energies of an X-H bond can be derived from the X-H  $pK_a$  and the  $X^-$  oxidation potential using a Hess cycle. Thus, an increase in cpd II ferryl basicity [higher  $pK_a$  for  $\text{Fe}(\text{IV})\text{O}-\text{H}$ ] would lead to a stronger O-H bond formed in cpd II and a more thermodynamic driving force (1.37 kcal/mol per  $pK_a$  unit) for the C-H abstraction by cpd I. For instance, the more electron-donating cysteine (thiolate) axial ligand in P450s can increase the basicity of compound II by over 7  $pK_a$  units compared to the histidine-ligated myoglobin and

**Table 3.**  $pK_a$  and  $BDE_{\text{OH}}$  of Cpd II and Reduction Potentials of Cpd I

entry	$E^\circ(\text{cpd I}/\text{cpd II})$ vs NHE	$pK_a(\text{cpd II})$	$BDE_{\text{OH}}(\text{cpd II})$	ref
HRP	0.95 V (pH 6.0)	$\leq 3.5$	$\sim 87$ kcal/mol	282
CPO	$1.3 \pm 0.1$ V (pH 6.0)	$\geq 8.2$	$\sim 98 \pm 4$ kcal/mol	250
AaeUPO	1.4 V (pH 7.0)	10.0	$\sim 100$ kcal/mol	283

horseradish peroxidase.<sup>19,260,281</sup> Considering the  $pK_a$  term in the Bordwell equation, this change in basicity corresponds to at least a 9 kcal/mol increase in O-H BDE of compound II.<sup>260,261</sup>

The reduction potential of cpd I to cpd II also plays an important role in determining cpd I reactivity.  $E^\circ(\text{cpd I}/\text{cpd II})$  of horseradish peroxidase (HRP) has been determined to be  $\sim 0.95$  V versus NHE at pH 6.0 (Table 3).<sup>282</sup> Intriguingly, HRP showed almost identical reduction potentials for cpd I and cpd II. It is much harder to determine  $E^\circ(\text{cpd I}/\text{cpd II})$  for P450s and CPO because of the short lifetimes of these intermediates. Instead, the two-electron reduction potential  $E^\circ(\text{cpd I}/\text{ferric})$  has usually been measured, which, in turn, can be used to estimate  $E^\circ(\text{cpd I}/\text{cpd II})$  with certain assumptions. For instance, assuming a similar redox potential for CPO-I and CPO-II, Green, Dawson, and Gray estimated the redox potential of CPO-I to be  $1.3 \pm 0.1$  V at pH 6, which is 0.35 V higher than that of HRP, corresponding to an  $\sim 8$  kcal/mol increase in  $D_{\text{OH}}(\text{cpd II})$ .<sup>250</sup> This enhancement together with the contribution of a basic CPO-II led to an overall over 11 kcal/mol increase in  $D_{\text{OH}}(\text{CPO-II})$  compared to  $D_{\text{OH}}(\text{HRP-II})$ .

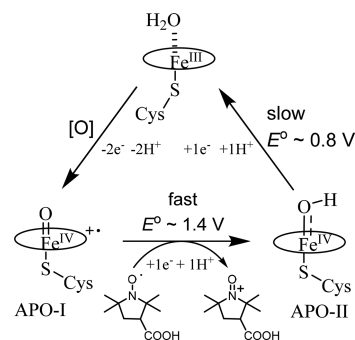
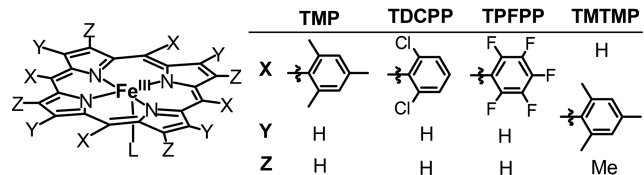


**Figure 28.** Selective reduction of APO-I to APO-II by a nitroxyl radical with  $E^\circ = 0.9$  V. Redox potentials are obtained from ref 283

Very recently, Wang and Groves were able to determine the thermodynamic properties of the heme-thiolate peroxxygenase AaeAPO-I.<sup>283</sup> This approach utilized the rapid, reversible oxygen atom transfer between cpd I and halide ions to determine the two-electron cpd I reduction potential. The measured  $E^\circ(\text{cpd I}/\text{ferric})$  was in the range of 1.12–1.32 V versus NHE from pH 7.0 to 3.0. From plots of the rate for C-H abstraction versus substrate C-H BDE, the  $D_{\text{OH}}(\text{CPO-II})$  was estimated to be 100 kcal/mol. This value leads to an  $E^\circ(\text{cpd I}/\text{cpd II})$  of 1.4 V and  $E^\circ(\text{cpd II}/\text{ferric})$  of 0.8 V at pH 7.0 (Figure 28). This estimate was further supported by the reaction of nitroxyl radicals with AaeAPO-I. 3-Carboxyproxyl ( $E^\circ \sim 0.9$  V) reacted rapidly with APO-I to form APO-II, which decayed much more slowly under these conditions. This pronounced reactivity difference shows that APO-II is a much milder oxidant. By contrast, the two analogous reduction potentials of HRP-I are both around 0.9 V. Thus, APO has increased the reduction potential of APO-I to perform the difficult C-H scission at the expense of APO-II, which needs only to interact with the incipient substrate radical. With nitroxyl radical as a selective reductant for APO-I, APO-II could be produced in high yield and the  $pK_a$  has been determined to be 10.0 via rapid-mixing, pH-jump spectrophotometry. With these values, the  $D_{\text{OH}}(\text{APO-II})$  was calculated to be around 100 kcal/mol, consistent with the estimate above determined from kinetic measurements.

**3.1.2. Effect of Axial Ligands and Porphyrin Peripheral Substituents on Cpd I Reactivity.** It is clear from the above discussion that axial ligands can have a huge impact on cpd I reactivity. Such effects have been observed in a number of model compound studies. For example, a 650-fold rate enhancement was reported for cyclohexene hydroxylation by changing the axial ligand of  $\text{Fe}^{\text{III}}(\text{TPFPP})\text{L}$  from  $\text{CF}_3\text{SO}_3^-$  to  $\text{Cl}^-$ .<sup>284</sup> Subsequent DFT calculations showed that this ligand replacement was predicted to cause a 6 kcal/mol increase in  $\text{Fe}^{\text{IV}}\text{O}-\text{H}$  BDE, and that the main attribute of this BDE enhancement is the increase in cpd II basicity.<sup>285</sup> The axial ligand effect on C–H hydroxylation was also investigated for  $\text{Fe}^{\text{IV}}(\text{O})(\text{TMP}^{\bullet+})$  with *para*-substituted pyridine *N*-oxide (*p*-Y-PyO) axial ligands.<sup>285</sup> In this system, the hydroxylation reactivity increased with the increasing electron-donating ability of *para*-substituent Y. A good correlation between calculated activation energies and  $\text{Fe}^{\text{IV}}\text{O}-\text{H}$  acidity was obtained, which,



Porphyrin	Axial ligand (L)	$\text{Fe}^{\text{IV}}\text{O}(\text{Por})/\text{Fe}^{\text{IV}}(\text{O})(\text{Por}^{\bullet+})^b$			
		$E_{\text{pa}}$	$E_{\text{pc}}$	$E_{1/2}$	
TMP	$\text{ClO}_4^-$	0.97	0.79	0.88 (0.91)	
	$\text{ClO}_4^-^c$	0.91	0.84	0.88 (0.90)	
	$\text{F}^-$	1.03	0.89	0.96 (0.95)	
	$\text{Cl}^-$	1.06	0.88	0.97 (0.94)	
	$\text{CH}_3\text{COO}^-$	1.10	0.89	1.04 (1.04)	
	$\text{CF}_3\text{COO}^-$	1.02	0.90	0.96 (0.96)	
	benzoate	1.09	0.89	0.99 (1.04)	
	$\text{NO}_3^-$	1.03	0.88	0.95 (0.94)	
	3-fluoro-4-nitrophenolate	1.03	0.89	0.96 (0.96)	
TDCPP	imidazole	0.84	0.76	0.80 (0.76)	
	2-methylimidazole	0.81	0.73	0.77 (0.75)	
	5-methylimidazole	0.78	0.73	0.76 (0.72)	
	TDCPP	$\text{ClO}_4^-^c$	1.30	1.25	1.275
	TPFPP	$\text{ClO}_4^-^d$	1.43	1.35	1.39 (1.39)
TMTMP	$\text{ClO}_4^-$	0.98	0.83	0.90 (0.92)	
	$\text{NO}_3^-$	1.01	0.89	0.95 (0.94)	
	imidazole	0.87	0.80	0.84	

**Figure 29.** Redox potentials (vs  $\text{SCE}^a$ ) of cpd I models in  $\text{CH}_2\text{Cl}_2$  at  $-60^\circ\text{C}$ . <sup>a</sup>Under these conditions, the redox potential ( $E_{1/2}$ ) of ferrocene was 0.460 V at  $-60^\circ\text{C}$  and 0.528 V at  $20^\circ\text{C}$ . <sup>b</sup>Values in parentheses were obtained from differential pulse voltammetry. <sup>c</sup>In  $\text{CH}_3\text{CN}$  at  $-35^\circ\text{C}$ . <sup>d</sup>In  $\text{CH}_2\text{Cl}_2/\text{CH}_3\text{CN}$  (1:1). Adapted from ref 290. Copyright 2011 American Chemical Society.

again, suggested that axial ligand could affect cpd I reactivity via tuning cpd II basicity.

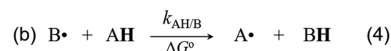
While the increase in cpd II ferryl basicity via introducing electron-donating axial ligands has now been observed, the effect of axial ligands on cpd I reduction potential [ $E^\circ(\text{cpd I})$ ] is less clear. A number of theoretical calculations have shown that  $E^\circ(\text{cpd I})$  decreased with increasing electron-donation from axial ligand and that cpd I with negatively charged ligands such as  $\text{F}^-$  and  $\text{Cl}^-$  exhibited lower  $E^\circ(\text{cpd I})$  than those with neutral

ligands such as imidazole.<sup>286–289</sup> However, Fujii et al. measured the reduction potential of a series  $\text{Fe}^{\text{IV}}(\text{O})(\text{TMP}^{\bullet+})\text{L}$  and found an opposite trend (Figure 29). With  $\text{L} = \text{ClO}_4^-$  as a reference, a 0.08–0.16 V positive shift of  $E^\circ(\text{cpd I})$  was determined for anionic axial ligands such as  $\text{Cl}^-$ ,  $\text{F}^-$ ,  $\text{CH}_3\text{CO}_2^-$ , and benzoate, whereas a negative shift ( $-0.08$  to  $-0.12$  V) was found for neutral imidazole-type ligands.<sup>290</sup> The cause of this discrepancy between theory and experiments is not clear at this writing and further investigations are needed.

Synthetic porphyrin ligands almost always contain substitutions at the pyrrole  $\beta$ -carbon and/or the *meso*-porphyrin positions. These substitutions, as discussed in previous sections, are important for the reactivity of synthetic metalloporphyrins. They can prevent undesired side reactions that diminish the reactivity of metalloporphyrin catalysts during the oxidative reactions, such as the formation of  $\mu$ -oxo dimers and the destruction of porphyrin ligands. As discussed in section 2.4.2, the electronic properties of *meso*- and pyrrole- $\beta$  substituents substantially affect the energy of porphyrin  $a_{1u}$  and  $a_{2u}$   $\pi$ -orbitals, thus changing the singly occupied orbitals of porphyrin radicals of compounds I. Although the electronic structure of the porphyrin radical ( $a_{1u}$  or  $a_{2u}$ ) apparently does not affect cpd I reactivity very much,<sup>27</sup> the introduction of electron-withdrawing groups at both positions were shown to greatly increase the reduction potential of cpd I (Figure 29)<sup>290,291</sup> and thus increase the thermodynamic driving force of HAT.<sup>209,290</sup> Indeed, the second order-rate constants for aliphatic hydroxylation mediated by an electron-deficient cpd I  $\text{Fe}^{\text{IV}}(\text{O})-$

### Scheme 3. (a) Brønsted–Evans–Polanyi (BEP) Correlation for HAT Reactions and (b) Cross Correlation of HAT Reactions

$$(a) \log(k_{\text{H}}) = \alpha\Delta H^\ddagger + c \quad (3)$$



$$\Delta G^\circ = -RT\ln K_{\text{eq}} \quad (7)$$

$$k_{\text{AH/B}} = \sqrt{k_{\text{AH/A}}k_{\text{BH/B}}K_{\text{eq}}} \quad (8)$$

(TPFPP<sup>•+</sup>) were 2–10 times larger than those obtained with  $\text{Fe}^{\text{IV}}(\text{O})(\text{TMP}^{\bullet+})$ .<sup>211</sup>

**3.1.3. Correlation of Thermodynamic Driving Force with Rate Constants of HAT.** The thermodynamic driving force of HAT via cpd I is the net free-energy change resulting from the C–H bond that is broken and the O–H bond that is formed at the ferryl oxygen. In many C–H activation reactions mediated by iron–oxo intermediates, an empirical Brønsted–Evans–Polanyi (BEP) correlation has been observed,<sup>292</sup> in which the free-energy barriers ( $\Delta G^\ddagger$ ), and thus the rates of hydrogen atom transfer (HAT) are negatively correlated with bond dissociation energies (BDE) of the scissile C–H bonds (eq 3, Scheme 3a).<sup>273,293</sup> We use BDE here instead of bond dissociation free energies for simplicity because comparative data is more readily available and the differences are small. The slope  $\alpha$  (Brønsted coefficient,  $0 < \alpha < 1$ ) is interpreted to reflect the position of hydrogen along the reaction coordinate in the linear transition state  $[\text{Fe}-\text{O}---\text{H}---\text{C}]^\ddagger$ , with  $\alpha = 0$

referring to a reactant-like (“early”) transition state with a strong C–H bond character and  $\alpha = 1$  for a product-like (“late”) transition state with a strong O–H bond feature.<sup>294</sup>

While being broadly applied to a variety of HAT processes, the BEP relationship is less successful at correlating reactants with disparate molecular features. For instance, phenol O–H bonds have similar BDEs to benzylic C–H bonds but show much faster rates for HAT to iron–oxo intermediates.<sup>261</sup> Such limitations of the BEP equation have led Mayer et al. to apply the Marcus cross correlation to analyze HAT, in analogy to Marcus electron transfer theory.<sup>295,296</sup> Thus, for a HAT reaction,  $AH + B \cdot \rightarrow BH + A \cdot$  (eq 4, Scheme 3b), the reaction rate for HAT ( $k_{AH/B}$ ) is estimated from the equilibrium constant  $K_{eq}$  of the reaction and the two self-exchange rate constants ( $k_{AH/A}$  and  $k_{BH/B}$ ) for the individual reactants A/AH and B/BH (eq 5 and 6). Since the rates of the self-exchange reactions can be experimentally determined in favorable cases (e.g., via NMR line broadening), Mayer’s method offers a powerful approach to predict kinetic properties of HAT from intrinsic properties of individual reactants.<sup>273</sup> With this method, it was found that the self-exchange rate constants of phenols were  $\sim 10^8$  larger than those of alkanes, which matched the observed difference in their HAT rate constants.<sup>295</sup> The origin of the faster phenol rates is likely due to the fact that a phenol is a good hydrogen bond donor while an aliphatic C–H proton is not.

BDEs (or BDFEs) are purely thermodynamic properties and should not necessarily mirror the structural and entropy effects that affect transition-state energies of HAT events. As recently summarized by Bietti et al. for aliphatic C–H activation by alkoxyl radicals, structural effects (such as polar effects, stereoelectronic effects, and strain-release) and medium effects can have very large impacts on the reactivity of C–H bonds.<sup>297</sup> Thus, the thermodynamically weakest C–H bond is not necessarily the most reactive one. This phenomenon has also been observed in C–H activation reactions of heme proteins and metalloporphyrins. A good example is the deactivation of  $\alpha$  C–H bonds near electron-withdrawing groups such as ketones, esters, and nitriles in metalloporphyrin-catalyzed C–H hydroxylations and halogenations,<sup>298</sup> although these bonds have lower BDEs than other reactants. This is a typical polar effect. Another factor that can affect rates of HAT is the entropic contribution to the free-energy barriers. Entropy effects would be most evident for C–H activation of substrates with weak C–H BDEs. These reactions will have early transition states with the C–H bonds elongated to a minimal extent. Thus, activation enthalpies ( $\Delta H^\ddagger$ ) are insensitive to C–H BDEs in this scenario, and overall free-energy barriers will be determined by the entropy term  $T\Delta S^\ddagger$ . Tanko et al. have measured rate constants of C–H abstraction by  $^t\text{BuO}\cdot$ , for which the O–H bond formed during HAT has a BDE of 104 kcal/mol.<sup>299</sup> A good BEP correlation was found for C–H BDEs greater than 92 kcal/mol, whereas for C–H BDEs below 92 kcal/mol, a flat  $\log k_H$  versus BDE plot was observed. Further analysis showed similar  $\Delta H^\ddagger$  values ( $\sim 2$  kcal/mol) for the flat region, and the entropy contribution outweighs that of enthalpy for most hydrogen abstractions by  $^t\text{BuO}\cdot$ .

We have found a similar nonlinear BEP correlation for C–H hydroxylation by the fungal heme-thiolate peroxxygenase AaeAPO compound I (AaeAPO-I) (Figure 30).<sup>200</sup> A Bronsted coefficient of about 0.4 was determined for  $\log k_H$  versus BDE for substrates with C–H bonds stronger than 90 kcal/mol, indicating a nearly symmetrical  $[\text{Fe}-\text{O}---\text{H}---\text{C}]^\ddagger$  transition

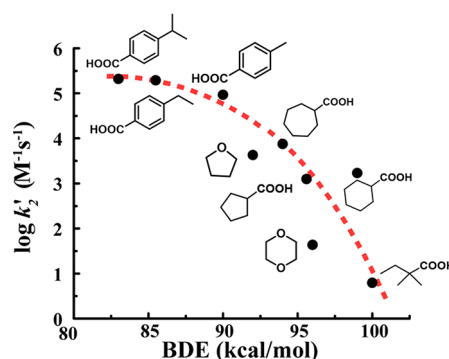


**Figure 30.** Nonlinear BEP correlation for C–H hydroxylation by AaeAPO-I. Adapted from ref 200. Copyright 2012 American Chemical Society.

state in this region. But for BDE < 90 kcal/mol, the rate constant was not sensitive to C–H BDEs. Since the observed rate constants in the flat region were shown to be slower than both the active site substrate exchange and the diffusion limit, HAT by AaeAPO-I for C–H BDEs less than 90 kcal/mol is entropy-controlled and is more dependent on factors such as orientation, accessibility, and trajectory toward the transition state. These results are consistent with a  $\text{Fe}^{\text{IV}}\text{O}-\text{H}$  BDE in AaeAPO-II of  $\sim 100$  kcal/mol. The entropy effect was also found to affect the chemoselectivity of oxygenation reactions catalyzed by metalloporphyrins. Fujii et al. determined the activation parameters for epoxidation and allylic hydroxylation for cyclohexene oxidation mediated by  $\text{Fe}^{\text{IV}}(\text{O})(\text{TMP}^{\bullet+})\text{Cl}$ . By varying temperatures between 193 and 233 K, they determined the enthalpy and entropy of activation ( $\Delta H^\ddagger$  and  $\Delta S^\ddagger$ ) to be  $8.0 \pm 0.4$  kcal/mol,  $-24.0 \pm 1.6$  cal mol $^{-1}$  K $^{-1}$  and  $4.6 \pm 0.6$  kcal/mol and  $-40.3 \pm 2.1$  cal mol $^{-1}$  K $^{-1}$  for epoxidation and allylic hydroxylation, respectively.<sup>300</sup> On the basis of these values, the contribution of the entropy term  $-T\Delta S^\ddagger$  would exceed that of enthalpy term in the free energy of activation ( $\Delta G^\ddagger$ ) for allylic oxidation at temperatures above 114 K, while the entropy term

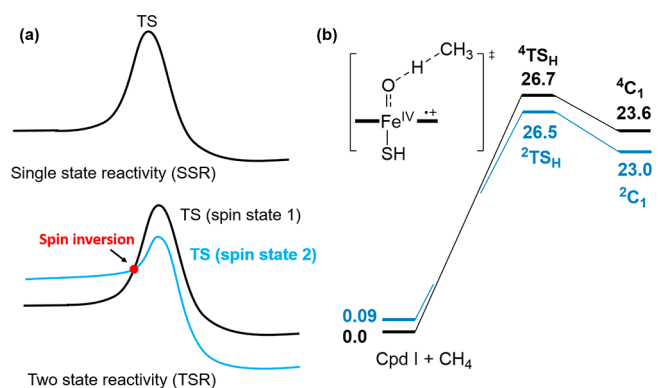


**Figure 31.** (a) Schematic illustration of two-state reactivity (TSR). (b) Two-state reactivity for C–H activation via an iron porphyrin catalyst (energies in kcal/mol, obtained from ref 305).

provides the major contribution to  $\Delta G^\ddagger$  for epoxidation at temperatures above 334 K.

**3.1.4. Two-State and Multistate Reactivity.** Compared to simple organic radicals such as  $^t\text{BuO}\cdot$ , a distinct feature of paramagnetic transition metal complexes is the existence of multiple spin states that can be close in energy. Thus, a given reaction may occur along different spin surfaces, and a higher-

energy spin state could have the lowest-energy transition state. Such a situation can lead to spin crossover along the reaction coordinate from reactants to products. This concept was first proposed by Shaik, Schröder, and Schwarz and termed “two-state reactivity” (TSR) or “multistate reactivity” (MSR) (Figure

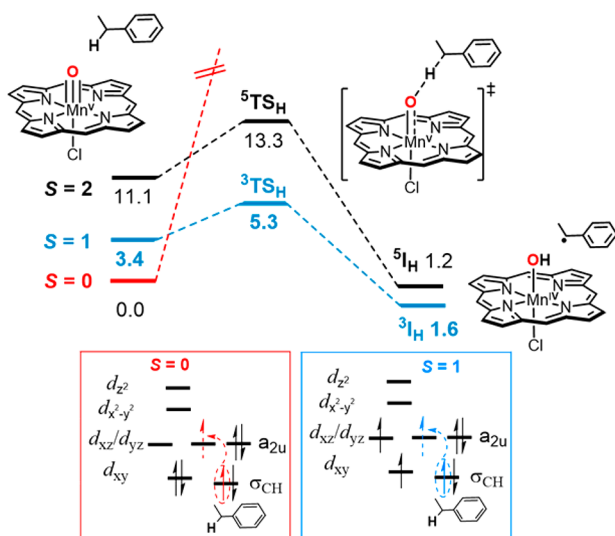


**Figure 32.** Energy profile for C–H activation mediated by an oxoMn(V) porphyrin complex.

31a).<sup>301–303</sup> HAT by compound I was one of the first systems to be studied for TSR in transition metal catalysis (Figure 31b). DFT calculations of cpd I of iron porphine revealed that the quartet and doublet spin states, wherein the porphyrin cation radical is either ferromagnetically or antiferromagnetically coupled to the  $S = 1$  ferryl, were very close in energy and had comparable activation barriers for C–H activation, suggesting important contributions of both spin states for HAT.<sup>304</sup> QM/MM studies also showed similar mechanistic features for HAT by P450 compound I.<sup>305,306</sup>

C–H activation mediated by oxoMn(V) porphyrins represents another example of potential TSR in metal-porphyrin-mediated reactions (Figure 32).<sup>226,227</sup> DFT calculations showed that the singlet ground state of oxoMn(V),<sup>243</sup> which is known from the experiment,<sup>227,233,243</sup> had a very high energy barrier for C–H activation.<sup>244,307,308</sup> The triplet spin state, which is calculated to be only 3.4 kcal/mol higher than the singlet ground state, had the lowest-energy transition state (5.3 kcal/mol relative to the singlet ground state). The energy of the quintet state is much higher (11.1 kcal/mol) than the singlet state and is likely not accessible, despite the low activation energy of this spin state (2.2 kcal/mol). Therefore, during C–H activation, the unreactive singlet oxoMn(V) would undergo spin-crossing to the triplet energy surface.

Shaik recently introduced the concept of exchange-enhanced reactivity (EER) as a general principle to evaluate the preferred spin state for a given reaction state especially catalyzed by  $3d$  metals.<sup>309,310</sup> The main idea is that transition states with an increased number of unpaired spin-identical electrons at metal center would be stabilized by enhanced electron-exchange. Such an exchange can be assessed by multiplying the exchange interaction of two unpaired electrons ( $K_{dd}$ ) with the number of such interactions ( $n$ ). The gained exchange-energy ( $\Delta K_{dd}$ ) versus the orbital promotion energy ( $\Delta E_{orb}$ ) needed for

promoting an electron into a higher-lying orbital would determine the preferred spin state. This concept can be utilized to analyze the preference for the triplet state in oxoMn(V)-mediated C–H activation in Figure 32.<sup>311</sup> The transition state on the  $S = 0$  surface is an open shell singlet with no spin-exchange interactions, while for the triplet surface, three exchange interactions are present. The overall stabilization effect in the triplet state can be estimated by  $3K_{dd} - \Delta E_{orb}(d_{xy} \rightarrow d_{xz/yz})$ , in which  $\Delta E_{orb}(d_{xy} \rightarrow d_{xz/yz})$  is the energy needed for orbital excitation from  $d_{xy}$  to  $d_{xz/yz}$ . Although these energies have not been determined for manganese porphyrins, the  $K_{dd}$  of 11.1 kcal/mol and  $\Delta E_{orb}(d_{xy} \rightarrow d_{xz/yz})$  of 26.4 kcal/mol have been estimated for an analogous oxoMn(V) corrolazine species, indicating a net stabilization of  $\sim 6.9$  kcal/mol. This stabilization energy is comparable to the calculated energy barrier difference between singlet and triplet pathways for this species.<sup>311</sup>

The kinetic isotope effect (KIE) for hydrogen/deuterium HAT has been proposed to be a good mechanistic probe to probe the reactive spin state of a reaction. Theoretical calculations have shown that different spin states can display very different KIEs.<sup>312–314</sup> For instance, in the demethylation reaction of *para*-substituted *N,N*-dimethylaniline (*p*-Y-DMA), a positive linear correlation was found between experimental KIE values ( $KIE_{exp}$ ) and the Hammett substituent parameter of *para*-substituent Y.<sup>315–317</sup> The calculation showed that only the low-spin doublet state showed this trend, while the calculated KIEs of high-spin quartet state ( $KIE_{HS}$ ) were much larger than the experimental values and were not sensitive to the *para*-substituent.<sup>318</sup> This result suggested that the low spin state is the primary state for cpd I reactivity of *N*-demethylation. A further analysis of  $KIE_{exp}$  using a blend of  $KIE_{LS}$  and  $KIE_{HS}$  showed that for Y = H and Cl, the reaction occurred exclusively on the LS surface, while for Y = CN and NO<sub>2</sub>, the reaction occurred through both states with 70/30% and 50/50%, respectively.

The nature of the axial ligand can also impact the relative energies of different spin states and the spin-state crossing. For instance, the HAT activity of oxoMn<sup>V</sup> porphyrins with axial ligand X (X = H<sub>2</sub>O, OH<sup>−</sup>, and O<sup>2−</sup>) has shown to increase in the following order: H<sub>2</sub>O > OH<sup>−</sup> > O<sup>2−</sup>.<sup>227,233</sup> DFT calculations indicated that this trend correlated with corresponding energy gaps between unreactive singlet ground state and higher-energy triplet and quintet states.<sup>244</sup> In a related study of less reactive oxoMn<sup>V</sup> corrolazine (Cz) complexes, de Visser and Goldberg showed that fluoride and cyanide axial ligands increased the rate of HAT by 10<sup>3</sup>–10<sup>5</sup>-fold compared to that with no axial ligand.<sup>319</sup> Computational studies showed 12 and 17 kcal/mol increases in the O–H BDE of Mn(IV)–OH for fluoride and cyanide axial ligands, respectively. The origin of the rate-enhancement exerted by axial ligands is a matter of debate. A computational study by Shaik indicated that fluoride and cyanide also stabilized the triplet transition state by 14–16 kcal/mol, due to a reduction in the  $\sigma_{xy} \rightarrow \pi^*_{xz/yz}$  excitation energy and an increase in exchange coupling of unpaired  $d$  electrons in the triplet transition state.<sup>311</sup> However, DFT and CASSCF calculations by the Goldberg and de Visser groups on Mn<sup>V</sup>(O)(Cz)-mediated sulfoxidation of thioanisole indicated small spin–orbit coupling constants, suggesting a singlet-to-triplet spin-state crossing before the rate-limiting step is unlikely.<sup>320</sup> In support of this statement, only the singlet spin state can computationally reproduce a V-shaped pattern observed in a Hammett analysis with *para*-substituted thioanisoles, in which a negative slope was obtained for

electro-donating *para*-substituents but a positive slope was observed for electron-withdrawing substituents.<sup>320</sup>

In addition to increasing the reduction potential of cpd I, the porphyrin peripheral substituents can also affect cpd I reactivity via regulating the spin state crossover. Groves et al. have studied the influence of two cationic *meso*-substituents 2-*N*-methylpyridyl (2-TMPyP) and 4-*N*-methylpyridyl (4-TMPyP) on oxygen transfer reactivity of oxoMn(V) porphyrins.<sup>227</sup> Surprisingly, the less electron-deficient [Mn<sup>V</sup>(O)(4-TMPyP)], with the *N*-methyl pyridium ions farther from the porphyrin ring, was 10–10<sup>3</sup> times more reactive than Mn<sup>V</sup>(O)(2-TMPyP). Computational studies showed that the 4-pyridyl isomer [Mn<sup>V</sup>(O)(4-TMPyP)] had a smaller low-spin-high-spin promotion energy and was therefore kinetically favored in a two-state energy profile involving spin state crossing from the

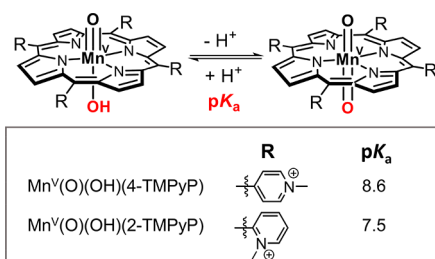


**Figure 33.** pK<sub>a</sub> of the hydroxo ligand of [Mn<sup>V</sup>(O)(OH)(4-TMPyP)] and [Mn<sup>V</sup>(O)(OH)(2-TMPyP)].

starting singlet oxoMn(V) species.<sup>243</sup> Furthermore, the *meso*-substituents were also shown to affect the acid–base equilibria involving the axial water ligand. As discussed in section 2.4.3, Mn<sup>V</sup>(O)(4-TMPyP) and Mn<sup>V</sup>(O)(2-TMPyP) have three different prototropic forms in water depending on the protonation state of the axial ligand, oxo-aqua, oxo-hydroxo, and *trans*-dioxo.<sup>232</sup> The reactivity of these three states increased in the following order: *trans*-dioxo < oxo-hydroxo < oxo-aqua. The less electron-deficient Mn<sup>V</sup>(O)(4-TMPyP) exhibited higher basicity for the axial aqua and hydroxo ligands (Figure 33). Thus, at the same pH, the kinetically more reactive

protonated species are more accessible for Mn<sup>V</sup>(O)(4-TMPyP), leading to the observed higher reactivity.<sup>227</sup>

**3.1.5. Quantum Tunneling in Hydrogen Atom Transfer.** Hydrogen is a small particle and as such can show quantum tunneling effects.<sup>321</sup> As a result, hydrogen can “tunnel” through the transition state barrier and thus increase the rate of HAT (Figure 34a). This energy reduction ( $\Delta\Delta E_{\text{tunneling}}^{\ddagger}$ ) associated with proton tunneling is commonly between 1–4 kcal/mol.<sup>322</sup> The kinetic hydrogen isotope effect is a useful tool to probe the tunneling phenomenon in HAT. There are three criteria proposed first by Kreevoy and co-workers with respect to organic radicals that are widely used for assessing a tunneling process: (1) a KIE significantly larger than 6.4 at 20 °C; (2) an activation energy difference between deuterium transfer and hydrogen transfer ( $E_a(\text{D}) - E_a(\text{H})$ ) larger than >5.0 kJ/mol (1.2 kcal/mol); and (3) a ratio of pre-exponential factors  $A_{\text{H}}/A_{\text{D}} < 0.7$ .<sup>323,324</sup>

Tunneling effects have been found in HAT processes mediated by a variety of metalloenzymes and related metal–oxygen model compounds.<sup>325–328</sup> Many of these systems are nonheme iron-containing enzymes and/or their model compounds.<sup>325–329</sup> In contrast, there are few examples of tunneling effects in cytochrome P450s and metalloporphyrins. Although KIEs (10–32) larger than usually adopted theoretical limit (~7) for nontunneling reactions have been reported for several P450-catalyzed reactions,<sup>330–334</sup> the extent of hydrogen tunneling in these reactions is not conclusive because of the difficulties in determining the activation energies and pre-exponential factors of these systems. In P450 model compounds, an early example of a possible tunneling event was reported by Sorokin and Khenkin.<sup>335</sup> They determined a KIE value of ~22 (20 °C) for cyclohexane oxidation catalyzed by Fe(TMP)Cl/NaOCl in benzene. They further determined a [ $E_a(\text{D}) - E_a(\text{H})$ ] of 4.5 ± 0.5 kcal/mol and  $A(\text{H})/A(\text{D}) = 0.01$ , indicating the presence of a tunneling effect. Similar effects have also been observed by Meunier et al. in a study of intramolecular KIEs of adamantane-1,3-*d*<sub>2</sub> hydroxylation catalyzed by a variety of metalloporphyrins.<sup>333</sup> For an Fe(TMP)Cl/NaOCl system, they observed a KIE of 9 (10 °C), [ $E_a(\text{D}) - E_a(\text{H})$ ] of 1.83 kcal/mol, and  $A(\text{H})/A(\text{D})$  of

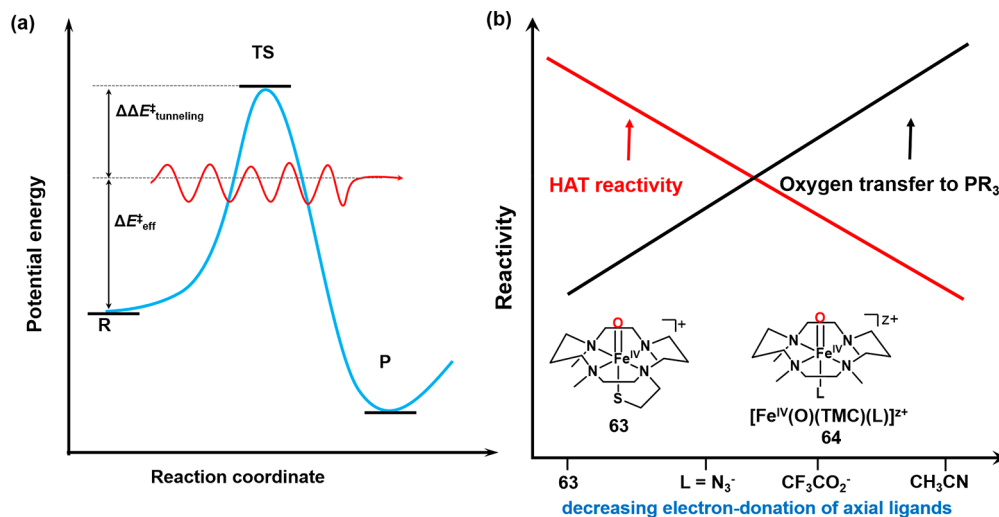


**Figure 34.** (a) Quantum tunneling (wavy arrow) leads to an effective energy barrier ( $\Delta E_{\text{eff}}^{\ddagger}$ ) 1–4 kcal/mol below TS. (b) Reactivity pattern for [Fe<sup>IV</sup>(O)(TMC)(L)]<sup>2+</sup> in HAT from alkanes (red line) and oxygen-transfer to phosphines (back line). Figure is adapted from ref 328. Copyright 2015 American Chemical Society.

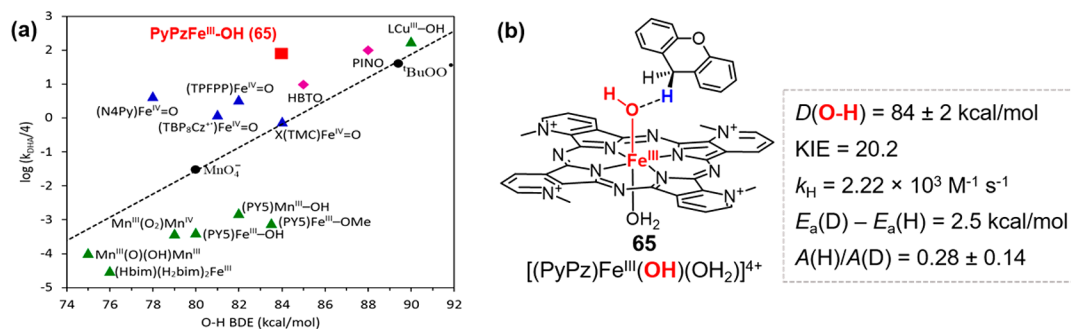


**Figure 35.** (a) Correlation of C–H HAT rate constants with O–H BDE for a variety of metal–oxo and metal–hydroxo oxidants at 298 K. The black dashed line passes through permanganate, *t*-butylperoxy, and *t*-butoxyl radicals for reference. The red ■ is  $(\text{PyPz})\text{Fe}^{\text{III}}\text{-OH}$ . Reported hydroxometal(III) complexes (green ▲), Fe(IV)=O complexes (blue ▲) and nitroxyl radicals HBTO and PINO (magenta ◆) are also shown for comparison. (b) A highly reactive hydroxo-iron(III) porphyrazine complex 65 for HAT. Adapted from ref 345. Copyright 2017 American Chemical Society.

0.35. Recently, large KIE values indicative of tunneling effects were also reported by Newcomb et al. for benzyl alcohol oxidation mediated by  $\text{Fe}^{\text{IV}}(\text{O})(\text{TMP}^{\bullet+})(\text{ClO}_4^-)$ <sup>336</sup> and by Fujii et al. for C–H(D) oxidations of xanthene and tetralin promoted by  $\text{Fe}^{\text{IV}}(\text{O})(\text{TMP}^{\bullet+})(\text{L})$  (L =  $\text{NO}_3^-$ ,  $\text{Cl}^-$ , imidazole).<sup>337</sup> It is worth noting that the KIE and tunneling effects are very dependent on the position of transition state along the reaction coordinate, which will be dramatically affected by the properties of ligands, metal centers, solvents, and substrates.<sup>326,327,338</sup> For instance, while most studies of tunneling effect have been conducted on iron porphyrins with electron-donating tetramesityl porphyrin ligand, manganese porphyrins and electron-withdrawing iron porphyrins like  $\text{Fe}(\text{TDCPP})\text{Cl}$  exhibited much smaller KIEs (3–7) and catalyzed the reactions through classical HAT pathways.<sup>333,335–337</sup>

H-tunneling could potentially contribute to the reactivity difference between hydrogen atom transfer (HAT) and oxygen atom transfer (OAT), as OAT reactions will not be affected by H-tunneling effect. For example, in a series of nonheme iron(IV)–oxo tetramethylcyclam (TMC) complexes with different axial ligands L ( $[\text{Fe}^{\text{IV}}(\text{O})(\text{TMC})(\text{L})]^{z+}$  ( $z = 1, 2$ )), the reactivity for HAT increased with the electron-donating ability of L, while oxygen atom transfer (OAT) showed an opposite trend (Figure 34b).<sup>339–341</sup> This reactivity difference was attributed to a combined effect of spin inversion probability and quantum tunneling.<sup>328,342</sup> In addition to decreasing the triplet/quintet energy gap and facilitating spin crossover, the most electron-donating thiolate axial ligand (compound 63, Figure 34b) also decreased the energy barrier by 3.4 kcal/mol via a quantum tunneling effect, in comparison to the 1.4 kcal/mol obtained with the  $\text{CH}_3\text{CN}$  axial ligand. Such a quantum tunneling effect was absent in oxygen atom transfer reactions and is the main attribute of the reactivity difference between HAT and OAT. The reactivity difference between HAT and OAT reactions were also explored for cyclohexene oxidation mediated by  $\text{Fe}^{\text{IV}}(\text{O})(\text{TMP}^{\bullet+})\text{L}$ . It was found that ratio of epoxidation/allylic oxidation products decreased dramatically with decreasing temperatures.<sup>343</sup> This trend is further studied by Fukuzumi and Nam et al.<sup>344</sup> They found that while epoxidation was preferred at higher temperatures (213–233 K), the allylic hydroxylation took over at lower temperatures (193–213 K). This switchover was accompanied by a drastic increase in KIEs for allylic hydroxylation (1.4 at 233 K vs 13 at 193 K). The large difference in activation energy [ $E_{\text{a}}(\text{D}) - E_{\text{a}}(\text{H}) = 5.0 \text{ kcal/mol}$ ] and a small ratio of exponential factors

( $A_{\text{H}}/A_{\text{D}} \sim 4 \times 10^{-5}$ ) suggest a significant contribution from tunneling for the allylic hydroxylation pathway.

The enhancement of HAT reactivity by H-tunneling is also manifested in an unusually reactive hydroxoiron(III) porphyrazine complex 65 (Figure 35) reported very recently by Gao and Groves.<sup>345</sup> This hydroxoferric species abstracts benzylic C–H bonds with rate constants of  $2.22 \times 10^3 \text{ M}^{-1} \text{ s}^{-1}$  for xanthene and  $81 \text{ M}^{-1} \text{ s}^{-1}$  for dihydroanthracene. These rate constants are 5–6 orders of magnitude faster than other typical  $\text{Fe}^{\text{III}}\text{-OH}$  complexes and more reactive than many ferryl complexes (Figure 35a).<sup>345</sup> 65 displayed an unusually high reduction potential of 0.84 V versus NHE and a very small activation enthalpy of  $6.1 \pm 0.3 \text{ kcal/mol}$  for C–H scission. A large tunneling component was inferred from the observed deuterium isotope parameters (Figure 35b),<sup>327,346,347</sup> KIE of 20.2,  $E_{\text{a}}(\text{D}) - E_{\text{a}}(\text{H}) = 2.5 \pm 0.4 \text{ kcal/mol}$ , and  $A(\text{H})/A(\text{D}) = 0.28 \pm 0.14$  for xanthene oxidation, contributing to the unusual activity of 65.

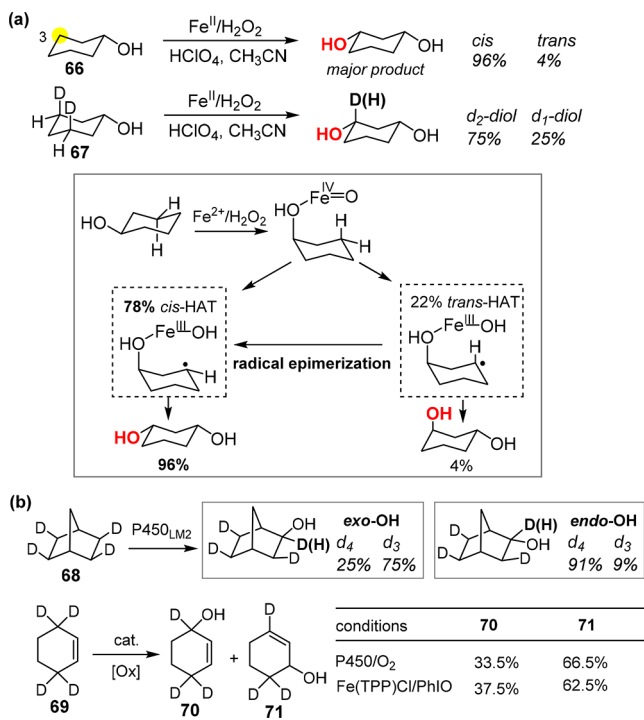
### 3.2. Intermediacy of Substrate Radicals–Oxygen Rebound

In P450-catalyzed hydroxylations, hydrogen atom transfer (HAT) has been shown to generate substrate radicals with short lifetimes. The results can be best understood as leading to an active site caged substrate radical  $[\text{Fe}^{\text{IV}}\text{-OH} \cdot \text{R}]$  that subsequently rebounds to the  $\text{Fe}^{\text{IV}}\text{-OH}$  intermediate to afford hydroxylation products. The intermediacy of substrate radicals in such processes was first implicated in model reactions related to Fenton's reagent, a mixture of  $\text{Fe}^{2+}$  and  $\text{H}_2\text{O}_2$ . The use of cyclohexanol (66) and *trans,trans*-3,5-dideuterocyclohexanol (67) as diagnostic substrates clearly indicated a radical epimerization process after HAT (Scheme 4a).<sup>188</sup> Later, similar radical epimerization or rearrangement processes were found in the hydroxylation of *exo,exo,exo,exo*-2,3,5,6-tetradeuteronorborene (68) and selectively deuterated cyclohexene (69) by phenobarbital-induced P450<sub>LM2</sub> (CYP2B4) as well as reactions mediated by synthetic iron porphyrins (Scheme 4b).<sup>189,348</sup> These results clearly indicated a stepwise, nonconcerted mechanism for C–H hydroxylation mediated by cpd I.

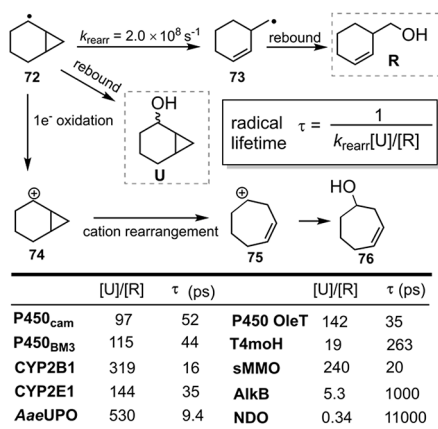
Additional insights regarding this stepwise radical C–H cleavage event were obtained using mechanistically diagnostic substrates and radical clock probes, which form radicals that undergo characteristic stereochemical/structural changes at known rates.<sup>349</sup> A highly informative diagnostic clock is the simple hydrocarbon norcarane, which will afford different rearranged products for pathways involving radical and cationic intermediates (Scheme 5).<sup>350</sup> Thus, the 2-norcaranyl radical



**Scheme 4.** (a) C–H Hydroxylation of Cyclohexanol and Dideuterocyclohexanol Revealed a Step-Wise Radical Mechanism for C–H Hydroxylation Mediated by  $\text{Fe}^{2+}/\text{H}_2\text{O}_2$  and (b) Radical Epimerization and Rearrangement Were Also Observed for Hydroxylation Catalyzed by P450s and Model Compounds



**Scheme 5.** Radical and Cation Rearrangement of Norcarane and Radical Lifetimes of Representative P450s and Nonheme Oxygenases As Determined by the Measured Ratios of Rearranged (R) and Unrearranged (U) Products

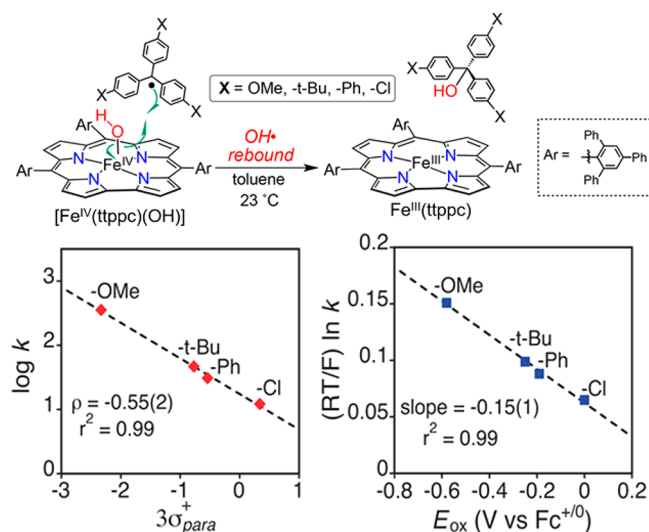


(72 in Scheme 5) will ring-open to a kinetically favored homoallylic radical (73), whereas formation of the thermodynamically more stable cyclohept-4-yl cation (75) is the favored rearrangement pathway for the 2-norcaranyl cation (74). Other small-ring systems, such as bicyclo[2.1.0]pentane and a variety of substituted cyclopropanes are also common radical clocks for the study of HAT in P450s and model systems.<sup>16</sup> Radical clocks provide a facile way to measure the average lifetime of radical intermediates from the ratio of unrearranged products (U) to rearranged products (R) (Scheme 5). It is now known that P450s and synthetic iron

porphyrins generally have very short radical lifetimes, tens to hundreds of picoseconds, with corresponding rebound rate constants between  $10^{10}$  and  $10^{11} \text{ s}^{-1}$ .<sup>16</sup> A similar time frame is also measured for hydroxylation catalyzed by several nonheme systems such as soluble methane monooxygenase (sMMO) and toluene 4-monooxygenase (T4moH).<sup>351–356</sup> Recently, with norcarane radical clock, the rebound rate of AaeUPO was determined to be  $1.06 \times 10^{11} \text{ s}^{-1}$  (radical lifetime: 9.4 ps), which is much faster than the values of other functional P450s.<sup>199</sup> Notably, substrate radical lifetimes in the picosecond time regime provide time for many molecular vibrations and rotations in an enzyme active site or solution solvent cage. However, there would not be time for such a short-lived radical to diffuse away from the active site.

Direct study of the radical rebound step is difficult because of the fast recombination rate between substrate radicals and  $\text{Fe}^{\text{IV}}\text{-OH}$  species ( $10^{10}\text{--}10^{11} \text{ s}^{-1}$ ) and the difficulty of

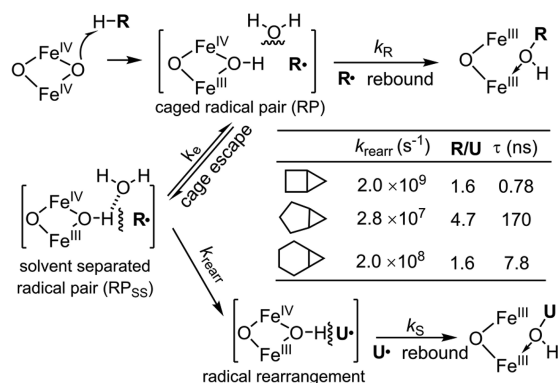
**Scheme 6.** Radical Recombination between Trityl Radicals and  $[\text{Fe}^{\text{IV}}(\text{ttpcc})(\text{OH})]$ . Adapted from ref 357. Copyright 2017 American Chemical Society.



preparing discrete  $\text{Fe}^{\text{IV}}\text{-OH}$  intermediates. Very recently, Green and Goldberg et al. have successfully prepared a stable monomeric  $\text{Fe}^{\text{IV}}\text{-OH}$  complex with a sterically hindered tris(2,4,6-triphenyl)phenyl corrole (ttpcc) ligand.<sup>357</sup> This complex (denoted as  $[\text{Fe}^{\text{IV}}(\text{ttpcc})(\text{OH})]$ ) exhibits a Fe–O bond distance of 1.857 Å, a resonance Raman vibration  $\nu(\text{Fe}-\text{O})$  of  $555 \text{ cm}^{-1}$ , a small Mössbauer isomer shift (0.13 mm/s) and a large quadrupole splitting (2.21 mm/s). These features are characteristic of a  $\text{Fe}^{\text{IV}}\text{-OH}$  species. Treating  $[\text{Fe}^{\text{IV}}(\text{ttpcc})(\text{OH})]$  with stable radicals like the trityl radical ( $\text{Ph}_3\text{C}\cdot$ ) led to the formation of the hydroxylation product ( $\text{Ph}_3\text{COH}$ ) and  $\text{Fe}^{\text{III}}(\text{ttpcc})$  (Scheme 6). Kinetic measurements of this radical recombination step with a series of *para*-substituted trityl radicals afforded second-order rate constants ( $k$ ), ranging from 12.6 to  $357 \text{ M}^{-1} \text{ s}^{-1}$ . A Hammett analysis with  $\sigma_{\text{para}}^+$  parameter showed a small slope ( $\rho = -0.55$ ). A Marcus cross-relation between  $(RT/F) \ln(k)$  and redox potentials of substituted trityl radicals ( $E_{\text{ox}}[(p\text{-X-C}_6\text{H}_4)_3\text{C}^{\cdot/\bullet}]$ ) also yielded a small slope ( $-0.15$ ). These results clearly indicate that, despite the low oxidation potential of trityl radicals, their recombination with  $[\text{Fe}^{\text{IV}}(\text{ttpcc})(\text{OH})]$  follows a concerted pathway with small charge separation, as opposed to a stepwise mechanism in

which the carbon-centered radical is first oxidized to cations and then recombines with hydroxide.

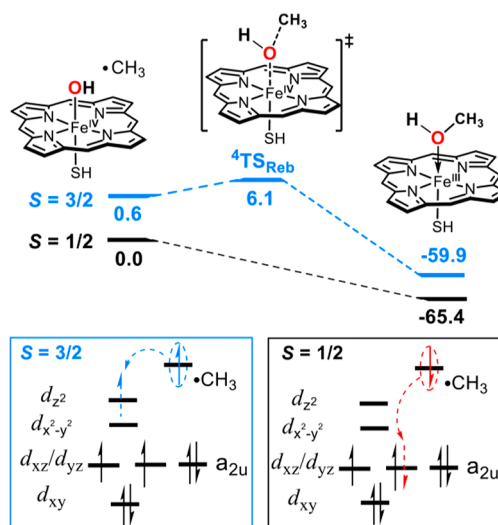
### Scheme 7. Oxidation of Radical Clocks with Different Rearrangement Rate Constants<sup>a</sup>



<sup>a</sup>The similar ratios of rearranged/unrearranged products (R/U) result from the competition between cage escape and rebound of substrate radicals. Adapted with permission from ref 358. Copyright 2008 Wiley-VCH.

After HAT, substrate radicals R $\cdot$  in the resulting [Fe<sup>IV</sup>-OH $\cdot$ R] cage are not static. Factors such as tightness of the cage, ease of solvent reorganization, the rate of radical rebound, and the nature of the substrate radical can all dramatically affect the behavior of R $\cdot$ .<sup>13</sup> An instructive manifestation of the interplay between these factors is the C-H hydroxylations catalyzed by nonheme diiron hydroxylase AlkB, in which the use of three clock substrates with very different rearrangement rates ( $k_r$ ) showed similar R/U ratios and led to drastically different apparent radical lifetimes, all in the low nanosecond time regime (1–200 ns) (Scheme 7).<sup>358,359</sup> The cause of this enigmatic behavior is a competition between the relatively slow radical rebound and diffusive radical cage escape to generate a solvent-separated radical pair (RP<sub>SS</sub>). If the rate of radical cage escape ( $k_e$ ) is comparable to that of radical rebound  $k_R$  and larger than the radical rearrangement rates  $k_{\text{rearr}}$ , then R/U ratios will be insensitive to the differences in  $k_{\text{rearr}}$  but only reflect the competition between cage escape and radical rebound  $k_e/k_R$ . Significantly, measured radical lifetimes for AlkB hydroxylases were found to be in the nanosecond time regime, much longer than those obtained for heme proteins such as P450 and APO. An embodiment of the cage escape effect in AlkB system is a decrease in radical lifetimes by increasing the substrate concentration. Higher substrate concentration would lead to more substrate molecules present in the long and hydrophobic substrate channel in AlkB,<sup>360</sup> which could displace and reorganize the water in the active site and create a crowded environment that reduces the radical cage escape.

In addition to the environment of the radical cage, the nature of the metal center can also dramatically affect the radical lifetime. For instance, manganese porphyrin-catalyzed hydroxylation exhibited long radical lifetime (ns), whereas no rearranged product was observed for ruthenium porphyrin-catalyzed reactions.<sup>220,361</sup> The former might relate to a lower reduction potential of Mn<sup>IV</sup>-OH compared to Fe<sup>IV</sup>-OH, and the latter might be caused by an unusually high electrophilic nature of Ru<sup>V</sup>=O.<sup>362</sup> Like HAT, radical rebound can also occur along different spin surfaces and are subject to spin

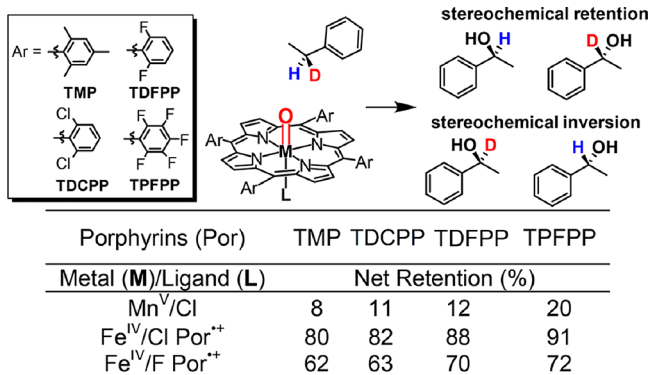
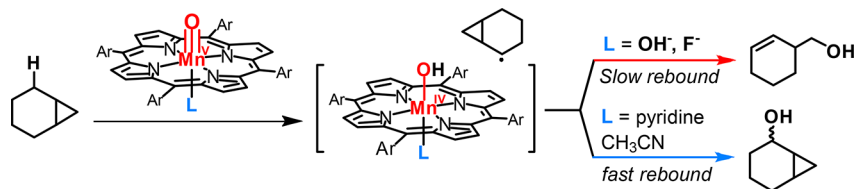


**Figure 36.** Oxygen rebound of different spin states (energies in kcal/mol, obtained from ref 305).

crossover events (Figure 36). DFT calculations for methane hydroxylation by a simplified heme cpd I showed that the rebound barrier on the quartet transition state is much higher than that on the doublet spin state due to the difference in frontier orbital interactions.<sup>304</sup> In the quartet state, the unpaired electron of the radical goes into a higher-energy  $3d_z^2$  orbital, whereas in the doublet state, the electron transfers into a lower-energy singly occupied  $d_{xz}$  (or  $d_{yz}$ ) orbital.

Groves et al. have found a significant impact of the donor properties of the axial ligands on rates of radical rebound. Manganese porphyrins with anionic electron-donating ligands such as OH<sup>-</sup> and F<sup>-</sup> were found to afford mainly radical rearranged products in hydroxylation of norcarane, whereas radical unrearranged products prevailed in reactions catalyzed by Mn porphyrins with neutral axial ligands such as pyridine and CH<sub>3</sub>CN (Scheme 8).<sup>298,363</sup> This effect is reminiscent of axial ligand effect on HAT. Electron-donating ligands would diminish the reduction potential of Mn<sup>IV</sup>-OH and destabilize frontier orbitals ( $3d_z^2$  and  $d_{xz}/d_{yz}$ ), leading to a higher rebound barrier. The deceleration of rebound would facilitate the escaping of substrate radicals from the radical cage. Indeed, a large amount of radical dimerization products were observed in xanthene hydroxylation by manganese porphyrins in the presence of F<sup>-</sup> with yield dependent on the concentration of F<sup>-</sup>.

The rebound step in the hydroxylation of deuterated ethylbenzene catalyzed by iron and manganese porphyrins has been explored recently.<sup>363</sup> The results showed that more electron-deficient porphyrins displayed less stereochemical inversion at the benzylic hydroxylation site (Figure 37). The extent of stereochemical inversion was found to be sensitive to the metal center, with only 8–20% retention of configuration for Cl-Mn<sup>V</sup>(O)(Por), while Cl-Fe<sup>IV</sup>(O)(Por<sup>•+</sup>) showed 80–90% retention. Significantly, F-Fe<sup>IV</sup>(O)(Por<sup>•+</sup>) afforded only 60–70% retention, showing that the donor properties of the ligand can also affect iron porphyrin stereochemistry. These results are also consistent with the general idea that oxygen rebound is faster for stronger oxidants and more able to compete with radical cage escape. The radical cage escape event was recently explored in nonheme systems by Nam and Shaik.<sup>364</sup> It was determined that such processes occurred in a

Scheme 8. Effect of Axial Ligands on Radical Rebound to  $Mn^{IV}$ -OH Porphyrins

**Figure 37.** Stereochemistry of the rebound process for iron and manganese porphyrins. Adapted from ref 363. Copyright 2017 American Chemical Society.

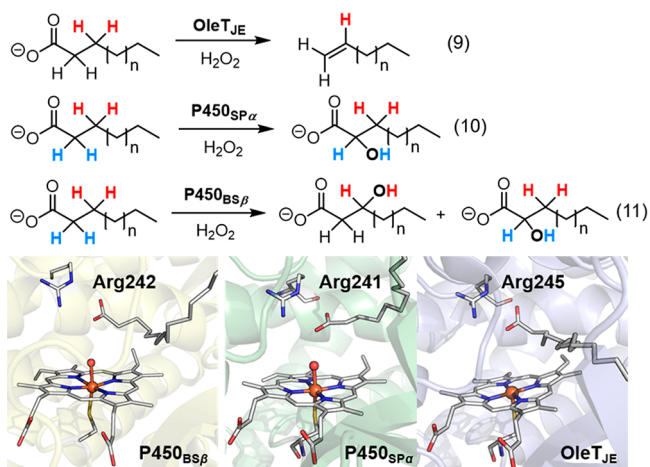


**Figure 38.** Native reactions catalyzed by P450 OleT<sub>JE</sub> (PDB: 4L40), P450<sub>SPα</sub> (PDB: 3AWM), and P450<sub>BSβ</sub> (PDB: 1IZO). All three enzymes have a conserved arginine residue that can form a salt bridge with the carboxylate group of fatty acid substrates.

number of nonheme metal-oxo systems such as  $Mn^{IV}O$ ,  $Fe^{IV}O$ ,  $Cr^{IV}O$ ,  $Fe^{V}O$ , and  $Ru^{IV}O$ . DFT calculations revealed small dissociation energies and relatively large rebound barriers for these systems.

### 3.3. Redirecting Substrate Radicals to Reaction Pathways Other than Oxygen Rebound

**3.3.1. Decarboxylation Mediated by P450 OleT<sub>JE</sub>.** P450 OleT<sub>JE</sub>, found in *Jeotgalicoccus sp.*, converts  $C_n$  fatty acids to  $C_{n-1}$  terminal alkenes through a desaturative decarboxylation (eq 9, Figure 38).<sup>365</sup> This enzyme has attracted considerable interest for its potential applications in biofuel production and fine chemical synthesis.<sup>366–369</sup> P450 OleT<sub>JE</sub> belongs to the P450 peroxxygenase family CYP152. Other notable members in this family are P450<sub>SPα</sub> (CYP152B1) and P450<sub>BSβ</sub> (CYP152A1),<sup>135,140,370</sup> which have 36% and 40% amino acid

identity to P450 OleT<sub>JE</sub>, respectively. All three enzymes utilize an active-site arginine and the carboxylate group provided by the substrate to effect the heterolytic cleavage of  $H_2O_2$  to generate compound I. Despite the similarity in  $H_2O_2$  activation and active site structures to P450 OleT<sub>JE</sub>, P450<sub>SPα</sub> and P450<sub>BSβ</sub> catalyze hydroxylations of fatty acid substrates rather than decarboxylation (Figure 38).<sup>135,136,277,370</sup> P450<sub>SPα</sub> hydroxylates only at the  $C_\alpha$  position (eq 10), whereas P450<sub>BSβ</sub> hydroxylates both the  $C_\alpha$  and  $C_\beta$  positions of fatty acid substrates (eq 11).

The decarboxylation reaction catalyzed by P450 OleT<sub>JE</sub> is initiated by a hydrogen atom transfer (HAT) from the  $C_\beta$  position, as indicated by the large primary kinetic isotope effect (KIE  $\geq 8.1$ ) for fully deuterated fatty acid substrates.<sup>371</sup> This finding indicates that the oxygen rebound that normally occurs after HAT in P450 catalysis is inhibited in P450 OleT<sub>JE</sub>. The substrate radical is thus redirected to decarboxylation presumably via a single electron transfer to cpd II and a subsequent C–C cleavage with concomitant loss of  $CO_2$  (Figure 39). It is worth noting that a similar  $C_\beta$ -H scission step has also been identified as the key step for the decarboxylative desaturation catalyzed by UndA, a nonheme iron oxidase that can synthesize medium-chain 1-alkenes from fatty acids.<sup>372,373</sup> Very recently, Makris and co-workers observed OleT compound I and compound II using stopped-flow spectroscopic techniques by employing deuterated substrates to slow the initial HAT step.<sup>374</sup> Intriguingly, OleT compound II was remarkably stable, having a lifetime of hundreds of milliseconds after its preparation from compound I via substrate C–H abstraction. The unusual stability of OleT-II supports the proposal that this enzyme imposes an inhibition of oxygen rebound, which would normally occur with rate constants in the range of  $10^{10}$ – $10^{11}$  s<sup>-1</sup> for heme-thiolate proteins. What causes this remarkable slow-down of the radical rebound process is still not entirely clear. But the fact that the amount of hydroxylated side products varied substantially with fatty acid chain length suggests that the binding and the positioning of substrates play a crucial role in affecting the reaction pathway.<sup>369,375</sup> Evidence in favor of rebound inhibition by substrate–protein interactions has recently been provided by the observation that the radical clock probe norcaradiene is a substrate for OleT<sub>JE</sub>.<sup>376</sup> Further, the radical lifetime for the norcaradienyl radical intermediate was typical for other P450 proteins, in the picosecond time regime. Apparently, the radical intermediate of a small hydrocarbon substrate cannot be restrained by the active site architecture and rebound proceeds normally.

Li et al. have recently examined several key active site residues of OleT<sub>JE</sub> and found that Arg254, His85, and Ile170 are all required for the decarboxylation activity (Figure 40).<sup>377</sup> The roles of these residues are thought to be the formation of a salt-bridge with the substrate carboxyl group (Arg245), acting as a proton donor (His85), and regulating substrate positioning in the active site (Ile170). As discussed in section 2.3.1, the active site structure of the CYP152 family of enzymes is similar

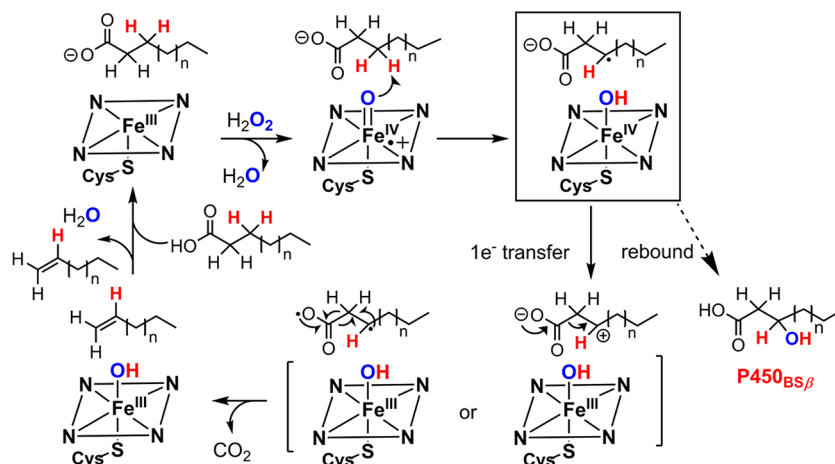


Figure 39. Proposed mechanism for the oxidative decarboxylation catalyzed by OleT<sub>JE</sub>.

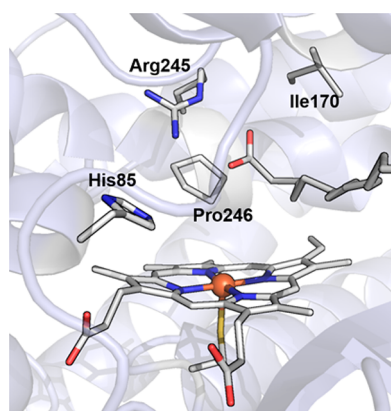


Figure 40. Key active site residues of OleT<sub>JE</sub> (PDB: 4L40).

to that of *AaeUPO* in that both proteins have an arginine in the distal pocket that forms a salt bridge with a nearby carboxylate that facilitates hydrogen peroxide binding and O–O bond scission. In *AaeUPO*, the carboxyl group is provided by a glutamate residue, while in CYP152 the carboxyl group is from the fatty acid substrate. Makris et al. recently found that a mutation of Pro246 to Asp in OleT circumvents the requirement for fatty acid substrates for H<sub>2</sub>O<sub>2</sub> activation.<sup>367</sup>

The resulting OleT P246D variant is not active toward native fatty acids but showed high activity for a broad range of hydrocarbon substrates.

**3.3.2. P450-Catalyzed Desaturation Reactions.** In addition to obtaining olefins via decarboxylative elimination, P450 has also shown capabilities for forming C=C bonds via dehydrogenation. An early example is the formation of  $\Delta^4$ -valproic acid ( $\Delta^4$ -VPA) during the metabolism of the antiepileptic drug valproic acid (VPA) (Figure 41a).<sup>378</sup> Other representative substrates that undergo P450-catalyzed desaturation include warfarin, ethyl carbamate, and retinol.<sup>279,379</sup> The fact that purified P450 catalyzed both desaturation and hydroxylation in most cases and the alcohol and desaturation products did not interconvert indicates a bifurcation of the usual rebound mechanism. Furthermore, almost identical values for the primary kinetic isotope effects were determined for hydroxylation and desaturation products of VPA.<sup>380</sup> On the basis of these results, it is proposed that the substrate radical resulting from the initial hydrogen-atom transfer (HAT) by cpd I will undergo a second HAT or proton-coupled electron transfer process (PCET) by compound II at C–H bonds vicinal to the carbon-centered radical, affording the desaturation product and H<sub>2</sub>O (Figure 41a). This mechanism is reminiscent of the desaturation pathway of fatty acid desaturases, in which a

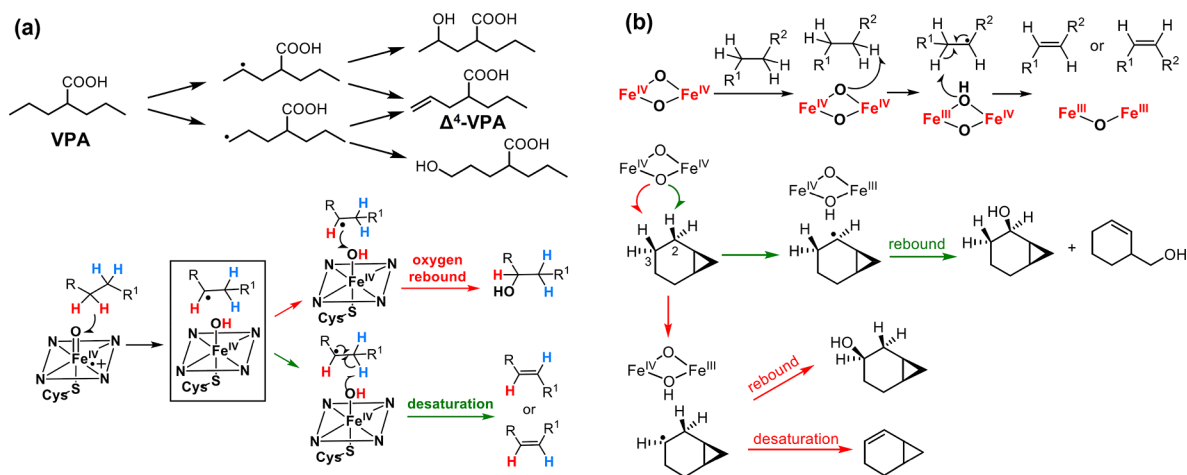
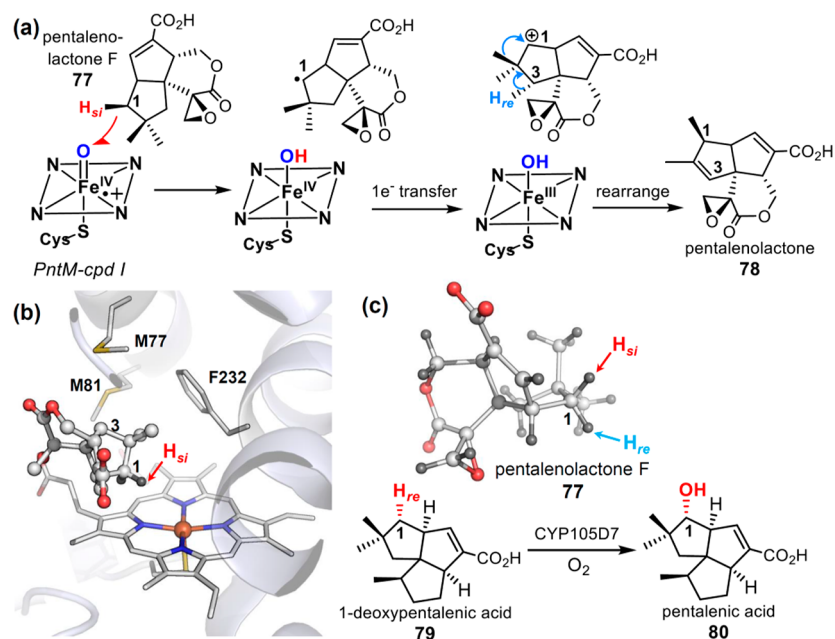


Figure 41. (a) P450-catalyzed hydroxylation and desaturation of valproic acid (VPA) and the proposed mechanism. (b) Proposed mechanism of fatty acid desaturases and the hydroxylation and desaturation of norcaradiene catalyzed by nonheme diiron hydroxylase AlkB.



**Figure 42.** (a) Proposed mechanism for the oxidative rearrangement of pentalenolactone F catalyzed by PntM. (b) Active site structures of PntM with bound pentalenolactone F (PDB: 5L1O). (c) Steric environment of C1 *si* and *re* sides of pentalenolactone F and hydroxylation of 1-deoxypentalenic acid by CYP105D7.

bis- $\mu$ -oxo diiron(IV) cluster mediates two sequential HAT to form C=C bonds in long-chain fatty acyl derivatives (Figure 41b).<sup>381,382</sup> A recent mechanistic study of the histidine-rich nonheme diiron enzyme AlkB using diagnostic substrates norcarane and deuterated norcarane revealed H atom abstraction occurred at both C2 and C3 (Figure 41b).<sup>359</sup> While the C2 radical leads to the formation of 2-norcaranol and the radical-rearranged homoallylic alcohol product, desaturation and hydroxylation products were obtained from the C3 radical with similarly large KIEs ( $\sim 20$ ). From these results, a bifurcation of the reaction pathways leading from the Fe–OH/ $R\cdot$  intermediate appears to be a common feature for both heme- and nonheme-catalyzed desaturation reactions.

The factors that control the hydroxylation/desaturation pathways have been studied via computational methods.<sup>383,384</sup> In general, the desaturation pathway was found to be less exothermic than the hydroxylation pathway. The energy barriers of two reaction channels varied depending on the spin state and electronic state of the Fe<sup>IV</sup>OH intermediate, the properties of the substrate radicals, and the active site environment. For instance, comparable energy barriers were calculated for desaturation and oxygen rebound on low-spin doublet surface, whereas the desaturation step is more unfavorable along quartet surfaces.<sup>383,384</sup> Shaik also suggested that Fe<sup>IV</sup>–OH species can also exist as a Fe<sup>III</sup>–OH porphyrin cation radical electromer, whose energy barrier for the desaturation pathway is 8–20 kcal/mol higher than that of oxygen rebound.<sup>384</sup> The desaturation pathway also requires the approach of Fe<sup>IV</sup>–OH to C–H bonds vicinal to the substrate radical. If this step is restricted by the substrate/enzyme interaction then the desaturation pathway will be inhibited. In the case of camphor, gas-phase calculations showed similar barriers for desaturation and oxygen rebound on both doublet and quartet surfaces, however, the desaturation pathway was over 15 kcal/mol higher than oxygen rebound in the enzyme active site. An energy scan along the reaction coordinate revealed that the tight binding of camphor in the active site

disfavored the reactive conformation that leads to the desaturation product.<sup>384</sup>

**3.3.3. Oxidative Rearrangement Catalyzed by PntM (CYP161C2).** CYP161C2 catalyzes the conversion of pentalenolactone F (77) to pentalenolactone (78), a sesquiterpenoid antibiotic synthesized in *Streptomyces arenae* (Figure 42a).<sup>385</sup> This transformation features an oxidative cationic rearrangement, which is very unusual in P450-mediated transformations but similar to the cation rearrangement pathways typically encountered in terpene cyclases. The reaction involves an initial hydrogen atom abstraction of H<sub>si</sub> at C1 followed by an electron-transfer oxidation of the substrate radical by compound II. The carbocation intermediate can then undergo 1,2-migration of a methyl group with a subsequent loss of a proton at C3 (Figure 42a). Cane et al. have studied the mechanism of PntM using X-ray crystallography, kinetic measurements, site-directed mutagenesis, and product analyses.<sup>386</sup> The inhibition of the rebound step in PntM could arise from the active site residues that stabilize the carbon cation intermediate. Examination of substrate-bound crystal structure of PntM revealed three active-site residues (F232, M77, and M81) that are in close proximity to C1, C2, and C3 and are unique among all known P450s (Figure 42b). However, mutation of these sites still afforded the pentalenolactone 78 as the only product, albeit with lower activity. Another possible cause of the inhibition of the rebound step is steric hindrance at the carbon-centered radical. After hydrogen abstraction at C1–H<sub>si</sub>, the subsequent rebound step can be retarded by methyl and vinylidene groups at the *si* face of C1, whereas the outer-sphere 1e<sup>–</sup> transfer would not be affected by the steric bulkiness at C1. The hydroxylation of 1-deoxypentalenic acid (79, Figure 42), which is structurally analogous to pentalenolactone F, by CYP105D7 provides additional support for this hypothesis. CYP105D7 abstracts the hydrogen at the *re* side of C1 followed by a normal oxygen rebound process (Figure 42b).<sup>387</sup> Compared to the *si* face, C1 *re* face has much smaller steric

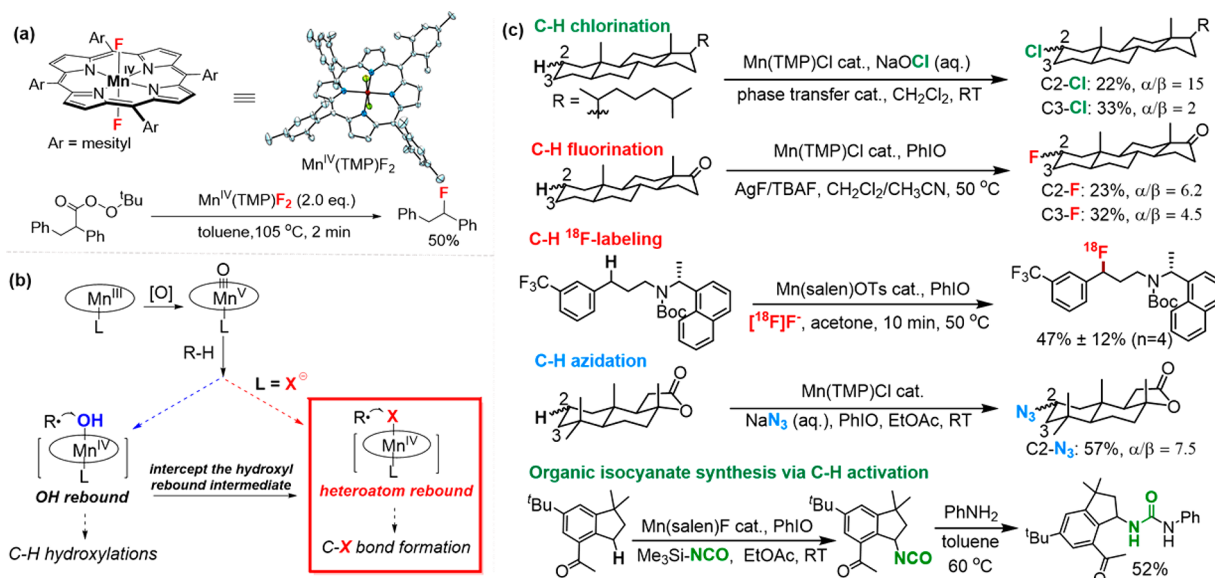
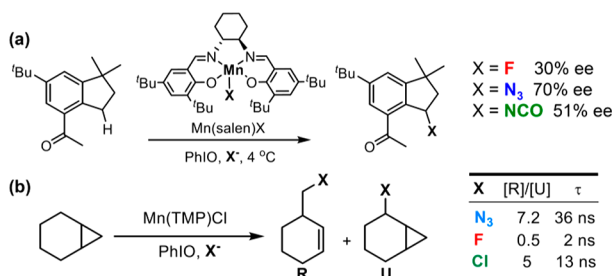


**Figure 43.** (a) Formation of fluorination products via trapping of in situ generated alkyl radicals by  $\text{Mn}^{\text{IV}}(\text{TMP})\text{F}_2$ . (b) Concept of manganese-catalyzed C–H halogenation reactions via heteroatom rebound. (c) Mn-catalyzed C–H halogenation and pseudohalogenation reactions.

hindrance with only a hydrogen atom and a methyl group at neighboring carbons (Figure 42c).

**3.3.4. Mn-Catalyzed C–H Halogenations.** In the early studies of Mn porphyrin-catalyzed hydroxylations, chlorination side products were observed. The chlorine source in those side reactions was determined to be the chloride ligand on the Mn porphyrin catalysts.<sup>220</sup> Radical clock studies indicated an unusually long radical lifetime for the chlorination side product (~25 ns). A lifetime this long suggests that the substrate radical intermediate may be freely diffusing. A detailed mechanistic study later revealed that radical lifetimes in Mn porphyrin-catalyzed hydroxylation can be controlled by axial ligands, as noted above, in which the rebound can be slowed down by anionic electron-donating axial ligands.<sup>298,388</sup> Another important finding was that a  $\text{Mn}(\text{IV})\text{-X}$  type of intermediate ( $\text{X}$  = halogens), such as the well-characterized *trans*-difluoromanganese(IV) porphyrins, can trap independently generated alkyl radicals to yield halogenation products in a process analogous to the oxygen rebound (Figure 43a).<sup>389</sup> These two mechanistic findings enabled the development of a series of aliphatic C–H halogenation reactions catalyzed by manganese porphyrin or manganese salen complexes (Figure 43, panels b and c).<sup>298,390–394</sup> The catalyst-dependent regioselectivity and large primary kinetic isotope effect (KIE

**Scheme 9.** (a) Enantioselective C–H Halogenation-Catalyzed by a Chiral Manganese Salen Catalyst and (b) Radical lifetimes of Mn-Catalyzed C–H Halogenation Reactions



> 5) unambiguously indicated the involvement of oxoMn(V) intermediate in the C–H activation step. The radical nature of the halogen transfer step was implied by a large amount of radical rearranged products observed with the probe substrate norcarane. Furthermore, moderate enantioselectivity (20%–70%) was observed when a chiral manganese salen catalyst was used (Scheme 9a). Kagan analysis has shown a linear relationship between enantiomer excess (ee) of products and ee of manganese salen chiral catalysts.<sup>394</sup> These results indicate that halogen transfer proceeded through a catalyst-bound halogen intermediate, namely  $\text{Mn}(\text{IV})\text{-X}$ .

What determines the bifurcation of substrate radicals to halogen rebound instead of oxygen rebound in this case? Clearly the nature of metal center is important, as switching from manganese porphyrins to iron porphyrins afforded mainly oxygenation products.<sup>363</sup> In addition, hydroxylation products prevailed if more electron-withdrawing manganese porphyrins such as manganese 5,10,15,20-tetrapentafluorophenylporphyrin (TPFPF) were used. These results are consistent with a deceleration of oxygen rebound, as both the iron center and electron-withdrawing porphyrins were known to cause a faster oxygen recombination. This analysis is consistent with radical clock analysis, as all C–H halogenations exhibit unusually long radical lifetimes (2–30 ns) (Scheme 9b). Although the identity of the  $\text{Mn}(\text{IV})\text{-X}$  intermediate is still not fully elucidated, especially the nature of the axial ligand *trans* to the halogen. DFT calculations showed that halogen rebound of alkyl radicals to  $\text{Mn}(\text{IV})\text{-X}$  has low energy barriers, comparable to or even lower than the oxygen rebound.<sup>389,391</sup> The facile halogen transfer is also indicated by the successful application of C–H fluorination for  $^{18}\text{F}$  labeling.<sup>390</sup> Unlike normal catalytic conditions, [ $^{18}\text{F}$ ]fluoride is present only in minuscule amounts (pmol–nmol) and other reagents (substrate, oxidant, and catalysts) are all in vast excess. Thus,  $\text{Mn}(\text{IV})\text{-}^{18}\text{F}$  intermediates must be competing effectively with a large amount of  $\text{Mn}(\text{IV})\text{-OH}$  intermediates to trap alkyl radicals via fluorine transfer. Therefore, the observed high  $^{18}\text{F}$  conversion into target molecules indicates a preferential radical rebound to  $\text{Mn}(\text{IV})\text{-F}$ .

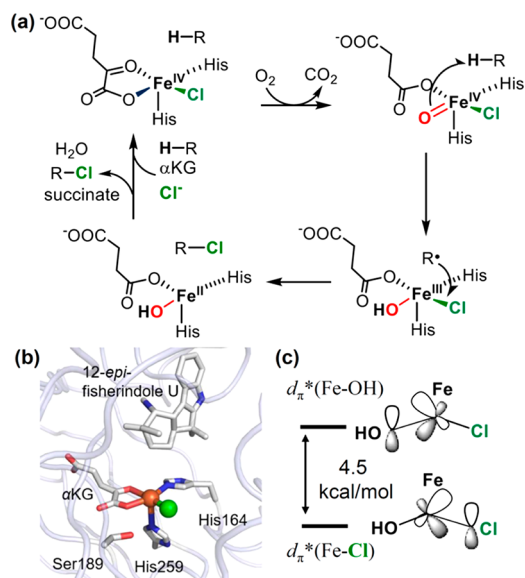


**Figure 44.** (a) Mechanism of C–H chlorination catalyzed by  $\alpha$ KG nonheme halogenases. (b) Active site structure of a nonheme halogenase, WelO5 (PDB: 51QT), with a bound 12-*epi*-Fischerindole U substrate. (c) Orbital diagram of  $d_{\pi}^*(\text{Fe-OH})$  and  $d_{\pi}^*(\text{Fe-Cl})$ .

These Mn-catalyzed halogenations are reminiscent of C–H chlorinations catalyzed by  $\alpha$ -ketoglutarate ( $\alpha$ KG)-dependent nonheme iron halogenases, in which a chloroferryl intermediate ( $\text{Cl-Fe}^{\text{IV}}=\text{O}$ ) has been detected spectroscopically. This chloroferryl intermediate abstracts a C–H bond from substrates, and substrate radicals recombine with the chlorine rather than the hydroxyl group *cis* to the chloride in the rebound intermediate,  $\text{Cl-Fe}^{\text{III}}-\text{OH}$  (Figure 44a).<sup>395–401</sup> It has been shown by Bollinger and Krebs that substrate orientation is crucial for the preference for chlorine rebound.<sup>395,396,402,403</sup> Computational and structural studies revealed that the oxo group repositions itself from an axial position to the equatorial plane defined by the chloride and  $\alpha$ -KG (Figure 44, panels a and b).<sup>395,396,399</sup> This geometry facilitates  $\pi$  pathways for both the C–H abstraction and the subsequent radical recombination step. Solomon et al. analyzed the frontier molecular orbitals of  $\text{Cl-Fe}^{\text{III}}-\text{OH}$ . Although the Fe–OH bond is intrinsically weaker, the  $d_{\pi}^*(\text{Fe-OH})$  was found to be 4.5 kcal/mol higher in energy than  $d_{\pi}^*(\text{Fe-Cl})$ , leading to a lower energy barrier for chlorine rebound (Figure 44c).<sup>404</sup> Further, their results

showed that the chlorine rebound to a substrate radical is best described as an asynchronous electron transfer from the substrate radical to iron followed by late ligand transfer to the substrate in the same single transition state, instead of a direct ligand radical transfer. This description should apply as well for the fluorine transfer step in manganese porphyrin-catalyzed fluorinations, as the generation of fluorine radicals is unlikely due to the enormously high one-electron oxidation potential of fluoride.<sup>405</sup>

### 3.4. Oxygen-Atom Transfer Reactions Catalyzed by Compound I

In addition to activating aliphatic C–H bonds, P450s and their model compounds could also catalyze a myriad of oxygen-atom transfer reactions. These reactions, including alkene epoxidation, aromatic hydroxylation, and *N*- and *S*-oxidation, have been extensively reviewed.<sup>25,26,92,306,379</sup> Herein we will only briefly discuss their mechanistic features. *O*-, *S*-, and *N*-dealkylations, although not belonging to OAT reactions, will also be discussed in this section for comparison with corresponding OAT reactions.

Alkene epoxidations catalyzed by P450s are widely present in natural product biosynthesis and drug metabolism.<sup>406</sup> Also, the infamous epoxidation of benzpyrene by CYP1A1 is an important initial step in the etiology of human cancer.<sup>407</sup> The mechanism of this oxygen transfer event appears to begin with an electrophilic ferryl addition to a C=C bond to form an alkyl radical intermediate, which undergoes a subsequent radical rebound step to forge the epoxide ring (Figure 45a). DFT calculations have indicated that the addition and rebound steps occur nonsynchronously in a single transition state or in a stepwise fashion with a rate-determining C–O bond forming step followed by a low-energy-barrier ring closure step.<sup>306,408,409</sup> In several alkene oxidation reactions, a cationic intermediate, presumably generated via single electron transfer from alkyl radical to the ferryl center, was inferred from the formation of aldehydes, ketone, or heme *N*-alkylated side products.<sup>17,92,146,410,411</sup> The ketone or aldehyde products were generated via a 1,2-hydride shift, while heme *N*-alkylation products were likely to be formed via direct electrophilic attack of the carbocation from a pyrrole nitrogen of the porphyrin ligand.<sup>412</sup> Very recently, Hammer, Arnold, and co-workers have harnessed the side activity of P450s for aldehyde formation to develop the first olefin anti-Markovnikov oxygenase (aMOx) via directed evolution (Figure 45b).<sup>413</sup> aMOx contains 12

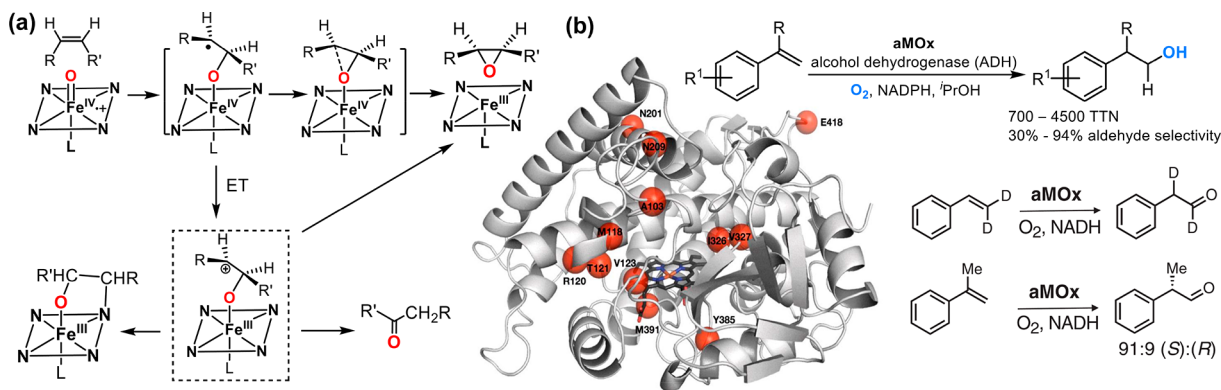


**Figure 45.** (a) Proposed mechanism for alkene epoxidation catalyzed by P450s. (b) Olefin anti-Markovnikov oxidation catalyzed by an engineered cytochrome P450 (aMOx). The homology model of wild-type P450<sub>L1A1</sub> is shown with mutation sites highlighted by red sphere. Adapted with permission from ref 413. Copyright 2017 American Association for the Advancement of Science.

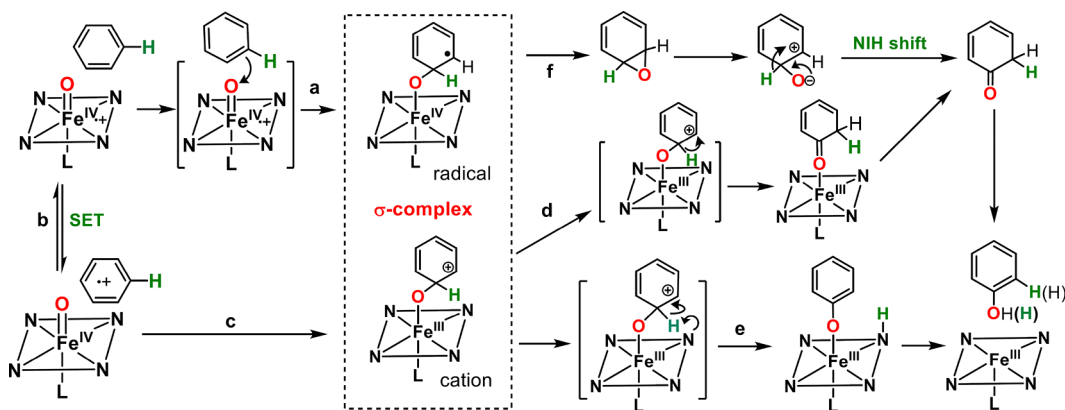


Figure 46. Proposed mechanisms for aromatic hydroxylation.

mutations from its parent P450<sub>LA1</sub>, a P450 from the rhodobacterium *Labrenzia aggregata*, and exhibits high anti-Markovnikov oxidation activity (up to 4500 TTN) and aldehyde/epoxide selectivity (up to 16:1). Furthermore, aMOx can convert  $\alpha$ -methylstyrene to (*S*)-2-phenylpropionaldehyde with 91:9 enantiomeric ratio (er), representing the first catalytic asymmetric aldehyde synthesis via direct anti-Markovnikov oxidation. This result combined with a deuterium-labeling experiment indicate a mechanism involving an initial oxo-transfer followed by a highly ordered 1,2-hydride migration. It is still not clear how the 12 mutations in aMOx benefit the anti-Markovnikov activity. Some of these mutations are in the distal pocket and might help lock the substrate conformation for 1,2-hydride transfer. Intriguingly, one mutation (M391L) is in the highly conserved proximal cysteine loop, which indicates that the proximal heme ligand might also play an important role for anti-Markovnikov activity, as changes in Cys loop are known to affect the electron donation ability of proximal cysteine thiolate.<sup>181</sup>

Aromatic hydroxylation is a paradigmatic cpd I-mediated reaction that has attracted decades of research interest, because of its importance in drug metabolism and the potential applications in organic synthesis. The mechanism involves an initial addition of cpd I to the arene  $\pi$ -system to form a tetrahedral  $\sigma$ -complex (Figure 46).<sup>414–419</sup> While many mechanistic studies support a direct electrophilic attack of cpd I to arenes (step a, Figure 46),<sup>417–421</sup> a recent study by Fujii et al. using a Marcus-type analysis showed a significant contribution of an electron transfer process in the rate-limiting step. The results were interpreted to indicate a mechanism involving a fast electron transfer equilibrium between cpd I and the arene, which is coupled to a subsequent C–O bond formation (steps b and c, Figure 46).<sup>422</sup> The tetrahedral  $\sigma$ -complex could adopt two forms: a cationic species with a ferric center and a radical form with a ferryl center. DFT calculations suggest that two electromers are admixed in the  $\sigma$ -complex.<sup>417–420</sup> A common mechanistic feature of P450-mediated aromatic hydroxylation is the migration of the *ipso*-hydrogen to the adjacent carbon (“NIH shift”) and the partial retention of this hydrogen in the final product.<sup>30,423,424</sup> There are several proposed mechanisms for the hydrogen migration and the formation of the hydroxylation product. The “NIH shift” could occur directly at the cationic  $\sigma$ -complex and led to the formation of a ketone product, which undergoes keto–enol tautomerization to form the product with partial retention of the migrated hydrogen. This mechanism is

generally supported by DFT calculations,<sup>25</sup> showing that the hydrogen migration can proceed through a 1,2-hydride shift (step d, Figure 46),<sup>419</sup> or through a proton-shuttle mechanism mediated by the pyrrole nitrogen (step e).<sup>417,418</sup> In an alternative mechanism, an arene oxide intermediate is formed from the  $\sigma$ -complex (step f), which then converts into the hydroxylation product via “NIH shift” and tautomerization.<sup>30,423,424</sup> There are also examples in which the complete loss of the *ipso*-hydrogen was observed, indicating the formation of aromatic ring via direct deprotonation of the *ipso*-hydrogen without migration or that the keto–enol rearrangement is mediated by the active site architecture.<sup>425,426</sup>

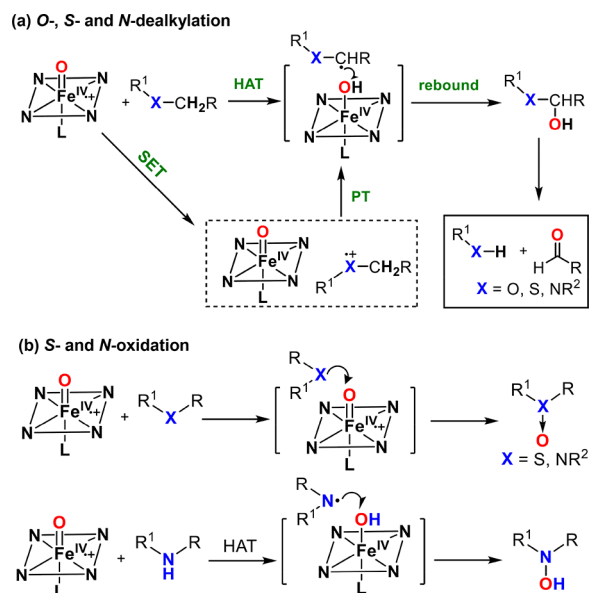


Figure 47. Proposed mechanisms for (a) O-, S-, and N-dealkylation. (b) S- and N-oxidation.

Molecules containing O-, S-, N-alkyl groups undergo dealkylation, which are commonly seen in xenobiotic and drug metabolism.<sup>427,428</sup> Dealkylation reactions are triggered by the formation of  $\alpha$ -hydroxylation intermediates, which decompose to afford aldehyde and dealkylated products.<sup>25</sup> There are two mechanisms proposed for the generation of  $\alpha$ -hydroxylation intermediates: H atom-transfer (HAT) and single-electron transfer (SET) followed by proton transfer (PT) (Figure 47a). The O-dealkylation reactions generally follow an HAT mechanism as evidenced by the large primary



kinetic isotope effect.<sup>429–431</sup> The mechanism for *N*-dealkylation is a topic of long debate. In support of an HAT mechanism, the use of radical clock substrates such as *N*-cyclopropyl-*N*-methylamine afforded the ring-intact products.<sup>432–434</sup> Additionally, a large kinetic isotope effect (KIE > 6) was observed for dealkylation of *N*-alkylamides.<sup>435,436</sup> However, the KIE values of dealkylation of *N*-alkylamines are much lower (generally < 3).<sup>437,438</sup> Furthermore, the reaction rates of dealkylation of substituted *N*-alkylamine correlate well with their redox potentials and Hammett electronic parameters with negative slopes.<sup>25</sup> All these results seem to favor an SET–first mechanism. DFT calculations have provided critical insight for the understanding of *N*-dealkylation mechanism and support the HAT–first mechanism. It has been shown that the SET step is not energetically favorable. Moreover, the low KIE and the linear correlation with substrate oxidation potentials could be reproduced with calculations based on the HAT mechanism.<sup>318,439</sup> Further analysis showed that the nitrogen lone pair can interact with the radical character developed at the carbon center during the C–H bond cleavage. This interaction leads to partial positive charge accumulation at the amine moiety in the transition state, causing the experimentally observed substituent effect.

In addition to dealkylation, *N*-alkyl and *S*-alkyl groups could undergo direct heteroatom oxidation to afford *N*-oxide and sulfoxide products (Figure 47b). The mechanisms for both reactions have been shown to be a concerted direct oxygen atom transfer.<sup>313,440–443</sup> In theory, the heteroatom oxidation and dealkylation could compete with each other. Indeed, both products were observed in some examples.<sup>17,444,445</sup> Intriguingly, it seems that *N*-alkyl groups favor dealkylation while *S*-alkyl groups prefer sulfoxidation. A recent computational study reproduced this trend and found that the activation energies of dealkylation pathway was largely affected by the radical stabilization ability of the neighboring heteroatom.<sup>443</sup> The nitrogen inversion barrier of tertiary amines was recently found to affect the *N*-oxidation. Olsen et al. studied a series of tertiary amines and found that those compounds with *N*-oxidation reactivity had lower *N*-inversion barriers.<sup>446</sup>

Computational studies of sulfoxidation and *N*-oxidation have shown that the energy of the quartet transition state was much higher than that of the doublet transition state. Thus, the reaction is predicted to occur along the low-spin pathway.<sup>313,440–443,446,447</sup> This is in sharp contrast to aliphatic hydroxylation, epoxidation, and aromatic hydroxylation reactions,<sup>305,306</sup> in which close-lying transition states were found for both doublet and quartet spin surfaces.<sup>408,409,421,448–451</sup> The main distinction of *S*- and *N*-oxidation compared to other oxidation reactions is that they were indicated to proceed through a synchronous  $2e^-$  transfer process. Therefore, in the high-spin quartet transition state, one electron from sulfur or nitrogen has to migrate to a high-energy  $\sigma_z^*$  orbital,<sup>441</sup> giving rise to the high energy barriers of quartet transition states. Primary and secondary amines can also be oxidized via *N*-hydroxylation. This reaction has been much less explored. DFT calculations support two possible mechanisms with comparable activation energies, a direct oxygen atom transfer (OAT)/isomerization pathway and a hydrogen atom transfer (HAT)/radical rebound pathway.<sup>452–455</sup>

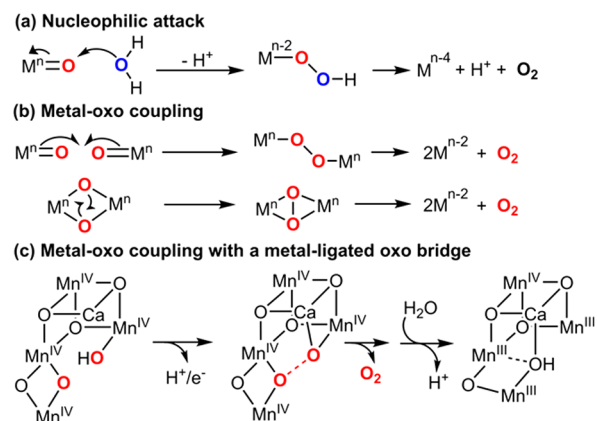
The axial ligand effect has also been explored for oxygen atom transfer reactions (OATs). Initial studies by Gross et al. showed that electron-donating ligands (such as  $F^-$  and  $Cl^-$ ) substantially increased the epoxidation reactivity of model cpd I

complexes, whereas cpd I species with weakly coordinating ligands, such as  $CF_3SO_3^-$  and  $ClO_4^-$  displayed lower reactivity.<sup>456–458</sup> A decrease in  $Fe^{IV}=O$  bond strength for electron-donating ligands was indicated by their lower stretching frequencies ( $\nu_{Fe=O} = 801\text{ cm}^{-1}$  as determined by resonance Raman spectroscopy) compared to those with weakly ligating ligands ( $\nu_{Fe=O} = 834\text{--}835\text{ cm}^{-1}$ ).<sup>457,458</sup> Recently, phenolate and electron-neutral imidazole axial ligands were found to accelerate epoxidations with second-order rate constants 10 times faster than that of chloride ligand.<sup>459</sup> The effect of *para*-substituted pyridine *N*-oxides ligands (*p*-Y-PyO) were also explored for alkene epoxidation and aromatic hydroxylation, and a rate enhancement was observed for both reactions by increasing the electron-donating ability of *para*-substituent Y.<sup>285</sup> DFT calculations were employed to study the impact of axial ligands on a number of OAT reactions, including alkene epoxidation,<sup>409,449</sup> aromatic hydroxylation,<sup>448,451</sup> and sulfoxidation.<sup>440</sup> In all of these reactions, calculated activation energies were not dependent on the reduction potential of cpd I but did exhibit a good negative linear correlation with  $BDE_{OH}$  of cpd II. This correlation might suggest that the C–O or S–O bond formation step in OATs shares similarities with the O–H bond formation in HAT reactions. Alternatively, it might imply the importance of  $Fe^{IV}=O$  weakening in cpd I for OAT, since calculations showed that, in addition to increasing the cpd II basicity, the electron donation from axial ligand also weakened the  $Fe^{IV}=O$  bond in cpd I.<sup>285</sup>

### 3.5. O–O Bond Formation Mediated by Oxometalloporphyrins

**3.5.1. Oxygen Evolution from Oxometal Complexes.** A key step in photosynthesis is the oxidation of water to dioxygen. This four-electron, four-proton process generates the electrons finally used to convert  $CO_2$  to carbohydrates.<sup>460</sup> In photosystem II, the water oxidation occurs via multiple proton-coupled electron transfers (PCETs) at the  $Mn_4Ca$  oxygen-evolving complex (OEC).<sup>461</sup> The development of molecular

#### Scheme 10. Proposed Mechanisms for Water Oxidation Mediated by Metal–Oxo Intermediates



catalysts that can catalyze this process under mild conditions and low energy cost is important for solar energy conversion and storage.<sup>461</sup> Metalloporphyrins, with their ability to form high-valent metal–oxo intermediates, are promising catalysts for water oxidation and oxygen evolution.<sup>33,462,463</sup> The major pathways considered for metal–oxo-mediated water oxidation

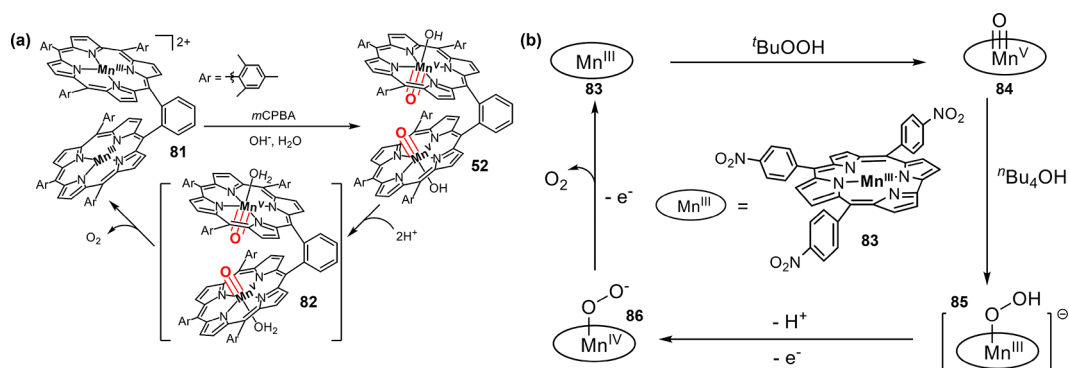


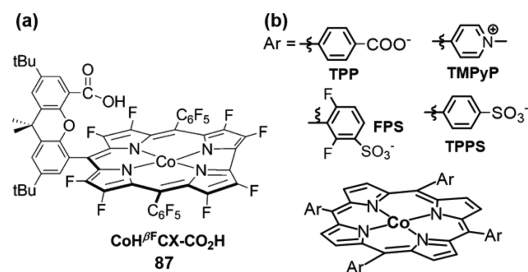
**Figure 48.** (a) Water oxidation mediated by a dimeric manganese porphyrin complex. Adapted from ref 231. Copyright 2004 Wiley-VCH. (b) Water oxidation catalyzed by a manganese corrole complex **83**. Adapted from ref 472. Copyright 2009 American Chemical Society.

include nucleophilic attack of water/hydroxide by oxoMn(V) and the coupling of two metal–oxo (or μ-oxo) units (Scheme 10). The former is formally the microscopic reverse of the O–O bond cleavage for cpd I generation, while the coupling between two μ-oxo units in the latter pathway will afford a (μ-η<sup>2</sup>:η<sup>2</sup>-peroxo)dimetal complex similar to the oxygen adduct of hemocyanine.<sup>464–466</sup> In a third mechanism, the O–O bond is formed via coupling of a metal-bound oxide with a metal-ligated μ-oxo bridge.<sup>467–470</sup> This mechanism is mainly proposed for O<sub>2</sub> evolution of photosystem II OEC and related polynuclear metal–oxygen complexes.

An early example of a water–oxidation catalyst based on metalloporphyrins is a dimeric manganese porphyrin complex **81** synthesized by Naruta et al. (Figure 48a).<sup>471</sup> This species can catalyze the anodic water oxidation in aqueous acetonitrile solution containing <sup>n</sup>Bu<sub>4</sub>NOH with a potential range of 1.2–2.0 V (vs Ag/Ag<sup>+</sup>) and Faradaic efficiency of 5–17%. A dimeric oxoMn(V) intermediate **52** was later prepared by treating the Mn(III) dimer complex with *m*CPBA as a potential reactive intermediate for water oxidation (Figure 48a).<sup>231</sup> This species is very stable under basic conditions but decomposes to Mn(III) and dioxygen upon neutralization with acid. Åkermark, Sun, and co-workers reported a monomeric manganese porphyrinoid system for water oxidation (Figure 48b).<sup>472</sup> A manganese corrole complex **83** was shown to efficiently mediate the oxygen evolution at a low potential ~0.8 V versus Ag/AgNO<sub>3</sub>. An oxoMn(V) intermediate **84** was prepared from **83**. The addition of hydroxide **84** led to the formation of O<sub>2</sub> presumably via the nucleophilic attack of OH<sup>-</sup>. A Mn(IV)-peroxo intermediate **86** was detected during this process, which was likely formed from the further oxidation of the Mn(III)-hydroperoxo intermediate **85**. Nam also reported the formation of a Mn(IV)-peroxo intermediate upon adding base to a oxoMn(V) corrole complex, Mn<sup>V</sup>(O)(TFMPC) (TFMPC = 5,10,15-tris(3,5-trifluoromethylphenyl)corrolato trianion).<sup>473</sup> This step is reversible as the addition of acid to peroxo-Mn(IV)(TFMPC) could regenerate the oxoMn(V) intermediate.

In addition to manganese, cobalt is another base metal that has been extensively studied for water oxidation. Nocera et al. reported the first cobalt porphyrinoid system for water oxidation (**87**, Scheme 11a) using a cobalt “hangman” β-octafluoro corrole complex **87**. When immobilized in Nafion films, **87** can catalyze water oxidation at 1.4 V versus Ag/AgCl at pH 7 with turnover frequency (TOF) of 0.81 s<sup>-1</sup>.<sup>474</sup> Sakai et al. reported several Co(III) porphyrins, including Co(TPP), Co(TMPyP), and Co(TPPS), for water oxidation via photon-initiation using Ru<sup>II</sup>(bpy)<sub>3</sub><sup>2+</sup>/Na<sub>2</sub>S<sub>2</sub>O<sub>8</sub> (Scheme 11b). The

### Scheme 11. (a) Cobalt Hangman Corrole Complex for Water Oxidation<sup>a</sup> and (b) Several Cobalt Porphyrins Utilized for Water Oxidation



<sup>a</sup>Reprinted from ref 474. Copyright 2011 American Chemical Society.

maximum TOFs were in the range of 0.16–0.35 s<sup>-1</sup> at pH 11.<sup>475</sup> A second-order dependence of the initial rate on catalyst concentration was observed, suggesting a bimolecular oxyl–oxyl coupling pathway for O–O bond formation. The degradation of the catalyst has been observed presumably due to the highly oxidizing sulfate radical anions and single dioxygen. More recently, the same group developed a

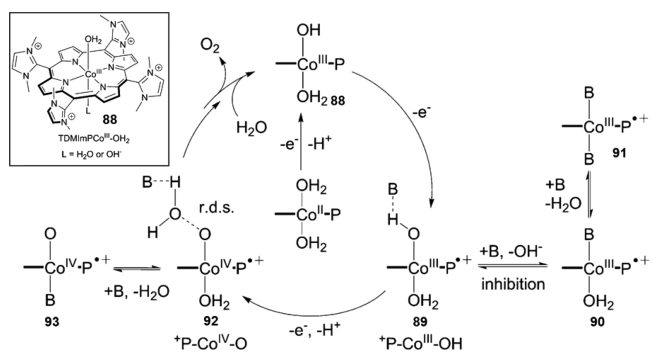


**Figure 49.** Proposed mechanism for water oxidation catalyzed by Co-porphyrins (B = buffer anions). Adapted with permission from ref 477. Copyright 2013 National Academy of Sciences.

fluorinated Co(III) porphyrin catalyst CoFPS for water oxidation with improved stability and efficiency (TOF = 1.1 s<sup>-1</sup>).<sup>476</sup> In contrast to their previous studies, a first-order catalyst concentration dependence was observed for CoFPS, suggesting a nucleophilic attack pathway for the water oxidation reaction catalyzed by CoFPS.

Groves and Wang developed a series of electron-deficient cationic cobalt porphyrins for highly efficient electrocatalytic

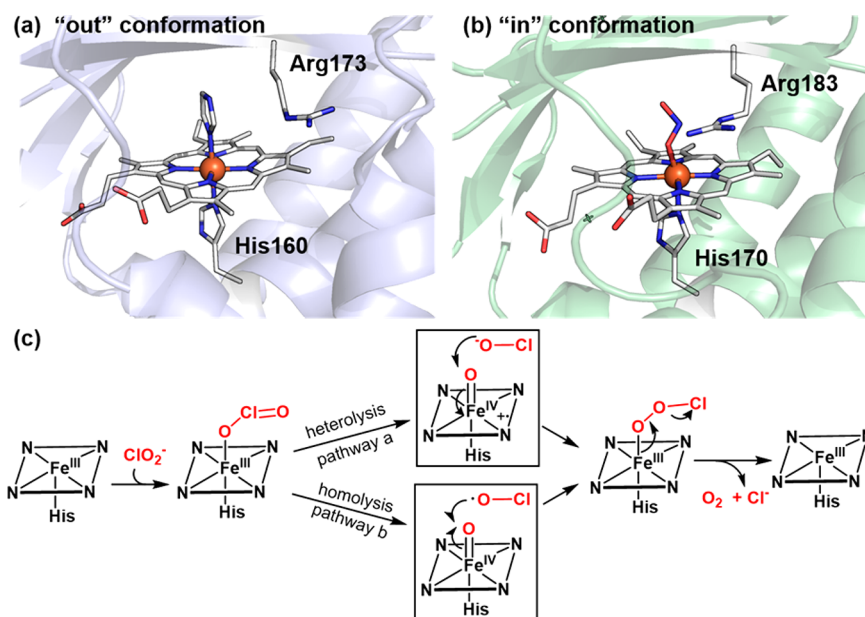


**Figure 50.** (a) Active site of chlorite dismutase (ClD) from *Candidatus Nitrospira defluvii* (*NdClD*) with an imidazole ligand (PDB: 3NN1). Catalytically important arginine (Arg173) exhibits an “out” conformation in this structure. (b) Active site of ClD from *Dechloromonas aromatica* (*DaClD*) with a nitrite ligand (PDB: 3Q09). Catalytically important arginine (Arg183) exhibits an “in” conformation in this structure. (c) The proposed mechanism for chlorite dismutase.

water oxidation.<sup>477</sup> For  $\text{Co}^{\text{III}}$ (TDMImP) (**88**, Figure 49), at a potential of 1.3 V versus Ag/AgCl at pH 7, the  $\text{O}_2$  formation rate was determined to be  $170 \text{ nmol cm}^{-2} \text{ min}^{-1}$  ( $k_{\text{obs}} = 1.4 \times 10^3 \text{ s}^{-1}$ ) with a near 90% Faradaic efficiency. The authors conducted detailed mechanistic studies of these cobalt-based water-oxidation systems. They identified that a  $\text{Co}^{\text{IV}}\text{-O}$  porphyrin cation radical species  $\text{P}^{\bullet+}\text{Co}^{\text{IV}}\text{-O}$  (**92**, Figure 49) is the active intermediate for water oxidation. A linear dependence between catalytic current and catalyst concentration suggested that the rate-limiting O–O bond formation occurred at a single cobalt site. Intriguingly, the buffer anion was identified to play multiple important roles in the catalytic cycle. First, it acts as a proton acceptor in the conversion of  $\text{P}^{\bullet+}\text{Co}^{\text{III}}\text{-OH}$  to  $\text{P}^{\bullet+}\text{Co}^{\text{IV}}\text{-O}$ , which is found to be a single PCET process with a slope of  $-54 \text{ mV p}K_{\text{a}}^{-1}$  for a plot of onset potential of water oxidation versus buffer  $\text{p}K_{\text{a}}$ . Furthermore, it acts as a base to deprotonate water in the rate-limiting O–O formation step, as indicated by a linear correlation between  $(i_{\text{cat}}/i_{\text{water}})^2$  versus buffer base concentration and a KIE of 2.8 measured in  $\text{H}_2\text{O}$  versus in  $\text{D}_2\text{O}$ . Finally, an inhibition of water oxidation was observed at high buffer concentrations, presumably resulting from the formation of an inactive bis-coordinated  $\text{Co}(\text{III})$  intermediate **91** with buffer anions. The unchanged intensity and UV–vis spectroscopic features of **88** after bulk electrolysis, the absence of an inhibition effect of EDTA, and the clean electrode surface with no sign of heterogeneous cobalt phase clearly exclude the possibility of forming heterogeneous metal oxide films at electrode surface, which is known to be a potential issue for homogeneous water-oxidation catalysts.<sup>478</sup> More recently, Cao et al. reported a nickel-based water-oxidation catalyst with a cationic porphyrin ligand.<sup>479</sup> A TOF of  $0.67 \text{ s}^{-1}$  was observed at a potential of 1.32 V (vs NHE). The reactive intermediate of this system is proposed to be a  $\text{Ni}(\text{III})\text{-oxyl}$  radical species. As in the case of analogous cobalt cationic porphyrins, buffer base was shown to participate in the rate-determining O–O bond

formation step. An inhibition effect of buffer base at high concentrations was also observed.

**3.5.2. Chlorite Dismutase.** The conversion of chlorite to chloride and dioxygen is another reaction that might involve the O–O bond formation mediated by cpd I. This process is important for the microbial perchlorate respiration, as it removes the toxic end-product chlorite.<sup>480</sup> In nature, the decomposition of chlorite is catalyzed by chlorite dismutase (ClD), a heme-containing protein with a histidine proximal ligand.<sup>481</sup> The active site structure of ClD is shown in Figure 50, which is featured by an arginine positioned above the heme and the lack of other hydrogen-bonding residues that are essential for O–O bond heterolytic cleavage.<sup>482</sup> The proposed mechanism for functional ClD involves an initial formation of a ferric-chlorito intermediate ( $\text{Fe}^{\text{III}}\text{-OClO}$ ), analogous to compounds **0** in P450s and peroxidases (Figure 50c).<sup>483</sup> A subsequent O–Cl bond heterolytic cleavage will generate cpd I and hypochlorite, which will undergo nucleophilic attack at cpd I to generate  $\text{Cl}^-$  and  $\text{O}_2$ .<sup>484</sup> Alternatively, the homolysis of Cl–O bond of  $\text{Fe}^{\text{III}}\text{-OClO}$  will afford compound II (cpd II) and chlorine monoxide radical ( $\text{ClO}\cdot$ ).  $\text{Cl}^-$  and  $\text{O}_2$  are formed via a rebound process between  $\text{ClO}\cdot$  and cpd II. The latter mechanism is analogous to the mechanism proposed for NO oxidation catalyzed by nitric oxide dioxygenase (see section 4.2). The distal arginine can adopt either “in” and “out” conformations (Figure 50a and 50b),<sup>482</sup> which is proposed to play an important role in positioning the transiently formed hypochlorite to ensure its efficient capturing by cpd I (or cpd II).<sup>485–487</sup> There are two phylogenetically distinct class of ClDs (clades 1 and 2). Clade 1 ClDs (including *NdClD* and *DaClD* shown in Figure 50) are pentameric and hexameric, whereas clade 2 ClDs are dimeric. Very recently, Obinger and co-workers have carried out detail structural and kinetic studies of a dimeric clade 2 ClD from *Cyanothecce* sp. PCC7425 (CCLD).<sup>488</sup> The spectral features of various intermediates of dimeric CCLD appeared to be much better resolved than those of clade 1 ClDs, which allowed for the presteady-state kinetic studies of CCLD.

Their results showed that mixing CCl<sub>4</sub> with chlorite under stopped-flow conditions led to the formation of cpd II within milliseconds at pH > 5.0. Furthermore, no O<sub>2</sub> formation was observed by treating CCl<sub>4</sub> cpd I with excess hypochlorite

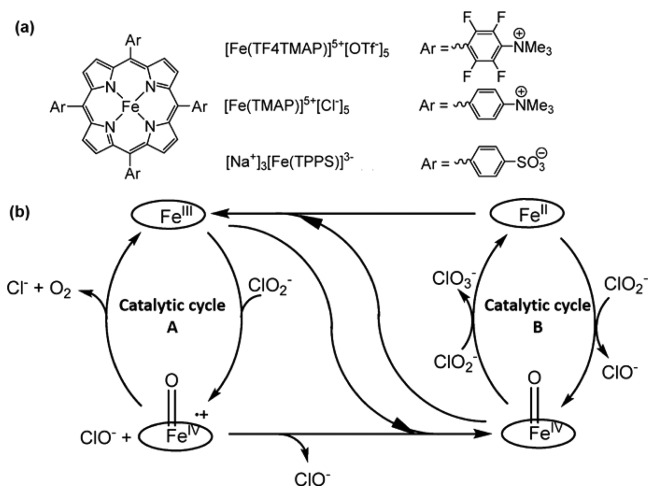


**Figure 51.** (a) Iron porphyrins to mimic Cld reactivity. (b) The proposed mechanism of ClO<sub>2</sub><sup>-</sup> decomposition to form Cl<sup>-</sup> and O<sub>2</sub> and that of ClO<sub>2</sub><sup>-</sup> disproportionation to ClO<sub>3</sub><sup>-</sup> and Cl<sup>-</sup> catalyzed by iron porphyrins. Adapted from ref 490. Copyright 2009 American Chemical Society.

(HOCl/OCl). These results suggest a homolysis pathway for chlorite degradation by CCl<sub>4</sub>.

The chlorite decomposition reactions have also been explored with metalloporphyrins. In a Mn porphyrin-catalyzed alkane oxidation with chlorite as oxidant, Collman et al. found a catalytic side reaction that produced Cl<sup>-</sup> and O<sub>2</sub> from chlorite.<sup>489</sup> The disproportionation of ClO<sub>2</sub><sup>-</sup> into Cl<sup>-</sup> and ClO<sub>3</sub><sup>-</sup> was also observed especially in the absence of

hydrocarbon substrates. More recently, Abu-Omar and co-workers studied the reaction between chlorite and several water-soluble iron porphyrins (Figure 51a).<sup>490</sup> They also identified two degradation pathways of ClO<sub>2</sub><sup>-</sup>, in which one afforded ClO<sub>3</sub><sup>-</sup> and Cl<sup>-</sup> and the other yielded O<sub>2</sub> and Cl<sup>-</sup>. The more electron-withdrawing fluorinated Fe(TF<sub>4</sub>MAP) catalyzed both reactions, while less electron-deficient Fe(TMAPP) and Fe(TPPS) only catalyzed the disproportionation of ClO<sub>2</sub><sup>-</sup> to ClO<sub>3</sub><sup>-</sup> and Cl<sup>-</sup>. On the basis of isotope labeling studies, they proposed Cl<sup>-</sup> and O<sub>2</sub> were formed via a cpd I/rebound pathway similar to that proposed for Cld (cycle A, Figure 51), whereas that ClO<sub>3</sub><sup>-</sup>/Cl<sup>-</sup> pathway proceeds through a Fe(II) porphyrin/cpd II catalytic cycle (cycle B, Figure 51).

Recently, electron-deficient cationic manganese porphyrins have been shown to catalyze the generation of chlorine dioxide from chlorite by Groves and Abu-Omar groups, respectively.<sup>491–493</sup> The reaction proceeds rapidly under mild conditions. For Mn(TDMImP), TOFs were determined to be 0.47 s<sup>-1</sup> at pH 6.8 and 1.0 s<sup>-1</sup> at pH 4.7. The catalytic efficiency can be dramatically increased by changing Mn(TDMImP) to an electron-deficient manganese porphyrine catalyst MnTM23PyPz (TOF = 32.0 s<sup>-1</sup> at pH 4.5) (Figure 52a).<sup>492</sup> A detailed mechanistic study by Groves et al. with Mn<sup>III</sup>(TDMImP) catalyst revealed an initial generation of oxoMn(V) and ClO<sup>-</sup>, which then diffuses to oxidize a second Mn(III) site to oxoMn(V) (Figure 52b).<sup>492</sup> This is in sharp contrast to Cld and iron porphyrins, in which an in-cage recombination between cpd I and ClO<sup>-</sup> would afford O<sub>2</sub> and Cl<sup>-</sup>. Each oxoMn(V) species could produce two ClO<sub>2</sub> molecules via successive out-sphere electron transfer to ClO<sub>2</sub><sup>-</sup>. The oxidation of ClO<sub>2</sub><sup>-</sup> to ClO<sub>2</sub> by oxoMn<sup>V</sup> and oxoMn<sup>IV</sup> showed comparable rates at pH 6.8 ( $k_{app} = 3.13–6.30 \times 10^3 \text{ M}^{-1} \text{ s}^{-1}$ ). The oxidation of ClO<sub>2</sub><sup>-</sup> by oxoMn<sup>IV</sup> is also reversible [ $k_{app} = (4.59 \pm 2.37) \times 10^2 \text{ M}^{-1} \text{ s}^{-1}$ ]. Furthermore, the evolved ClO<sub>2</sub> can be further oxidized to ClO<sub>3</sub><sup>-</sup> by oxoMn<sup>V</sup> and oxoMn<sup>IV</sup> in a subsequent phase of the reaction. Similar mechanistic features but at much slower rates have been

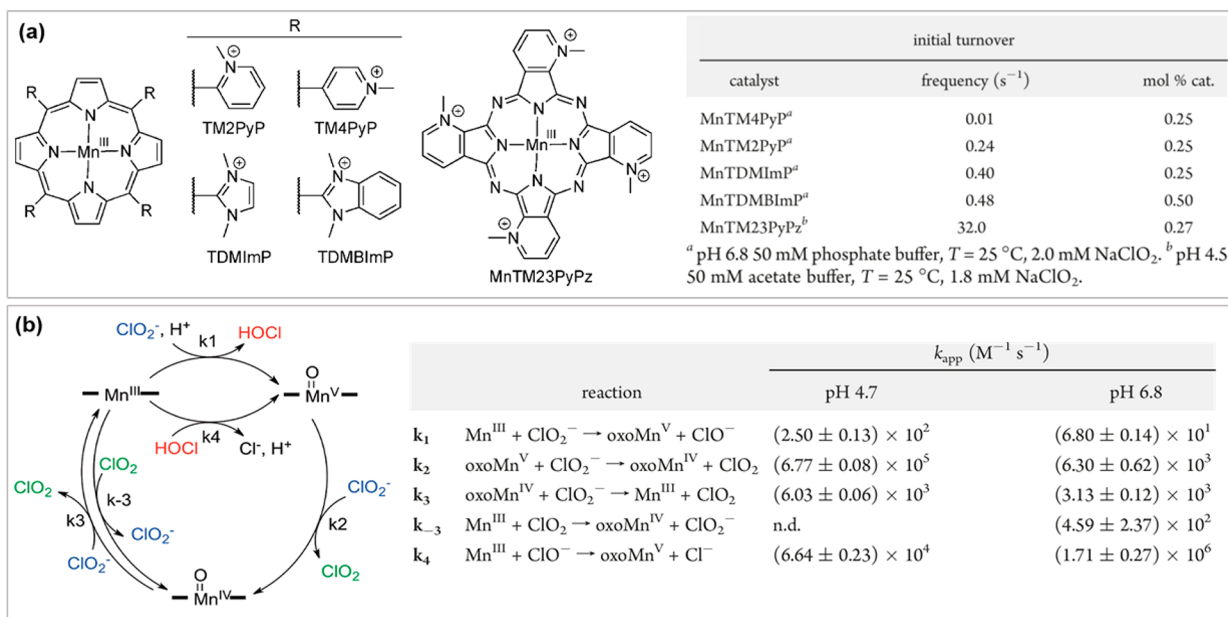
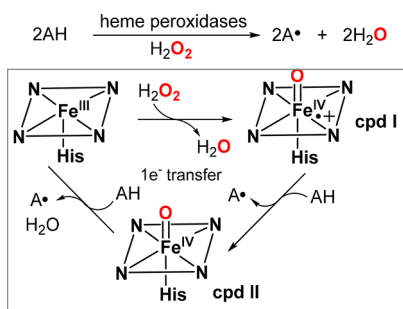


**Figure 52.** (a) Mn porphyrin and porphyrazine catalysts for generation of ClO<sub>2</sub> from chlorite and their turnover frequencies. (b) Mechanism of chlorite dismutation catalyzed by Mn(TDMImP) and the apparent second-order rate constants for the elementary steps. Hypochlorite is written in protonated form as the measurements were carried out at a pH range of 4.7–6.8. Adapted from ref 492. Copyright 2011 American Chemical Society.

described by Abu-Omar et al. for a  $\text{Mn}(\text{TF}_4\text{TMAP})/\text{NaClO}_2$  system.<sup>494</sup>

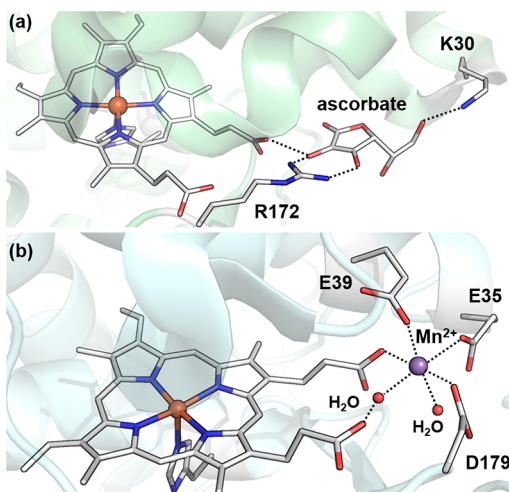
### Scheme 12. Heme Peroxidase Generates Cpd I with $\text{H}_2\text{O}_2$ and Catalyzes Two Discrete Single Electron Transfer (SET) Reactions to Substrates



### 3.6. Single Electron Transfer (SET) Reactions of Cpd I

In addition to participating in hydrogen atom transfer (HAT) and oxygen atom transfer (OAT) reactions, compound I can also display single electron transfer (SET) reactivity, which is commonly seen in heme-containing peroxidases. Unlike most P450s, peroxidase compound I is generated directly from the resting ferric heme and  $\text{H}_2\text{O}_2$  or organic hydroperoxides via the “peroxide shunt” mechanism. Peroxidase cpd I can carry out two discrete single-electron transfers to two substrate molecules and regenerate the ferric heme state (Scheme 12). This three-step mechanism was first proposed by Dunford et al. for the oxidation of ferrocyanide by  $\text{H}_2\text{O}_2$  and HRP.<sup>246</sup> The resulting substrate radicals can undergo further transformations.<sup>495</sup> Thus, substrates of heme peroxidases are generally good one-electron donors, such as electron-rich aromatics, ascorbate, ferrocyanide, etc.<sup>496</sup> Even strongly oxidizing  $\text{Mn}^{3+}$  can be produced from  $\text{Mn}^{2+}$  in this way by manganese peroxidase.

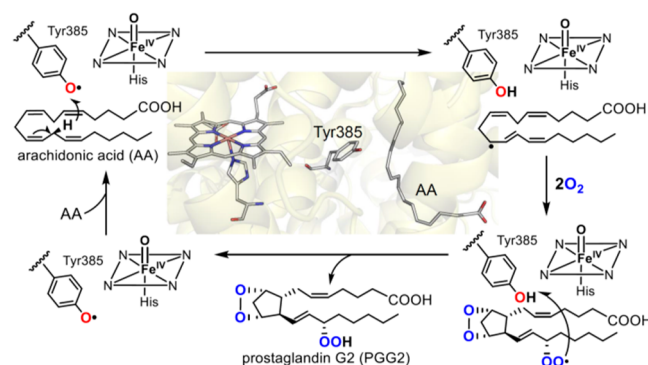
Heme peroxidases are not the only enzymes that utilize  $\text{H}_2\text{O}_2$  to form compound I. Unspecific peroxygenases (UPO) and chloroperoxidase (CPO) employ a similar “peroxide shunt” pathway to generate compound I to catalyze HAT and OAT



**Figure 53.** Examples of substrate binding to the heme periphery of peroxidases and forming hydrogen bonds with heme propionates and active site residues. (a) Ascorbate peroxidase (APX, PDB: 1OAF). (b) Manganese peroxidase (MnP, PDB: 1YYD).

reactions.<sup>497</sup> As discussed in section 3.1, a major cause of this reactivity difference is the much larger O–H BDEs of UPO-II and CPO-II (98–100 kcal/mol) compared to that of HRP-II, originating from the elevated reduction potentials of UPO-I and CPO-I and the decreased acidities of UPO-II and CPO-II. Furthermore, the  $1e^-$  reactions in peroxidases are facilitated by the proper positioning of substrates.<sup>498</sup> The local protein environment of peroxidases hinders the approach of substrates to the  $\text{Fe}^{\text{IV}}=\text{O}$  moiety. Therefore, many substrates bind in the heme periphery and participate in a hydrogen-bonding network with heme propionate and active site residues (Figure 53).<sup>499</sup> This network can serve as a relay to mediate the proton and electron transfer.<sup>500,501</sup> Alternatively, substrates can be oxidized at a remote site through a chain of redox-active amino acids via long-range electron transfer.<sup>502–505</sup>

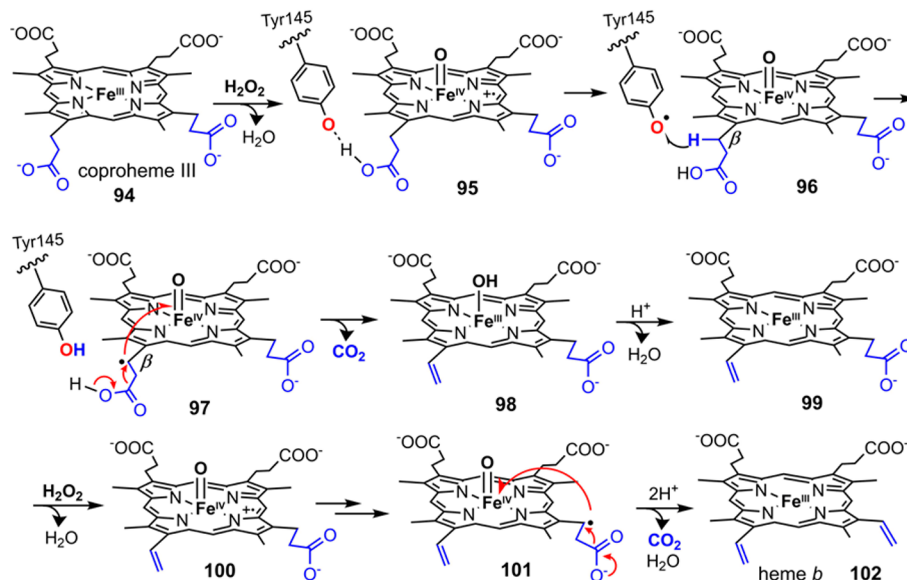
In some peroxidases, the porphyrin cation radical form of compound I is transient and will rapidly transfer one electron to



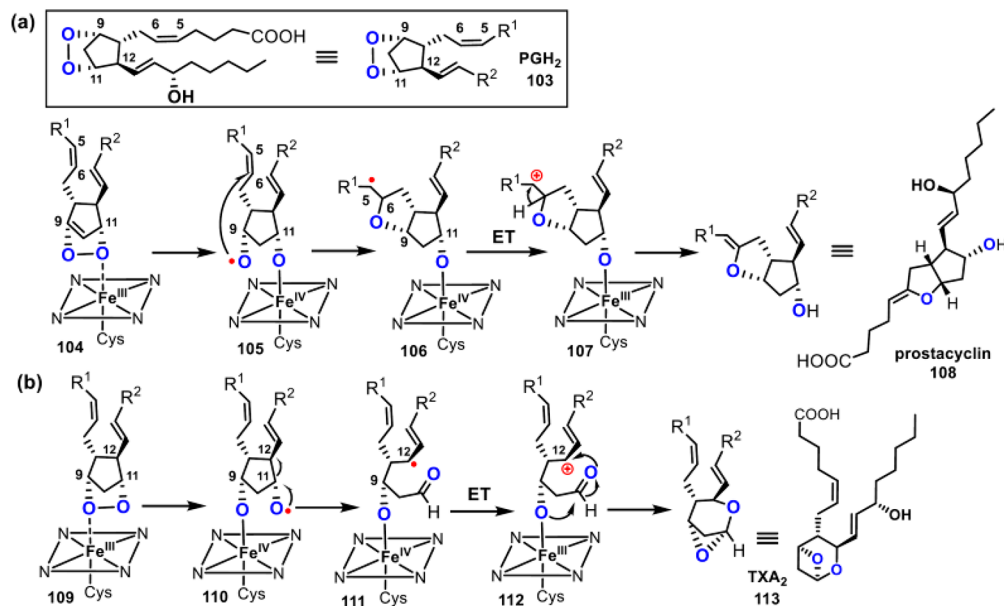
**Figure 54.** Conversion of arachidonic acid (AA) into PGG2 by PGHS.

a nearby redox-active residue like tyrosine or tryptophan. One example is the compound ES of cytochrome *c* peroxidase (CcP), which is an iron(IV)-oxo intermediate with an uncoupled Trp191 cation radical near the proximal histidine.<sup>184</sup> Although the Trp191 radical in CcP just serves as a storage for one oxidation equivalent, in some heme proteins, such radicals can directly mediate reactions. For instance, in prostaglandin H synthase (PGHS), the compound I formed via the normal peroxide activation pathway will oxidize a tyrosine (Tyr385) about 10 Å away to give a tyrosyl radical, which abstracts a hydrogen atom from arachidonic acid (Figure 54).<sup>506,507</sup> The resulting substrate radical will further react with two  $\text{O}_2$  molecules to give product PGG2 and finally prostaglandin  $\text{H}_2$  ( $\text{PGH}_2$ ). This reaction also represents an example of substrate activation for  $\text{O}_2$  reactions in heme proteins.<sup>2</sup>

Another example of using protein radicals for substrate activation is the synthesis of heme *b* by coproheme decarboxylase (HemQ).<sup>508</sup> HemQ catalyzes a  $\text{H}_2\text{O}_2$ -dependent decarboxylation of two propionates in coproheme (94, Scheme 13). Recent mechanistic studies by DuBois et al. showed that Tyr145, which hydrogen bonds with one of the cleaved propionates, is first converted to a tyrosyl radical by coproheme compound I (95, Scheme 13).<sup>509,510</sup> The Tyr145 radical then abstracts a hydrogen from the heme propionate group presumably at the  $\text{C}_\beta$  position (96). The resulting carbon-centered radical transfers one electron through porphyrin to  $\text{Fe}(\text{IV})$  and reduces it to iron(III) with loss of  $\text{CO}_2$  (97 → 98). The decomposition of the second propionate is thought to follow a similar mechanism, but the identity of the mediator of  $\text{C}_\beta\text{-H}$  cleavage is not clear.

Scheme 13. HemQ-Catalyzed Synthesis of Heme *b* from Coproheme III<sup>a</sup>

<sup>a</sup>Adapted from ref 509. Copyright 2017 American Chemical Society.

Scheme 14. (a) Synthesis of Prostacyclin from PGH<sub>2</sub> Mediated by Prostacyclin Synthase and (b) Synthesis of Thromboxane A<sub>2</sub> (TXA<sub>2</sub>) Catalyzed by Thromboxane A Synthase

#### 4. REACTIONS MEDIATED BY HEME–OXYGEN INTERMEDIATES OTHER THAN CPD I

In addition to cpd I, other heme–oxygen intermediates generated during O<sub>2</sub> activation also exhibit rich redox chemistries that are harnessed by heme proteins for a variety of oxidative transformations, giving rise to the diverse biological functions of heme proteins. In this section, we analyze several representative reactions catalyzed by heme proteins and metalloporphyrins to delineate their mechanistic features and to discuss how the fundamental properties of heme–oxygen intermediates and their active site environments impact reaction outcomes.

##### 4.1. Homolytic O–O Bond Cleavage of Peroxides by Heme Proteins

In addition to generating compound I via O–O bond heterolysis, organic peroxides can also react with ferric hemes via single-electron-transfer processes, which will oxidize the ferric heme to ferryl with concurrent homolytic cleavage of O–O bond. These transformations play important roles in the synthesis of important bioactive molecules, especially oxylipins.<sup>511</sup> Natural sources of peroxides include fatty acid hydroperoxides formed via O<sub>2</sub> trapping of substrate allylic radicals.<sup>512</sup> Subsequent O–O bond homolysis leads to oxy radicals that can undergo a plethora of rearrangements, bond cleavages, and other transformations.

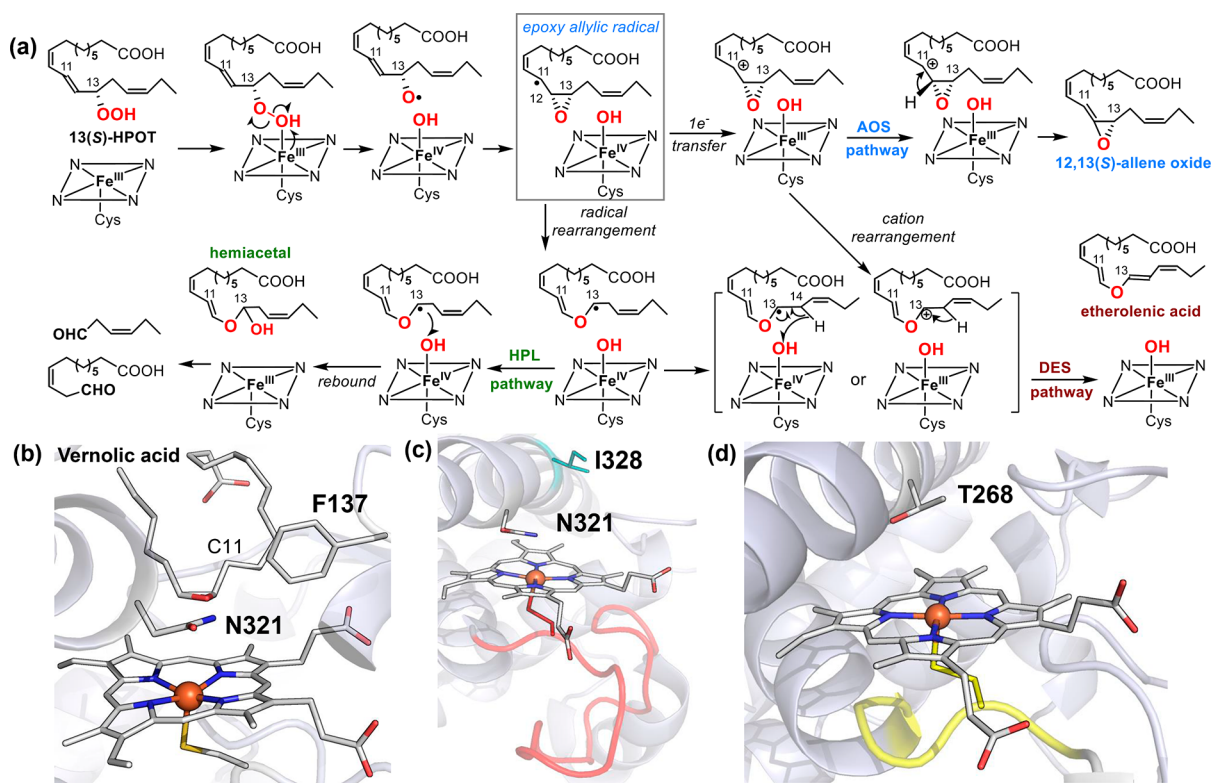


**Figure 55.** (a) Reactions catalyzed by the CYP74 family of enzymes. The mechanisms of all three pathways involve a common epoxyallylic radical intermediate. (b) Active site structure of *Arabidopsis thaliana* AOS complexed with vernolic acid (PDB: 2RCL). (c) Key N321 and I328 residues of *AtAOS* (PDB: 3CLI). The cysteine loop region is highlighted in red. (d) Key threonine residue of *P450<sub>BM3</sub>* (PDB: 1BVY). The cysteine loop region is highlighted in yellow.

One example is the synthesis of prostacyclin from prostaglandin  $H_2$  (PGH<sub>2</sub>) via prostacyclin synthase (Scheme 14a).<sup>507,513,514</sup> This transformation starts with the interaction between endoperoxide of PGH<sub>2</sub> and ferric heme center of prostacyclin synthase (104, Scheme 14a), leading to the homolytic O–O bond cleavage of endoperoxide to afford the C9-alkoxyl radical and ferryl heme intermediate (105). The C9-alkoxyl radical then adds to the C5–C6 alkene to forge the new five-membered heterocycle and C5 radical (106), which is later oxidized to carbocation by the ferryl heme to regenerate the C5–C6 alkene moiety via loss of a proton (107). The homolytic cleavage of endoperoxide of PGH<sub>2</sub> is also used in the synthesis of thromboxane A<sub>2</sub> (TXA<sub>2</sub>) mediated by thromboxane A synthase (Scheme 14b).<sup>515–517</sup> In this reaction, the ferric heme center interacts with O9 and affords C11-alkoxyl radical (109 and 110, Scheme 14b), which is later rearranged to an allylic radical at C12 (111). Subsequent electron transfer and ring cyclization would afford TXA<sub>2</sub>.

In another instructive example, 13S-hydroperoxyoctadecatrienoic acid [13(S)-HPOT] can be activated by the CYP74 family of enzymes, affording three different products: 12,13(S)-allene oxide, etherolenic acid, and an analogous hemiacetal (Figure 55a).<sup>518,519</sup> The first step in all of these three transformations is the homolysis of an iron-bound O–O bond to afford an epoxyallylic radical and a cysteine-ligated Fe<sup>IV</sup>–OH intermediate similar to compound II in P450 monooxygenases. The reactions then diverge depending on how the incipient substrate radical interacts with the Fe<sup>IV</sup>–OH intermediate. In allene oxide synthase (AOS), the C11 epoxyallylic radical is oxidized by electron transfer to Fe<sup>IV</sup>–OH to generate a substrate-derived carbocation intermediate,

which eliminates a proton to form the new C=C bond. In hydroperoxide lyase (HPL), by contrast, the radical undergoes rearrangement to form a radical at C13, which then recombines with Fe<sup>IV</sup>–OH via an oxygen-rebound mechanism. In the divinyl ether synthase (DES) pathway, the product is thought to be formed via a hydrogen atom abstraction from C14 by Fe<sup>IV</sup>–OH or via an electron-transfer process followed by cation rearrangement and proton elimination. Sequence analysis and mutagenesis studies revealed that, in all three enzymes, an asparagine positioned directly above heme is important for mediating the O–O bond homolysis.<sup>520</sup> The crystal structure of *Arabidopsis thaliana* AOS (*AtAOS*) complexed with 12R,13S-vernolic acid, a mimic of the epoxyallylic intermediate, showed that C11 is in proximity to F137 (Figure 55b), whereas in HPL and DES, a similar position is occupied by a leucine. The aromatic ring of F137 is thought to stabilize the C11 carbocation and thus facilitate the single electron transfer in the AOS pathway. In support of this rationale, a F137L mutation induced HPL activity for AOS.

It is intriguing to compare the structural difference between CYP74 and P450 hydroxylases, since CYP74 has a typical P450 protein fold but does not perform O–O bond heterolysis. In addition to the critical Asn residue (N321) located above the heme, there are two more structural features that distinguish CYP74 from P450 hydroxylases.<sup>520</sup> As can be seen from the crystal structure of *AtAOS*, the highly conserved threonine in the proton relay channel of P450 hydroxylases, which is crucial for O–O bond heterolysis, is replaced by an isoleucine (I328) (Figure 55, panels c and d). Further, there is a nine-residue insert in the heme-binding loop of AOS, which seems to contribute to the long Fe–S bond (2.4 Å) of AOS. A long Fe–

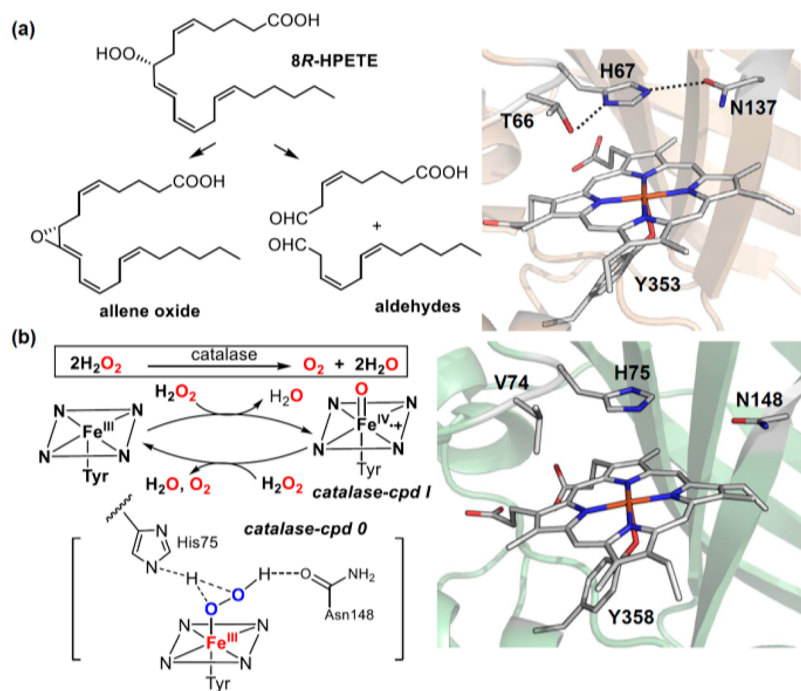


**Figure 56.** (a) Reactions catalyzed by cAOS and the active site structure of cAOS (PDB: 1USU). (b) Active site structure of human catalase (PDB: 1QQW) and the mechanism of O–O bond activation in catalase-compound 0.

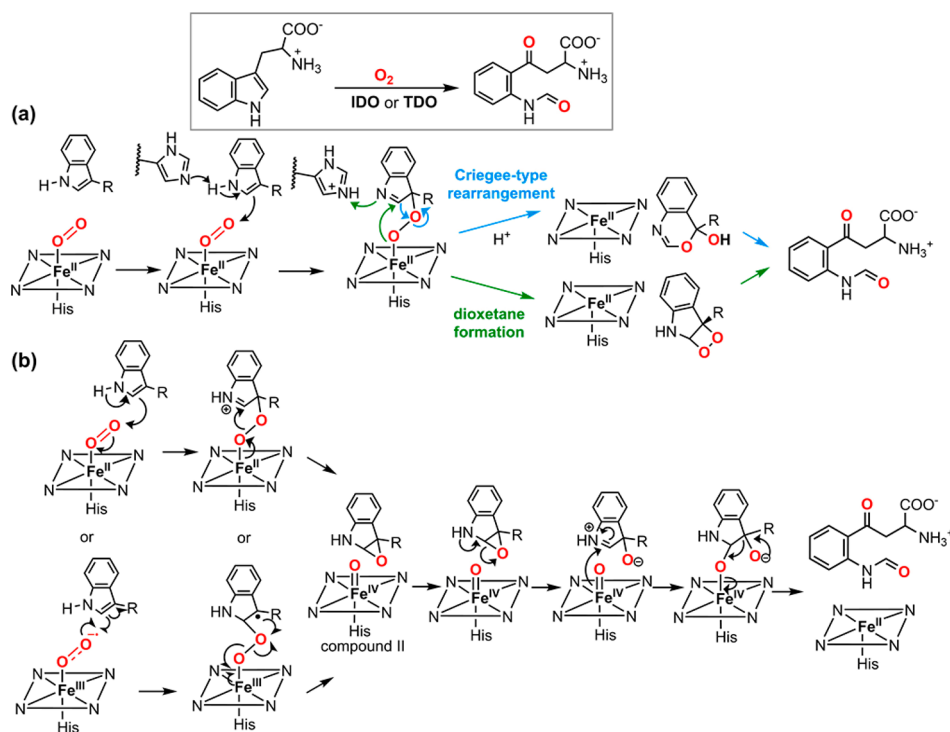


**Figure 57.** (a) Previously proposed base-abstraction mechanism followed by either Criegee rearrangement or dioxetane formation. Adapted from ref 539. Copyright 2011 American Chemical Society. (b) A recently proposed mechanism involves the formation of an Fe<sup>IV</sup>=O intermediate and a 2,3-indoline epoxide intermediate. Adapted from ref 550. Copyright 2016 American Chemical Society.

S distance has been shown to decrease the electron-donating ability of cysteine thiolate, which, in turn, would lead to a higher Fe reduction potential and a more facile SET reactivity of compound II.<sup>181</sup>

In addition to CYP74, there is another enzyme that can also catalyze the synthesis of allene oxides via homolytic cleavage of fatty acid hydroperoxides. This enzyme is structurally similar to

catalase and thus termed catalase-related allene oxide synthase (cAOS).<sup>521</sup> cAOS converts 8R-hydroperoxyarachidonic acid (8R-HPETE) into corresponding 8,9-epoxy allene oxide in the biosynthesis of preclavulone A. The crystal structure comparison between cAOS and catalase showed very similar active site structures, including the proximal heme-ligating tyrosine and the critical distal histidine and asparagine that are important for



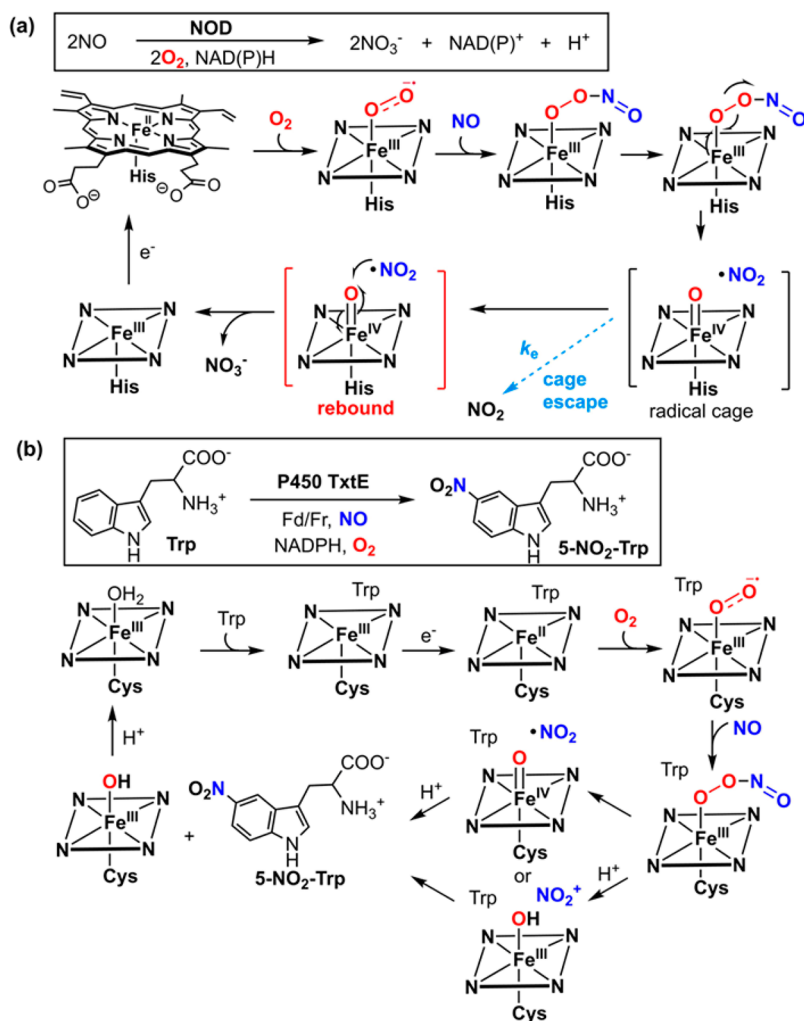


**Figure 58.** (a) Proposed mechanism for NO oxidation catalyzed by NOD. (b) Proposed mechanism for tryptophan nitration catalyzed by P450 TxtE.

the O–O bond activation in catalase (Figure 56). A key difference is identified at a residue adjacent to the distal histidine, which is normally a valine in catalases but is changed to a threonine (T66) in cAOS.<sup>522</sup> The histidine in cAOS hydrogen bonds with both T66 and asparagine. This hydrogen bonding network could function to dampen H<sub>2</sub>O<sub>2</sub> activation in cAOS by inhibiting the hydrogen bonding between histidine and the hydroperoxy moiety of Fe<sup>III</sup>–OOH (cpd 0). Indeed, a T66V mutation greatly increased the catalase activity of cAOS, albeit with short lifetime due to the heme degradation. cAOS is thought to proceed through a similar epoxy allylic radical intermediate. As in the case of CYP74, products other than allene oxide were also observed in reactions catalyzed by cAOS and its relatives.<sup>523–528</sup>

#### 4.2. Reactions Initiated by Ferric-Superoxo Intermediates

In most heme proteins, ferric-superoxo complexes either serve as stable complexes, such as in oxymyoglobin and gas sensing proteins such as heme-nitric oxide/oxygen (H-NOX) binding proteins,<sup>529–531</sup> or rapidly convert to high-valent iron–oxo intermediates via reduction and O–O bond scission. Tryptophan 2,3-dioxygenase (TDO) and indoleamine 2,3-dioxygenase (IDO), however, utilize ferric-superoxo intermediates to initiate the oxidation of substrates.<sup>532,533</sup> TDO and IDO are histidine-ligated heme-containing dioxygenases involved in

tryptophan oxidation.<sup>534–536</sup> TDO employs dioxygen to cleave the 2,3-bond of L-tryptophan to form N-formyl kynurenine, whereas IDO catalyzes the same reaction but has a much broader substrate scope, including a variety of indoleamine derivatives such as D-tryptophan, melatonin, and serotonin. IDO has recently gained substantial research interest because of its immunomodulatory potential for cancer treatment.<sup>537,538</sup>

The initially proposed mechanism for TDO and IDO-catalyzed tryptophan oxygenation involved a histidine-catalyzed proton abstraction of the indole N–H, followed by electrophilic attack at C3 of indoleamine by the distal oxygen of ferric-superoxo intermediate (Figure 57a).<sup>539</sup> But this mechanism is not consistent with later findings showing that N-methyl-tryptophan was an active substrate and that human IDO lacked the proposed proton-abstracting histidine.<sup>540–542</sup> DFT calculations indicated high energy barriers for the formation of either a dioxetane intermediate or a Criegee-type rearrangement.<sup>543</sup> Further studies by Yeh et al. using resonance Raman and UV–vis spectroscopies revealed the presence of a ferryl species during catalytic turnover of IDO.<sup>544–546</sup> Similar ferryl species can also be generated by treating IDO and TDO using H<sub>2</sub>O<sub>2</sub>.<sup>541,547–549</sup> On the basis of these results, a new mechanism has been proposed (Figure 57b), in which the ferric-superoxo complexes directly attacks the indoleamine ring via either electrophilic addition or radical addition to afford an

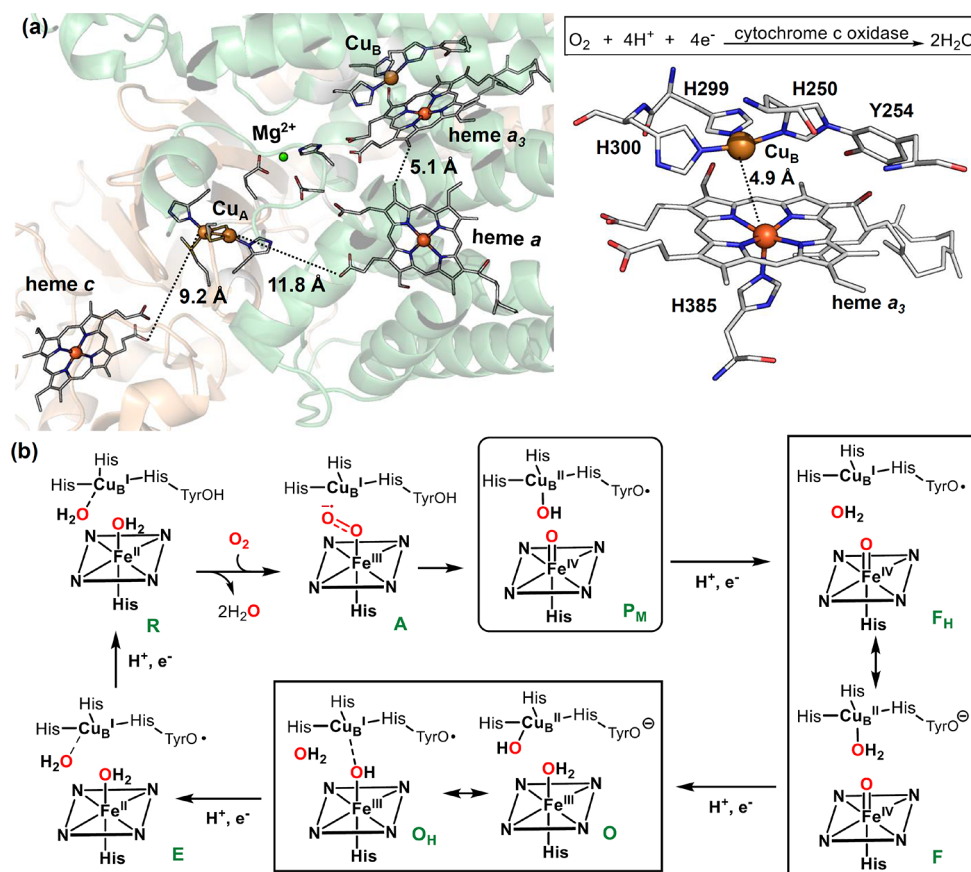


**Figure 59.** (a) Cofactor arrangement in a cytochrome *c* oxidase (PDB: 2YEV) and the structure of binuclear heme  $a_3$ /Cu<sub>B</sub> center (BNC). (b) General catalytic cycle of CcO and important intermediates involved (R, A, P<sub>M</sub>, F, O, and E). This mechanism is produced according to the catalytic cycles shown in refs 561 and 562.

indoline-2,3-epoxide intermediate and a ferryl compound II. Subsequent reactions between the epoxide and Fe(IV)=O are currently speculative but do lead to the formation of kynurenine type product and regenerate the ferrous heme. While the ferryl intermediate of IDO accumulates under steady-state conditions, TDO cpd II has yet to be observed during turnover. Rather, the [Fe(II)–O<sub>2</sub>, L-Trp] ternary complex accumulates under catalytic conditions. Raven et al. have recently suggested that this difference is caused by a change of the rate-limiting step from compound II decay in IDO to oxygen addition to formation of the 2,3-epoxide intermediate in TDO.<sup>550</sup>

Another enzyme that utilizes an ferric-superoxo intermediate for oxygenation is nitric oxide dioxygenase (NOD).<sup>551</sup> As shown in Figure 58a, NO first reacts with an ferric-superoxo intermediate to form a proposed ferric-peroxynitrite intermediate. This intermediate then undergoes homolytic cleavage to generate NO<sub>2</sub> and compound II.<sup>552</sup> The recombination between NO<sub>2</sub> and compound II yields nitrate and ferric heme. This recombination process is reminiscent of the oxygen rebound of carbon-centered radicals in P450s. The study of peroxynitrite decomposition mediated by *met*-myoglobin offered critical insight into the radical rebound mechanism, especially the radical cage escape effect.<sup>553,554</sup> Unlike carbon-centered radicals, the diffusion of NO<sub>2</sub> can be easily detected via fluorogenic probes such as fluorescein. Kinetic simulations revealed that 10% of the NO<sub>2</sub> escaped from the radical cage [MbFe<sup>IV</sup>=O·NO<sub>2</sub>] formed after peroxynitrite decomposition. Cytochrome P450 TxtE from *Streptomyces scabies* also employs

a ferric-superoxo intermediate to generate NO<sub>2</sub> from NO, which is then used to nitrate L-tryptophan to form 4-nitro-L-tryptophan.<sup>555,556</sup> The proposed mechanism involves the formation of a ferric-peroxynitrite intermediate by the trapping of NO by the ferric-superoxo intermediate (Figure 58b). The NO<sub>2</sub> generated after peroxynitrite decomposition can then add to the aromatic ring, which is further oxidized by compound II to afford the nitration product. An alternative mechanism involves heterolytic cleavage to generate nitronium ion (NO<sub>2</sub><sup>+</sup>) for direct electrophilic nitration.<sup>555</sup>

#### 4.3. O<sub>2</sub> Reduction Catalyzed by Heme/Cu Terminal Oxidases and Related Model Compounds

Heme/Cu terminal oxidases such as cytochrome *c* oxidases (CcO) catalyze the 4e<sup>−</sup>/4H<sup>+</sup> reduction of O<sub>2</sub> as a final step in respiration with concomitant membrane proton-translocation leading to ATP synthesis.<sup>557</sup> The active site structure of CcO is unusual compared to many heme proteins as it contains a binuclear heme  $a_3$ /Cu<sub>B</sub> center (BNC) with a Fe–Cu separation of around 5 Å (Figure 59a). Cu<sub>B</sub> is coordinated to three histidine residues, one of which is covalently cross-linked to a tyrosine residue.<sup>558–560</sup> During O<sub>2</sub> reduction by CcO, electrons from cyt *c* are delivered one at a time to BNC via a dicopper complex (Cu<sub>A</sub>) and a low-spin heme  $a$ . The mechanism of CcO action has been extensively studied. The catalytic cycle involves four consecutive proton and electron transfer steps and multiple intermediates are involved. Figure 59b showed a simplified mechanism of CcO-catalyzed oxygen reduction.<sup>561</sup> The Fe(III)–Cu(II) resting state of BNC (compound O) is

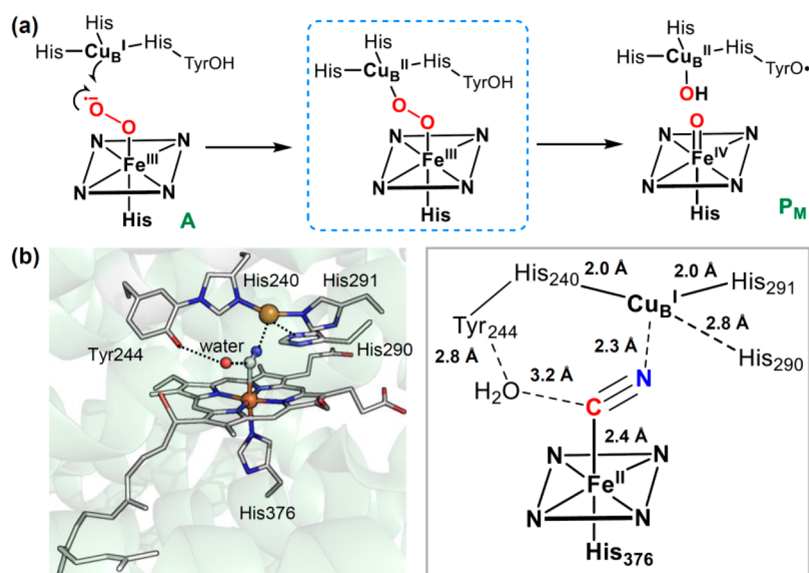


**Figure 60.** (a) The proposed ferric-peroxy-cupric intermediate for the generation of  $P_M$  state. (b) A CN-bound CcO might share similar structural features to the putative ferric-peroxy-cupric intermediate (PDB: 3AG4).

### Scheme 15. Formation of $\text{Fe}^{\text{III}}-\mu\text{-oxo}-\text{Cu}^{\text{II}}$ Complexes by Treating $\text{Fe}(\text{II})$ Porphyrin/ $\text{Cu}^{\text{I}}$ Complex with $\text{O}_2$

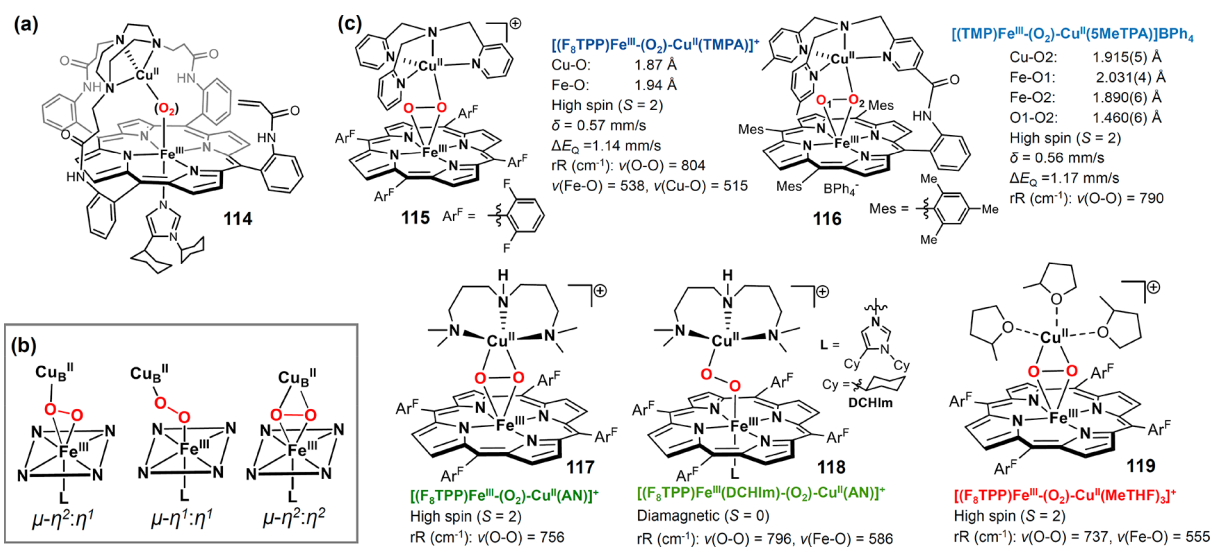
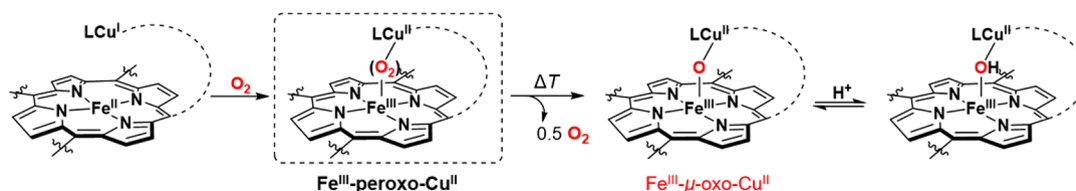


**Figure 61.** (a) A heme-peroxy-copper model compound based on “capped” porphyrin with an appended TACN ligand for copper binding. (b) Different peroxy bonding mode for heme-peroxy-copper complexes. (c) Several representative heme-peroxy-copper model compounds.

converted to an E state and then to a  $\text{Fe}(\text{II})\text{-Cu}(\text{I})$  reduced state (**R**) via two one-electron reductions and two proton transfer steps. The ferrous heme  $a_3$  in **R** will bind oxygen rapidly ( $\sim 1.4 \times 10^8 \text{ M}^{-1} \text{ s}^{-1}$ ), generating a low-spin end-on  $\text{Fe-O}_2$  intermediate (**A**) similar to other oxygen-binding heme proteins. O–O bond cleavage in **A**, which can be viewed as an O–O hemolysis in a bridged  $\text{Fe}(\text{III})\text{-O-O-Cu}(\text{II})$  intermediate, yields a four-electron oxidized intermediate  $P_M$ , containing a ferric heme  $a$ , a  $\text{Fe}(\text{IV})=\text{O}$ ,  $\text{Cu}(\text{II})\text{-OH}$ , and a

tyrosyl radical. Four subsequent  $1e^-$  reductions and proton transfers will lead sequentially through the **F**, **O** and **E** states, poisoning the protein for another oxygen-binding event. It is worth noting that in Figure 59b, we only showed intermediates formed after both electron- and proton-transfer steps. Furthermore, depending on the status of copper ligation and redox potentials of copper center, the cross-linked tyrosine could exist as tyrosyl radical with  $\text{Cu}(\text{II})$  center being reduced to  $\text{Cu}(\text{I})$ .<sup>561,562</sup> Each of these reduction/protonation steps

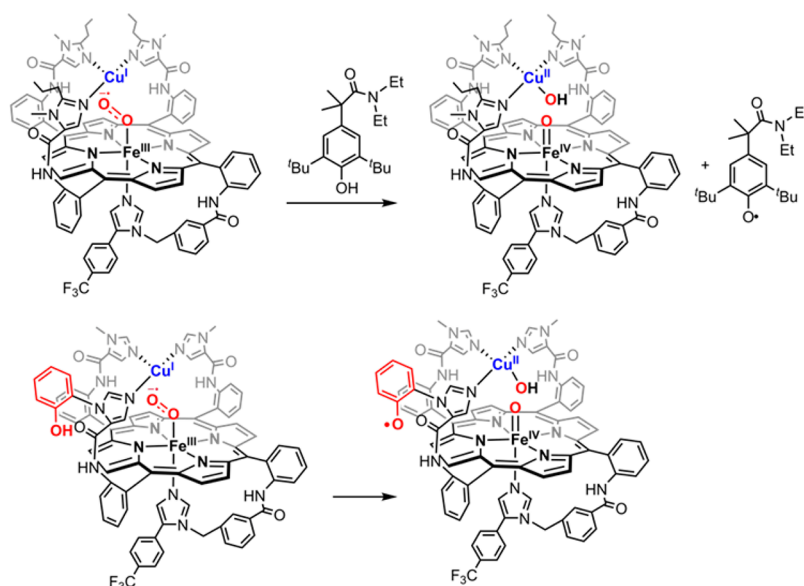


**Figure 62.** Reactions between  $\text{Fe}^{\text{III}}$ -superoxide- $\text{Cu}^{\text{I}}$  complexes and phenols.

(scalar protons) are also coupled to one vectorial proton pumped across the membrane, thus maintaining the proton gradient required for ATPase phosphorylation.<sup>561</sup>

While many aspects of the CcO mechanism have been clarified, the details of the O–O cleavage to generate compound  $\text{P}_M$  and the role of the  $\text{Cu}_B$  His-Tyr unit in this step remains elusive. As noted above, a putative ferric peroxo intermediate ( $\text{Fe}^{\text{III}}\text{--O--O--Cu}^{\text{II}}$ ) is thought to be generated via  $1e^-$  reduction of ferric-superoxo intermediate by  $\text{Cu}^{\text{I}}$  center (Figure 60a).<sup>558</sup> A subsequent proton-coupled electron transfer (PCET) from tyrosine to  $\text{Fe}^{\text{III}}\text{--O--O--Cu}^{\text{II}}$  could promote the O–O cleavage and generate the ferryl center and tyrosyl radical. Yoshikawa et al. have examined the binding of diatomic molecules (CO, NO, and  $\text{CN}^-$ ) to the reduced bovine CcO via X-ray structural analysis.<sup>563</sup> Compared to CO- and NO-bound structures,  $\text{CN}^-$  binding leads to the displacement and dissociation of a copper-bound histidine and the coordination of cyanide nitrogen to the copper. Furthermore, a water molecule is incorporated to form a hydrogen bond with both  $\text{CN}^-$  and covalently ligated tyrosine (Tyr244) (Figure 60b). These structural features were thought to be highly relevant to the ferric-superoxo intermediate of CcO, where  $\text{O}_2$  is negatively polarized similarly to  $\text{CN}^-$ . The hydrogen-bonding network in the active site could provide a channel for PCET from Tyr244 to the peroxo moiety. Another intriguing feature of this CN-bound CcO structure is the significant bending of the Fe–C–N angle ( $96^\circ$ ). This bent structure is in line with previous resonance Raman characterizations and might be caused by the weak  $\pi$ -accepting ability of cyanide, which makes it easier to adopt a bent geometry compared to the isoelectronic Fe–CO complexes.<sup>564–567</sup>

Model compounds have offered critical insights to the O–O heterolytic cleavage in CcO.<sup>23,568</sup> The study of CcO model compounds has led to the development of electrocatalytic systems for the four-electron reduction of  $\text{O}_2$  to water, which would have potential applications in fuel cells.<sup>20,33,569–571</sup> These systems have been reviewed in detail very recently.<sup>33</sup> Common strategies for preparing CcO models include treating ferrous porphyrins with covalently appended copper(I) with  $\text{O}_2$  or adding  $\text{Cu}^{\text{I}}$  complexes to preformed, discrete ferric peroxo

porphyrins. In early attempts,  $\mu$ -oxo heme- $\text{Fe}^{\text{III}}\text{--O--Cu}^{\text{II}}$  species were obtained, presumably from the disproportionation of the corresponding complexes.<sup>23</sup> The oxygen of  $\text{Fe}^{\text{III}}\text{--}\mu\text{-oxo--Cu}^{\text{II}}$  species are basic and can undergo reversible protonation (Scheme 15). A  $\text{pK}_a$  of 8 has been reported for  $[(\text{F}_8\text{TTP})\text{Fe}^{\text{III}}\text{--}(\text{OH})\text{--Cu}^{\text{II}}(\text{TMPA})]^{2+}$  ( $\text{F}_8\text{TTP}$  = tetrakis(2,6-difluorophenyl)porphyrinate,  $\text{TMPA}$  = tris(2-pyridylmethyl)amine).<sup>572</sup>

The first well-characterized heme-peroxo-copper adduct was reported by Collman with a complex “capped” porphyrin scaffold with an appended triazacyclononane (TACN) ligand for copper binding (114, Figure 61a).<sup>573</sup> This species has a high spin ( $S = 2$ ) ground state with a  $\nu(\text{O--O})$  of  $758\text{ cm}^{-1}$ . More recently, a variety of heme-peroxo-copper adducts were characterized and shown to display a rich coordination chemistry. The peroxo moiety can adopt  $\mu\text{-}\eta^2\text{:}\eta^1$ ,  $\mu\text{-}\eta^1\text{:}\eta^1$ , or  $\mu\text{-}\eta^2\text{:}\eta^2$  bonding modes depending on the precise copper ligand environment and heme axial ligand (Figure 61, panels b and c).<sup>20,568,574</sup> Karlin has described a  $\mu\text{-}\eta^2\text{:}\eta^1$  heme-peroxo-copper compound obtained by treating a ferric peroxo complex  $[(\text{F}_8\text{TTP})\text{Fe}^{\text{III}}(\text{O}_2^{2-})]^-$  with a tetracoordinated  $\text{Cu}^{\text{II}}$  complex  $\text{Cu}^{\text{II}}(\text{TMPA})$  (115, Figure 61c).<sup>575,576</sup> The compound showed a high spin ( $S = 2$ ) electronic state with a  $\nu(\text{O--O})$  of  $804\text{ cm}^{-1}$ . Naruta has successfully obtained the crystal structure of a  $\mu\text{-}\eta^2\text{:}\eta^1$  heme-peroxo-copper adduct,  $[(\text{TMP})\text{Fe}^{\text{III}}\text{--}(\text{O}_2)\text{--}(\text{SMeTPA})\text{Cu}^{\text{II}}]\text{BPh}_4$  (116, Figure 61c).<sup>577</sup> The  $\mu\text{-}\eta^2\text{:}\eta^1$  peroxo core showed two Fe–O bond distances of 2.031(4) and 1.890(6), respectively. Like  $[(\text{F}_8\text{TTP})\text{Fe}^{\text{III}}\text{--}(\text{O}_2)\text{--Cu}^{\text{II}}(\text{TMPA})]^+$ ,  $[(\text{TMP})\text{Fe}^{\text{III}}\text{--}(\text{O}_2)\text{--Cu}^{\text{II}}(\text{SMeTPA})]\text{BPh}_4$  is EPR silent with an  $S = 2$  spin state resulting from a strong antiferromagnetic coupling between high spin  $\text{Fe}^{\text{III}}$  ( $S = 5/2$ ) and  $\text{Cu}^{\text{II}}$  ( $S = 1/2$ ).

The peroxo bonding mode can be regulated by copper coordination and axial ligand of iron porphyrins. For example, addition of a tridentate  $\text{Cu}^{\text{II}}$  complex  $\text{Cu}(\text{AN})$  ( $\text{AN} = 3,3'$ -iminobis( $N,N$ -dimethylpropylamine)) to  $[(\text{F}_8\text{TTP})\text{Fe}^{\text{III}}(\text{O}_2^{2-})]^-$  afforded a  $\mu\text{-}\eta^2\text{:}\eta^2$  peroxo coordination (117, Figure 61c), whereas adding imidazole-type axial ligand to  $[(\text{F}_8\text{TTP})\text{Fe}^{\text{III}}\text{--}(\text{O}_2)\text{--Cu}^{\text{II}}(\text{AN})]$  shifted the peroxo coordination to the  $\mu\text{-}\eta^1\text{:}\eta^1$  mode (118, Figure 61c).<sup>578–581</sup> The end on  $\mu\text{-}\eta^1\text{:}\eta^1$  heme-peroxo-copper complex is diamagnetic with a low

spin  $S = 1/2$  Fe(III) antiferromagnetically coupled to Cu(II) ( $S = 1/2$ ).<sup>581,582</sup> Very recently, Karlin et al. reported a  $[\text{Fe}^{\text{III}}(\text{O}_2^{2-})\text{-Cu}^{\text{II}}(\text{MeTHF})_3]^+$  (MeTHF = 2-methyltetrahydrofuran) complex (**119**, Figure 61c). The weak coordination of the MeTHF ether oxygen allows for facile ligand exchange, providing ready access to a variety of heme-peroxo-Cu<sup>II</sup> species.<sup>583</sup> In addition to the heme-peroxo-Cu<sup>II</sup> intermediate, isoelectronic Fe<sup>III</sup>-superoxide-Cu<sup>I</sup> complexes were synthesized using picket fence porphyrins.<sup>584,585</sup> These Fe<sup>III</sup>-superoxide-Cu<sup>I</sup> complexes are relatively stable at room temperature, suggesting

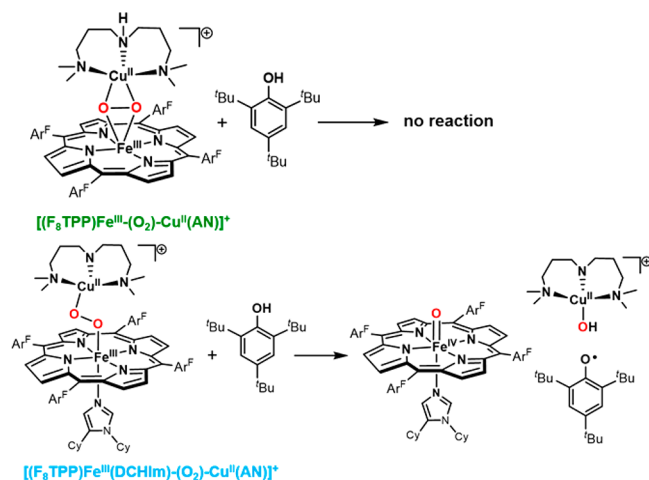


**Figure 63.** Comparison of reactions with phenols between low-spin and high-spin Fe<sup>III</sup>-peroxo-Cu<sup>II</sup> complexes.

that Cu<sup>I</sup> could also play a nonredox role in stabilizing iron dioxygen adducts.

The reactivity of CcO models toward phenols was also explored. Collman et al. found that an Fe<sup>III</sup>-superoxide-Cu<sup>I</sup> complex could react with phenol both intra- and intermolecularly to afford a ferryl species, a tyrosyl radical, and Cu(II)-OH,<sup>586,587</sup> a process that resembles the transition from CcO A state to P<sub>M</sub> state (Figure 62). Solomon and Karlin have tested the reactivity of both low- and high-spin heme-peroxo-copper complexes by treating them with phenols (Figure 63).<sup>578</sup> While high-spin  $[(\text{F}_8\text{TPP})\text{Fe}^{\text{III}}(\text{O}_2^{2-})\text{-Cu}^{\text{II}}(\text{AN})]^+$  was not reactive toward phenols, the low-spin  $[(\text{DCHIm})(\text{F}_8\text{TPP})\text{Fe}^{\text{III}}(\text{O}_2^{2-})\text{-Cu}^{\text{II}}(\text{AN})]^+$  (DCHIm = dicyclohexyl imidazole) reacted with phenols readily, even at  $-80^\circ\text{C}$ , to afford a ferryl intermediate, Cu(II)-OH, and a tyrosyl radical.<sup>578</sup>

The impact of copper complex structure and the nature of the proton source on the O-O bond activation step was recently investigated.<sup>588</sup> Two Fe<sup>III</sup>-peroxo-Cu<sup>II</sup> complexes with tridentate and tetradentate copper complexes, respectively (LS-3DCHIm and LS-4DCHIm), were prepared and examined for their reactivity toward different acids or electron donor decamethylferrocene ( $\text{Fc}^*$ ) (Figure 64). While LS-4DCHIm alone was not reactive toward  $\text{Fc}^*$ , the addition of 4-nitrophenol led to the formation of an  $[\text{LS-4DCHIm}\cdots 4\text{-NO}_2\text{-phenol}]$  association complex, which underwent facile O-O bond cleavage via proton-coupled electron transfer from 4-nitrophenol and  $\text{Fc}^*$  to peroxo moiety. Intriguingly, under similar conditions, LS-3DCHIm was not reactive. Further examination showed that LS-3DCHIm could not form the association complex with phenol presumably due to a more compressed and sterically inaccessible peroxo core. Strong acids like triflic acid led to the direct decomposition of both LS-3DCHIm and LS-4DCHIm and the release of hydrogen peroxide, regardless of the steric environment of peroxo group.

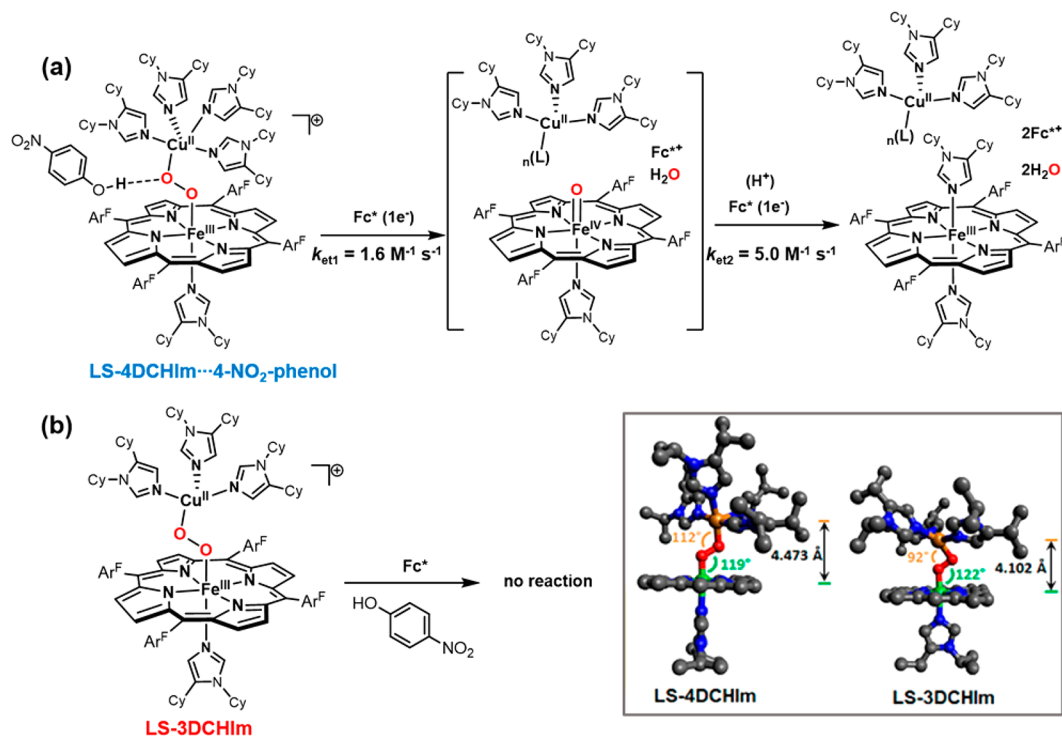


**Figure 64.** (a) Phenol association will promote the O-O bond cleavage of LS-4DCHIm in the presence of electron donor  $\text{Fc}^*$ . (b) LS-3DCHIm could not form the phenol association complex and is not reactive toward  $\text{Fc}^*$ . DFT calculation showed a more compressed structure of LS-3DCHIm. Adapted from ref 588. Copyright 2017 American Chemical Society.

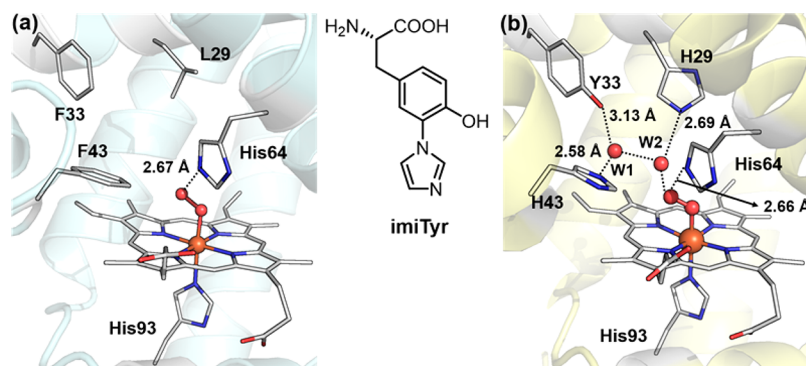


**Figure 65.** (a) Crystal structure of oxy-Mb (PDB: 1A6M). (b) Crystal structure and the hydrogen bonding network in the active site of oxy-F33Y-Cu<sub>B</sub>Mb (PDB: SHAV).

In addition to small molecule models of CcO, redesigned metalloproteins that mimic the reactivity of CcO represents another powerful approach to study its mechanism.<sup>589</sup> Lu et al. found that the introduction of two mutations (L29H and F43H) would create a copper binding site in the heme pocket of myoglobin (Figure 65a).<sup>590</sup> The resulting copper-bound myoglobin (Cu<sub>B</sub>Mb) showed heme oxygenase reactivity that degrades heme to verdoheme. In 2012, Lu and Wang generated a Cu<sub>B</sub>Mb with a cross-linked Tyr-His ligand via genetic incorporation of the unnatural amino acid imiTyr at the F33 position (Figure 65). The imiTyr-Cu<sub>B</sub>Mb exhibited enhanced oxidase reactivity (2/min).<sup>591</sup> In the same year, Lu et al. found that the introduction of a tyrosine mutation to Cu<sub>B</sub>Mb at F33 also improved O<sub>2</sub> reduction activity (24/min). Intriguingly, the observed oxidase activity is not copper-dependent. A subsequent study showed that a ferric-hydroperoxy species was formed for F33Y-Cu<sub>B</sub>Mb upon cryoreduction at 77K, whereas a peroxo-ferric state was formed for wild-type Mb.<sup>592</sup> The X-ray crystal structure of F33Y-Cu<sub>B</sub>Mb revealed an extensive H-bond network with two water molecules (W1 and W2), in which W1 is H-bonded to H43 and Y33 and W2 is stabilized by H-bonds to W1 and H29 (Figure 65b).<sup>593</sup> This hydrogen-bonding network could polarize the O–O bond and facilitate its reduction and protonation. Very recently, Lu and co-workers studied the effect of nonheme metals on oxidase activity of the repurposed Mb.<sup>594</sup> While Zn-Mb formed a stable ferric-superoxo intermediate, both Cu-Mb and Fe-Mb showed oxidase reactivity with Cu-Mb almost three times more reactive than Fe-Mb. The higher reactivity of Cu<sup>I</sup> is attributed to the higher Cu<sup>II</sup>/Cu<sup>I</sup> potential and an enhanced weakening of O–O bond through *dπ-pπ* back bonding, as revealed by the longer O–O bond length (1.391 Å) in Cu-Mb than that in Fe-Mb (1.351 Å).

## 5. CONCLUSIONS AND OUTLOOK

The central goal of this review was to survey the range of redox reactions mediated by heme proteins. Parallel developments with model metalloporphyrins and computational approaches are also reviewed and have served both to elucidate the nature of reactive enzymatic intermediates and to discover new chemistry, some of which is unknown in the repertoire of heme protein reactions. Another goal was to provide context for the recent advances with key discoveries from the formative years of the field. This coverage took inspiration from a course we developed at Princeton University called Metals in Biology: From Stardust to DNA. It is interesting to consider that heme and heme proteins apparently evolved long before oxygen was

present in the environment in significant quantities. From this perspective, it is clear that oxygen binding and oxygen activation are relatively recent innovations in biology. Accordingly, it is likely that access to hydrogen peroxide allowed heme proteins to be repurposed by exploring the rich chemistry made possible by the ferryl group as well as ferric and iron(IV) hydroxides. In this context, heme and nonheme iron proteins are essentially similar, tied together by the sequential reduction of oxygen to superoxide, hydrogen peroxide, and ultimately water. As we have seen in the examples discussed above, the porphyrin ring can be oxidized at ~1 V versus NHE to a porphyrin cation radical. Accordingly, there is a direct mechanistic analogy between heme iron and nonheme diiron proteins such as sMMO and AlkB, wherein the second oxidizing equivalent resides on the second iron rather than the porphyrin ligand. There are also nonheme, monoiron systems such as TauD and naphthalene dioxygenase that exploit Fe(IV)/Fe(II) and Fe(III)/Fe(V) couples, respectively, in their substrate oxidations. Studies of heme protein and metalloporphyrin reaction mechanisms and the insights gained from that work have in recent years led to significant developments in drug design. Clopidogrel (Plavix) and similar drugs are effective at lowering the risk of heart attack and stroke due to the nature of their oxidative metabolism by liver cytochrome P450s. Likewise, inhibitors of P450 aromatase proteins, such as anastrozole, are emerging as key agents for the treatment of certain human breast cancers. New methods of C–H functionalization, such as C–H fluorination with fluoride ion-manganese systems, and their applications have offered novel and practical routes to more efficacious drugs and to the development of potential PET imaging agents. More generally, the recent upsurge of radical chemistry in organic synthesis has provided an explosion of methods for generating substrate radicals under mild conditions.<sup>595–597</sup> One can well imagine that a merger of these radical-generating processes (such as photoredox catalysis and electrocatalysis) with metalloenzymes and their model systems could lead to the development of entirely new synthetic transformations that are inaccessible today. These developments are further strengthened by recent advancements in biocatalysis for non-natural transformations, in which existing enzymes or proteins can be adapted and repurposed to catalyze abiological chemistry via directed evolution.<sup>598,599</sup> We envision that an orchestration between metalloenzymes/metal–oxygen systems and these emerging fields in catalysis have the potential to push the frontiers of biocatalysis and organic synthesis as well as the conceptual underpinnings of the field that continue to provide fresh air.

## AUTHOR INFORMATION

## Corresponding Author

\*E-mail: jtgroves@princeton.edu.

ORCID 

Xiongyi Huang: 0000-0001-7156-8881

John T. Groves: 0000-0002-9944-5899

## Notes

The authors declare no competing financial interest.

## Biographies

Xiongyi Huang received his B.S. degree in chemistry in 2010 from University of Science and Technology of China (USTC), where he performed undergraduate research in computational chemistry under the guidance of Prof. Yao Fu and Prof. Jing Shi. He received his Ph.D. in 2016 at Princeton University with Prof. John T. Groves. His Ph.D. work mainly focused on developing new synthetic strategies for the construction of aliphatic C–halogen, C–F, and C–N bonds using biomimetic manganese catalysts. While at Princeton, Xiongyi was a recipient of the HHMI International Student Research Fellowship (2013–2015) and the 2016 Chinese Government Award for Outstanding Students Abroad. He is currently an NIH Ruth L. Kirschstein postdoctoral fellow in the laboratory of Prof. Frances H. Arnold at Caltech, where he works on developing new enzymatic reactions via directed evolution.

John T. Groves is the Hugh Stott Taylor Chair of Chemistry at Princeton University. He received an S.B. in Chemistry at MIT and a Ph.D. in Organic Chemistry at Columbia University, where he worked with Ronald Breslow. Groves' early academic career was at the University of Michigan where he was director of the Michigan Center for Catalysis and Surface Science and received the Phi Lambda Upsilon Award for Teaching and Leadership. Moving to Princeton University as Professor of Chemistry, he became Department Chair in 1988. He has received the Arthur C. Cope Scholar Award, the Alfred Bader Award in Bioorganic and Bioinorganic Chemistry, the Ira Remsen Award and the Award in Inorganic Chemistry, all from the American Chemical Society. He was co-Chair of the ACS-NSF Committee and Workshop on the Molecular Basis of Life Processes. He is a fellow of the American Academy of Arts and Sciences, the American Association for the Advancement of Science, the Japan Society for the Promotion of Science, and the Royal Society of Chemistry. Groves is a member of the U.S. National Academy of Sciences. International awards include the Grand Prix, Maison de la Chimie (Paris), the Frontiers in Biological Chemistry Award from the Max Planck Institute (Mülheim), and the Hans Fischer Award in Porphyrin Chemistry. Groves' research has focused on the roles of metal–oxo species in chemical and biological oxidations.

## ACKNOWLEDGMENTS

We are deeply indebted to our co-workers at Princeton University and at the University of Michigan in the early years, for their imaginative and energetic contributions to the work from our laboratories described herein. We are also grateful for the continuous support of this research by federal granting agencies. Research directed toward C–H oxidative functionalization was supported by the U.S. National Science Foundation Awards CHE-1148597 and CHE-1464578 and by the Center for Catalytic Hydrocarbon Functionalization, an Energy Frontier Research Center, U.S. Department of Energy, Office of Science, Basic Energy Sciences, under Award DESC0001298. Cytochrome P450 and APO enzymology has been supported

by the National Institutes of Health (2R37 GM036298). X.H. thanks Merck, Inc., the Howard Hughes Foundation, and NIH (Award F32GM125231) for fellowship support.

## ABBREVIATIONS

AOS	allene oxide synthase
APX	ascorbate peroxidase
CcO	cytochrome <i>c</i> oxidase
Cld	chlorite dismutase
Cpd 0	compound 0
Cpd I	compound I
Cpd II	compound II
DES	divinyl ether synthase
HAT	hydrogen atom transfer
Hb	hemoglobin
HRP	horseradish peroxidase
Mb	myoglobin
OAT	oxygen atom transfer
TPFPBr <sub>8</sub>	2,3,7,8,12,13,17,18-octabromo-5,10,15,20-tetrakis(pentafluorophenyl)porphyrin
TpivPP	5,10,15,20-tetra( $\alpha,\alpha,\alpha$ - <i>O</i> -pivalamidophenyl)porphyrin
TPP	5,10,15,20-tetraphenylporphyrin
TMP	5,10,15,20-tetramesitylporphyrin
TPFPF	5,10,15,20-tetrakis(pentafluorophenyl)porphyrin
TDMPP	meso-tetrakis(2,6-dimethylphenyl)porphyrin
TTMPP	meso-tetrakis(3,4,5-trimethoxyphenyl)porphyrin
4-TMPyP	meso-tetrakis(4- <i>N</i> -methylpyridyl)porphyrin
2-TMPyP	meso-tetrakis(2- <i>N</i> -methylpyridyl)porphyrin
TF <sub>4</sub> TMAP	meso-tetrakis(2,3,5,6-tetrafluoro- <i>N,N,N</i> -trimethyl-4-aniliniumyl)porphyrinato dianion
TFMPC	5,10,15-tris(3,5-trifluoromethylphenyl)corrolato trianion
PHM	peptidylglycine $\alpha$ -hydroxylating monooxygenase
TDO	tryptophan 2,3-dioxygenase
IDO	indoleamine 2,3-dioxygenase

## REFERENCES

- (1) Kovaleva, E. G.; Lipscomb, J. D. Versatility of Biological Non-Heme Fe(II) Centers in Oxygen Activation Reactions. *Nat. Chem. Biol.* **2008**, *4*, 186–193.
- (2) Pau, M. Y. M.; Lipscomb, J. D.; Solomon, E. I. Substrate Activation for O<sub>2</sub> Reactions by Oxidized Metal Centers in Biology. *Proc. Natl. Acad. Sci. U. S. A.* **2007**, *104*, 18355–18362.
- (3) Groves, J. T. The Bioinorganic Chemistry of Iron in Oxygenases and Supramolecular Assemblies. *Proc. Natl. Acad. Sci. U. S. A.* **2003**, *100*, 3569–3574.
- (4) Groves, J. T. High-Valent Iron in Chemical and Biological Oxidations. *J. Inorg. Biochem.* **2006**, *100*, 434–447.
- (5) Sheng, Y.; Abreu, I. A.; Cabelli, D. E.; Maroney, M. J.; Miller, A.-F.; Teixeira, M.; Valentine, J. S. Superoxide Dismutases and Superoxide Reductases. *Chem. Rev.* **2014**, *114*, 3854–3918.
- (6) Decker, A.; Solomon, E. I. Dioxygen Activation by Copper, Heme and Non-Heme Iron Enzymes: Comparison of Electronic Structures and Reactivities. *Curr. Opin. Chem. Biol.* **2005**, *9*, 152–163.
- (7) Poulos, T. L. Heme Enzyme Structure and Function. *Chem. Rev.* **2014**, *114*, 3919–3962.
- (8) Mbughuni, M. M.; Chakrabarti, M.; Hayden, J. A.; Bominaar, E. L.; Hendrich, M. P.; Münck, E.; Lipscomb, J. D. Trapping and Spectroscopic Characterization of an Fe<sup>III</sup>-Superoxo Intermediate from a Nonheme Mononuclear Iron-Containing Enzyme. *Proc. Natl. Acad. Sci. U. S. A.* **2010**, *107*, 16788–16793.
- (9) Itoh, S. Mononuclear Copper Active-Oxygen Complexes. *Curr. Opin. Chem. Biol.* **2006**, *10*, 115–122.

- (10) Mirica, L. M.; Ottenwaelder, X.; Stack, T. D. P. Structure and Spectroscopy of Copper–Dioxygen Complexes. *Chem. Rev.* **2004**, *104*, 1013–1046.
- (11) Elwell, C. E.; Gagnon, N. L.; Neisen, B. D.; Dhar, D.; Spaeth, A. D.; Yee, G. M.; Tolman, W. B. Copper–Oxygen Complexes Revisited: Structures, Spectroscopy, and Reactivity. *Chem. Rev.* **2017**, *117*, 2059–2107.
- (12) Costas, M.; Mehn, M. P.; Jensen, M. P.; Que, L. Dioxygen Activation at Mononuclear Nonheme Iron Active Sites: Enzymes, Models, and Intermediates. *Chem. Rev.* **2004**, *104*, 939–986.
- (13) Huang, X.; Groves, J. T. Beyond Ferryl-Mediated Hydroxylation: 40 Years of the Rebound Mechanism and C–H Activation. *JBIC, J. Biol. Inorg. Chem.* **2017**, *22*, 185–207.
- (14) van Eldik, R. Fascinating Inorganic/Bioinorganic Reaction Mechanisms. *Coord. Chem. Rev.* **2007**, *251*, 1649–1662.
- (15) Oszajca, M.; Franke, A.; Brindell, M.; Stochel, G.; van Eldik, R. Redox Cycling in the Activation of Peroxides by Iron Porphyrin and Manganese Complexes. ‘Catching’ Catalytic Active Intermediates. *Coord. Chem. Rev.* **2016**, *306*, 483–509.
- (16) Ortiz de Montellano, P. R. Hydrocarbon Hydroxylation by Cytochrome P450 Enzymes. *Chem. Rev.* **2010**, *110*, 932–948.
- (17) Ortiz de Montellano, P. R.; De Voss, J. J. Oxidizing Species in the Mechanism of Cytochrome P450. *Nat. Prod. Rep.* **2002**, *19*, 477–493.
- (18) Krest, C. M.; Onderko, E. L.; Yosca, T. H.; Calixto, J. C.; Karp, R. F.; Livada, J.; Rittle, J.; Green, M. T. Reactive Intermediates in Cytochrome P450 Catalysis. *J. Biol. Chem.* **2013**, *288*, 17074–17081.
- (19) Yosca, T. H.; Ledray, A. P.; Ngo, J.; Green, M. T. A New Look at the Role of Thiolate Ligation in Cytochrome P450. *JBIC, J. Biol. Inorg. Chem.* **2017**, *22*, 209–220.
- (20) Collman, J. P.; Boulatov, R.; Sunderland, C. J.; Fu, L. Functional Analogues of Cytochrome c Oxidase, Myoglobin, and Hemoglobin. *Chem. Rev.* **2004**, *104*, 561–588.
- (21) Denisov, I. G.; Makris, T. M.; Sligar, S. G.; Schlichting, I. Structure and Chemistry of Cytochrome P450. *Chem. Rev.* **2005**, *105*, 2253–2278.
- (22) Jones, R. D.; Summerville, D. A.; Basolo, F. Synthetic Oxygen Carriers Related to Biological-Systems. *Chem. Rev.* **1979**, *79*, 139–179.
- (23) Kim, E.; Chufán, E. E.; Kamaraj, K.; Karlin, K. D. Synthetic Models for Heme–Copper Oxidases. *Chem. Rev.* **2004**, *104*, 1077–1134.
- (24) Momenteau, M.; Reed, C. A. Synthetic Heme-Dioxygen Complexes. *Chem. Rev.* **1994**, *94*, 659–698.
- (25) Shaik, S.; Cohen, S.; Wang, Y.; Chen, H.; Thiel, W. P450 Enzymes: Their Structure, Reactivity, and Selectivity-Modeled by QM/MM Calculations. *Chem. Rev.* **2010**, *110*, 949–1017.
- (26) Costas, M. Selective C–H oxidation catalyzed by metalloporphyrins. *Coord. Chem. Rev.* **2011**, *255*, 2912–2932.
- (27) Fujii, H. Electronic Structure and Reactivity of High-Valent Oxo Iron Porphyrins. *Coord. Chem. Rev.* **2002**, *226*, 51–60.
- (28) Fukuzumi, S.; Kojima, T.; Lee, Y.-M.; Nam, W. High-Valent Metal-Oxo Complexes Generated in Catalytic Oxidation Reactions Using Water as an Oxygen Source. *Coord. Chem. Rev.* **2017**, *333*, 44–56.
- (29) Sahu, S.; Goldberg, D. P. Activation of Dioxygen by Iron and Manganese Complexes: A Heme and Nonheme Perspective. *J. Am. Chem. Soc.* **2016**, *138*, 11410–11428.
- (30) Sono, M.; Roach, M. P.; Coulter, E. D.; Dawson, J. H. Heme-Containing Oxygenases. *Chem. Rev.* **1996**, *96*, 2841–2888.
- (31) Watanabe, Y.; Nakajima, H.; Ueno, T. Reactivities of Oxo and Peroxo Intermediates Studied by Hemoprotein Mutants. *Acc. Chem. Res.* **2007**, *40*, 554–562.
- (32) Nam, W. High-Valent Iron(IV)–Oxo Complexes of Heme and Non-Heme Ligands in Oxygenation Reactions. *Acc. Chem. Res.* **2007**, *40*, 522–531.
- (33) Zhang, W.; Lai, W.; Cao, R. Energy-Related Small Molecule Activation Reactions: Oxygen Reduction and Hydrogen and Oxygen Evolution Reactions Catalyzed by Porphyrin- and Corrole-Based Systems. *Chem. Rev.* **2017**, *117*, 3717–3797.
- (34) Sorokin, A. B. Phthalocyanine Metal Complexes in Catalysis. *Chem. Rev.* **2013**, *113*, 8152–8191.
- (35) Baglia, R. A.; Zaragoza, J. P. T.; Goldberg, D. P. Biomimetic Reactivity of Oxygen-Derived Manganese and Iron Porphyrinoid Complexes. *Chem. Rev.* **2017**, asap, 11713320 10.1021/acs.chemrev.7b00180.
- (36) Marti, M. A.; Crespo, A.; Capece, L.; Boechi, L.; Bikiel, D. E.; Scherlis, D. A.; Estrin, D. A. Dioxygen Affinity in Heme Proteins Investigated by Computer Simulation. *J. Inorg. Biochem.* **2006**, *100*, 761–770.
- (37) Scott, E. E.; Gibson, Q. H.; Olson, J. S. Mapping the Pathways for O<sub>2</sub> Entry into and Exit from Myoglobin. *J. Biol. Chem.* **2001**, *276*, 5177–5188.
- (38) Tsai, A.-L.; Berka, V.; Martin, E.; Olson, J. S. A “Sliding Scale Rule” for Selectivity among NO, CO, and O<sub>2</sub> by Heme Protein Sensors. *Biochemistry* **2012**, *51*, 172–186.
- (39) Tsai, A. L.; Martin, E.; Berka, V.; Olson, J. S. How Do Heme-Protein Sensors Exclude Oxygen? Lessons Learned from Cytochrome c’, *Nostoc punctiforme* Heme Nitric Oxide/Oxygen-Binding Domain, and Soluble Guanylyl Cyclase. *Antioxid. Redox Signaling* **2012**, *17*, 1246–1263.
- (40) Peterson, J. A.; Ishimura, Y.; Griffin, B. W. *Pseudomonas putida* Cytochrome P450: Characterization of an Oxygenated Form of the Hemoprotein. *Arch. Biochem. Biophys.* **1972**, *149*, 197–208.
- (41) Zangar, R. C.; Davydov, D. R.; Verma, S. Mechanisms That Regulate Production of Reactive Oxygen Species by Cytochrome P450. *Toxicol. Appl. Pharmacol.* **2004**, *199*, 316–331.
- (42) Grinstaff, M.; Hill, M.; Labinger, J.; Gray, H. Mechanism of Catalytic Oxygenation of Alkanes by Halogenated Iron Porphyrins. *Science* **1994**, *264*, 1311–1313.
- (43) Pauling, L.; Coryell, C. D. The Magnetic Properties and Structure of Hemoglobin, Oxyhemoglobin and Carbonmonoxyhemoglobin. *Proc. Natl. Acad. Sci. U. S. A.* **1936**, *22*, 210–216.
- (44) Pauling, L. Nature of the Iron-Oxygen Bond in Oxyhaemoglobin. *Nature* **1964**, *203*, 182–183.
- (45) Collman, J. P.; Gagne, R. R.; Reed, C. A.; Robinson, W. T.; Rodley, G. A. Structure of an Iron(II) Dioxygen Complex; A Model for Oxygen Carrying Hemoproteins. *Proc. Natl. Acad. Sci. U. S. A.* **1974**, *71*, 1326–1329.
- (46) Phillips, S. E. V. Structure and Refinement of Oxymyoglobin at 1.6 Å Resolution. *J. Mol. Biol.* **1980**, *142*, 531–554.
- (47) Shaanan, B. The Iron-Oxygen Bond in Human Oxyhaemoglobin. *Nature* **1982**, *296*, 683–684.
- (48) Berglund, G. I.; Carlsson, G. H.; Smith, A. T.; Szoke, H.; Henriksen, A.; Hajdu, J. The Catalytic Pathway of Horseradish Peroxidase at High Resolution. *Nature* **2002**, *417*, 463–468.
- (49) Schlichting, I.; Berendzen, J.; Chu, K.; Stock, A. M.; Maves, S. A.; Benson, D. E.; Sweet, R. M.; Ringe, D.; Petsko, G. A.; Sligar, S. G. The Catalytic Pathway of Cytochrome P450cam at Atomic Resolution. *Science* **2000**, *287*, 1615–1622.
- (50) Nagano, S.; Poulos, T. L. Crystallographic Study on the Dioxygen Complex of Wild-Type and Mutant Cytochrome P450cam. Implications for the Dioxygen Activation Mechanism. *J. Biol. Chem.* **2005**, *280*, 31659–31663.
- (51) Nagano, S.; Cupp-Vickery, J. R.; Poulos, T. L. Crystal Structures of the Ferrous Dioxygen Complex of Wild-Type Cytochrome P450eryF and Its Mutants, A245S and A245T: Investigation of the Proton Transfer System in p450eryF. *J. Biol. Chem.* **2005**, *280*, 22102–22107.
- (52) Vojtěchovský, J.; Chu, K.; Berendzen, J.; Sweet, R. M.; Schlichting, I. Crystal Structures of Myoglobin-Ligand Complexes at Near-Atomic Resolution. *Biophys. J.* **1999**, *77*, 2153–2174.
- (53) Chen, H.; Ikeda-Saito, M.; Shaik, S. Nature of the Fe–O<sub>2</sub> Bonding in Oxy-Myoglobin: Effect of the Protein. *J. Am. Chem. Soc.* **2008**, *130*, 14778–14790.
- (54) Bren, K. L.; Eisenberg, R.; Gray, H. B. Discovery of the Magnetic Behavior of Hemoglobin: a Beginning of Bioinorganic Chemistry. *Proc. Natl. Acad. Sci. U. S. A.* **2015**, *112*, 13123–13127.



- (55) Weiss, J. J. Nature of the Iron-Oxygen Bond in Oxyhaemoglobin. *Nature* **1964**, *202*, 83–84.
- (56) Goddard, W. A.; Olafson, B. D. Ozone Model for Bonding of an O<sub>2</sub> to Heme in Oxyhemoglobin. *Proc. Natl. Acad. Sci. U. S. A.* **1975**, *72*, 2335–2339.
- (57) McClure, D. S. Electronic Structure of Transition-Metal Complex Ions. *Radiat. Res., Suppl.* **1960**, *2*, 218–242.
- (58) Lang, G.; Marshali, W. Mössbauer Effect in Some Haemoglobin Compounds. *Proc. Phys. Soc., London* **1966**, *87*, 3–34.
- (59) Sharrock, M.; Debrunner, P. G.; Schulz, C.; Lipscomb, J. D.; Marshall, V.; Gunsalus, I. C. Cytochrome P450<sub>cam</sub> and Its Complexes, Mössbauer Parameters of the Heme Iron. *Biochim. Biophys. Acta, Protein Struct.* **1976**, *420*, 8–26.
- (60) Das, T. K.; Couture, M.; Ouellet, Y.; Guertin, M.; Rousseau, D. L. Simultaneous Observation of the O-O and Fe-O<sub>2</sub> Stretching Modes in Oxyhemoglobins. *Proc. Natl. Acad. Sci. U. S. A.* **2001**, *98*, 479–484.
- (61) Spiro, T. G.; Streckas, T. C. Resonance Raman Spectra of Heme Proteins. Effects of Oxidation and Spin State. *J. Am. Chem. Soc.* **1974**, *96*, 338–345.
- (62) Yamamoto, T.; Palmer, G.; Gill, D.; Salmeen, I. T.; Rimai, L. The Valence and Spin State of Iron in Oxyhemoglobin as Inferred from Resonance Raman Spectroscopy. *J. Biol. Chem.* **1973**, *248*, 5211–5213.
- (63) Wilson, S. A.; Green, E.; Mathews, I. I.; Benfatto, M.; Hodgson, K. O.; Hedman, B.; Sarangi, R. X-Ray Absorption Spectroscopic Investigation of the Electronic Structure Differences in Solution and Crystalline Oxyhemoglobin. *Proc. Natl. Acad. Sci. U. S. A.* **2013**, *110*, 16333–16338.
- (64) Wilson, S. A.; Kroll, T.; Decreau, R. A.; Hocking, R. K.; Lundberg, M.; Hedman, B.; Hodgson, K. O.; Solomon, E. I. Iron L-Edge X-ray Absorption Spectroscopy of Oxy-Picket Fence Porphyrin: Experimental Insight into Fe–O<sub>2</sub> Bonding. *J. Am. Chem. Soc.* **2013**, *135*, 1124–1136.
- (65) Chang, C. K.; Traylor, T. G. Proximal Base Influence on the Binding of Oxygen and Carbon Monoxide to Heme. *J. Am. Chem. Soc.* **1973**, *95*, 8477–8479.
- (66) Collman, J. P. Synthetic Models for the Oxygen-Binding Hemoproteins. *Acc. Chem. Res.* **1977**, *10*, 265–272.
- (67) Li, J.; Noll, B. C.; Oliver, A. G.; Schulz, C. E.; Scheidt, W. R. Correlated Ligand Dynamics in Oxyiron Picket Fence Porphyrins: Structural and Mössbauer Investigations. *J. Am. Chem. Soc.* **2013**, *135*, 15627–15641.
- (68) Anderson, J. S.; Gallagher, A. T.; Mason, J. A.; Harris, T. D. A Five-Coordinate Heme Dioxygen Adduct Isolated within a Metal–Organic Framework. *J. Am. Chem. Soc.* **2014**, *136*, 16489–16492.
- (69) Basolo, F.; Hoffman, B. M.; Ibers, J. A. Synthetic Oxygen Carriers of Biological Interest. *Acc. Chem. Res.* **1975**, *8*, 384–392.
- (70) Collman, J. P.; Brauman, J. I.; Doxsee, K. M.; Halbert, T. R.; Hayes, S. E.; Suslick, K. S. Oxygen Binding to Cobalt Porphyrins. *J. Am. Chem. Soc.* **1978**, *100*, 2761–2766.
- (71) Kitagawa, T.; Ondrias, M. R.; Rousseau, D. L.; IkedaSaito, M.; Yonetani, T. Evidence for Hydrogen-Bonding of Bound Dioxygen to the Distal Histidine of Oxy cobalt Myoglobin and Hemoglobin. *Nature* **1982**, *298*, 869–871.
- (72) Wang, M. Y. R.; Hoffman, B. M.; Shire, S. J.; Gurd, F. R. N. Oxygen Binding to Myoglobins and Their Cobalt Analogs. *J. Am. Chem. Soc.* **1979**, *101*, 7394–7397.
- (73) Brucker, E. A.; Olson, J. S.; Phillips, G. N.; Dou, Y.; IkedaSaito, M. High Resolution Crystal Structures of the Deoxy, Oxy, and Aquomet Forms of Cobalt Myoglobin. *J. Biol. Chem.* **1996**, *271*, 25419–25422.
- (74) Li, J.; Noll, B. C.; Oliver, A. G.; Scheidt, W. R. Structural Insights into Ligand Dynamics: Correlated Oxygen and Picket Motion in Oxy cobalt Picket Fence Porphyrins. *J. Am. Chem. Soc.* **2012**, *134*, 10595–10606.
- (75) Gallagher, A. T.; Kelty, M. L.; Park, J. G.; Anderson, J. S.; Mason, J. A.; Walsh, J. P. S.; Collins, S. L.; Harris, T. D. Dioxygen Binding at a Four-Coordinate Cobaltous Porphyrin Site in a Metal–Organic Framework: Structural, EPR, and O<sub>2</sub> Adsorption Analysis. *Inorg. Chem. Front.* **2016**, *3*, 536–540.
- (76) Friesen, B. A.; Bhattarai, A.; Mazur, U.; Hipps, K. W. Single Molecule Imaging of Oxygenation of Cobalt Octaethylporphyrin at the Solution/Solid Interface: Thermodynamics from Microscopy. *J. Am. Chem. Soc.* **2012**, *134*, 14897–14904.
- (77) Weschler, C. J.; Hoffman, B. M.; Basolo, F. Synthetic Oxygen Carrier. Dioxygen Adduct of a Manganese Porphyrin. *J. Am. Chem. Soc.* **1975**, *97*, 5278–5280.
- (78) Gonzalez, B.; Kouba, J.; Yee, S.; Reed, C. A.; Kirner, J. F.; Scheidt, W. R. Manganese(II) Porphyrins - Synthesis, Structures, and Preference for 5-Coordination. *J. Am. Chem. Soc.* **1975**, *97*, 3247–3249.
- (79) Reed, C. A.; Kouba, J. K.; Grimes, C. J.; Cheung, S. K. Manganese(II) and Chromium(II) Porphyrin Complexes - Synthesis and Characterization. *Inorg. Chem.* **1978**, *17*, 2666–2670.
- (80) Hoffman, B. M.; Weschler, C. J.; Basolo, F. The Dioxygen Adduct of *Meso*-Tetraphenylporphyrinmanganese(II), a Synthetic Oxygen Carrier. *J. Am. Chem. Soc.* **1976**, *98*, 5473–5482.
- (81) Hoffman, B. M.; Szymanski, T.; Brown, T. G.; Basolo, F. Dioxygen Adducts of Several Manganese(II) Porphyrins - Electron-Paramagnetic Resonance Studies. *J. Am. Chem. Soc.* **1978**, *100*, 7253–7259.
- (82) Watanabe, T.; Ama, T.; Nakamoto, K. Matrix-Isolation Infrared-Spectra of (Octaethylporphyrinato)Manganese(II) and (Phthalocyaninato)Manganese(II) and Their Dioxygen Adducts. *Inorg. Chem.* **1983**, *22*, 2470–2472.
- (83) Collman, J. P.; Brauman, J. I.; Fitzgerald, J. P.; Sparapan, J. W.; Ibers, J. A. Reversible Binding of Dinitrogen and Dioxygen by a Ruthenium Picket-Fence Porphyrin. *J. Am. Chem. Soc.* **1988**, *110*, 3486–3495.
- (84) Paulson, D. R.; Addison, A. W.; Dolphin, D.; James, B. R. Preparation of Ruthenium(II) and Ruthenium(III) Myoglobin and the Reaction of Dioxygen, and Carbon Monoxide, with Ruthenium(II) Myoglobin. *J. Biol. Chem.* **1979**, *254*, 7002–7006.
- (85) Farrell, N.; Dolphin, D. H.; James, B. R. Reversible Binding of Dioxygen to Ruthenium(II) Porphyrins. *J. Am. Chem. Soc.* **1978**, *100*, 324–326.
- (86) Cheung, S. K.; Grimes, C. J.; Wong, J.; Reed, C. A. Chromium(II) Porphyrins and an Irreversible Dioxygen Complex. *J. Am. Chem. Soc.* **1976**, *98*, 5028–5030.
- (87) Blumenfeld, L. A.; Davydov, R. M.; Fel, N. S.; Magonov, S. N.; Vilu, R. O. Studies on Conformational-Changes of Metalloproteins Induced by Electrons in Water-Ethylene Glycol Solutions at Low-Temperatures - Cytochrome *c*. *FEBS Lett.* **1974**, *45*, 256–258.
- (88) Blumenfeld, L. A.; Davydov, R. M.; Magonov, S. N.; Vilu, R. O. Studies on Conformational-Changes of Metalloproteins Induced by Electrons in Water-Ethylene-Glycol Solutions at Low-Temperatures - Hemoglobin. *FEBS Lett.* **1974**, *49*, 246–248.
- (89) Symons, M. C. R.; Petersen, R. L. Electron Capture at the Iron-Oxygen Centre in Single Crystals of Oxy myoglobin Studied by Electron Spin Resonance Spectroscopy. *Biochim. Biophys. Acta, Protein Struct.* **1978**, *535*, 241–246.
- (90) Denisov, I. G.; Makris, T. M.; Sligar, S. G. In *Cytochrome P450, Part C*; Johnson, E. F., Waterman, M. R., Eds.; Elsevier Academic Press: San Diego, 2002; Vol. 357.
- (91) Davydov, R.; Hoffman, B. M. Active Intermediates in Heme Monooxygenase Reactions as Revealed by Cryoreduction/Annealing, EPR/ENDOR Studies. *Arch. Biochem. Biophys.* **2011**, *507*, 36–43.
- (92) Denisov, I. G.; Sligar, S. G. In *Cytochrome P450: Structure, Mechanism, and Biochemistry*; Ortiz de Montellano, P. R., Ed.; Springer International Publishing: Cham, 2015.
- (93) Davydov, R.; Chemerisov, S.; Werst, D. E.; Rajh, T.; Matsui, T.; Ikeda-Saito, M.; Hoffman, B. M. Proton Transfer at Helium Temperatures During Dioxygen Activation by Heme Monooxygenases. *J. Am. Chem. Soc.* **2004**, *126*, 15960–15961.
- (94) Davydov, R.; Makris, T. M.; Kofman, V.; Werst, D. E.; Sligar, S. G.; Hoffman, B. M. Hydroxylation of Camphor By-Reduced Oxy-Cytochrome P450<sub>cam</sub>: Mechanistic Implications of EPR and ENDOR

Studies of Catalytic Intermediates in Native and Mutant Enzymes. *J. Am. Chem. Soc.* **2001**, *123*, 1403–1415.

(95) Denisov, I. G.; Makris, T. M.; Sligar, S. G. Formation and Decay of Hydroperoxo-Ferric Heme Complex in Horseradish Peroxidase Studied by Cryoradiolysis. *J. Biol. Chem.* **2002**, *277*, 42706–42710.

(96) Mak, P. J.; Thammawichai, W.; Wiedenhoeft, D.; Kincaid, J. R. Resonance Raman Spectroscopy Reveals pH-Dependent Active Site Structural Changes of Lactoperoxidase Compound 0 and Its Ferryl Heme O–O Bond Cleavage Products. *J. Am. Chem. Soc.* **2015**, *137*, 349–361.

(97) Kuhnle, K.; Derat, E.; Terner, J.; Shaik, S.; Schlichting, I. Structure and Quantum Chemical Characterization of Chloroperoxidase Compound 0, a Common Reaction Intermediate of Diverse Heme Enzymes. *Proc. Natl. Acad. Sci. U. S. A.* **2007**, *104*, 99–104.

(98) Unno, M.; Chen, H.; Kusama, S.; Shaik, S.; Ikeda-Saito, M. Structural Characterization of the Fleeting Ferric Peroxo Species in Myoglobin: Experiment and Theory. *J. Am. Chem. Soc.* **2007**, *129*, 13394–13395.

(99) Hersleth, H. P.; Hsiao, Y. W.; Ryde, U.; Gorbitz, C. H.; Andersson, K. K. The Crystal Structure of Peroxymyoglobin Generated Through Cryoradiolytic Reduction of Myoglobin Compound Iii During Data Collection. *Biochem. J.* **2008**, *412*, 257–264.

(100) Burstyn, J. N.; Roe, J. A.; Mikszal, A. R.; Shaevitz, B. A.; Lang, G.; Valentine, J. S. Magnetic and Spectroscopic Characterization of an Iron Porphyrin Peroxide Complex - Peroxoferri-octaethylporphyrin(1-). *J. Am. Chem. Soc.* **1988**, *110*, 1382–1388.

(101) McCandlish, E.; Mikszal, A. R.; Nappa, M.; Sprenger, A. Q.; Valentine, J. S.; Stong, J. D.; Spiro, T. G. Reactions of Superoxide with Iron Porphyrins in Aprotic Solvents. a High Spin Ferric Porphyrin Peroxo Complex. *J. Am. Chem. Soc.* **1980**, *102*, 4268–4271.

(102) Welborn, C. H.; Dolphin, D.; James, B. R. One-Electron Electrochemical Reduction of a Ferrous Porphyrin Dioxigen Complex. *J. Am. Chem. Soc.* **1981**, *103*, 2869–2871.

(103) Tajima, K. A Possible Model of a Hemoprotein Hydrogen-Peroxide Complex. *Inorg. Chim. Acta* **1989**, *163*, 115–122.

(104) Tajima, K.; Shigematsu, M.; Jinno, J.; Ishizu, K.; Ohyanishiguchi, H. Generation of Fe(III)OEP-Hydrogen Peroxide Complex (OEP = Octaethylporphyrinato) by Reduction of Fe(II)-OEP-O<sub>2</sub> with Ascorbic Acid Sodium Salt. *J. Chem. Soc., Chem. Commun.* **1990**, 144–145.

(105) Tajima, K.; Oka, S.; Edo, T.; Miyake, S.; Mano, H.; Mukai, K.; Sakurai, H.; Ishizu, K. Optical-Absorption and Epr Studies on a 6-Coordinate Iron(III)-Tetramesitylporphyrin-Hydrogen Peroxide Complex Having a Nitrogenous Axial Ligand. *J. Chem. Soc., Chem. Commun.* **1995**, 0, 1507–1508.

(106) Liu, J. G.; Ohta, T.; Yamaguchi, S.; Ogura, T.; Sakamoto, S.; Maeda, Y.; Naruta, Y. Spectroscopic Characterization of a Hydroperoxo-Heme Intermediate: Conversion of a Side-On Peroxo to an End-On Hydroperoxo Complex. *Angew. Chem., Int. Ed.* **2009**, *48*, 9262–9267.

(107) de Visser, S. P.; Valentine, J. S.; Nam, W. A Biomimetic Ferric Hydroperoxo Porphyrin Intermediate. *Angew. Chem., Int. Ed.* **2010**, *49*, 2099–2101.

(108) Garcia-Serres, R.; Davydov, R. M.; Matsui, T.; Ikeda-Saito, M.; Hoffman, B. M.; Huynh, B. H. Distinct Reaction Pathways Followed upon Reduction of Oxy-Heme Oxygenase and Oxy-Myoglobin as Characterized by Mössbauer Spectroscopy. *J. Am. Chem. Soc.* **2007**, *129*, 1402–1412.

(109) Liu, J. G.; Shimizu, Y.; Ohta, T.; Naruta, Y. Formation of an End-On Ferric Peroxo Intermediate upon One-Electron Reduction of a Ferric Superoxo Heme. *J. Am. Chem. Soc.* **2010**, *132*, 3672–3673.

(110) Nagaraju, P.; Ohta, T.; Liu, J.-G.; Ogura, T.; Naruta, Y. The Secondary Coordination Sphere Controlled Reactivity of a Ferric-Superoxo Heme: Unexpected Conversion to a Ferric Hydroperoxo Intermediate by Reaction with a High-Spin Ferrous Heme. *Chem. Commun.* **2016**, *52*, 7213–7216.

(111) Sengupta, K.; Chatterjee, S.; Dey, A. Catalytic H<sub>2</sub>O<sub>2</sub> Disproportionation and Electrocatalytic O<sub>2</sub> Reduction by a Functional

Mimic of Heme Catalase: Direct Observation of Compound 0 and Compound I in Situ. *ACS Catal.* **2016**, *6*, 1382–1388.

(112) Oliveira, R.; Zouari, W.; Herrero, C.; Banse, F.; Schöllhorn, B.; Fave, C.; Anxolabéhère-Mallart, E. Characterization and Subsequent Reactivity of an Fe-Peroxo Porphyrin Generated by Electrochemical Reductive Activation of O<sub>2</sub>. *Inorg. Chem.* **2016**, *55*, 12204–12210.

(113) Costentin, C.; Dridi, H.; Savéant, J.-M. Molecular Catalysis of O<sub>2</sub> Reduction by Iron Porphyrins in Water: Heterogeneous versus Homogeneous Pathways. *J. Am. Chem. Soc.* **2015**, *137*, 13535–13544.

(114) Sengupta, K.; Chatterjee, S.; Samanta, S.; Dey, A. Direct Observation of Intermediates Formed During Steady-State Electrocatalytic O<sub>2</sub> Reduction by Iron Porphyrins. *Proc. Natl. Acad. Sci. U. S. A.* **2013**, *110*, 8431–8436.

(115) Keilin, D.; Mann, T. On the Haematin Compound of Peroxidase. *Proc. R. Soc. London, Ser. B* **1937**, *122*, 119–133.

(116) Theorell, H. Crystalline Peroxidase. *Enzymologia* **1942**, *10*, 250–252.

(117) Stern, K. G. On the Mechanism of Enzyme Action: A study of the Decomposition of Monoethyl Hydrogen Peroxide by Catalase and of an Intermediate Enzyme Substrate Compound. *J. Biol. Chem.* **1936**, *114*, 473–494.

(118) Chance, B.; Rosted, C. O.; Sillén, L. G.; Linnasalmi, A.; Laukkanen, P. An Intermediate Compound in the Catalase-Hydrogen Peroxide Reaction. *Acta Chem. Scand.* **1947**, *1*, 236–267.

(119) Nicholls, P. Classical Catalase: Ancient and Modern. *Arch. Biochem. Biophys.* **2012**, *525*, 95–101.

(120) Jones, P.; Dunford, H. B. On the Mechanism of Compound I Formation from Peroxidases and Catalases. *J. Theor. Biol.* **1977**, *69*, 457–470.

(121) Baek, H. K.; Van Wart, H. E. Elementary Steps in the Formation of Horseradish Peroxidase Compound I: Direct Observation of Compound 0, a New Intermediate with a Hyperporphyrin Spectrum. *Biochemistry* **1989**, *28*, 5714–5719.

(122) Dunford, H. B.; Stillman, J. S. On the Function and Mechanism of Action of Peroxidases. *Coord. Chem. Rev.* **1976**, *19*, 187–251.

(123) Jones, P.; Dunford, H. B. The Mechanism of Compound I Formation Revisited. *J. Inorg. Biochem.* **2005**, *99*, 2292–2298.

(124) Poulos, T. L.; Kraut, J. The Stereochemistry of Peroxidase Catalysis. *J. Biol. Chem.* **1980**, *255*, 8199–8205.

(125) Poulos, T. L.; Freer, S. T.; Alden, R. A.; Edwards, S. L.; Skoglund, U.; Takio, K.; Eriksson, B.; Xuong, N.; Yonetani, T.; Kraut, J. The Crystal Structure of Cytochrome *c* Peroxidase. *J. Biol. Chem.* **1980**, *255*, 575–580.

(126) Casadei, C. M.; Gumiero, A.; Metcalfe, C. L.; Murphy, E. J.; Basran, J.; Concilio, M. G.; Teixeira, S. C. M.; Schrader, T. E.; Fielding, A. J.; Ostermann, A.; et al. Neutron Cryo-Crystallography Captures the Protonation State of Ferryl Heme in a Peroxidase. *Science* **2014**, *345*, 193–197.

(127) Groves, J. T.; Boaz, N. C. Fishing for Peroxidase Protons. *Science* **2014**, *345*, 142–143.

(128) Dawson, J. Probing Structure-Function Relations in Heme-Containing Oxygenases and Peroxidases. *Science* **1988**, *240*, 433–439.

(129) Usharani, D.; Zazza, C.; Lai, W.; Chourasia, M.; Waskell, L.; Shaik, S. A Single-Site Mutation (F429H) Converts the Enzyme CYP 2B4 into a Heme Oxygenase: A QM/MM Study. *J. Am. Chem. Soc.* **2012**, *134*, 4053–4056.

(130) Dawson, J. H.; Sono, M. Cytochrome P450 and Chloroperoxidase: Thiolate-Ligated Heme Enzymes. Spectroscopic Determination of Their Active-Site Structures and Mechanistic Implications of Thiolate Ligation. *Chem. Rev.* **1987**, *87*, 1255–1276.

(131) Fita, I.; Rossmann, M. G. The Active Center of Catalase. *J. Mol. Biol.* **1985**, *185*, 21–37.

(132) Sundaramoorthy, M.; Terner, J.; Poulos, T. L. The Crystal Structure of Chloroperoxidase: a Heme Peroxidase–Cytochrome P450 Functional Hybrid. *Structure* **1995**, *3*, 1367–1378.

(133) Yi, X.; Conesa, A.; Punt, P. J.; Hager, L. P. Examining the Role of Glutamic Acid 183 in Chloroperoxidase Catalysis. *J. Biol. Chem.* **2003**, *278*, 13855–13859.

- (134) Piontek, K.; Strittmatter, E.; Ullrich, R.; Grobe, G.; Pecyna, M. J.; Kluge, M.; Scheibner, K.; Hofrichter, M.; Plattner, D. A. Structural Basis of Substrate Conversion in a New Aromatic Peroxygenase: Cytochrome P450 Functionality with Benefits. *J. Biol. Chem.* **2013**, *288*, 34767–34776.
- (135) Lee, D. S.; Yamada, A.; Sugimoto, H.; Matsunaga, I.; Ogura, H.; Ichihara, K.; Adachi, S.; Park, S. Y.; Shiro, Y. Substrate Recognition and Molecular Mechanism of Fatty Acid Hydroxylation by Cytochrome P450 from *Bacillus Subtilis*. Crystallographic, Spectroscopic, and Mutational Studies. *J. Biol. Chem.* **2003**, *278*, 9761–9767.
- (136) Belcher, J.; McLean, K. J.; Matthews, S.; Woodward, L. S.; Fisher, K.; Rigby, S. E. J.; Nelson, D. R.; Potts, D.; Baynham, M. T.; Parker, D. A.; et al. Structure and Biochemical Properties of the Alkene Producing Cytochrome P450 OleTJE (CYP152L1) from the *Jeotgalicoccus* sp. 8456 Bacterium. *J. Biol. Chem.* **2014**, *289*, 6535–6550.
- (137) Wang, B.; Li, C.; Dubey, K. D.; Shaik, S. Quantum Mechanical/Molecular Mechanical Calculated Reactivity Networks Reveal How Cytochrome P450cam and Its T252A Mutant Select Their Oxidation Pathways. *J. Am. Chem. Soc.* **2015**, *137*, 7379–7390.
- (138) Cho, K.-B.; Derat, E.; Shaik, S. Compound I of Nitric Oxide Synthase: The Active Site Protonation State. *J. Am. Chem. Soc.* **2007**, *129*, 3182–3188.
- (139) Ramanan, R.; Dubey, K. D.; Wang, B.; Mandal, D.; Shaik, S. Emergence of Function in P450-Proteins: A Combined Quantum Mechanical/Molecular Mechanical and Molecular Dynamics Study of the Reactive Species in the H<sub>2</sub>O<sub>2</sub>-Dependent Cytochrome P450<sub>SPZ</sub> and Its Regio- and Enantioselective Hydroxylation of Fatty Acids. *J. Am. Chem. Soc.* **2016**, *138*, 6786–6797.
- (140) Shoji, O.; Watanabe, Y. Peroxygenase Reactions Catalyzed by Cytochromes P450. *JBC, J. Biol. Inorg. Chem.* **2014**, *19*, 529–539.
- (141) Shoji, O.; Fujishiro, T.; Nakajima, H.; Kim, M.; Nagano, S.; Shiro, Y.; Watanabe, Y. Hydrogen Peroxide Dependent Monooxygenations by Tricking the Substrate Recognition of Cytochrome P450<sub>BSβ</sub>. *Angew. Chem., Int. Ed.* **2007**, *46*, 3656–3659.
- (142) Kumar, D.; Altun, A.; Shaik, S.; Thiel, W. Water as Biocatalyst in Cytochrome P450. *Faraday Discuss.* **2011**, *148*, 373–383.
- (143) Li, Q.-S.; Ogawa, J.; Schmid, R. D.; Shimizu, S. Engineering Cytochrome P450 BM3 for Oxidation of Polycyclic Aromatic Hydrocarbons. *Appl. Environ. Microbiol.* **2001**, *67*, 5735–5739.
- (144) Cirino, P. C.; Arnold, F. H. A Self-Sufficient Peroxide-Driven Hydroxylation Biocatalyst. *Angew. Chem., Int. Ed.* **2003**, *42*, 3299–3301.
- (145) Li, Q. S.; Ogawa, J.; Shimizu, S. Critical Role of the Residue Size at Position 87 in H<sub>2</sub>O<sub>2</sub>-Dependent Substrate Hydroxylation Activity and H<sub>2</sub>O<sub>2</sub> Inactivation of Cytochrome P450<sub>BM3</sub>. *Biochem. Biophys. Res. Commun.* **2001**, *280*, 1258–1261.
- (146) Shoji, O.; Fujishiro, T.; Nishio, K.; Kano, Y.; Kimoto, H.; Chien, S.-C.; Onoda, H.; Muramatsu, A.; Tanaka, S.; Hori, A.; et al. A Substrate-Binding-State Mimic of H<sub>2</sub>O<sub>2</sub>-Dependent Cytochrome P450 Produced by One-Point Mutagenesis and Peroxygenation of Non-Native Substrates. *Catal. Sci. Technol.* **2016**, *6*, 5806–5811.
- (147) Traylor, T. G.; Lee, W. A.; Stynes, D. V. Model Compound Studies Related to Peroxidases. Mechanisms of Reactions of Hemins with Peracids. *J. Am. Chem. Soc.* **1984**, *106*, 755–764.
- (148) Lee, W. A.; Bruice, T. C. Homolytic and Heterolytic Oxygen-Oxygen Bond Scissions Accompanying Oxygen Transfer to Iron(III) Porphyrins by Pericarboxylic Acids and Hydroperoxides. A Mechanistic Criterion for Peroxidase and Cytochrome P-450. *J. Am. Chem. Soc.* **1985**, *107*, 513–514.
- (149) Groves, J. T.; Watanabe, Y. Oxygen Activation by Metalloporphyrins Related to Peroxidase and Cytochrome P450. Direct Observation of the Oxygen-Oxygen Bond Cleavage Step. *J. Am. Chem. Soc.* **1986**, *108*, 7834–7836.
- (150) Traylor, T. G.; Xu, F. A Biomimetic Model for Catalase: the Mechanisms of Reaction of Hydrogen Peroxide and Hydroperoxides with Iron(III) Porphyrins. *J. Am. Chem. Soc.* **1987**, *109*, 6201–6202.
- (151) Groves, J. T.; Watanabe, Y. Reactive Iron Porphyrin Derivatives Related to the Catalytic Cycles of Cytochrome P450 and Peroxidase. Studies of the Mechanism of Oxygen Activation. *J. Am. Chem. Soc.* **1988**, *110*, 8443–8452.
- (152) Yamaguchi, K.; Watanabe, Y.; Morishima, I. Direct Observation of the Push Effect on the Oxygen-Oxygen Bond Cleavage of Acylperoxoiron(III) Porphyrin Complexes. *J. Am. Chem. Soc.* **1993**, *115*, 4058–4065.
- (153) Hessenauer-Ilicheva, N.; Franke, A.; Meyer, D.; Woggon, W.-D.; van Eldik, R. Low-Temperature Rapid-Scan Detection of Reactive Intermediates in Epoxidation Reactions Catalyzed by a New Enzyme Mimic of Cytochrome P450. *J. Am. Chem. Soc.* **2007**, *129*, 12473–12479.
- (154) Seo, M. S.; Kamachi, T.; Kouno, T.; Murata, K.; Park, M. J.; Yoshizawa, K.; Nam, W. Experimental and Theoretical Evidence for Nonheme Iron(III) Alkylperoxo Species as Sluggish Oxidants in Oxygenation Reactions. *Angew. Chem., Int. Ed.* **2007**, *46*, 2291–2294.
- (155) Soper, J. D.; Kryatov, S. V.; Rybak-Akimova, E. V.; Nocera, D. G. Proton-Directed Redox Control of O–O Bond Activation by Heme Hydroperoxidase Models. *J. Am. Chem. Soc.* **2007**, *129*, 5069–5075.
- (156) Franke, A.; Fertinger, C.; van Eldik, R. Which Oxidant Is Really Responsible for P450 Model Oxygenation Reactions? A Kinetic Approach. *Angew. Chem., Int. Ed.* **2008**, *47*, 5238–5242.
- (157) Han, A.-R.; Jin Jeong, Y.; Kang, Y.; Yoon Lee, J.; Sook Seo, M.; Nam, W. Direct Evidence for an Iron(IV)-Oxo Porphyrin  $\pi$ -Cation Radical as an Active Oxidant in Catalytic Oxygenation Reactions. *Chem. Commun.* **2008**, 1076–1078.
- (158) Fertinger, C.; Hessenauer-Ilicheva, N.; Franke, A.; van Eldik, R. Direct Comparison of the Reactivity of Model Complexes for Compounds 0, I, and II in Oxygenation, Hydrogen-Abstraction, and Hydride-Transfer Processes. *Chem. - Eur. J.* **2009**, *15*, 13435–13440.
- (159) Nam, W.; Choi, H. J.; Han, H. J.; Cho, S. H.; Lee, H. J.; Han, S.-Y. Use of 2-Methyl-1-Phenylpropan-2-yl Hydroperoxide (Mpph) as a Mechanistic Probe for the Heterolytic Versus Homolytic O–O Bond Cleavage of Tert-Alkyl Hydroperoxide by Iron(III) Porphyrin Complex. *Chem. Commun.* **1999**, 387–388.
- (160) Almarsson, O.; Bruice, T. C. A Homolytic Mechanism of O–O Bond Scission Prevails in the Reactions of Alkyl Hydroperoxides with an Octacationic Tetraphenylporphyrinato-Iron(III) Complex in Aqueous Solution. *J. Am. Chem. Soc.* **1995**, *117*, 4533–4544.
- (161) Nam, W.; Goh, Y. M.; Lee, Y. J.; Lim, M. H.; Kim, C. Biomimetic Alkane Hydroxylations by an Iron(III) Porphyrin Complex with H<sub>2</sub>O<sub>2</sub> and by a High-Valent Iron(IV) Oxo Porphyrin Cation Radical Complex. *Inorg. Chem.* **1999**, *38*, 3238–3240.
- (162) Nam, W.; Lim, M. H.; Oh, S. Y.; Lee, J. H.; Lee, H. J.; Woo, S. K.; Kim, C.; Shin, W. Remarkable Anionic Axial Ligand Effects of Iron(III) Porphyrin Complexes on the Catalytic Oxygenations of Hydrocarbons by H<sub>2</sub>O<sub>2</sub> and the Formation of Oxoiron(IV) Porphyrin Intermediates by M-Chloroperoxybenzoic Acid. *Angew. Chem., Int. Ed.* **2000**, *39*, 3646–3649.
- (163) Yang, S. J.; Nam, W. Water-Soluble Iron Porphyrin Complex-Catalyzed Epoxidation of Olefins with Hydrogen Peroxide and tert-Butyl Hydroperoxide in Aqueous Solution. *Inorg. Chem.* **1998**, *37*, 606–607.
- (164) Traylor, T. G.; Kim, C.; Richards, J. L.; Xu, F.; Perrin, C. L. Reactions of Iron(III) Porphyrins with Oxidants. Structure-Reactivity Studies. *J. Am. Chem. Soc.* **1995**, *117*, 3468–3474.
- (165) Traylor, T. G.; Xu, F. Mechanisms of Reactions of Iron(III) Porphyrins with Hydrogen Peroxide and Hydroperoxides: Solvent and Solvent Isotope Effects. *J. Am. Chem. Soc.* **1990**, *112*, 178–186.
- (166) Brausam, A.; Eigler, S.; Jux, N.; van Eldik, R. Mechanistic Investigations of the Reaction of an Iron(III) Octa-Anionic Porphyrin Complex with Hydrogen Peroxide and the Catalyzed Oxidation of Diammonium-2,2'-azinobis(3-ethylbenzothiazoline-6-sulfonate). *Inorg. Chem.* **2009**, *48*, 7667–7678.
- (167) Franke, A.; Fertinger, C.; van Eldik, R. Axial Ligand and Spin-State Influence on the Formation and Reactivity of Hydroperoxo-Iron(III) Porphyrin Complexes. *Chem. - Eur. J.* **2012**, *18*, 6935–6949.
- (168) Groves, J. T.; Watanabe, Y.; McMurry, T. J. Oxygen Activation by Metalloporphyrins. Formation and Decomposition of an

Acylperoxymanganese(III) Complex. *J. Am. Chem. Soc.* **1983**, *105*, 4489–4490.

(169) Schappacher, M.; Weiss, R. Formation of Manganese(IV)-Oxo-Porphyrin Derivatives by Decomposition of Peroxycarbonate Complexes. *Inorg. Chem.* **1987**, *26*, 1189–1190.

(170) Yuan, L. C.; Bruice, T. C. Influence of Nitrogen Base Ligation and Hydrogen Bonding on the Rate Constants for Oxygen Transfer from Peroxycarboxylic Acids and Alkyl Hydroperoxides to (meso-Tetraphenylporphyrinato)Manganese(III) Chloride. *J. Am. Chem. Soc.* **1986**, *108*, 1643–1650.

(171) Jin, N.; Lahaye, D. E.; Groves, J. T. A "Push-Pull" Mechanism for Heterolytic O-O Bond Cleavage in Hydroperoxo Manganese Porphyrins. *Inorg. Chem.* **2010**, *49*, 11516–11524.

(172) Schulz, C. E.; Devaney, P. W.; Winkler, H.; Debrunner, P. G.; Doan, N.; Chiang, R.; Rutter, R.; Hager, L. P. Horseradish Peroxidase Compound I: Evidence for Spin Coupling Between the Heme Iron and a 'Free' Radical. *FEBS Lett.* **1979**, *103*, 102–105.

(173) Schulz, C. E.; Rutter, R.; Sage, J. T.; Debrunner, P. G.; Hager, L. P. Mössbauer and Electron Paramagnetic Resonance Studies of Horseradish Peroxidase and Its Catalytic Intermediates. *Biochemistry* **1984**, *23*, 4743–4754.

(174) Khindaria, A.; Aust, S. D. EPR Detection and Characterization of Lignin Peroxidase Porphyrin  $\pi$ -Cation Radical. *Biochemistry* **1996**, *35*, 13107–13111.

(175) Patterson, W. R.; Poulos, T. L.; Goodin, D. B. Identification of a Porphyrin  $\pi$ -Cation Radical in Ascorbate Peroxidase Compound I. *Biochemistry* **1995**, *34*, 4342–4345.

(176) Benecky, M. J.; Frew, J. E.; Scowen, N.; Jones, P.; Hoffman, B. M. EPR and Endor Detection of Compound I from *Micrococcus lysodeikticus* Catalase. *Biochemistry* **1993**, *32*, 11929–11933.

(177) Green, M. T. The Structure and Spin Coupling of Catalase Compound I: A Study of Noncovalent Effects. *J. Am. Chem. Soc.* **2001**, *123*, 9218–9219.

(178) Green, M. T. Imidazole-Ligated Compound I Intermediates: The Effects of Hydrogen Bonding. *J. Am. Chem. Soc.* **2000**, *122*, 9495–9499.

(179) Rutter, R.; Hager, L. P.; Dhonau, H.; Hendrich, M.; Valentine, M.; Debrunner, P. Chloroperoxidase Compound I: Electron Paramagnetic Resonance and Mössbauer Studies. *Biochemistry* **1984**, *23*, 6809–6816.

(180) Yosca, T. H.; Green, M. T. Preparation of Compound I in P450<sub>cam</sub>: The Prototypical P450. *Isr. J. Chem.* **2016**, *56*, 834–840.

(181) Krest, C. M.; Silakov, A.; Rittle, J.; Yosca, T. H.; Onderko, E. L.; Calixto, J. C.; Green, M. T. Significantly Shorter Fe-S Bond in Cytochrome p450-I Is Consistent with Greater Reactivity Relative to Chloroperoxidase. *Nat. Chem.* **2015**, *7*, 696–702.

(182) Rittle, J.; Green, M. T. Cytochrome P450 Compound I: Capture, Characterization, and C-H Bond Activation Kinetics. *Science* **2010**, *330*, 933–937.

(183) Coulson, A. F.; Yonetani, T. Oxidation of Cytochrome *c* Peroxidase with Hydrogen Peroxide: Identification of the "Endogenous Donor". *Biochem. Biophys. Res. Commun.* **1972**, *49*, 391–398.

(184) Sivaraja, M.; Goodin, D.; Smith, M.; Hoffman, B. Identification by Endor of trp191 as the Free-Radical Site in Cytochrome *c* Peroxidase Compound Es. *Science* **1989**, *245*, 738–740.

(185) Dolphin, D.; Forman, A.; Borg, D. C.; Fajer, J.; Felton, R. H. Compounds I of Catalase and Horse Radish Peroxidase:  $\pi$ -Cation Radicals. *Proc. Natl. Acad. Sci. U. S. A.* **1971**, *68*, 614–618.

(186) Palcic, M. M.; Rutter, R.; Araisio, T.; Hager, L. P.; Dunford, H. B. Spectrum of Chloroperoxidase Compound I. *Biochem. Biophys. Res. Commun.* **1980**, *94*, 1123–1127.

(187) Chance, B.; Powers, L.; Ching, Y.; Poulos, T.; Schonbaum, G. R.; Yamazaki, I.; Paul, K. G. X-Ray Absorption Studies of Intermediates in Peroxidase Activity. *Arch. Biochem. Biophys.* **1984**, *235*, 596–611.

(188) Groves, J. T.; Vanderpuy, M. Stereospecific Aliphatic Hydroxylation by Iron-Hydrogen Peroxide - Evidence for a Stepwise Process. *J. Am. Chem. Soc.* **1976**, *98*, 5290–5297.

(189) Groves, J. T.; McClusky, G. A.; White, R. E.; Coon, M. J. Aliphatic Hydroxylation by Highly Purified Liver Microsomal Cytochrome P450. Evidence for a Carbon Radical Intermediate. *Biochem. Biophys. Res. Commun.* **1978**, *81*, 154–160.

(190) Groves, J. T.; McClusky, G. A. Aliphatic Hydroxylation via Oxygen Rebound. Oxygen Transfer Catalyzed by Iron. *J. Am. Chem. Soc.* **1976**, *98*, 859–861.

(191) Egawa, T.; Shimada, H.; Ishimura, Y. Evidence for Compound I Formation in the Reaction of Cytochrome-P450<sub>cam</sub> with *m*-Chloroperbenzoic Acid. *Biochem. Biophys. Res. Commun.* **1994**, *201*, 1464–1469.

(192) Spolitak, T.; Dawson, J. H.; Ballou, D. P. Reaction of Ferric Cytochrome p450<sub>cam</sub> with Peracids: Kinetic Characterization of Intermediates on the Reaction Pathway. *J. Biol. Chem.* **2005**, *280*, 20300–20309.

(193) Kellner, D. G.; Hung, S.-C.; Weiss, K. E.; Sligar, S. G. Kinetic Characterization of Compound I Formation in the Thermostable Cytochrome P450 CYP119. *J. Biol. Chem.* **2002**, *277*, 9641–9644.

(194) van Rantwijk, F.; Sheldon, R. A. Selective Oxygen Transfer Catalysed by Heme Peroxidases: Synthetic and Mechanistic Aspects. *Curr. Opin. Biotechnol.* **2000**, *11*, 554–564.

(195) Chandrasena, R. E. P.; Vatsis, K. P.; Coon, M. J.; Hollenberg, P. F.; Newcomb, M. Hydroxylation by the Hydroperoxy-Iron Species in Cytochrome P450 Enzymes. *J. Am. Chem. Soc.* **2004**, *126*, 115–126.

(196) Newcomb, M.; Aebischer, D.; Shen, R. N.; Chandrasena, R. E. P.; Hollenberg, P. F.; Coon, M. J. Kinetic Isotope Effects Implicate Two Electrophilic Oxidants in Cytochrome P450-Catalyzed Hydroxylations. *J. Am. Chem. Soc.* **2003**, *125*, 6064–6065.

(197) Wang, Q.; Sheng, X.; Horner, J. H.; Newcomb, M. Quantitative Production of Compound I from a Cytochrome P450 Enzyme at Low Temperatures. Kinetics, Activation Parameters, and Kinetic Isotope Effects for Oxidation of Benzyl Alcohol. *J. Am. Chem. Soc.* **2009**, *131*, 10629–10636.

(198) Hofrichter, M.; Ullrich, R. Oxidations Catalyzed by Fungal Peroxygenases. *Curr. Opin. Chem. Biol.* **2014**, *19*, 116–125.

(199) Peter, S.; Kinne, M.; Wang, X.; Ullrich, R.; Kayser, G.; Groves, J. T.; Hofrichter, M. Selective Hydroxylation of Alkanes by an Extracellular Fungal Peroxygenase. *FEBS J.* **2011**, *278*, 3667–3675.

(200) Wang, X. S.; Peter, S.; Kinne, M.; Hofrichter, M.; Groves, J. T. Detection and Kinetic Characterization of a Highly Reactive Heme-Thiolate Peroxygenase Compound I. *J. Am. Chem. Soc.* **2012**, *134*, 12897–12900.

(201) Onderko, E. L.; Silakov, A.; Yosca, T. H.; Green, M. T. Characterization of a Selenocysteine-Ligated P450 Compound I Reveals Direct Link between Electron Donation and Reactivity. *Nat. Chem.* **2017**, *9*, 623–628.

(202) Groves, J. T.; Haushalter, R. C.; Nakamura, M.; Nemo, T. E.; Evans, B. J. High-Valent Iron-Porphyrin Complexes Related to Peroxidase and Cytochrome P450. *J. Am. Chem. Soc.* **1981**, *103*, 2884–2886.

(203) Pennerhahn, J. E.; McMurry, T. J.; Renner, M.; Latosgrazynsky, L.; Eble, K. S.; Davis, I. M.; Balch, A. L.; Groves, J. T.; Dawson, J. H.; Hodgson, K. O. X-Ray Absorption Spectroscopic Studies of High Valent Iron Porphyrins - Horseradish-Peroxidase Compound-I and Compound-II and Synthetic Models. *J. Biol. Chem.* **1983**, *258*, 2761–2764.

(204) Boso, B.; Lang, G.; McMurry, T. J.; Groves, J. T. Mossbauer-Effect Study of Tight Spin Coupling in Oxidized Chloro-5,10,15,20-Tetra(Mesityl)Porphyrinatoiron(III). *J. Chem. Phys.* **1983**, *79*, 1122–1126.

(205) Groves, J. T.; Nemo, T. E. Aliphatic Hydroxylation Catalyzed by Iron Porphyrin Complexes. *J. Am. Chem. Soc.* **1983**, *105*, 6243–6248.

(206) Hohenberger, J.; Ray, K.; Meyer, K. The Biology and Chemistry of High-Valent Iron-Oxo and Iron-Nitrido Complexes. *Nat. Commun.* **2012**, *3*, 720.

(207) Jung, C. The Mystery of Cytochrome P450 Compound I: a Mini-Review Dedicated to Klaus Ruckpaul. *Biochim. Biophys. Acta, Proteins Proteomics* **2011**, *1814*, 46–57.

- (208) Dolphin, D.; Traylor, T. G.; Xie, L. Y. Polyhaloporphyrins: Unusual Ligands for Metals and Metal-Catalyzed Oxidations. *Acc. Chem. Res.* **1997**, *30*, 251–259.
- (209) Fujii, H. Effects of the Electron-Withdrawing Power of Substituents on the Electronic Structure and Reactivity in Oxidation of Iron(IV) Porphyrin  $\pi$ -Cation Radical Complexes. *J. Am. Chem. Soc.* **1993**, *115*, 4641–4648.
- (210) Fujii, H.; Yoshimura, T.; Kamada, H. ESR Studies of A1u and A2u Oxidation of Iron(IV) Porphyrin  $\pi$ -Cation Radical Complexes. Spin Coupling between Ferryl Iron and A1u/A2u Orbitals. *Inorg. Chem.* **1996**, *35*, 2373–2377.
- (211) Pan, Z. Z.; Zhang, R.; Newcomb, M. Kinetic Studies of Reactions of Iron(IV)-Oxo Porphyrin Radical Cations with Organic Reductants. *J. Inorg. Biochem.* **2006**, *100*, 524–532.
- (212) Bell, S. R.; Groves, J. T. A Highly Reactive P450 Model Compound I. *J. Am. Chem. Soc.* **2009**, *131*, 9640–9641.
- (213) Sheng, X.; Horner, J. H.; Newcomb, M. Spectra and Kinetic Studies of the Compound I Derivative of Cytochrome P450 119. *J. Am. Chem. Soc.* **2008**, *130*, 13310–13320.
- (214) Afanasiev, P.; Sorokin, A. B.  $\mu$ -Nitrido Diiron Macrocyclic Platform: Particular Structure for Particular Catalysis. *Acc. Chem. Res.* **2016**, *49*, 583–593.
- (215) Afanasiev, P.; Kudrik, E. V.; Millet, J.-M. M.; Bouchu, D.; Sorokin, A. B. High-Valent Diiron Species Generated from N-Bridged Diiron Phthalocyanine and H<sub>2</sub>O<sub>2</sub>. *Dalton Trans.* **2011**, *40*, 701–710.
- (216) Kudrik, E. V.; Afanasiev, P.; Alvarez, L. X.; Dubourdeaux, P.; Clémancey, M.; Latour, J.-M.; Blondin, G.; Bouchu, D.; Albrieux, F.; Nefedov, S. E.; et al. An N-Bridged High-Valent Diiron–Oxo Species on a Porphyrin Platform That Can Oxidize Methane. *Nat. Chem.* **2012**, *4*, 1024–1029.
- (217) Sorokin, A. B.; Kudrik, E. V.; Bouchu, D. Bio-Inspired Oxidation of Methane in Water Catalyzed by N-Bridged Diiron Phthalocyanine Complex. *Chem. Commun.* **2008**, 2562–2564.
- (218) Isci, U.; Faponle, A. S.; Afanasiev, P.; Albrieux, F.; Briois, V.; Ahsen, V.; Dumoulin, F.; Sorokin, A. B.; de Visser, S. P. Site-Selective Formation of an Iron(IV)-Oxo Species at the More Electron-Rich Iron Atom of Heteroleptic  $\mu$ -Nitrido Diiron Phthalocyanines. *Chem. Sci.* **2015**, *6*, 5063–5075.
- (219) Quesne, M. G.; Senthilnathan, D.; Singh, D.; Kumar, D.; Maldivi, P.; Sorokin, A. B.; de Visser, S. P. Origin of the Enhanced Reactivity of  $\mu$ -Nitrido-Bridged Diiron(IV)-Oxo Porphyrinoid Complexes over Cytochrome P450 Compound I. *ACS Catal.* **2016**, *6*, 2230–2243.
- (220) Groves, J. T.; Kruper, W. J.; Haushalter, R. C. Hydrocarbon Oxidations with Oxometalloporphyrins. Isolation and Reactions of a (Porphinato)manganese(V) Complex. *J. Am. Chem. Soc.* **1980**, *102*, 6375–6377.
- (221) Czernuszewicz, R. S.; Su, Y. O.; Stern, M. K.; Macor, K. A.; Kim, D.; Groves, J. T.; Spiro, T. G. Oxomanganese(IV) Porphyrins Identified by Resonance Raman and Infrared-Spectroscopy - Weak Bonds and the Stability of the Half-Filled t<sub>2g</sub> Subshell. *J. Am. Chem. Soc.* **1988**, *110*, 4158–4165.
- (222) Groves, J. T.; Stern, M. K. Synthesis, Characterization, and Reactivity of Oxomanganese(IV) Porphyrin Complexes. *J. Am. Chem. Soc.* **1988**, *110*, 8628–8638.
- (223) Bernadou, J.; Fabiano, A.-S.; Robert, A.; Meunier, B. "Redox Tautomerism" in High-Valent Metal-Oxo-Aquo Complexes. Origin of the Oxygen Atom in Epoxidation Reactions Catalyzed by Water-Soluble Metalloporphyrins. *J. Am. Chem. Soc.* **1994**, *116*, 9375–9376.
- (224) Groves, J. T.; Marla, S. S. Peroxynitrite-Induced DNA Strand Scission Mediated by a Manganese Porphyrin. *J. Am. Chem. Soc.* **1995**, *117*, 9578–9579.
- (225) Pitie, M.; Bernadou, J.; Meunier, B. Oxidation at Carbon-1' of DNA Deoxyriboses by the Mn-TMPyP/KHSO<sub>5</sub> System Results from a Cytochrome P-450-type Hydroxylation Reaction. *J. Am. Chem. Soc.* **1995**, *117*, 2935–2936.
- (226) Groves, J. T.; Lee, J. B.; Marla, S. S. Detection and Characterization of an Oxomanganese(V) Porphyrin Complex by Rapid-Mixing Stopped-Flow Spectrophotometry. *J. Am. Chem. Soc.* **1997**, *119*, 6269–6273.
- (227) Jin, N.; Groves, J. T. Unusual Kinetic Stability of a Ground-State Singlet Oxomanganese(V) Porphyrin. Evidence for a Spin State Crossing Effect. *J. Am. Chem. Soc.* **1999**, *121*, 2923–2924.
- (228) Nick, R. J.; Ray, G. B.; Fish, K. M.; Spiro, T. G.; Groves, J. T. Evidence for a Weak Mn:O Bond and a Non-Porphyrin Radical in Manganese-Substituted Horseradish Peroxidase Compound I. *J. Am. Chem. Soc.* **1991**, *113*, 1838–1840.
- (229) Nam, W.; Kim, I.; Lim, M. H.; Choi, H. J.; Lee, J. S.; Jang, H. G. Isolation of an Oxomanganese(V) Porphyrin Intermediate in the Reaction of a Manganese(III) Porphyrin Complex and H<sub>2</sub>O<sub>2</sub> in Aqueous Solution. *Chem. - Eur. J.* **2002**, *8*, 2067–2071.
- (230) Zhang, R.; Horner, J. H.; Newcomb, M. Laser Flash Photolysis Generation and Kinetic Studies of Porphyrin–Manganese–Oxo Intermediates. Rate Constants for Oxidations Effected by Porphyrin–MnV–Oxo Species and Apparent Disproportionation Equilibrium Constants for Porphyrin–MnIV–Oxo Species. *J. Am. Chem. Soc.* **2005**, *127*, 6573–6582.
- (231) Shimazaki, Y.; Nagano, T.; Takesue, H.; Ye, B.-H.; Tani, F.; Naruta, Y. Characterization of a Dinuclear Mn<sup>V</sup>=O Complex and Its Efficient Evolution of O<sub>2</sub> in the Presence of Water. *Angew. Chem., Int. Ed.* **2004**, *43*, 98–100.
- (232) Jin, N.; Bourassa, J. L.; Tizio, S. C.; Groves, J. T. Rapid, Reversible Oxygen Atom Transfer Between an Oxomanganese(V) Porphyrin and Bromide: a Haloperoxidase Mimic with Enzymatic Rates. *Angew. Chem., Int. Ed.* **2000**, *39*, 3849–3851.
- (233) Jin, N.; Ibrahim, M.; Spiro, T. G.; Groves, J. T. Trans-Dioxo Manganese(V) Porphyrins. *J. Am. Chem. Soc.* **2007**, *129*, 12416–12417.
- (234) Gross, Z. The Groves–Spiro Dioxomanganese(V) Story. *Angew. Chem., Int. Ed.* **2008**, *47*, 2737–2739.
- (235) Song, W. J.; Seo, M. S.; DeBeer George, S.; Ohta, T.; Song, R.; Kang, M. J.; Tosha, T.; Kitagawa, T.; Solomon, E. I.; Nam, W. Synthesis, Characterization, and Reactivities of Manganese(V)-Oxo Porphyrin Complexes. *J. Am. Chem. Soc.* **2007**, *129*, 1268–1277.
- (236) Green, M. T. Application of Badger's Rule to Heme and Non-Heme Iron–Oxygen Bonds: An Examination of Ferryl Protonation States. *J. Am. Chem. Soc.* **2006**, *128*, 1902–1906.
- (237) Badger, R. M. The Relation Between the Internuclear Distances and Force Constants of Molecules and Its Application to Polyatomic Molecules. *J. Chem. Phys.* **1935**, *3*, 710–714.
- (238) Ho, C.; Leung, W.-H.; Che, C.-M. Kinetics of C-H Bond and Alkene Oxidation by Trans-Dioxoruthenium(VI) Porphyrins. *J. Chem. Soc., Dalton Trans.* **1991**, 2933–2939.
- (239) Leung, W. H.; Che, C. M. High-Valent Ruthenium(IV) and -(VI) Oxo Complexes of Octaethylporphyrin. Synthesis, Spectroscopy, and Reactivities. *J. Am. Chem. Soc.* **1989**, *111*, 8812–8818.
- (240) Groves, J. T.; Quinn, R. Models of Oxidized Heme Proteins. Preparation and Characterization of a Trans-Dioxoruthenium(VI) Porphyrin Complex. *Inorg. Chem.* **1984**, *23*, 3844–3846.
- (241) Che, C. M.; Poon, C. K.; Chung, W. C.; Gray, H. B. Synthesis and Characterization of Osmium Porphyrins. *Inorg. Chem.* **1985**, *24*, 1277–1278.
- (242) Che, C. M.; Chung, W. C.; Lai, T. F. Synthesis, Reactivity, and X-Ray Structural Characterization of Trans-Dioxoosmium(VI) Porphyrin Complexes. *Inorg. Chem.* **1988**, *27*, 2801–2804.
- (243) De Angelis, F.; Jin, N.; Car, R.; Groves, J. T. Electronic Structure and Reactivity of Isomeric Oxo-Mn(V) Porphyrins: Effects of Spin-State Crossing and pK<sub>a</sub> Modulation. *Inorg. Chem.* **2006**, *45*, 4268–4276.
- (244) Balcells, D.; Raynaud, C.; Crabtree, R. H.; Eisenstein, O. A Rational Basis for the Axial Ligand Effect in C-H Oxidation by MnO(porphyrin)(X)(+) (X = H<sub>2</sub>O, OH<sup>-</sup>, O<sub>2</sub><sup>-</sup>) from a DFT Study. *Inorg. Chem.* **2008**, *47*, 10090–10099.
- (245) Behan, R. K.; Green, M. T. On the Status of Ferryl Protonation. *J. Inorg. Biochem.* **2006**, *100*, 448–459.

- (246) Dunford, H. B.; Hasinoff, B. B. Kinetics of the Oxidation of Ferrocyanide by Horseradish Peroxidase Compounds I and II. *Biochemistry* **1970**, *9*, 4930–4939.
- (247) Sitter, A. J.; Reczek, C. M.; Terner, J. Observation of the Fe(IV)=O Stretching Vibration of Ferryl Myoglobin by Resonance Raman Spectroscopy. *Biochim. Biophys. Acta, Protein Struct. Mol. Enzymol.* **1985**, *828*, 229–235.
- (248) Chance, M.; Powers, L.; Poulos, T.; Chance, B. Cytochrome *c* Peroxidase Compound ES Is Identical with Horseradish Peroxidase Compound I in Iron-Ligand Distances. *Biochemistry* **1986**, *25*, 1266–1270.
- (249) Chin, D.-H.; La Mar, G. N.; Balch, A. L. Mechanism of Autoxidation of Iron(II) Porphyrins. Detection of a Peroxo-Bridged Iron(III) Porphyrin Dimer and the Mechanism of Its Thermal Decomposition to the Oxo-Bridged Iron(III) Porphyrin Dimer. *J. Am. Chem. Soc.* **1980**, *102*, 4344–4350.
- (250) Green, M. T.; Dawson, J. H.; Gray, H. B. Oxoiron(IV) in Chloroperoxidase Compound II Is Basic: Implications for P450 Chemistry. *Science* **2004**, *304*, 1653–1656.
- (251) Penner-Hahn, J. E.; Smith Eble, K.; McMurry, T. J.; Renner, M.; Balch, A. L.; Groves, J. T.; Dawson, J. H.; Hodgson, K. O. Structural Characterization of Horseradish Peroxidase Using EXAFS Spectroscopy. Evidence for Fe=O Ligation in Compounds I and II. *J. Am. Chem. Soc.* **1986**, *108*, 7819–7825.
- (252) Chance, M.; Powers, L.; Kumar, C.; Chance, B. X-Ray Absorption Studies of Myoglobin Peroxide Reveal Functional Differences Between Globins and Heme Enzymes. *Biochemistry* **1986**, *25*, 1259–1265.
- (253) Bonagura, C. A.; Bhaskar, B.; Shimizu, H.; Li, H.; Sundaramoorthy, M.; McRee, D. E.; Goodin, D. B.; Poulos, T. L. High-Resolution Crystal Structures and Spectroscopy of Native and Compound I Cytochrome *c* Peroxidase. *Biochemistry* **2003**, *42*, 5600–5608.
- (254) Hersleth, H.-P.; Dalhus, B.; Görbitz, C.; Andersson, K. An Iron Hydroxide Moiety in the 1.35 Å Resolution Structure of Hydrogen Peroxide Derived Myoglobin Compound II at pH 5.2. *JBIC, J. Biol. Inorg. Chem.* **2002**, *7*, 299–304.
- (255) Meharena, Y. T.; Doukov, T.; Li, H.; Soltis, S. M.; Poulos, T. L. Crystallographic and Single-Crystal Spectral Analysis of the Peroxidase Ferryl Intermediate. *Biochemistry* **2010**, *49*, 2984–2986.
- (256) Yosca, T. H.; Behan, R. K.; Krest, C. M.; Onderko, E. L.; Langston, M. C.; Green, M. T. Setting an Upper Limit on the Myoglobin Iron(IV) Hydroxide pK<sub>a</sub>: Insight into Axial Ligand Tuning in Heme Protein Catalysis. *J. Am. Chem. Soc.* **2014**, *136*, 9124–9131.
- (257) Behan, R. K.; Hoffart, L. M.; Stone, K. L.; Krebs, C.; Green, M. T. Evidence for Basic Ferryls in Cytochromes P450. *J. Am. Chem. Soc.* **2006**, *128*, 11471–11474.
- (258) Stone, K. L.; Behan, R. K.; Green, M. T. Resonance Raman Spectroscopy of Chloroperoxidase Compound II Provides Direct Evidence for the Existence of an Iron(IV)-Hydroxide. *Proc. Natl. Acad. Sci. U. S. A.* **2006**, *103*, 12307–12310.
- (259) Stone, K. L.; Hoffart, L. M.; Behan, R. K.; Krebs, C.; Green, M. T. Evidence for Two Ferryl Species in Chloroperoxidase Compound II. *J. Am. Chem. Soc.* **2006**, *128*, 6147–6153.
- (260) Yosca, T. H.; Rittle, J.; Krest, C. M.; Onderko, E. L.; Silakov, A.; Calixto, J. C.; Behan, R. K.; Green, M. T. Iron(IV)hydroxide pK<sub>a</sub> and the Role of Thiolate Ligation in C-H Bond Activation by Cytochrome P450. *Science* **2013**, *342*, 825–829.
- (261) Wang, X. S.; Ullrich, R.; Hofrichter, M.; Groves, J. T. Heme-Thiolate Ferryl of Aromatic Peroxygenase Is Basic and Reactive. *Proc. Natl. Acad. Sci. U. S. A.* **2015**, *112*, 3686–3691.
- (262) Yosca, T. H.; Langston, M. C.; Krest, C. M.; Onderko, E. L.; Grove, T. L.; Livada, J.; Green, M. T. Spectroscopic Investigations of Catalase Compound II: Characterization of an Iron(IV) Hydroxide Intermediate in a Non-thiolate-Ligated Heme Enzyme. *J. Am. Chem. Soc.* **2016**, *138*, 16016–16023.
- (263) Kwon, H.; Basran, J.; Casadei, C. M.; Fielding, A. J.; Schrader, T. E.; Ostermann, A.; Devos, J. M.; Aller, P.; Blakeley, M. P.; Moody, P. C. E.; et al. Direct Visualization of a Fe(IV)–OH Intermediate in a Heme Enzyme. *Nat. Commun.* **2016**, *7*, 13445.
- (264) Gumiero, A.; Metcalfe, C. L.; Pearson, A. R.; Raven, E. L.; Moody, P. C. E. Nature of the Ferryl Heme in Compounds I and II. *J. Biol. Chem.* **2011**, *286*, 1260–1268.
- (265) Boaz, N. C.; Bell, S. R.; Groves, J. T. Ferryl Protonation in Oxoiron(IV) Porphyrins and Its Role in Oxygen Transfer. *J. Am. Chem. Soc.* **2015**, *137*, 2875–2885.
- (266) Kurahashi, T.; Kikuchi, A.; Tosha, T.; Shiro, Y.; Kitagawa, T.; Fujii, H. Transient Intermediates from Mn(salen) with Sterically Hindered Mesityl Groups: Interconversion between Mn<sup>IV</sup>-Phenolate and Mn<sup>III</sup>-Phenoxy Radicals as an Origin for Unique Reactivity. *Inorg. Chem.* **2008**, *47*, 1674–1686.
- (267) Kurahashi, T.; Kikuchi, A.; Shiro, Y.; Hada, M.; Fujii, H. Unique Properties and Reactivity of High-Valent Manganese–Oxo versus Manganese–Hydroxo in the Salen Platform. *Inorg. Chem.* **2010**, *49*, 6664–6672.
- (268) Chen, Z.; Yin, G. The Reactivity of the Active Metal Oxo and Hydroxo Intermediates and Their Implications in Oxidations. *Chem. Soc. Rev.* **2015**, *44*, 1083–1100.
- (269) Lansky, D. E.; Goldberg, D. P. Hydrogen Atom Abstraction by a High-Valent Manganese(V)–Oxo Corrolazine. *Inorg. Chem.* **2006**, *45*, 5119–5125.
- (270) Parsell, T. H.; Yang, M.-Y.; Borovik, A. S. C–H Bond Cleavage with Reductants: Re-Investigating the Reactivity of Monomeric Mn<sup>III/IV</sup>–Oxo Complexes and the Role of Oxo Ligand Basicity. *J. Am. Chem. Soc.* **2009**, *131*, 2762–2763.
- (271) Yin, G.; Danby, A. M.; Kitko, D.; Carter, J. D.; Scheper, W. M.; Busch, D. H. Understanding the Selectivity of a Moderate Oxidation Catalyst: Hydrogen Abstraction by a Fully Characterized, Activated Catalyst, the Robust Dihydroxo Manganese(IV) Complex of a Bridged Cyclam. *J. Am. Chem. Soc.* **2007**, *129*, 1512–1513.
- (272) Bordwell, F. G. Equilibrium Acidities in Dimethyl Sulfoxide Solution. *Acc. Chem. Res.* **1988**, *21*, 456–463.
- (273) Mayer, J. M. Understanding Hydrogen Atom Transfer: From Bond Strengths to Marcus Theory. *Acc. Chem. Res.* **2011**, *44*, 36–46.
- (274) Warren, J. J.; Tronic, T. A.; Mayer, J. M. Thermochemistry of Proton-Coupled Electron Transfer Reagents and its Implications. *Chem. Rev.* **2010**, *110*, 6961–7001.
- (275) Gray, H. B.; Winkler, J. R. Hole Hopping Through Tyrosine/Tryptophan Chains Protects Proteins from Oxidative Damage. *Proc. Natl. Acad. Sci. U. S. A.* **2015**, *112*, 10920–10925.
- (276) Winkler, J. R.; Gray, H. B. Electron Flow Through Biological Molecules: Does Hole Hopping Protect Proteins from Oxidative Damage? *Q. Rev. Biophys.* **2015**, *48*, 411–420.
- (277) Guengerich, F. P.; Munro, A. W. Unusual Cytochrome P450 Enzymes and Reactions. *J. Biol. Chem.* **2013**, *288*, 17065–17073.
- (278) Guengerich, F. P.; Waterman, M. R.; Egli, M. Recent Structural Insights into Cytochrome P450 Function. *Trends Pharmacol. Sci.* **2016**, *37*, 625–640.
- (279) Kramlinger, V. M.; Nagy, L. D.; Fujiwara, R.; Johnson, K. M.; Phan, T. T. N.; Xiao, Y.; Enright, J. M.; Toomey, M. B.; Corbo, J. C.; Guengerich, F. P. Human Cytochrome P450 27C1 Catalyzes 3,4-Desaturation of Retinoids. *FEBS Lett.* **2016**, *590*, 1304–1312.
- (280) Breslow, R.; Balasubramanian, K. The pK<sub>a</sub> of Triphenylcyclopropene. Electrochemical Determination of an Inaccessible Equilibrium Constant. *J. Am. Chem. Soc.* **1969**, *91*, 5182–5183.
- (281) Groves, J. T. Enzymatic C-H Bond Activation: Using Push to Get Pull. *Nat. Chem.* **2014**, *6*, 89–91.
- (282) Hayashi, Y.; Yamazaki, I. The Oxidation-Reduction Potentials of Compound I/Compound II and Compound II/Ferric Couples of Horseradish Peroxidases A2 and C. *J. Biol. Chem.* **1979**, *254*, 9101–9106.
- (283) Wang, X. S.; Peter, S.; Ullrich, R.; Hofrichter, M.; Groves, J. T. Driving Force for Oxygen-Atom Transfer by Heme-Thiolate Enzymes. *Angew. Chem., Int. Ed.* **2013**, *52*, 9238–9241.
- (284) Song, W. J.; Ryu, Y. O.; Song, R.; Nam, W. Oxoiron(IV) Porphyrin  $\pi$ -Cation Radical Complexes with a Chameleon Behavior in

Cytochrome P450 Model Reactions. *JBIC, J. Biol. Inorg. Chem.* **2005**, *10*, 294–304.

(285) Kang, Y.; Chen, H.; Jeong, Y. J.; Lai, W.; Bae, E. H.; Shaik, S.; Nam, W. Enhanced Reactivities of Iron(IV)-Oxo Porphyrin  $\pi$ -Cation Radicals in Oxygenation Reactions by Electron-Donating Axial Ligands. *Chem. - Eur. J.* **2009**, *15*, 10039–10046.

(286) Castro, L.; Bühl, M. Calculations of One-Electron Redox Potentials of Oxoiron(IV) Porphyrin Complexes. *J. Chem. Theory Comput.* **2014**, *10*, 243–251.

(287) Rydberg, P.; Sigfridsson, E.; Ryde, U. On the Role of the Axial Ligand in Heme Proteins: a Theoretical Study. *JBIC, J. Biol. Inorg. Chem.* **2004**, *9*, 203–223.

(288) Dey, A.; Jiang, Y.; Ortiz de Montellano, P.; Hodgson, K. O.; Hedman, B.; Solomon, E. I. S K-edge XAS and DFT Calculations on Cytochrome P450: Covalent and Ionic Contributions to the Cysteine-Fe Bond and Their Contribution to Reactivity. *J. Am. Chem. Soc.* **2009**, *131*, 7869–7878.

(289) de Visser, S. P. Trends in Substrate Hydroxylation Reactions by Heme and Nonheme Iron(IV)-Oxo Oxidants Give Correlations between Intrinsic Properties of the Oxidant with Barrier Height. *J. Am. Chem. Soc.* **2010**, *132*, 1087–1097.

(290) Takahashi, A.; Kurahashi, T.; Fujii, H. Redox Potentials of Oxoiron(IV) Porphyrin  $\pi$ -Cation Radical Complexes: Participation of Electron Transfer Process in Oxygenation Reactions. *Inorg. Chem.* **2011**, *50*, 6922–6928.

(291) Sugimoto, H.; Tung, H. C.; Sawyer, D. T. The Formation, Characterization, and Reactivity of the Oxene Adduct of [Tetrakis(2,6-Dichlorophenyl)Porphinato]Iron(III) Perchlorate in Acetonitrile. Model for the Reactive Intermediate of Cytochrome P450. *J. Am. Chem. Soc.* **1988**, *110*, 2465–2470.

(292) Evans, M. G.; Polanyi, M. Inertia and Driving Force of Chemical Reactions. *Trans. Faraday Soc.* **1938**, *34*, 11–24.

(293) Panov, G. I.; Parfenov, M. V.; Parmon, V. N. The Brønsted–Evans–Polanyi Correlations in Oxidation Catalysis. *Catal. Rev.: Sci. Eng.* **2015**, *57*, 436–477.

(294) Mayr, H.; Ofial, A. R. The Reactivity–Selectivity Principle: An Imperishable Myth in Organic Chemistry. *Angew. Chem., Int. Ed.* **2006**, *45*, 1844–1854.

(295) Roth, J. P.; Yoder, J. C.; Won, T.-J.; Mayer, J. M. Application of the Marcus Cross Relation to Hydrogen Atom Transfer Reactions. *Science* **2001**, *294*, 2524–2526.

(296) Warren, J. J.; Mayer, J. M. In *Proton-Coupled Electron Transfer: A Carrefour of Chemical Reactivity Traditions*; The Royal Society of Chemistry, 2012.

(297) Salamone, M.; Bietti, M. Tuning Reactivity and Selectivity in Hydrogen Atom Transfer from Aliphatic C–H Bonds to Alkoxy Radicals: Role of Structural and Medium Effects. *Acc. Chem. Res.* **2015**, *48*, 2895–2903.

(298) Liu, W.; Groves, J. T. Manganese Catalyzed C-H Halogenation. *Acc. Chem. Res.* **2015**, *48*, 1727–1735.

(299) Finn, M.; Friedline, R.; Suleman, N. K.; Wohl, C. J.; Tanko, J. M. Chemistry of the t-Butoxy Radical: Evidence that Most Hydrogen Abstractions from Carbon are Entropy-Controlled. *J. Am. Chem. Soc.* **2004**, *126*, 7578–7584.

(300) Takahashi, A.; Kurahashi, T.; Fujii, H. Activation Parameters for Cyclohexene Oxygenation by an Oxoiron(IV) Porphyrin  $\pi$ -Cation Radical Complex: Entropy Control of an Allylic Hydroxylation Reaction. *Inorg. Chem.* **2007**, *46*, 6227–6229.

(301) Schröder, D.; Shaik, S.; Schwarz, H. Two-State Reactivity as a New Concept in Organometallic Chemistry. *Acc. Chem. Res.* **2000**, *33*, 139–145.

(302) Shaik, S.; Danovich, D.; Fiedler, A.; Schröder, D.; Schwarz, H. Two-State Reactivity in Organometallic Gas-Phase Ion Chemistry. *Helv. Chim. Acta* **1995**, *78*, 1393–1407.

(303) Usharani, D.; Wang, B.; Sharon, D. A.; Shaik, S. In *Spin States in Biochemistry and Inorganic Chemistry*; John Wiley & Sons, Ltd: Chichester, UK, 2015.

(304) Oglario, F.; Harris, N.; Cohen, S.; Filatov, M.; de Visser, S. P.; Shaik, S. A Model “Rebound” Mechanism of Hydroxylation by

Cytochrome P450: Stepwise and Effectively Concerted Pathways, and Their Reactivity Patterns. *J. Am. Chem. Soc.* **2000**, *122*, 8977–8989.

(305) Shaik, S.; de Visser, S. P.; Oglario, F.; Schwarz, H.; Schroder, D. Two-State Reactivity Mechanisms of Hydroxylation and Epoxidation by Cytochrome P450 Revealed by Theory. *Curr. Opin. Chem. Biol.* **2002**, *6*, 556–567.

(306) Shaik, S.; Kumar, D.; de Visser, S. P.; Altun, A.; Thiel, W. Theoretical Perspective on the Structure and Mechanism of Cytochrome p450 Enzymes. *Chem. Rev.* **2005**, *105*, 2279–2328.

(307) Balcells, D.; Raynaud, C.; Crabtree, R. H.; Eisenstein, O. C-H Oxidation by Hydroxo Manganese(V) Porphyrins: a DFT Study. *Chem. Commun.* **2009**, 1772–1774.

(308) Balcells, D.; Raynaud, C.; Crabtree, R. H.; Eisenstein, O. The Rebound Mechanism in Catalytic C-H Oxidation by MnO(TPP)Cl from DFT Studies: Electronic Nature of the Active Species. *Chem. Commun.* **2008**, 744–746.

(309) Usharani, D.; Janardanan, D.; Li, C. S.; Shaik, S. A Theory for Bioinorganic Chemical Reactivity of Oxometal Complexes and Analogous Oxidants: The Exchange and Orbital-Selection Rules. *Acc. Chem. Res.* **2013**, *46*, 471–482.

(310) Shaik, S.; Chen, H.; Janardanan, D. Exchange-Enhanced Reactivity in Bond Activation by Metal-Oxo Enzymes and Synthetic Reagents. *Nat. Chem.* **2011**, *3*, 19–27.

(311) Janardanan, D.; Usharani, D.; Shaik, S. The Origins of Dramatic Axial Ligand Effects: Closed-Shell Mn<sup>VO</sup> Complexes Use Exchange-Enhanced Open-Shell States to Mediate Efficient H Abstraction Reactions. *Angew. Chem., Int. Ed.* **2012**, *51*, 4421–4425.

(312) Li, C. S.; Wu, W.; Kumar, D.; Shaik, S. Kinetic Isotope Effect Is a Sensitive Probe of Spin State Reactivity in C-H Hydroxylation of *N,N*-Dimethylaniline by Cytochrome P450. *J. Am. Chem. Soc.* **2006**, *128*, 394–395.

(313) Li, C.; Wu, W.; Cho, K.-B.; Shaik, S. Oxidation of Tertiary Amines by Cytochrome P450—Kinetic Isotope Effect as a Spin-State Reactivity Probe. *Chem. - Eur. J.* **2009**, *15*, 8492–8503.

(314) Klinker, E. J.; Shaik, S.; Hirao, H.; Que, L. A Two-State Reactivity Model Explains Unusual Kinetic Isotope Effect Patterns in C–H Bond Cleavage by Nonheme Oxoiron(IV) Complexes. *Angew. Chem., Int. Ed.* **2009**, *48*, 1291–1295.

(315) Manchester, J. L.; Dinnocenzo, J. P.; Higgins; Jones, J. P. A New Mechanistic Probe for Cytochrome P450: An Application of Isotope Effect Profiles. *J. Am. Chem. Soc.* **1997**, *119*, 5069–5070.

(316) Dinnocenzo, J. P.; Karki, S. B.; Jones, J. P. On Isotope Effects for the Cytochrome P450 Oxidation of Substituted *N,N*-Dimethylanilines. *J. Am. Chem. Soc.* **1993**, *115*, 7111–7116.

(317) Karki, S. B.; Dinnocenzo, J. P.; Jones, J. P.; Korzekwa, K. R. Mechanism of Oxidative Amine Dealkylation of Substituted *N,N*-Dimethylanilines by Cytochrome P450: Application of Isotope Effect Profiles. *J. Am. Chem. Soc.* **1995**, *117*, 3657–3664.

(318) Wang, Y.; Kumar, D.; Yang, C.; Han, K.; Shaik, S. Theoretical Study of *N*-Demethylation of Substituted *N,N*-Dimethylanilines by Cytochrome P450: The Mechanistic Significance of Kinetic Isotope Effect Profiles. *J. Phys. Chem. B* **2007**, *111*, 7700–7710.

(319) Prokop, K. A.; de Visser, S. P.; Goldberg, D. P. Unprecedented Rate Enhancements of Hydrogen-Atom Transfer to a Manganese(V)–Oxo Corrolazine Complex. *Angew. Chem., Int. Ed.* **2010**, *49*, 5091–5095.

(320) Yang, T.; Quesne, M. G.; Neu, H. M.; Cantú Reinhard, F. G.; Goldberg, D. P.; de Visser, S. P. Singlet versus Triplet Reactivity in an Mn(V)–Oxo Species: Testing Theoretical Predictions Against Experimental Evidence. *J. Am. Chem. Soc.* **2016**, *138*, 12375–12386.

(321) Kohen, A.; Klinman, J. P. Enzyme Catalysis: Beyond Classical Paradigms. *Acc. Chem. Res.* **1998**, *31*, 397–404.

(322) Truhlar, D. G.; Gao, J.; Alhambra, C.; Garcia-Viloca, M.; Corchado, J.; Sánchez, M. L.; Villà, J. The Incorporation of Quantum Effects in Enzyme Kinetics Modeling. *Acc. Chem. Res.* **2002**, *35*, 341–349.

(323) Kim, Y.; Kreevoy, M. M. The Experimental Manifestations of Corner-Cutting Tunneling. *J. Am. Chem. Soc.* **1992**, *114*, 7116–7123.

- (324) Kwart, H. Temperature Dependence of the Primary Kinetic Hydrogen Isotope Effect as a Mechanistic Criterion. *Acc. Chem. Res.* **1982**, *15*, 401–408.
- (325) Kwon, Y. H.; Mai, B. K.; Lee, Y. M.; Dhuri, S. N.; Mandal, D.; Cho, K. B.; Kim, Y.; Shaik, S.; Nam, W. Determination of Spin Inversion Probability, H-Tunneling Correction, and Regioselectivity in the Two-State Reactivity of Nonheme Iron(IV)-Oxo Complexes. *J. Phys. Chem. Lett.* **2015**, *6*, 1472–1476.
- (326) Klinman, J. P. The Role of Tunneling in Enzyme Catalysis of C–H Activation. *Biochim. Biophys. Acta, Bioenerg.* **2006**, *1757*, 981–987.
- (327) Layfield, J. P.; Hammes-Schiffer, S. Hydrogen Tunneling in Enzymes and Biomimetic Models. *Chem. Rev.* **2014**, *114*, 3466–3494.
- (328) Mandal, D.; Ramanan, R.; Usharani, D.; Janardanan, D.; Wang, B.; Shaik, S. How Does Tunneling Contribute to Counterintuitive H-Abstraction Reactivity of Nonheme Fe(IV)O Oxidants with Alkanes? *J. Am. Chem. Soc.* **2015**, *137*, 722–733.
- (329) Mandal, D.; Shaik, S. Interplay of Tunneling, Two-State Reactivity, and Bell–Evans–Polanyi Effects in C–H Activation by Nonheme Fe(IV)O Oxidants. *J. Am. Chem. Soc.* **2016**, *138*, 2094–2097.
- (330) Zhang, Y.; Lin, H. Quantum Tunneling in Testosterone 6 $\beta$ -Hydroxylation by Cytochrome P450: Reaction Dynamics Calculations Employing Multiconfiguration Molecular–Mechanical Potential Energy Surfaces. *J. Phys. Chem. A* **2009**, *113*, 11501–11508.
- (331) Krauser, J. A.; Guengerich, F. P. Cytochrome P450 3A4-catalyzed Testosterone 6 $\beta$ -Hydroxylation Stereochemistry, Kinetic Deuterium Isotope Effects, and Rate-limiting Steps. *J. Biol. Chem.* **2005**, *280*, 19496–19506.
- (332) Nelson, S. D.; Trager, W. F. The Use of Deuterium Isotope Effects to Probe the Active Site Properties, Mechanism of Cytochrome P450-Catalyzed Reactions, and Mechanisms of Metabolically Dependent Toxicity. *Drug Metab. Dispos.* **2003**, *31*, 1481–1497.
- (333) Sorokin, A.; Robert, A.; Meunier, B. Intramolecular Kinetic Isotope Effects in Alkane Hydroxylations Catalyzed by Manganese and Iron Porphyrin Complexes. *J. Am. Chem. Soc.* **1993**, *115*, 7293–7299.
- (334) White, R. E.; Miller, J. P.; Favreau, L. V.; Bhattacharyya, A. Stereochemical Dynamics of Aliphatic Hydroxylation by Cytochrome P450. *J. Am. Chem. Soc.* **1986**, *108*, 6024–6031.
- (335) Sorokin, A. B.; Khenkin, A. M. The Contribution of Tunneling to High Values of Kinetic Isotope Effect in Aliphatic Hydroxylation by a Cytochrome P450 Model. *J. Chem. Soc., Chem. Commun.* **1990**, 45–46.
- (336) Pan, Z.; Horner, J. H.; Newcomb, M. Tunneling in C–H Oxidation Reactions by an Oxoiron(IV) Porphyrin Radical Cation: Direct Measurements of Very Large H/D Kinetic Isotope Effects. *J. Am. Chem. Soc.* **2008**, *130*, 7776–7777.
- (337) Cong, Z.; Kinemuchi, H.; Kurahashi, T.; Fujii, H. Factors Affecting Hydrogen-Tunneling Contribution in Hydroxylation Reactions Promoted by Oxoiron(IV) Porphyrin  $\pi$ -Cation Radical Complexes. *Inorg. Chem.* **2014**, *53*, 10632–10641.
- (338) Meisner, J.; Kästner, J. Atom Tunneling in Chemistry. *Angew. Chem., Int. Ed.* **2016**, *55*, 5400–5413.
- (339) Bukowski, M. R.; Koehntop, K. D.; Stubna, A.; Bominaar, E. L.; Halfen, J. A.; Münck, E.; Nam, W.; Que, L. A Thiolate-Ligated Nonheme Oxoiron(IV) Complex Relevant to Cytochrome P450. *Science* **2005**, *310*, 1000–1002.
- (340) Rohde, J.-U.; Que, L. Axial Coordination of Carboxylate Activates the Non-heme Fe<sup>IV</sup>=O Unit. *Angew. Chem., Int. Ed.* **2005**, *44*, 2255–2258.
- (341) Sastri, C. V.; Lee, J.; Oh, K.; Lee, Y. J.; Lee, J.; Jackson, T. A.; Ray, K.; Hirao, H.; Shin, W.; Halfen, J. A.; et al. Axial Ligand Tuning of a Nonheme Iron(IV)–Oxo Unit for Hydrogen Atom Abstraction. *Proc. Natl. Acad. Sci. U. S. A.* **2007**, *104*, 19181–19186.
- (342) Hirao, H.; Que, L.; Nam, W.; Shaik, S. A Two-State Reactivity Rationale for Counterintuitive Axial Ligand Effects on the C–H Activation Reactivity of Nonheme Fe(IV)=O Oxidants. *Chem. - Eur. J.* **2008**, *14*, 1740–1756.
- (343) Groves, J. T.; Gross, Z. In *Bioinorganic Chemistry: An Inorganic Perspective of Life*; Kessissoglou, D. P., Ed.; Springer: Netherlands, 1995.
- (344) Gupta, R.; Li, X. X.; Cho, K. B.; Guo, M.; Lee, Y. M.; Wang, Y.; Fukuzumi, S.; Nam, W. Tunneling Effect That Changes the Reaction Pathway from Epoxidation to Hydroxylation in the Oxidation of Cyclohexene by a Compound I Model of Cytochrome P450. *J. Phys. Chem. Lett.* **2017**, *8*, 1557–1561.
- (345) Gao, H.; Groves, J. T. Fast Hydrogen Atom Abstraction by a Hydroxo Iron(III) Porphyrin. *J. Am. Chem. Soc.* **2017**, *139*, 3938–3941.
- (346) Lewandowska-Andralojc, A.; Grills, D. C.; Zhang, J.; Bullock, R. M.; Miyazawa, A.; Kawanishi, Y.; Fujita, E. Kinetic and Mechanistic Studies of Carbon-to-Metal Hydrogen Atom Transfer Involving Os-Centered Radicals: Evidence for Tunneling. *J. Am. Chem. Soc.* **2014**, *136*, 3572–3578.
- (347) Slaughter, L. M.; Wolczanski, P. T.; Klinckman, T. R.; Cundari, T. R. Inter- and Intramolecular Experimental and Calculated Equilibrium Isotope Effects for (Silox)<sub>2</sub>(<sup>t</sup>Bu<sub>3</sub>SiND)TiR + RH (Silox = <sup>t</sup>Bu<sub>3</sub>SiO): Inferred Kinetic Isotope Effects for Rh/D Addition to Transient (Silox)<sub>2</sub>Ti = NSi<sup>t</sup>Bu<sub>3</sub>. *J. Am. Chem. Soc.* **2000**, *122*, 7953–7975.
- (348) Groves, J. T.; Subramanian, D. V. Hydroxylation by Cytochrome P450 and Metalloporphyrin Models. Evidence for Allylic Rearrangement. *J. Am. Chem. Soc.* **1984**, *106*, 2177–2181.
- (349) Griller, D.; Ingold, K. U. Free-Radical Clocks. *Acc. Chem. Res.* **1980**, *13*, 317–323.
- (350) Rozhkova-Novosad, E. A.; Chae, J. C.; Zylstra, G. J.; Bertrand, E. M.; Alexander-Ozinskas, M.; Deng, D. Y.; Moe, L. A.; van Beilen, J. B.; Danahy, M.; Groves, J. T.; et al. Profiling Mechanisms of Alkane Hydroxylase Activity *in vivo* Using the Diagnostic Substrate Norcarane. *Chem. Biol.* **2007**, *14*, 165–172.
- (351) Baik, M. H.; Newcomb, M.; Friesner, R. A.; Lippard, S. J. Mechanistic Studies on the Hydroxylation of Methane by Methane Monooxygenase. *Chem. Rev.* **2003**, *103*, 2385–2419.
- (352) Brazeau, B. J.; Austin, R. N.; Tarr, C.; Groves, J. T.; Lipscomb, J. D. Intermediate Q from Soluble Methane Monooxygenase Hydroxylates the Mechanistic Substrate Probe Norcarane: Evidence for a Stepwise Reaction. *J. Am. Chem. Soc.* **2001**, *123*, 11831–11837.
- (353) Jin, Y.; Lipscomb, J. D. Probing the Mechanism of C–H Activation: Oxidation of Methylcubane by Soluble Methane Monooxygenase from *Methylosinus Trichosporium* OB3b. *Biochemistry* **1999**, *38*, 6178–6186.
- (354) Jin, Y.; Lipscomb, J. D. Mechanistic Insights into C–H Activation from Radical Clock Chemistry: Oxidation of Substituted Methylcyclopropanes Catalyzed by Soluble Methane Monooxygenase from *Methylosinus Trichosporium* OB3b. *Biochim. Biophys. Acta, Protein Struct. Mol. Enzymol.* **2000**, *1543*, 47–59.
- (355) Austin, R. N.; Buzzi, K.; Kim, E.; Zylstra, G. J.; Groves, J. T. Xylene Monooxygenase, a Membrane-Spanning Non-Heme Diiron Enzyme That Hydroxylates Hydrocarbons via a Substrate Radical Intermediate. *J. Biol. Inorg. Chem.* **2003**, *8*, 733–740.
- (356) Moe, L. A.; Hu, Z. B.; Deng, D. Y.; Austin, R. N.; Groves, J. T.; Fox, B. G. Remarkable Aliphatic Hydroxylation by the Diiron Enzyme Toluene 4-Monooxygenase in Reactions with Radical or Cation Diagnostic Probes Norcarane, 1,1-Dimethylcyclopropane, and 1,1-Diethylcyclopropane. *Biochemistry* **2004**, *43*, 15688–15701.
- (357) Zaragoza, J. P. T.; Yosca, T. H.; Siegler, M. A.; Moënne-Loccoz, P.; Green, M. T.; Goldberg, D. P. Direct Observation of Oxygen Rebound with an Iron-Hydroxide Complex. *J. Am. Chem. Soc.* **2017**, *139*, 13640–13643.
- (358) Austin, R. N.; Luddy, K.; Erickson, K.; Pender-Cudlip, M.; Bertrand, E.; Deng, D.; Buzdygon, R. S.; van Beilen, J. B.; Groves, J. T. Cage Escape Competes with Geminate Recombination during Alkane Hydroxylation by the Diiron Oxygenase AlkB. *Angew. Chem., Int. Ed.* **2008**, *47*, 5232–5234.
- (359) Cooper, H. L.; Mishra, G.; Huang, X.; Pender-Cudlip, M.; Austin, R. N.; Shanklin, J.; Groves, J. T. Parallel and Competitive Pathways for Substrate Desaturation, Hydroxylation, and Radical



Rearrangement by the Non-Heme Diiron Hydroxylase AlkB. *J. Am. Chem. Soc.* **2012**, *134*, 20365–20375.

(360) Bertrand, E.; Sakai, R.; Rozhkova-Novosad, E.; Moe, L.; Fox, B. G.; Groves, J. T.; Austin, R. N. Reaction Mechanisms of Non-Heme Diiron Hydroxylases Characterized in Whole Cells. *J. Inorg. Biochem.* **2005**, *99*, 1998–2006.

(361) Cooper, H. L. R.; Groves, J. T. Molecular Probes of the Mechanism of Cytochrome P450. Oxygen Traps a Substrate Radical Intermediate. *Arch. Biochem. Biophys.* **2011**, *507*, 111–118.

(362) Oglario, F.; de Visser, S. P.; Groves, J. T.; Shaik, S. Chameleon States: High-Valent Metal–Oxo Species of Cytochrome P450 and Its Ruthenium Analogue. *Angew. Chem., Int. Ed.* **2001**, *40*, 2874–2878.

(363) Liu, W.; Cheng, M.-J.; Nielsen, R. J.; Goddard, W. A.; Groves, J. T. Probing the C–O Bond-Formation Step in Metalloporphyrin-Catalyzed C–H Oxygenation Reactions. *ACS Catal.* **2017**, *7*, 4182–4188.

(364) Cho, K. B.; Hirao, H.; Shaik, S.; Nam, W. To Rebound or Dissociate? This Is the Mechanistic Question in C–H Hydroxylation by Heme and Nonheme Metal–Oxo Complexes. *Chem. Soc. Rev.* **2016**, *45*, 1197–1210.

(365) Rude, M. A.; Baron, T. S.; Brubaker, S.; Alibhai, M.; Del Cardayre, S. B.; Schirmer, A. Terminal Olefin (1-Alkene) Biosynthesis by a Novel P450 Fatty Acid Decarboxylase from *Jeotgalicoccus* Species. *Appl. Environ. Microbiol.* **2011**, *77*, 1718–1727.

(366) Wang, J.-b.; Lonsdale, R.; Reetz, M. T. Exploring Substrate Scope and Stereoselectivity of P450 Peroxygenase OleT<sub>JE</sub> in Olefin-Forming Oxidative Decarboxylation. *Chem. Commun.* **2016**, *52*, 8131–8133.

(367) Hsieh, C. H.; Makris, T. M. Expanding the Substrate Scope and Reactivity of Cytochrome P450 OleT. *Biochem. Biophys. Res. Commun.* **2016**, *476*, 462–466.

(368) Wise, C. E.; Grant, J. L.; Amaya, J. A.; Ratigan, S. C.; Hsieh, C. H.; Manley, O. M.; Makris, T. M. Divergent Mechanisms of Iron-Containing Enzymes for Hydrocarbon Biosynthesis. *JBIC, J. Biol. Inorg. Chem.* **2017**, *22*, 221–235.

(369) Dennig, A.; Kuhn, M.; Tassoti, S.; Thiessenhusen, A.; Gilch, S.; Bulter, T.; Haas, T.; Hall, M.; Faber, K. Oxidative Decarboxylation of Short-Chain Fatty Acids to 1-Alkenes. *Angew. Chem., Int. Ed.* **2015**, *54*, 8819–8822.

(370) Fujishiro, T.; Shoji, O.; Nagano, S.; Sugimoto, H.; Shiro, Y.; Watanabe, Y. Crystal Structure of H<sub>2</sub>O<sub>2</sub>-Dependent Cytochrome P450<sub>SP $\alpha$</sub>  With Its Bound Fatty Acid Substrate: Insight into the Regioselective Hydroxylation of Fatty Acids at the Alpha Position. *J. Biol. Chem.* **2011**, *286*, 29941–29950.

(371) Grant, J. L.; Hsieh, C. H.; Makris, T. M. Decarboxylation of Fatty Acids to Terminal Alkenes by Cytochrome P450 Compound I. *J. Am. Chem. Soc.* **2015**, *137*, 4940–4943.

(372) Kourist, R. A New Class of Enzymes Discovered: A Non-Heme Oxidase Produces Medium-Chain 1-Alkenes. *Angew. Chem., Int. Ed.* **2015**, *54*, 4156–4158.

(373) Rui, Z.; Li, X.; Zhu, X.; Liu, J.; Domigan, B.; Barr, I.; Cate, J. H. D.; Zhang, W. Microbial Biosynthesis of Medium-Chain 1-Alkenes by a Nonheme Iron Oxidase. *Proc. Natl. Acad. Sci. U. S. A.* **2014**, *111*, 18237–18242.

(374) Grant, J. L.; Mitchell, M. E.; Makris, T. M. Catalytic Strategy for Carbon–Carbon Bond Scission by the Cytochrome P450 OleT. *Proc. Natl. Acad. Sci. U. S. A.* **2016**, *113*, 10049–10054.

(375) Zachos, I.; Gafmeyer, S. K.; Sieber, V.; Hollmann, F.; Kourist, R.; Bauer, D. Photobiocatalytic Decarboxylation for Olefin Synthesis. *Chem. Commun.* **2015**, *51*, 1918–1921.

(376) Hsieh, C. H.; Huang, X.; Amaya, J. A.; Rutland, C. D.; Keys, C. L.; Groves, J. T.; Austin, R. N.; Makris, T. M. The Enigmatic P450 Decarboxylase OleT Is Capable of, but Evolved To Frustrate, Oxygen Rebound Chemistry. *Biochemistry* **2017**, *56*, 3347–3357.

(377) Fang, B.; Xu, H.; Liu, Y.; Qi, F.; Zhang, W.; Chen, H.; Wang, C.; Wang, Y.; Yang, W.; Li, S. Mutagenesis and Redox Partners Analysis of the P450 Fatty Acid Decarboxylase OleT<sub>JE</sub>. *Sci. Rep.* **2017**, *7*, 44258.

(378) Rettie, A.; Rettenmeier, A.; Howald, W.; Baillie, T. Cytochrome P450-Catalyzed Formation of Delta 4-VPA, a Toxic Metabolite of Valproic Acid. *Science* **1987**, *235*, 890–893.

(379) Guengerich, F. P. Common and Uncommon Cytochrome P450 Reactions Related to Metabolism and Chemical Toxicity. *Chem. Res. Toxicol.* **2001**, *14*, 611–650.

(380) Rettie, A. E.; Boberg, M.; Rettenmeier, A. W.; Baillie, T. A. Cytochrome P450-Catalyzed Desaturation of Valproic Acid *in vitro*. Species Differences, Induction Effects, and Mechanistic Studies. *J. Biol. Chem.* **1988**, *263*, 13733–13738.

(381) Buist, P. H. Fatty Acid Desaturases: Selecting the Dehydrogenation Channel. *Nat. Prod. Rep.* **2004**, *21*, 249–262.

(382) Behrouzian, B.; Buist, P. H. Fatty Acid Desaturation: Variations on an Oxidative Theme. *Curr. Opin. Chem. Biol.* **2002**, *6*, 577–582.

(383) Ji, L.; Faponle, A. S.; Quesne, M. G.; Sainna, M. A.; Zhang, J.; Franke, A.; Kumar, D.; van Eldik, R.; Liu, W.; de Visser, S. P. Drug Metabolism by Cytochrome P450 Enzymes: What Distinguishes the Pathways Leading to Substrate Hydroxylation Over Desaturation? *Chem. - Eur. J.* **2015**, *21*, 9083–9092.

(384) Lai, W.; Chen, H.; Cohen, S.; Shaik, S. Will P450cam Hydroxylate or Desaturate Alkanes? QM and QM/MM Studies. *J. Phys. Chem. Lett.* **2011**, *2*, 2229–2235.

(385) Zhu, D.; Seo, M.-J.; Ikeda, H.; Cane, D. E. Genome Mining in *Streptomyces*. Discovery of an Unprecedented P450-Catalyzed Oxidative Rearrangement That Is the Final Step in the Biosynthesis of Pentalenolactone. *J. Am. Chem. Soc.* **2011**, *133*, 2128–2131.

(386) Duan, L.; Jogl, G.; Cane, D. E. The Cytochrome P450-Catalyzed Oxidative Rearrangement in the Final Step of Pentalenolactone Biosynthesis: Substrate Structure Determines Mechanism. *J. Am. Chem. Soc.* **2016**, *138*, 12678–12689.

(387) Cane, D. E.; Oliver, J. S.; Harrison, P. H. M.; Abell, C.; Hubbard, B. R.; Kane, C. T.; Lattman, R. Biosynthesis of Pentalenene and Pentalenolactone. *J. Am. Chem. Soc.* **1990**, *112*, 4513–4524.

(388) Liu, W.; Groves, J. T. Manganese Porphyrins Catalyze Selective C–H Bond Halogenations. *J. Am. Chem. Soc.* **2010**, *132*, 12847–12849.

(389) Liu, W.; Huang, X. Y.; Cheng, M. J.; Nielsen, R. J.; Goddard, W. A.; Groves, J. T. Oxidative Aliphatic C–H Fluorination with Fluoride Ion Catalyzed by a Manganese Porphyrin. *Science* **2012**, *337*, 1322–1325.

(390) Huang, X.; Liu, W.; Ren, H.; Neelamegam, R.; Hooker, J. M.; Groves, J. T. Late Stage Benzylic C–H Fluorination with F-18 Fluoride for PET Imaging. *J. Am. Chem. Soc.* **2014**, *136*, 6842–6845.

(391) Huang, X. Y.; Bergsten, T. M.; Groves, J. T. Manganese-Catalyzed Late-Stage Aliphatic C–H Azidation. *J. Am. Chem. Soc.* **2015**, *137*, 5300–5303.

(392) Liu, W.; Huang, X.; Groves, J. T. Oxidative Aliphatic C–H Fluorination with Manganese Catalysts and Fluoride Ion. *Nat. Protoc.* **2013**, *8*, 2348–2354.

(393) Liu, W.; Groves, J. T. Manganese-Catalyzed Oxidative Benzylic C–H Fluorination by Fluoride Ions. *Angew. Chem., Int. Ed.* **2013**, *52*, 6024–6027.

(394) Huang, X.; Zhuang, T.; Kates, P. A.; Gao, H.; Chen, X.; Groves, J. T. Alkyl Isocyanates via Manganese-Catalyzed C–H Activation for the Preparation of Substituted Ureas. *J. Am. Chem. Soc.* **2017**, *139*, 15407–15413.

(395) Martinie, R. J.; Livada, J.; Chang, W. C.; Green, M. T.; Krebs, C.; Bollinger, J. M.; Silakov, A. Experimental Correlation of Substrate Position with Reaction Outcome in the Aliphatic Halogenase, SyrB2. *J. Am. Chem. Soc.* **2015**, *137*, 6912–6919.

(396) Wong, S. D.; Srncic, M.; Matthews, M. L.; Liu, L. V.; Kwak, Y.; Park, K.; Bell, C. B., III; Alp, E. E.; Zhao, J.; Yoda, Y.; et al. Elucidation of the Fe(IV)=O Intermediate in the Catalytic Cycle of the Halogenase SyrB2. *Nature* **2013**, *499*, 320–323.

(397) Blasiak, L. C.; Vaillancourt, F. H.; Walsh, C. T.; Drennan, C. L. Crystal Structure of the Non-Haem Iron Halogenase SyrB2 in Syringomycin Biosynthesis. *Nature* **2006**, *440*, 368–371.

(398) Vaillancourt, F. H.; Yin, J.; Walsh, C. T. SyrB2 in Syringomycin E Biosynthesis Is a Nonheme Fe<sup>II</sup> Alpha-Ketoglutarate- and O<sub>2</sub>-

Dependent Halogenase. *Proc. Natl. Acad. Sci. U. S. A.* **2005**, *102*, 10111–10116.

(399) Mitchell, A. J.; Zhu, Q.; Maggiolo, A. O.; Ananth, N. R.; Hillwig, M. L.; Liu, X.; Boal, A. K. Structural Basis for Halogenation by Iron- and 2-Oxo-Glutarate-Dependent Enzyme WelO5. *Nat. Chem. Biol.* **2016**, *12*, 636–640.

(400) Hillwig, M. L.; Zhu, Q.; Ittiarnornkul, K.; Liu, X. Discovery of a Promiscuous Non-Heme Iron Halogenase in Ambiguine Alkaloid Biogenesis: Implication for an Evolvable Enzyme Family for Late-Stage Halogenation of Aliphatic Carbons in Small Molecules. *Angew. Chem., Int. Ed.* **2016**, *55*, 5780–5784.

(401) Wong, C.; Fujimori, D. G.; Walsh, C. T.; Drennan, C. L. Structural Analysis of an Open Active Site Conformation of Nonheme Iron Halogenase CytC3. *J. Am. Chem. Soc.* **2009**, *131*, 4872–4879.

(402) Kulik, H. J.; Blasiak, L. C.; Marzari, N.; Drennan, C. L. First-Principles Study of Non-heme Fe(II) Halogenase SyrB2 Reactivity. *J. Am. Chem. Soc.* **2009**, *131*, 14426–14433.

(403) Matthews, M. L.; Neumann, C. S.; Miles, L. A.; Grove, T. L.; Booker, S. J.; Krebs, C.; Walsh, C. T.; Bollinger, J. M. Substrate Positioning Controls the Partition Between Halogenation and Hydroxylation in the Aliphatic Halogenase, SyrB2. *Proc. Natl. Acad. Sci. U. S. A.* **2009**, *106*, 17723–17728.

(404) Srncic, M.; Solomon, E. I. Frontier Molecular Orbital Contributions to Chlorination versus Hydroxylation Selectivity in the Non-Heme Iron Halogenase SyrB2. *J. Am. Chem. Soc.* **2017**, *139*, 2396–2407.

(405) Furuya, T.; Kamlet, A. S.; Ritter, T. Catalysis for Fluorination and Trifluoromethylation. *Nature* **2011**, *473*, 470–477.

(406) Thibodeaux, C. J.; Chang, W.-C.; Liu, H.-W. Enzymatic Chemistry of Cyclopropane, Epoxide, and Aziridine Biosynthesis. *Chem. Rev.* **2012**, *112*, 1681–1709.

(407) Alexandrov, K.; Cascorbi, I.; Rojas, M.; Bouvier, G.; Kriek, E.; Bartsch, H. CYP1A1 and GSTM1 Genotypes Affect Benzo[a]Pyrene Dna Adducts in Smokers' Lung: Comparison with Aromatic/Hydrophobic Adduct Formation. *Carcinogenesis* **2002**, *23*, 1969–1977.

(408) de Visser, S. P.; Ogliaro, F.; Harris, N.; Shaik, S. Multi-State Epoxidation of Ethene by Cytochrome P450: a Quantum Chemical Study. *J. Am. Chem. Soc.* **2001**, *123*, 3037–3047.

(409) Kumar, D.; Karamzadeh, B.; Sastry, G. N.; de Visser, S. P. What Factors Influence the Rate Constant of Substrate Epoxidation by Compound I of Cytochrome P450 and Analogous Iron(IV)-Oxo Oxidants? *J. Am. Chem. Soc.* **2010**, *132*, 7656–7667.

(410) Gross, Z.; Nimri, S.; Barzilay, C. M.; Simkhovich, L. Reaction Profile of the Last Step in Cytochrome P450 Catalysis Revealed by Studies of Model Complexes. *JBIC, J. Biol. Inorg. Chem.* **1997**, *2*, 492–506.

(411) Groves, J. T.; Gross, Z.; Stern, M. K. Preparation and Reactivity of Oxoiron(IV) Porphyrins. *Inorg. Chem.* **1994**, *33*, 5065–5072.

(412) de Visser, S. P.; Kumar, D.; Shaik, S. How Do Aldehyde Side Products Occur During Alkene Epoxidation by Cytochrome P450? Theory Reveals a State-Specific Multi-State Scenario Where the High-Spin Component Leads to All Side Products. *J. Inorg. Biochem.* **2004**, *98*, 1183–1193.

(413) Hammer, S. C.; Kubik, G.; Watkins, E.; Huang, S.; Minges, H.; Arnold, F. H. Anti-Markovnikov Alkene Oxidation by Metal-Oxo-Mediated Enzyme Catalysis. *Science* **2017**, *358*, 215–218.

(414) Jerina, D. M.; Daly, J. W.; Witkop, B.; Zaltzman-Nirenberg, P.; Udenfriend, S. 1,2-Naphthalene Oxide as an Intermediate in the Microsomal Hydroxylation of Naphthalene. *V. Biochemistry* **1970**, *9*, 147–156.

(415) Korzekwa, K. R.; Swinney, D. C.; Trager, W. F. Isotopically Labeled Chlorobenzenes as Probes for the Mechanism of Cytochrome P450 Catalyzed Aromatic Hydroxylation. *Biochemistry* **1989**, *28*, 9019–9027.

(416) Rietjens, I. M. C. M.; Soffers, A. E. M. F.; Veeger, C.; Vervoort, J. Regioselectivity of Cytochrome P450 Catalyzed Hydroxylation of Fluorobenzenes Predicted by Calculated Frontier Orbital Substrate Characteristics. *Biochemistry* **1993**, *32*, 4801–4812.

(417) Bathelt, C. M.; Ridder, L.; Mulholland, A. J.; Harvey, J. N. Mechanism and Structure-Reactivity Relationships for Aromatic Hydroxylation by Cytochrome P450. *Org. Biomol. Chem.* **2004**, *2*, 2998–3005.

(418) de Visser, S. P.; Shaik, S. A Proton-Shuttle Mechanism Mediated by the Porphyrin in Benzene Hydroxylation by Cytochrome P450 Enzymes. *J. Am. Chem. Soc.* **2003**, *125*, 7413–7424.

(419) Bathelt, C. M.; Ridder, L.; Mulholland, A. J.; Harvey, J. N. Aromatic Hydroxylation by Cytochrome P450: Model Calculations of Mechanism and Substituent Effects. *J. Am. Chem. Soc.* **2003**, *125*, 15004–15005.

(420) Shaik, S.; Milko, P.; Schyman, P.; Usharani, D.; Chen, H. Trends in Aromatic Oxidation Reactions Catalyzed by Cytochrome P450 Enzymes: A Valence Bond Modeling. *J. Chem. Theory Comput.* **2011**, *7*, 327–339.

(421) Cantú Reinhard, F. G.; Sainna, M. A.; Upadhyay, P.; Balan, G. A.; Kumar, D.; Fornarini, S.; Crestoni, M. E.; de Visser, S. P. A Systematic Account on Aromatic Hydroxylation by a Cytochrome P450 Model Compound I: A Low-Pressure Mass Spectrometry and Computational Study. *Chem. - Eur. J.* **2016**, *22*, 18608–18619.

(422) Asaka, M.; Fujii, H. Participation of Electron Transfer Process in Rate-Limiting Step of Aromatic Hydroxylation Reactions by Compound I Models of Heme Enzymes. *J. Am. Chem. Soc.* **2016**, *138*, 8048–8051.

(423) Jerina, D. M.; Daly, J. W. Arene Oxides: A New Aspect of Drug Metabolism. *Science* **1974**, *185*, 573–582.

(424) Ortiz de Montellano, P. R. In *Cytochrome P450: Structure, Mechanism, and Biochemistry*; Ortiz de Montellano, P. R., Ed.; Springer International Publishing: Cham, 2015.

(425) Preston, B. D.; Miller, J. A.; Miller, E. C. Non-Arene Oxide Aromatic Ring Hydroxylation of 2,2',5,5'-Tetrachlorobiphenyl as the Major Metabolic Pathway Catalyzed by Phenobarbital-Induced Rat Liver Microsomes. *J. Biol. Chem.* **1983**, *258*, 8304–8311.

(426) Tomaszewski, J. E.; Jerina, D. M.; Daly, J. W. Deuterium Isotope Effects During Formation of Phenols by Hepatic Monooxygenases. Evidence for an Alternative to the Arene Oxide Pathway. *Biochemistry* **1975**, *14*, 2024–2031.

(427) Zanger, U. M.; Schwab, M. Cytochrome P450 Enzymes in Drug Metabolism: Regulation of Gene Expression, Enzyme Activities, and Impact of Genetic Variation. *Pharmacol. Ther.* **2013**, *138*, 103–141.

(428) Guengerich, F. P. Enzymatic Oxidation of Xenobiotic Chemicals. *Crit. Rev. Biochem. Mol. Biol.* **1990**, *25*, 97–153.

(429) Fukuto, J. M.; Kumagai, Y.; Cho, A. K. Determination of the Mechanism of Demethylenation of (Methylenedioxy)Phenyl Compounds by Cytochrome P450 Using Deuterium Isotope Effects. *J. Med. Chem.* **1991**, *34*, 2871–2876.

(430) Ichinose, R.; Kurihara, N. Deuterium and Tritium Isotope Effects on the Oxidative Demethylation Rate of Methoxychlor in Rat Liver Microsomes. *J. Pestic. Sci.* **1986**, *11*, 231–236.

(431) Miwa, G. T.; Walsh, J. S.; Lu, A. Y. Kinetic Isotope Effects on Cytochrome P-450-Catalyzed Oxidation Reactions. *J. Biol. Chem.* **1984**, *259*, 3000–3004.

(432) Roberts, K. M.; Jones, J. P. Anilinic N-Oxides Support Cytochrome P450-Mediated N-Dealkylation through Hydrogen-Atom Transfer. *Chem. - Eur. J.* **2010**, *16*, 8096–8107.

(433) Shaffer, C. L.; Morton, M. D.; Hanzlik, R. P. N-Dealkylation of an N-Cyclopropylamine by Horseradish Peroxidase. Fate of the Cyclopropyl Group. *J. Am. Chem. Soc.* **2001**, *123*, 8502–8508.

(434) Shaffer, C. L.; Morton, M. D.; Hanzlik, R. P. Enzymatic N-Dealkylation of an N-Cyclopropylamine: An Unusual Fate for the Cyclopropyl Group. *J. Am. Chem. Soc.* **2001**, *123*, 349–350.

(435) Constantino, L.; Rosa, E.; Iley, J. The Microsomal Demethylation of N,N-Dimethylbenzamides: Substituent and Kinetic Deuterium Isotope Effects. *Biochem. Pharmacol.* **1992**, *44*, 651–658.

(436) Hall, L. R.; Hanzlik, R. P. Kinetic Deuterium Isotope Effects on the N-Demethylation of Tertiary Amides by Cytochrome P-450. *J. Biol. Chem.* **1990**, *265*, 12349–12355.

- (437) Guengerich, F. P.; Yun, C. H.; Macdonald, T. L. Evidence for a 1-Electron Oxidation Mechanism in *N*-Dealkylation of *N,N*-Dialkylanilines by Cytochrome P450 2B1. Kinetic Hydrogen Isotope Effects, Linear Free Energy Relationships, Comparisons with Horseradish Peroxidase, and Studies with Oxygen Surrogates. *J. Biol. Chem.* **1996**, *271*, 27321–27329.
- (438) Miwa, G. T.; Walsh, J. S.; Kedderis, G. L.; Hollenberg, P. F. The Use of Intramolecular Isotope Effects to Distinguish Between Deprotonation and Hydrogen Atom Abstraction Mechanisms in Cytochrome P-450- and Peroxidase-Catalyzed *N*-Demethylation Reactions. *J. Biol. Chem.* **1983**, *258*, 14445–14449.
- (439) Li, C.; Wu, W.; Kumar, D.; Shaik, S. Kinetic Isotope Effect is a Sensitive Probe of Spin State Reactivity in C–H Hydroxylation of *N,N*-Dimethylaniline by Cytochrome P450. *J. Am. Chem. Soc.* **2006**, *128*, 394–395.
- (440) Kumar, D.; Sastry, G. N.; de Visser, S. P. Effect of the Axial Ligand on Substrate Sulfoxidation Mediated by Iron(IV)–Oxo Porphyrin Cation Radical Oxidants. *Chem. - Eur. J.* **2011**, *17*, 6196–6205.
- (441) Shaik, S.; Wang, Y.; Chen, H.; Song, J.; Meir, R. Valence Bond Modelling and Density Functional Theory Calculations of Reactivity and Mechanism of Cytochrome P450 Enzymes: Thioether Sulfoxidation. *Faraday Discuss.* **2010**, *145*, 49–70.
- (442) Li, C.; Zhang, L.; Zhang, C.; Hirao, H.; Wu, W.; Shaik, S. Which Oxidant Is Really Responsible for Sulfur Oxidation by Cytochrome P450? *Angew. Chem., Int. Ed.* **2007**, *46*, 8168–8170.
- (443) Rydberg, P.; Ryde, U.; Olsen, L. Sulfoxide, Sulfur, and Nitrogen Oxidation and Dealkylation by Cytochrome P450. *J. Chem. Theory Comput.* **2008**, *4*, 1369–1377.
- (444) Afzelius, L.; Hasselgren Arnby, C.; Broo, A.; Carlsson, L.; Isaksson, C.; Jurva, U.; Kjellander, B.; Kolmodin, K.; Nilsson, K.; Raubacher, F.; et al. State-of-the-art Tools for Computational Site of Metabolism Predictions: Comparative Analysis, Mechanistical Insights, and Future Applications. *Drug Metab. Rev.* **2007**, *39*, 61–86.
- (445) Seto, Y.; Guengerich, F. P. Partitioning Between *N*-Dealkylation and *N*-Oxygenation in the Oxidation of *N,N*-Dialkylarylamines Catalyzed by Cytochrome P450 2B1. *J. Biol. Chem.* **1993**, *268*, 9986–9997.
- (446) Rydberg, P.; Jørgensen, M. S.; Jacobsen, T. A.; Jacobsen, A.-M.; Madsen, K. G.; Olsen, L. Nitrogen Inversion Barriers Affect the *N*-Oxidation of Tertiary Alkylamines by Cytochromes P450. *Angew. Chem., Int. Ed.* **2013**, *52*, 993–997.
- (447) Li, C.; Zhang, L.; Zhang, C.; Hirao, H.; Wu, W.; Shaik, S. Which Oxidant is Really Responsible for Sulfur Oxidation by Cytochrome P450? *Angew. Chem., Int. Ed.* **2008**, *47*, 8148–8148.
- (448) de Visser, S. P.; Tahsini, L.; Nam, W. How Does the Axial Ligand of Cytochrome P450 Biomimetics Influence the Regioselectivity of Aliphatic versus Aromatic Hydroxylation? *Chem. - Eur. J.* **2009**, *15*, 5577–5587.
- (449) Kumar, D.; Latifi, R.; Kumar, S.; Rybak-Akimova, E. V.; Sainna, M. A.; de Visser, S. P. Rationalization of the Barrier Height for *p*-Z-styrene Epoxidation by Iron(IV)-Oxo Porphyrin Cation Radicals with Variable Axial Ligands. *Inorg. Chem.* **2013**, *52*, 7968–7979.
- (450) Sainna, M. A.; Kumar, S.; Kumar, D.; Fornarini, S.; Crestoni, M. E.; de Visser, S. P. A Comprehensive Test Set of Epoxidation Rate Constants for Iron(IV)-Oxo Porphyrin Cation Radical Complexes. *Chem. Sci.* **2015**, *6*, 1516–1529.
- (451) Kumar, D.; Sastry, G. N.; de Visser, S. P. Axial Ligand Effect On The Rate Constant of Aromatic Hydroxylation By Iron(IV)–Oxo Complexes Mimicking Cytochrome P450 Enzymes. *J. Phys. Chem. B* **2012**, *116*, 718–730.
- (452) Ji, L.; Schüürmann, G. Model and Mechanism: *N*-Hydroxylation of Primary Aromatic Amines by Cytochrome P450. *Angew. Chem., Int. Ed.* **2013**, *52*, 744–748.
- (453) Ripa, L.; Mee, C.; Sjö, P.; Shamovsky, I. Theoretical Studies of the Mechanism of *N*-Hydroxylation of Primary Aromatic Amines by Cytochrome P450 1A2: Radicaloid or Anionic? *Chem. Res. Toxicol.* **2014**, *27*, 265–278.
- (454) Seger, S. T.; Rydberg, P.; Olsen, L. Mechanism of the *N*-Hydroxylation of Primary and Secondary Amines by Cytochrome P450. *Chem. Res. Toxicol.* **2015**, *28*, 597–603.
- (455) Lonsdale, R.; Fort, R. M.; Rydberg, P.; Harvey, J. N.; Mulholland, A. J. Quantum Mechanics/Molecular Mechanics Modeling of Drug Metabolism: Mexiletine *N*-Hydroxylation by Cytochrome P450 1A2. *Chem. Res. Toxicol.* **2016**, *29*, 963–971.
- (456) Gross, Z.; Nimri, S. A Pronounced Axial Ligand Effect on the Reactivity of Oxoiron(IV) Porphyrin Cation Radicals. *Inorg. Chem.* **1994**, *33*, 1731–1732.
- (457) Czarnecki, K.; Nimri, S.; Gross, Z.; Proniewicz, L. M.; Kincaid, J. R. Direct Resonance Raman Evidence for a Trans Influence on the Ferryl Fragment in Models of Compound I Intermediates of Heme Enzymes. *J. Am. Chem. Soc.* **1996**, *118*, 2929–2935.
- (458) Gross, Z. The Effect of Axial Ligands on the Reactivity and Stability of the Oxoferryl Moiety in Model Complexes of Compound I of Heme-Dependent Enzymes. *JBIC, J. Biol. Inorg. Chem.* **1996**, *1*, 368–371.
- (459) Takahashi, A.; Kurahashi, T.; Fujii, H. Effect of Imidazole and Phenolate Axial Ligands on the Electronic Structure and Reactivity of Oxoiron(IV) Porphyrin  $\pi$ -Cation Radical Complexes: Drastic Increase in Oxo-Transfer and Hydrogen Abstraction Reactivities. *Inorg. Chem.* **2009**, *48*, 2614–2625.
- (460) Barber, J. Photosynthetic Energy Conversion: Natural and Artificial. *Chem. Soc. Rev.* **2009**, *38*, 185–196.
- (461) McEvoy, J. P.; Brudvig, G. W. Water-Splitting Chemistry of Photosystem II. *Chem. Rev.* **2006**, *106*, 4455–4483.
- (462) Blakemore, J. D.; Crabtree, R. H.; Brudvig, G. W. Molecular Catalysts for Water Oxidation. *Chem. Rev.* **2015**, *115*, 12974–13005.
- (463) Karkas, M. D.; Verho, O.; Johnston, E. V.; Åkermark, B. Artificial Photosynthesis: Molecular Systems for Catalytic Water Oxidation. *Chem. Rev.* **2014**, *114*, 11863–12001.
- (464) Solomon, E. I.; Heppner, D. E.; Johnston, E. M.; Ginsbach, J. W.; Cirera, J.; Qayyum, M.; Kieber-Emmons, M. T.; Kjaergaard, C. H.; Hadt, R. G.; Tian, L. Copper Active Sites in Biology. *Chem. Rev.* **2014**, *114*, 3659–3853.
- (465) Tolman, W. B. Making and Breaking the Dioxygen O–O Bond: New Insights from Studies of Synthetic Copper Complexes. *Acc. Chem. Res.* **1997**, *30*, 227–237.
- (466) Halfen, J. A.; Mahapatra, S.; Wilkinson, E. C.; Kaderli, S.; Young, V. G.; Que, L.; Zuberbühler, A. D.; Tolman, W. B. Reversible Cleavage and Formation of the Dioxygen O–O Band Within a Dicopper Complex. *Science* **1996**, *271*, 1397–1400.
- (467) Cox, N.; Retegan, M.; Neese, F.; Pantazis, D. A.; Boussac, A.; Lubitz, W. Electronic Structure of the Oxygen-Evolving Complex in Photosystem II Prior to O–O Bond Formation. *Science* **2014**, *345*, 804–808.
- (468) Siegbahn, P. E. M. Structures and Energetics for O<sub>2</sub> Formation in Photosystem II. *Acc. Chem. Res.* **2009**, *42*, 1871–1880.
- (469) Askerka, M.; Brudvig, G. W.; Batista, V. S. The O<sub>2</sub>-Evolving Complex of Photosystem II: Recent Insights from Quantum Mechanics/Molecular Mechanics (QM/MM), Extended X-ray Absorption Fine Structure (EXAFS), and Femtosecond X-ray Crystallography Data. *Acc. Chem. Res.* **2017**, *50*, 41–48.
- (470) Suga, M.; Akita, F.; Sugahara, M.; Kubo, M.; Nakajima, Y.; Nakane, T.; Yamashita, K.; Umena, Y.; Nakabayashi, M.; Yamane, T.; et al. Light-Induced Structural Changes and the Site of O=O Bond Formation in PSII Caught by XFEL. *Nature* **2017**, *543*, 131–135.
- (471) Naruta, Y.; Sasayama, M.-a.; Sasaki, T. Oxygen Evolution by Oxidation of Water with Manganese Porphyrin Dimers. *Angew. Chem., Int. Ed. Engl.* **1994**, *33*, 1839–1841.
- (472) Gao, Y.; Åkermark, T.; Liu, J.; Sun, L.; Åkermark, B. Nucleophilic Attack of Hydroxide on a Mn<sup>V</sup> Oxo Complex: A Model of the O–O Bond Formation in the Oxygen Evolving Complex of Photosystem II. *J. Am. Chem. Soc.* **2009**, *131*, 8726–8727.
- (473) Kim, S. H.; Park, H.; Seo, M. S.; Kubo, M.; Ogura, T.; Klajn, J.; Gryko, D. T.; Valentine, J. S.; Nam, W. Reversible O–O Bond Cleavage and Formation between Mn(IV)-Peroxo and Mn(V)-Oxo Corroles. *J. Am. Chem. Soc.* **2010**, *132*, 14030–14032.

- (474) Dogutan, D. K.; McGuire, R.; Nocera, D. G. Electrocatalytic Water Oxidation by Cobalt(III) Hexaammine  $\beta$ -Octafluoro Corroles. *J. Am. Chem. Soc.* **2011**, *133*, 9178–9180.
- (475) Nakazono, T.; Parent, A. R.; Sakai, K. Cobalt Porphyrins as Homogeneous Catalysts for Water Oxidation. *Chem. Commun.* **2013**, *49*, 6325–6327.
- (476) Nakazono, T.; Parent, A. R.; Sakai, K. Improving Singlet Oxygen Resistance during Photochemical Water Oxidation by Cobalt Porphyrin Catalysts. *Chem. - Eur. J.* **2015**, *21*, 6723–6726.
- (477) Wang, D.; Groves, J. T. Efficient Water Oxidation Catalyzed by Homogeneous Cationic Cobalt Porphyrins with Critical Roles for the Buffer Base. *Proc. Natl. Acad. Sci. U. S. A.* **2013**, *110*, 15579–15584.
- (478) Artero, V.; Fontecave, M. Solar Fuels Generation and Molecular Systems: Is It Homogeneous or Heterogeneous Catalysis? *Chem. Soc. Rev.* **2013**, *42*, 2338–2356.
- (479) Han, Y.; Wu, Y.; Lai, W.; Cao, R. Electrocatalytic Water Oxidation by a Water-Soluble Nickel Porphyrin Complex at Neutral pH with Low Overpotential. *Inorg. Chem.* **2015**, *54*, 5604–5613.
- (480) Coates, J. D.; Achenbach, L. A. Microbial Perchlorate Reduction: Rocket-Fuelled Metabolism. *Nat. Rev. Microbiol.* **2004**, *2*, 569–580.
- (481) DuBois, J. L.; Ojha, S. In *Sustaining Life on Planet Earth: Metalloenzymes Mastering Dioxygen and Other Chewy Gases*; Kroneck, P. M. H., Sosa Torres, M. E., Eds.; Springer International Publishing: Cham, 2015.
- (482) Schaffner, I.; Hofbauer, S.; Krutzler, M.; Pirker, K. F.; Furtmüller, P. G.; Obinger, C. Mechanism of Chlorite Degradation to Chloride and Dioxygen by the Enzyme Chlorite Dismutase. *Arch. Biochem. Biophys.* **2015**, *574*, 18–26.
- (483) Lee, A. Q.; Streit, B. R.; Zdilla, M. J.; Abu-Omar, M. M.; DuBois, J. L. Mechanism of and Exquisite Selectivity for O–O Bond Formation by the Heme-Dependent Chlorite Dismutase. *Proc. Natl. Acad. Sci. U. S. A.* **2008**, *105*, 15654–15659.
- (484) Mayfield, J. A.; Blanc, B.; Rodgers, K. R.; Lukat-Rodgers, G. S.; DuBois, J. L. Peroxidase-Type Reactions Suggest a Heterolytic/Nucleophilic O–O Joining Mechanism in the Heme-Dependent Chlorite Dismutase. *Biochemistry* **2013**, *52*, 6982–6994.
- (485) Celis, A. I.; Geeraerts, Z.; Ngmenterebo, D.; Machovina, M. M.; Kurker, R. C.; Rajakumar, K.; Ivancich, A.; Rodgers, K. R.; Lukat-Rodgers, G. S.; DuBois, J. L. A Dimeric Chlorite Dismutase Exhibits O<sub>2</sub>-Generating Activity and Acts as a Chlorite Antioxidant in *Klebsiella pneumoniae* MGH 78578. *Biochemistry* **2015**, *54*, 434–446.
- (486) Hofbauer, S.; Gruber, C.; Pirker, K. F.; Sündermann, A.; Schaffner, I.; Jakopitsch, C.; Oostenbrink, C.; Furtmüller, P. G.; Obinger, C. Transiently Produced Hypochlorite Is Responsible for the Irreversible Inhibition of Chlorite Dismutase. *Biochemistry* **2014**, *53*, 3145–3157.
- (487) Sündermann, A.; Reif, M. M.; Hofbauer, S.; Obinger, C.; Oostenbrink, C. Investigation of Ion Binding in Chlorite Dismutases by Means of Molecular Dynamics Simulations. *Biochemistry* **2014**, *53*, 4869–4879.
- (488) Schaffner, I.; Mlynek, G.; Flego, N.; Pühringer, D.; Libiseller-Egger, J.; Coates, L.; Hofbauer, S.; Bellei, M.; Furtmüller, P. G.; Battistuzzi, G.; et al. Molecular Mechanism of Enzymatic Chlorite Detoxification: Insights from Structural and Kinetic Studies. *ACS Catal.* **2017**, *7*, 7962–7976.
- (489) Slaughter, L. M.; Collman, J. P.; Eberspacher, T. A.; Brauman, J. I. Radical Autoxidation and Autogenous O<sub>2</sub> Evolution in Manganese–Porphyrin Catalyzed Alkane Oxidations with Chlorite. *Inorg. Chem.* **2004**, *43*, 5198–5204.
- (490) Zdilla, M. J.; Lee, A. Q.; Abu-Omar, M. M. Concerted Dismutation of Chlorite Ion: Water-Soluble Iron-Porphyrins As First Generation Model Complexes for Chlorite Dismutase. *Inorg. Chem.* **2009**, *48*, 2260–2268.
- (491) Umile, T. P.; Groves, J. T. Catalytic Generation of Chlorine Dioxide from Chlorite Using a Water-Soluble Manganese Porphyrin. *Angew. Chem., Int. Ed.* **2011**, *50*, 695–698.
- (492) Umile, T. P.; Wang, D.; Groves, J. T. Dissection of the Mechanism of Manganese Porphyrin-Catalyzed Chlorine Dioxide Generation. *Inorg. Chem.* **2011**, *50*, 10353–10362.
- (493) Hicks, S. D.; Petersen, J. L.; Bougher, C. J.; Abu-Omar, M. M. Chlorite Dismutation to Chlorine Dioxide Catalyzed by a Water-Soluble Manganese Porphyrin. *Angew. Chem., Int. Ed.* **2011**, *50*, 699–702.
- (494) Hicks, S. D.; Xiong, S.; Bougher, C. J.; Medvedev, G. A.; Caruthers, J.; Abu-Omar, M. M. Mechanistic Study of a Manganese Porphyrin Catalyst for On-Demand Production of Chlorine Dioxide in Water. *J. Porphyrins Phthalocyanines* **2015**, *19*, 492–499.
- (495) de Montellano, P. R. O. In *Biocatalysis Based on Heme Peroxidases: Peroxidases as Potential Industrial Biocatalysts*; Torres, E., Ayala, M., Eds.; Springer: Berlin, 2010.
- (496) Raven, E. L. In *Encyclopedia of Biophysics*; Roberts, G. C. K., Ed.; Springer: Berlin, 2013.
- (497) Hofrichter, M.; Kellner, H.; Pecyna, M. J.; Ullrich, R. In *Monooxygenase, Peroxidase and Peroxygenase Properties and Mechanisms of Cytochrome P450*; Hrycak, E. G., Bandiera, S. M., Eds.; Springer International Publishing: Cham, 2015.
- (498) Kwon, H.; Moody, P. C. E.; Raven, E. L. In *Heme Peroxidases*; The Royal Society of Chemistry: Cambridge, UK, 2016.
- (499) Macdonald, I. K.; Badyal, S. K.; Ghamsari, L.; Moody, P. C. E.; Raven, E. L. Interaction of Ascorbate Peroxidase with Substrates: A Mechanistic and Structural Analysis. *Biochemistry* **2006**, *45*, 7808–7817.
- (500) Efimov, I.; Badyal, S. K.; Metcalfe, C. L.; Macdonald, I.; Gumiero, A.; Raven, E. L.; Moody, P. C. E. Proton Delivery to Ferryl Heme in a Heme Peroxidase: Enzymatic Use of the Grotthuss Mechanism. *J. Am. Chem. Soc.* **2011**, *133*, 15376–15383.
- (501) Guallar, V. Heme Electron Transfer in Peroxidases: The Propionate e-Pathway. *J. Phys. Chem. B* **2008**, *112*, 13460–13464.
- (502) Ruiz-Duenas, F. J.; Pogni, R.; Morales, M.; Giansanti, S.; Mate, M. J.; Romero, A.; Martinez, M. J.; Basosi, R.; Martinez, A. T. Protein Radicals in Fungal Versatile Peroxidase: Catalytic Tryptophan Radical in Both Compound I and Compound II and Studies on W164Y, W164H, and W164S Variants. *J. Biol. Chem.* **2009**, *284*, 7986–7994.
- (503) Gray, H. B.; Winkler, J. R. Long-Range Electron Transfer. *Proc. Natl. Acad. Sci. U. S. A.* **2005**, *102*, 3534–3539.
- (504) Sáez-Jiménez, V.; Baratto, M. C.; Pogni, R.; Rencoret, J.; Gutiérrez, A.; Santos, J. I.; Martínez, A. T.; Ruiz-Dueñas, F. J. Demonstration of Lignin-To-Peroxidase Direct Electron Transfer: a Transient-State Kinetics, Directed Mutagenesis, EPR, and NMR Study. *J. Biol. Chem.* **2015**, *290*, 23201–23213.
- (505) Harvey, P. J.; Palmer, J. M. Oxidation of Phenolic Compounds by Ligninase. *J. Biotechnol.* **1990**, *13*, 169–179.
- (506) Tsai, A.-L.; Kulmacz, R. J. Prostaglandin H Synthase: Resolved and Unresolved Mechanistic Issues. *Arch. Biochem. Biophys.* **2010**, *493*, 103–124.
- (507) Rouzer, C. A.; Marnett, L. J. Mechanism of Free Radical Oxygenation of Polyunsaturated Fatty Acids by Cyclooxygenases. *Chem. Rev.* **2003**, *103*, 2239–2304.
- (508) Dailey, H. A.; Gerdes, S.; Dailey, T. A.; Burch, J. S.; Phillips, J. D. Noncanonical Coproporphyrin-Dependent Bacterial Heme Biosynthesis Pathway That Does Not Use Protoporphyrin. *Proc. Natl. Acad. Sci. U. S. A.* **2015**, *112*, 2210–2215.
- (509) Celis, A. I.; Gauss, G. H.; Streit, B. R.; Shisler, K.; Moraski, G. C.; Rodgers, K. R.; Lukat-Rodgers, G. S.; Peters, J. W.; DuBois, J. L. Structure-Based Mechanism for Oxidative Decarboxylation Reactions Mediated by Amino Acids and Heme Propionates in Coproheme Decarboxylase (HemQ). *J. Am. Chem. Soc.* **2017**, *139*, 1900–1911.
- (510) Streit, B. R.; Celis, A. I.; Shisler, K.; Rodgers, K. R.; Lukat-Rodgers, G. S.; DuBois, J. L. Reactions of Ferrous Coproheme Decarboxylase (HemQ) with O<sub>2</sub> and H<sub>2</sub>O<sub>2</sub> Yield Ferric Heme b. *Biochemistry* **2017**, *56*, 189–201.
- (511) Andreou, A.; Brodhun, F.; Feussner, I. Biosynthesis of Oxylipins in Non-Mammals. *Prog. Lipid Res.* **2009**, *48*, 148–170.

- (512) Brash, A. R. Mechanistic Aspects of CYP74 Allene Oxide Synthases and Related Cytochrome P450 Enzymes. *Phytochemistry* **2009**, *70*, 1522–1531.
- (513) Jahn, U.; Galano, J.-M.; Durand, T. Beyond Prostaglandins—Chemistry and Biology of Cyclic Oxygenated Metabolites Formed by Free-Radical Pathways from Polyunsaturated Fatty Acids. *Angew. Chem., Int. Ed.* **2008**, *47*, 5894–5955.
- (514) Das, S.; Chandrasekhar, S.; Yadav, J. S.; Grée, R. Recent Developments in the Synthesis of Prostaglandins and Analogues. *Chem. Rev.* **2007**, *107*, 3286–3337.
- (515) Ullrich, V.; Brugger, R. Prostacyclin and Thromboxane Synthase: New Aspects of Hemethiolate Catalysis. *Angew. Chem., Int. Ed. Engl.* **1994**, *33*, 1911–1919.
- (516) Smith, W. L.; Urade, Y.; Jakobsson, P.-J. Enzymes of the Cyclooxygenase Pathways of Prostanoid Biosynthesis. *Chem. Rev.* **2011**, *111*, 5821–5865.
- (517) Audran, G.; Brémond, P.; Marque, S. R. A.; Siri, D.; Santelli, M. Energetics of the Biosynthesis of Prostanoids from Arachidonate. *Tetrahedron* **2015**, *71*, 6920–6927.
- (518) Grechkin, A. N. Hydroperoxide Lyase and Divinyl Ether Synthase. *Prostaglandins Other Lipid Mediators* **2002**, *68–69*, 457–470.
- (519) Hughes, R. K.; De Domenico, S.; Santino, A. Plant Cytochrome CYP74 Family: Biochemical Features, Endocellular Localisation, Activation Mechanism in Plant Defence and Improvements for Industrial Applications. *ChemBioChem* **2009**, *10*, 1122–1133.
- (520) Lee, D.-S.; Nioche, P.; Hamberg, M.; Raman, C. S. Structural Insights into the Evolutionary Paths of Oxylipin Biosynthetic Enzymes. *Nature* **2008**, *455*, 363–368.
- (521) Oldham, M. L.; Brash, A. R.; Newcomer, M. E. The Structure of Coral Allene Oxide Synthase Reveals a Catalase Adapted for Metabolism of a Fatty Acid Hydroperoxide. *Proc. Natl. Acad. Sci. U. S. A.* **2005**, *102*, 297–302.
- (522) Mashhadi, Z.; Newcomer, M. E.; Brash, A. R. The Thr–His Connection on the Distal Heme of Catalase-Related Hemoproteins: A Hallmark of Reaction with Fatty Acid Hydroperoxides. *ChemBioChem* **2016**, *17*, 2000–2006.
- (523) Brash, A. R.; Hughes, M. A.; Hawkins, D. J.; Boeglin, W. E.; Song, W. C.; Meijer, L. Allene Oxide and Aldehyde Biosynthesis in Starfish Oocytes. *J. Biol. Chem.* **1991**, *266*, 22926–22931.
- (524) Gao, B.; Boeglin, W. E.; Zheng, Y.; Schneider, C.; Brash, A. R. Evidence for an Ionic Intermediate in the Transformation of Fatty Acid Hydroperoxide by a Catalase-related Allene Oxide Synthase from the Cyanobacterium *Acaryochloris marina*. *J. Biol. Chem.* **2009**, *284*, 22087–22098.
- (525) Teder, T.; Lohelaid, H.; Boeglin, W. E.; Calcutt, W. M.; Brash, A. R.; Samel, N. A Catalase-Related Hemoprotein in Coral Is Specialized for Synthesis of Short-Chain Aldehydes: Discovery of P450-Type Hydroperoxide Lyase Activity in a Catalase. *J. Biol. Chem.* **2015**, *290*, 19823–19832.
- (526) Brash, A. R.; Niraula, N. P.; Boeglin, W. E.; Mashhadi, Z. An Ancient Relative of Cyclooxygenase in Cyanobacteria Is a Linoleate 10S-Dioxygenase That Works in Tandem with a Catalase-related Protein with Specific 10S-Hydroperoxide Lyase Activity. *J. Biol. Chem.* **2014**, *289*, 13101–13111.
- (527) Hung, R.; Lee, S.; Bennett, J. W. Fungal Volatile Organic Compounds and Their Role in Ecosystems. *Appl. Microbiol. Biotechnol.* **2015**, *99*, 3395–3405.
- (528) Schneider, C.; Niisuke, K.; Boeglin, W. E.; Voehler, M.; Stec, D. F.; Porter, N. A.; Brash, A. R. Enzymatic Synthesis of a Bicyclobutane Fatty Acid by a Hemoprotein–Lipoxygenase Fusion Protein from the Cyanobacterium *Anabaena* PCC 7120. *Proc. Natl. Acad. Sci. U. S. A.* **2007**, *104*, 18941–18945.
- (529) Plate, L.; Marletta, M. A. Nitric Oxide-Sensing H-NOX Proteins Govern Bacterial Communal Behavior. *Trends Biochem. Sci.* **2013**, *38*, 566–575.
- (530) Cary, S. P. L.; Winger, J. A.; Derbyshire, E. R.; Marletta, M. A. Nitric Oxide Signaling: No Longer Simply on or Off. *Trends Biochem. Sci.* **2006**, *31*, 231–239.
- (531) Shimizu, T.; Huang, D.; Yan, F.; Stranova, M.; Bartosova, M.; Fojtíková, V.; Martínková, M. Gaseous O<sub>2</sub>, NO, and CO in Signal Transduction: Structure and Function Relationships of Heme-Based Gas Sensors and Heme-Redox Sensors. *Chem. Rev.* **2015**, *115*, 6491–6533.
- (532) Millett, E. S.; Efimov, I.; Basran, J.; Handa, S.; Mowat, C. G.; Raven, E. L. Heme-Containing Dioxygenases Involved in Tryptophan Oxidation. *Curr. Opin. Chem. Biol.* **2012**, *16*, 60–66.
- (533) Geng, J.; Liu, A. Heme-Dependent Dioxygenases in Tryptophan Oxidation. *Arch. Biochem. Biophys.* **2014**, *544*, 18–26.
- (534) Hayaishi, O.; Rothberg, S.; Mehler, A. H.; Saito, Y. Studies on Oxygenases; Enzymatic Formation of Kynurenine from Tryptophan. *J. Biol. Chem.* **1957**, *229*, 889–896.
- (535) Yamamoto, S.; Hayaishi, O. Tryptophan Pyrrolase of Rabbit Intestine. D- and L-Tryptophan-Cleaving Enzyme or Enzymes. *J. Biol. Chem.* **1967**, *242*, 5260–5266.
- (536) Hirata, F.; Hayaishi, O.; Tokuyama, T.; Senoh, S. *In Vitro* and *in vivo* Formation of Two New Metabolites of Melatonin. *J. Biol. Chem.* **1974**, *249*, 1311–1313.
- (537) Mellor, A. L.; Munn, D. H. Ido Expression by Dendritic Cells: Tolerance and Tryptophan Catabolism. *Nat. Rev. Immunol.* **2004**, *4*, 762–774.
- (538) Prendergast, G. C. Immune Escape as a Fundamental Trait of Cancer: Focus on Ido. *Oncogene* **2008**, *27*, 3889–3900.
- (539) Efimov, I.; Basran, J.; Thackray, S. J.; Handa, S.; Mowat, C. G.; Raven, E. L. Structure and Reaction Mechanism in the Heme Dioxygenases. *Biochemistry* **2011**, *50*, 2717–2724.
- (540) Chauhan, N.; Thackray, S. J.; Rafice, S. A.; Eaton, G.; Lee, M.; Efimov, I.; Basran, J.; Jenkins, P. R.; Mowat, C. G.; Chapman, S. K.; et al. Reassessment of the Reaction Mechanism in the Heme Dioxygenases. *J. Am. Chem. Soc.* **2009**, *131*, 4186–4187.
- (541) Geng, J.; Dornevil, K.; Liu, A. Chemical Rescue of the Distal Histidine Mutants of Tryptophan 2,3-Dioxygenase. *J. Am. Chem. Soc.* **2012**, *134*, 12209–12218.
- (542) Lu, C.; Lin, Y.; Yeh, S.-R. Inhibitory Substrate Binding Site of Human Indoleamine 2,3-Dioxygenase. *J. Am. Chem. Soc.* **2009**, *131*, 12866–12867.
- (543) Chung, L. W.; Li, X.; Sugimoto, H.; Shiro, Y.; Morokuma, K. Density Functional Theory Study on a Missing Piece in Understanding of Heme Chemistry: The Reaction Mechanism for Indoleamine 2,3-Dioxygenase and Tryptophan 2,3-Dioxygenase. *J. Am. Chem. Soc.* **2008**, *130*, 12299–12309.
- (544) Lewis-Ballester, A.; Batabyal, D.; Egawa, T.; Lu, C.; Lin, Y.; Marti, M. A.; Capece, L.; Estrin, D. A.; Yeh, S.-R. Evidence for a Ferryl Intermediate in a Heme-Based Dioxygenase. *Proc. Natl. Acad. Sci. U. S. A.* **2009**, *106*, 17371–17376.
- (545) Booth, E. S.; Basran, J.; Lee, M.; Handa, S.; Raven, E. L. Substrate Oxidation by Indoleamine 2,3-Dioxygenase: EVIDENCE FOR A COMMON REACTION MECHANISM. *J. Biol. Chem.* **2015**, *290*, 30924–30930.
- (546) Sachiko, Y.; Keiko, Y.; Yumi, H.; Masaki, H.; Hiroshi, S.; Yoshitsugu, S.; Appelman, E. H.; Takashi, O. Identification of the Fe–O<sub>2</sub> and the Fe=O Heme Species for Indoleamine 2,3-Dioxygenase during Catalytic Turnover. *Chem. Lett.* **2010**, *39*, 36–37 10.1246/cl.2010.36.
- (547) Freewan, M.; Rees, M. D.; Plaza, T. S.; Glaros, E.; Lim, Y. J.; Wang, X. S.; Yeung, A. W.; Witting, P. K.; Terentis, A. C.; Thomas, S. R. Human Indoleamine 2,3-Dioxygenase Is a Catalyst of Physiological Heme Peroxidase Reactions: Implications for the Inhibition of Dioxygenase Activity by Hydrogen Peroxide. *J. Biol. Chem.* **2013**, *288*, 1548–1567.
- (548) Lu, C.; Yeh, S.-R. Ferryl Derivatives of Human Indoleamine 2,3-Dioxygenase. *J. Biol. Chem.* **2011**, *286*, 21220–21230.
- (549) Fu, R.; Gupta, R.; Geng, J.; Dornevil, K.; Wang, S.; Zhang, Y.; Hendrich, M. P.; Liu, A. Enzyme Reactivation by Hydrogen Peroxide in Heme-based Tryptophan Dioxygenase. *J. Biol. Chem.* **2011**, *286*, 26541–26554.
- (550) Basran, J.; Booth, E. S.; Lee, M.; Handa, S.; Raven, E. L. Analysis of Reaction Intermediates in Tryptophan 2,3-Dioxygenase: A

Comparison with Indoleamine 2,3-Dioxygenase. *Biochemistry* **2016**, *55*, 6743–6750.

(551) Gardner, P. R.; Gardner, A. M.; Martin, L. A.; Salzman, A. L. Nitric Oxide Dioxygenase: an Enzymic Function for Flavohemoglobin. *Proc. Natl. Acad. Sci. U. S. A.* **1998**, *95*, 10378–10383.

(552) Gardner, P. R. Nitric Oxide Dioxygenase Function and Mechanism of Flavohemoglobin, Hemoglobin, Myoglobin and Their Associated Reductases. *J. Inorg. Biochem.* **2005**, *99*, 247–266.

(553) Su, J.; Groves, J. T. Mechanisms of Peroxynitrite Interactions with Heme Proteins. *Inorg. Chem.* **2010**, *49*, 6317–6329.

(554) Su, J.; Groves, J. T. Direct Detection of the Oxygen Rebound Intermediates, Ferryl Mb and NO<sub>2</sub>, in the Reaction of metMyoglobin with Peroxynitrite. *J. Am. Chem. Soc.* **2009**, *131*, 12979–12988.

(555) Barry, S. M.; Kers, J. A.; Johnson, E. G.; Song, L.; Aston, P. R.; Patel, B.; Krasnoff, S. B.; Crane, B. R.; Gibson, D. M.; Loria, R.; et al. Cytochrome P450-Catalyzed L-Tryptophan Nitration in Thaxtomin Phytotoxin Biosynthesis. *Nat. Chem. Biol.* **2012**, *8*, 814–816.

(556) Dodani, S. C.; Kiss, G.; Cahn, J. K. B.; Su, Y.; Pande, V. S.; Arnold, F. H. Discovery of a Regioselectivity Switch in Nitrating P450s Guided by Molecular Dynamics Simulations and Markov Models. *Nat. Chem.* **2016**, *8*, 419–425.

(557) Yoshikawa, S.; Shimada, A. Reaction Mechanism of Cytochrome *c* Oxidase. *Chem. Rev.* **2015**, *115*, 1936–1989.

(558) Yoshikawa, S.; Shinzawa-Itoh, K.; Nakashima, R.; Yaono, R.; Yamashita, E.; Inoue, N.; Yao, M.; Fei, M. J.; Libeu, C. P.; Mizushima, T.; et al. Redox-Coupled Crystal Structural Changes in Bovine Heart Cytochrome *c* Oxidase. *Science* **1998**, *280*, 1723–1729.

(559) Ostermeier, C.; Harrenga, A.; Ermler, U.; Michel, H. Structure at 2.7 Å Resolution of the *Paracoccus denitrificans* Two-Subunit Cytochrome *c* Oxidase Complexed with an Antibody Fv Fragment. *Proc. Natl. Acad. Sci. U. S. A.* **1997**, *94*, 10547–10553.

(560) Lyons, J. A.; Aragao, D.; Slattery, O.; Pislakov, A. V.; Soulimane, T.; Caffrey, M. Structural Insights into Electron Transfer in *caa*<sub>3</sub>-Type Cytochrome Oxidase. *Nature* **2012**, *487*, 514–518.

(561) Blomberg, M. R. A.; Siegbahn, P. E. M. How Cytochrome *c* Oxidase Can Pump Four Protons per Oxygen Molecule at High Electrochemical Gradient. *Biochim. Biophys. Acta, Bioenerg.* **2015**, *1847*, 364–376.

(562) Sharma, V.; Wikström, M. The Role of the *K*-Channel and the Active-Site Tyrosine in the Catalytic Mechanism of Cytochrome *c* Oxidase. *Biochim. Biophys. Acta, Bioenerg.* **2016**, *1857*, 1111–1115.

(563) Muramoto, K.; Ohta, K.; Shinzawa-Itoh, K.; Kanda, K.; Taniguchi, M.; Nabekura, H.; Yamashita, E.; Tsukihara, T.; Yoshikawa, S. Bovine Cytochrome *c* Oxidase Structures Enable O<sub>2</sub> Reduction with Minimization of Reactive Oxygens and Provide a Proton-Pumping Gate. *Proc. Natl. Acad. Sci. U. S. A.* **2010**, *107*, 7740–7745.

(564) Hirota, S.; Ogura, T.; Shinzawa-Itoh, K.; Yoshikawa, S.; Kitagawa, T. Observation of Multiple CN-Isotope-Sensitive Raman Bands for CN- Adducts of Hemoglobin, Myoglobin, and Cytochrome *c* Oxidase: Evidence for Vibrational Coupling between the Fe–C–N Bending and Porphyrin In-Plane Modes. *J. Phys. Chem.* **1996**, *100*, 15274–15279.

(565) Pinakoulaki, E.; Vamvouka, M.; Varotsis, C. Resonance Raman Detection of the Fe<sup>2+</sup>–C–N Modes in Heme–Copper Oxidases: A Probe of the Active Site. *Inorg. Chem.* **2004**, *43*, 4907–4910.

(566) Pinakoulaki, E.; Vamvouka, M.; Varotsis, C. The Active Site Structure of Heme a<sub>3</sub><sup>3+</sup>-C:N-Cu<sub>B</sub><sup>2+</sup> of Cytochrome a<sub>3</sub> Oxidase as Revealed from Resonance Raman Scattering. *J. Phys. Chem. B* **2003**, *107*, 9865–9868.

(567) Kim, Y.; Babcock, G. T.; Surerus, K. K.; Fee, J. A.; Dyer, R. B.; Woodruff, W. H.; Oertling, W. A. Cyanide Binding and Active Site Structure in Heme-Copper Oxidases: Normal Coordinate Analysis of Iron-Cyanide Vibrations of a<sub>3</sub><sup>2+</sup> CN<sup>-</sup> Complexes of Cytochromes ba<sub>3</sub> and aa<sub>3</sub>. *Biospectroscopy* **1998**, *4*, 1–15.

(568) Hematian, S.; Garcia-Bosch, I.; Karlin, K. D. Synthetic Heme/Copper Assemblies: Toward an Understanding of Cytochrome *c* Oxidase Interactions with Dioxygen and Nitrogen Oxides. *Acc. Chem. Res.* **2015**, *48*, 2462–2474.

(569) Mukherjee, S.; Mukherjee, A.; Bhagi-Damodaran, A.; Mukherjee, M.; Lu, Y.; Dey, A. A Biosynthetic Model of Cytochrome *c* Oxidase as an Electrocatalyst for Oxygen Reduction. *Nat. Commun.* **2015**, *6*, 8467.

(570) Halime, Z.; Kotani, H.; Li, Y.; Fukuzumi, S.; Karlin, K. D. Homogeneous Catalytic O<sub>2</sub> Reduction to Water by a Cytochrome *c* Oxidase Model with Trapping of Intermediates and Mechanistic Insights. *Proc. Natl. Acad. Sci. U. S. A.* **2011**, *108*, 13990–13994.

(571) Collman, J. P.; Devaraj, N. K.; Decréau, R. A.; Yang, Y.; Yan, Y.-L.; Ebina, W.; Eberspacher, T. A.; Chidsey, C. E. D. A Cytochrome *c* Oxidase Model Catalyzes Oxygen to Water Reduction Under Rate-Limiting Electron Flux. *Science* **2007**, *315*, 1565–1568.

(572) Fox, S.; Nanthakumar, A.; Wikström, M.; Karlin, K. D.; Blackburn, N. J. XAS Structural Comparisons of Reversibly Interconvertible Oxo- and Hydroxo-Bridged Heme-Copper Oxidase Model Compounds. *J. Am. Chem. Soc.* **1996**, *118*, 24–34.

(573) Collman, J. P.; Herrmann, P. C.; Boitrel, B.; Zhang, X.; Eberspacher, T. A.; Fu, L.; Wang, J.; Rousseau, D. L.; Williams, E. R. Synthetic Analog for the Oxygen Binding Site in Cytochrome *c* Oxidase. *J. Am. Chem. Soc.* **1994**, *116*, 9783–9784.

(574) Chufán, E. E.; Puiu, S. C.; Karlin, K. D. Heme–Copper/Dioxygen Adduct Formation, Properties, and Reactivity. *Acc. Chem. Res.* **2007**, *40*, 563–572.

(575) Chufán, E. E.; Karlin, K. D. An Iron–Peroxo Porphyrin Complex: New Synthesis and Reactivity Toward a Cu(II) Complex Giving a Heme–Peroxo–Copper Adduct. *J. Am. Chem. Soc.* **2003**, *125*, 16160–16161.

(576) del Río, D.; Sarangi, R.; Chufán, E. E.; Karlin, K. D.; Hedman, B.; Hodgson, K. O.; Solomon, E. I. Geometric and Electronic Structure of the Heme–Peroxo–Copper Complex [(F<sub>8</sub>TPP)Fe<sup>III</sup>–(O<sub>2</sub>)–Cu<sup>II</sup>(TMPA)](ClO<sub>4</sub>). *J. Am. Chem. Soc.* **2005**, *127*, 11969–11978.

(577) Chishiro, T.; Shimazaki, Y.; Tani, F.; Tachi, Y.; Naruta, Y.; Karasawa, S.; Hayami, S.; Maeda, Y. Isolation and Crystal Structure of a Peroxo-Bridged Heme–Copper Complex. *Angew. Chem.* **2003**, *115*, 2894–2897.

(578) Halime, Z.; Kieber-Emmons, M. T.; Qayyum, M. F.; Mondal, B.; Gandhi, T.; Puiu, S. C.; Chufán, E. E.; Sarjeant, A. A. N.; Hodgson, K. O.; Hedman, B.; et al. Heme–Copper–Dioxygen Complexes: Toward Understanding Ligand-Environmental Effects on the Coordination Geometry, Electronic Structure, and Reactivity. *Inorg. Chem.* **2010**, *49*, 3629–3645.

(579) Chufán, E. E.; Mondal, B.; Gandhi, T.; Kim, E.; Rubie, N. D.; Moëgne-Loccoz, P.; Karlin, K. D. Reactivity Studies on Fe<sup>III</sup>–(O<sub>2</sub>)–Cu<sup>II</sup> Compounds: Influence of the Ligand Architecture and Copper Ligand Denticity. *Inorg. Chem.* **2007**, *46*, 6382–6394.

(580) Kim, E.; Helton, M. E.; Wasser, I. M.; Karlin, K. D.; Lu, S.; Huang, H.-w.; Moëgne-Loccoz, P.; Incarvito, C. D.; Rheingold, A. L.; Honecker, M.; et al. Superoxo,  $\mu$ -Peroxo, and  $\mu$ -Oxo Complexes from Heme/O<sub>2</sub> and Heme-Cu/O<sub>2</sub> Reactivity: Copper Ligand Influences in Cytochrome *c* Oxidase Models. *Proc. Natl. Acad. Sci. U. S. A.* **2003**, *100*, 3623–3628.

(581) Kieber-Emmons, M. T.; Li, Y.; Halime, Z.; Karlin, K. D.; Solomon, E. I. Electronic Structure of a Low-Spin Heme/Cu Peroxide Complex: Spin-State and Spin-Topology Contributions to Reactivity. *Inorg. Chem.* **2011**, *50*, 11777–11786.

(582) Kieber-Emmons, M. T.; Qayyum, M. F.; Li, Y.; Halime, Z.; Hodgson, K. O.; Hedman, B.; Karlin, K. D.; Solomon, E. I. Spectroscopic Elucidation of a New Heme/Copper Dioxygen Structure Type: Implications for O–O Bond Rupture in Cytochrome *c* Oxidase. *Angew. Chem., Int. Ed.* **2012**, *51*, 168–172.

(583) Garcia-Bosch, I.; Adam, S. M.; Schaefer, A. W.; Sharma, S. K.; Peterson, R. L.; Solomon, E. I.; Karlin, K. D. A “Naked” Fe<sup>III</sup>–(O<sub>2</sub>)–Cu<sup>II</sup> Species Allows for Structural and Spectroscopic Tuning of Low-Spin Heme-Peroxo-Cu Complexes. *J. Am. Chem. Soc.* **2015**, *137*, 1032–1035.

(584) Collman, J. P.; Sunderland, C. J.; Berg, K. E.; Vance, M. A.; Solomon, E. I. Spectroscopic Evidence for a Heme–Superoxide/Cu(I) Intermediate in a Functional Model of Cytochrome *c* Oxidase. *J. Am. Chem. Soc.* **2003**, *125*, 6648–6649.

(585) Liu, J.-G.; Naruta, Y.; Tani, F. A Functional Model of the Cytochrome c Oxidase Active Site: Unique Conversion of a Heme- $\mu$ -peroxo-CuII Intermediate into Heme- superoxo/CuI. *Angew. Chem., Int. Ed.* **2005**, *44*, 1836–1840.

(586) Collman, J. P.; Decreau, R. A.; Sunderland, C. J. Single-Turnover Intermolecular Reaction Between a Fe-Superoxide-Cu Cytochrome C Oxidase Model and Exogeneous Tyr244 Mimics. *Chem. Commun.* **2006**, 3894–3896.

(587) Collman, J. P.; Decréau, R. A.; Yan, Y.; Yoon, J.; Solomon, E. I. Intramolecular Single-Turnover Reaction in a Cytochrome c Oxidase Model Bearing a Tyr244 Mimic. *J. Am. Chem. Soc.* **2007**, *129*, 5794–5795.

(588) Adam, S. M.; Garcia-Bosch, I.; Schaefer, A. W.; Sharma, S. K.; Siegler, M. A.; Solomon, E. I.; Karlin, K. D. Critical Aspects of Heme- Peroxo-Cu Complex Structure and Nature of Proton Source Dictate Metal-Operoxo Breakage versus Reductive O–O Cleavage Chemistry. *J. Am. Chem. Soc.* **2017**, *139*, 472–481.

(589) Natri, F.; Chino, M.; Maglio, O.; Bhagi-Damodaran, A.; Lu, Y.; Lombardi, A. Design and Engineering of Artificial Oxygen-Activating Metalloenzymes. *Chem. Soc. Rev.* **2016**, *45*, 5020–5054.

(590) Sigman, J. A.; Kim, H. K.; Zhao, X.; Carey, J. R.; Lu, Y. The Role of Copper and Protons in Heme-Copper Oxidases: Kinetic Study of an Engineered Heme-Copper Center in Myoglobin. *Proc. Natl. Acad. Sci. U. S. A.* **2003**, *100*, 3629–3634.

(591) Liu, X.; Yu, Y.; Hu, C.; Zhang, W.; Lu, Y.; Wang, J. Significant Increase of Oxidase Activity through the Genetic Incorporation of a Tyrosine-Histidine Cross-Link in a Myoglobin Model of Heme-Copper Oxidase. *Angew. Chem., Int. Ed.* **2012**, *51*, 4312–4316.

(592) Miner, K. D.; Mukherjee, A.; Gao, Y.-G.; Null, E. L.; Petrik, I. D.; Zhao, X.; Yeung, N.; Robinson, H.; Lu, Y. A Designed Functional Metalloenzyme that Reduces O<sub>2</sub> to H<sub>2</sub>O with Over One Thousand Turnovers. *Angew. Chem., Int. Ed.* **2012**, *51*, 5589–5592.

(593) Petrik, I. D.; Davydov, R.; Ross, M.; Zhao, X.; Hoffman, B.; Lu, Y. Spectroscopic and Crystallographic Evidence for the Role of a Water-Containing H-Bond Network in Oxidase Activity of an Engineered Myoglobin. *J. Am. Chem. Soc.* **2016**, *138*, 1134–1137.

(594) Bhagi-Damodaran, A.; Michael, M. A.; Zhu, Q.; Reed, J.; Sandoval, B. A.; Mirts, E. N.; Chakraborty, S.; Moënné-Loccoz, P.; Zhang, Y.; Lu, Y. Why Copper is Preferred over Iron for Oxygen Activation and Reduction in Haem-Copper Oxidases. *Nat. Chem.* **2016**, *9*, 257–263.

(595) Yan, M.; Lo, J. C.; Edwards, J. T.; Baran, P. S. Radicals: Reactive Intermediates with Translational Potential. *J. Am. Chem. Soc.* **2016**, *138*, 12692–12714.

(596) Prier, C. K.; Rankic, D. A.; MacMillan, D. W. C. Visible Light Photoredox Catalysis with Transition Metal Complexes: Applications in Organic Synthesis. *Chem. Rev.* **2013**, *113*, 5322–5363.

(597) Studer, A.; Curran, D. P. Catalysis of Radical Reactions: A Radical Chemistry Perspective. *Angew. Chem., Int. Ed.* **2016**, *55*, 58–102.

(598) Renata, H.; Wang, Z. J.; Arnold, F. H. Expanding the Enzyme Universe: Accessing Non-Natural Reactions by Mechanism-Guided Directed Evolution. *Angew. Chem., Int. Ed.* **2015**, *54*, 3351–3367.

(599) Prier, C. K.; Arnold, F. H. Chemomimetic Biocatalysis: Exploiting the Synthetic Potential of Cofactor-Dependent Enzymes To Create New Catalysts. *J. Am. Chem. Soc.* **2015**, *137*, 13992–14006.